THE UNIVERSITY *of* EDINBURGH

Cellular and molecular mechanisms of motor neuron vulnerability in degenerative disease and injury.

Rachel Ann Kline

A thesis submitted for the degree of

MSc by Research

The University of Edinburgh

2016

DECLARATION

I declare that the work presented in this thesis and its composition are entirely my own unless otherwise clearly stated in the text.

……..

Rachel Ann Kline

Acknowledgements

Beyond all, I would like to extend my sincere gratitude to The Gwendolyn Strong Foundation for funding the opportunity for me to undertake this project. The incredible courage of SMA patients and their families, like the Strongs, is my “Never Give Up.”

First and foremost, thank you to Lyndsay Murray, my supervisor, although you’ve been a wonderful mentor to me in so much more than just science. I cannot tell you how grateful I am that you always seem to find the time to help me. Most of all, I appreciate you teaching me the value of being able to take a deep breath and chill out! It has been a genuine privilege to work for you this year and I hope I can continue to do your teachings justice. I am also eternally grateful to Tom Wishart, my second supervisor; thank you for your technical expertise, continual support and seemingly unwavering patience. If I were to make cakes every time I wanted to say thank you for your help, I would be baking until the next century.

To Sam Eaton and Maica Llavero of the Wishart lab, thank you for the technical support with all things protein-related, and even more so, for always being so kind and helpful. To all members of the Gillingwater lab, thank you for the many interesting discussions, technical help, and valuable insight over the year, and for making Lab 222 a great one to work in. To all members of the best office in the Hugh Robson Building, Office 228, thank you for the great times…and endless supply of sweet things, although perhaps we ought to cut down! In particular, thank you, Natalie Courtney, for being a stalwart source of laughter and conversation that spans the realm of cranial muscles to “leg amputations” and beyond…you never fail to make me laugh and I hope that the future holds many more cups of tea and chats!

To the extended Dunn/McGrath clan: going on so many years away from home can feel very lonely at times, but being an adoptee of an amazingly welcoming, gigantic Scottish family makes it so much happier. In particular, thank you Chris, Maria and Aunty Trisha for being such a loving second family to me.

To my family whom I love and miss so very much: thank you for 23 years of love and support; it is because of you that I have had this, among so many other, wonderful opportunities in my life. Dad, for instilling your love of learning and ranting (sometimes at the same time!); Mom, for an inspirational embodiment of true grit. Bobby and Andrea, you two are the best siblings a person could ever ask for, and although you won't let me say it in person, I am very proud of you.

And finally, thank you, Peter, the most patient listener I believe this world has ever conceived. The toughest days are made a thousand times better with as little as a cup of tea and a smile from you.

ABSTRACT

The distal compartments of the motor neuron represent early and significant targets across situations of both neurodegenerative disease and traumatic injury. In this thesis, we address two distinct scenarios of axonal and synaptic degeneration. First, we explore neuromuscular junction pathology in a mouse model of the heritable motor neuron disease spinal muscular atrophy (SMA) and address the capacity for neuronal regeneration following restoration of the pathologically depleted Survival Motor Neuron (SMN) protein. We demonstrate that motor neurons exhibit a robust and phenotypically translatable recovery from considerable levels of cellular and molecular dysfunction. In the second chapter, we explore the phenomenon of delayed Wallerian degeneration in neonatal mice. We employ a quantitative mass spectrometry approach to profile proteins exhibiting a temporal expression pattern in line with previously observed postnatal changes in axonal and synaptic vulnerability to injury. We then utilise a variety of proteomics tools to identify pathways which may mechanistically contribute to age-dependent resistance to degeneration. Together, these results provide a preliminary insight into the cellular and molecular mechanisms underlying motor neuron vulnerability in two independent models of degenerative disease and injury.

Table of Contents

ABBREVIATIONS

AAL	Abductor auris longus
AChR	Acetylcholine receptor
ALS	Amyotrophic Lateral Sclerosis
AS	Auricularis superior
BCA	Bisinchoninic acid assay
BSA	Bovine serum albumin
BTX	Bungarotoxin
FITC	Fluorescein isothiocyanate
IPA	Ingenuity Pathway Analysis
iTRAQ	isobaric Tags for Relative and Absolute Quantitation
LAL(c/r)	Levator auris longus (caudal/rostral)
LC-MS/MS	Liquid chromatography-tandem mass spectrometry
MND	Motor neuron disease
NMJ	Neuromuscular junction

P	Postnatal (eg. Postnatal day 4= P4)
PAGE	Polyacrylamide gel electrophoresis
PBS	Phosphate-buffered saline
PCR	Polymerase chain reaction
PFA	Paraformaldehyde
qRT-PCR	Quantitative reverse-transcription polymerase chain reaction
RIPA	Radioimmunoprecipitation assay
SDS	Sodium dodecyl sulfate
SMA	Spinal muscular atrophy
Smn/*SMN*/SMN	Survival motor neuron: Murine gene/*HUMAN GENE*/PROTEIN
snRNP	Small nuclear ribonucleoprotein
TRITC	Tetramethylrhodamineisothiocyanate
TM	Tamoxifen
TVA	Transversus abdominis
Wld^S	Wallerian degeneration slow
WT	Wildtype

Chapter ONE: General Introduction

1.1 Motor neuron vulnerability in neurodegeneration

While it is evident that neurons in both the central and peripheral nervous systems (CNS and PNS) are vulnerable to degenerate in response to a number of injury, disease, and toxic-related insults, the mechanisms underlying these degenerative processes remain elusive. Amongst the diverse body of neurodegenerative conditions representing a significant emotional and economic burden across the globe, diseases and traumatic injury to the lower motor neuron remain largely untreatable, and therefore have garnered a great deal of interest from both basic researchers and clinicians. This chapter seeks to provide a very brief review of the literature comprising the current understanding of the architecture of the lower motor neuron, with a particular emphasis on the peripheral synapse between the lower motor neuron and the muscle, otherwise known as the neuromuscular junction.

1.2 The Neuromuscular Junction (NMJ)

1.2.1 Overview

Lower motor neurons are long neuronal processes that connect the spinal cord to the skeletal muscle in order to facilitate electrochemical signalling for voluntary movement. The cell bodies of motor neurons are located within the ventral horn of the spinal cord (for control of muscles of the trunk and limbs), or within the facial nuclei of the brainstem (for control of the muscles of the head and neck), from which they project as bundles of axons into the periphery (Bear et al., 2001). Lower motor neurons may be further classified as either gamma motor neurons, responsible for regulating the

muscle spindle stretch reflex, or as alpha motor neurons, which dictate the force of voluntary muscle contraction (Bear et al., 2001). This thesis will primarily concern alpha motor neurons and their peripheral synapses, the specialised nerve-muscle interfaces known as neuromuscular junctions (NMJs) (Bear et al., 2001).

Synapses within both the CNS and the PNS, including NMJs, are early and significant pathological targets in degeneration promoted by disease, injury, or toxic insult (Baxter, Gillingwater, & Parson, 2008; T H Gillingwater & Ribchester, 2001; Murray et al., 2008). As it is of utmost interest to elucidate what cellular and molecular factors contribute to, or conversely, attenuate the degenerative process, it is prudent to understand that the integrity of highly vulnerable NMJ often reflects the status of the remaining motor neuron under the influence of these factors. Prior to an examination of the cellular and molecular basis of motor neuron degeneration in the subsequent chapters of this thesis, I will provide a simplistic summary of healthy motor neuron structure and function, with a particular emphasis on the NMJ, before summarising two distinct mechanisms by which motor neurons may degenerate.

1.2.3 Cytoarchitecture

The term “neuromuscular junction,” referring to the interface of the motor neuron nerve terminal with the skeletal muscle, may be attributed to the celebrated German electrophysiologist Wilhelm Kühne in his 1862 description of nerve cells terminating on the leg muscles of a frog (Kühne, 1862).

Broadly speaking, the neuromuscular junction is an interface of three distinct cell types: the nerve terminal of the motor neuron, the skeletal muscle, and the terminal myelinating Schwann cell (Bear et al., 2001). A number of structural proteins are required to maintain the architectural integrity of this interface, including the

neurofilament family (Bear et al.,2001). The pre-synaptic nerve terminal of the motor neuron represents the physical locale of neurotransmitter release, and subsequently harbours a complex network of assembled microtubules responsible for the transport and reuptake of vesicle-enclosed neurotransmitters (Bear et al., 2001; Grinnel et al., 1995). An increasing body of evidence suggests that this pre-synaptic compartment harbours its own unique molecular and metabolic composition, including uniquely synapse-specific mitochondria and ubiquitin proteasome system components (Bertoni-Freddari et al., 1993; Wishart et al., 2014).

Unlike other synapses within the CNS or PNS, the NMJ facilitates electrochemical signalling utilising exclusively acetylcholine (ACh) as a neurotransmitter (Bear et al., 2001). The post-synaptic acetylcholine receptor (AChR), or endplate, receives all synaptic transmission and is comprised of a series of folds in the membrane of the post-synaptic muscle fibre (Bear et al., 2001).

1.2.3 Development

Both the mammalian pre-synaptic nerve terminal and the post-synaptic motor endplate undergo a series of developmental alterations, commencing *in utero* and ending during late gestation in humans, and in early postnatal life in mice (Sanes and Lichtman, 1999). In simplistic terms, the most important developmental events in the pre-synaptic nerve terminal may be summarised by axon pathfinding from the embryonic spinal cord to the muscle, culminating in the polyinnervation of the post-synaptic endplate by multiple nerve terminal inputs. This polyinnervation is selectively eliminated over postnatal maturation to yield the “adult” innervation pattern of a single nerve terminal input per endplate. The post-synaptic AChR also undergoes a marked degree of ultrastructural transformation during this developmental period, evolving from an

immature simple “plaque”-like structure to a complex, highly invaginated “pretzel”-like mature endplate (Kariya et al., 2008).

1.3 Mechanisms of neurodegeneration: Dying-back neuropathy

While a number of heritable or spontaneous diseases, as well as injuries, of the PNS have been demonstrated to significantly disrupt the integrity of the motor neuron, it is clear that there are distinct pathways, harbouring unique morphological characteristics, by which the motor neuron may degenerate (Murray et al., 2008). capable of disrupting the integrity of peripheral nerves. Motor neuron diseases, such as amyotrophic lateral sclerosis (ALS) and spinal muscular atrophy (SMA) are classified as “dying-back” neuropathies, due to their characteristic withdrawal of the pre-synaptic nerve terminal from the NMJ.

1.3.1 Dieback neuropathology: a loss of NMJ integrity

Die-back neuropathies, exemplified by conditions such as SMA and in the *wasted* mouse model of motor neuron degeneration, are characterised by the retrograde withdrawal of the pre-synaptic terminal from the distal synapse (Murray et al., 2008; Newbery et al., 2005). The retracting distal nerve terminal and axon appear to shrink back into themselves, in a structure referred to as a “retraction bulb,” leaving the skeletal muscle devoid of innervation (Gillingwater and Ribchester, 2003).

1.4 Mechanisms of neurodegeneration: Wallerian degeneration

The earliest characterisation of the neuronal response to traumatic injury was provided by Augustus Volney Waller in 1850, in his description of severed frog hypoglossal and glossopharyngeal nerves (Waller, 1850). He observed that a marked degree of neuronal fragmentation occurred distal to the point of injury and was subsequently cleared away by an unknown mechanism, while the portion of nerve proximal to the cut was retained for a comparably longer period of time (Waller, 1850). This process, now termed "Wallerian degeneration," is a highly regulated means of degeneration conserved between multiple species and is the typical neuronal response to traumatic injury, although it is also observed in multiple sclerosis (Gillingwater & Ribchester, 2001; Ge et al., 2006). For an in-depth review of the structural events comprising Wallerian degeneration, see Gillingwater & Ribchester, 2001; however, Wallerian degeneration may be simplistically summarised as the following: (1) A "latent" phase, occuring within 24-48 hours in mice (Beirowski et al., 2005), in which axons disintegrate distally from the point of injury and draw back from the nodes of Ranvier to form distinct small fragments. (2) Subsequent to fragmentation, phagocytosing cells such as Schwann cells and macrophages clear up fragments, while (3) Simultaneously, Schwann cells that are still intact secrete various growth factors to promote the regeneration of the disintegrated nerve terminal (Gillingwater & Ribchester, 2001).

1.4.2 Wallerian Degeneration Slow (Wld^S)

The spontaneous Wld^S mutation, resulting from the chimeric fusion of a portion of the ubiquitination factor Ube4b with the nicotinamide mononucleotide adenylyltransferase (Nmnat) gene, was identified in 1989, and has provided a significant degree of insight into the cellular and molecular factors constituting neuroprotection from degeneration

(Lunn et al., 1989; Mack et al., 2001). As described previously, Wallerian fragmentation following axotomy generally occurs within 24-28 hours after insult; an identical procedure performed in Wld^s mice results in the striking preservation of axonal and synaptic structural and functional integrity for up to two weeks following injury (Ribchester et al., 1995). Application of the Wld^S mutation to attenuate degeneration in a number of mouse models of disease, injury, or toxic-induced nerve trauma has suggested that the degenerative response to highly distinct insults may involve common mechanisms (Ferri, Sanes, Coleman, Cunningham, & Kato, 2003; Gillingwater et al., 2006; Wang, Davis, Culver, & Glass, 2002). Nevertheless, the processes comprising this commonality, as well as an understanding of why other conditions, such as SMA, are not influenced by the introduction of Wld, remain poorly understood (Kariya et al., 2009).

1.5 Aims of this thesis

1.5.1 Summary

From both the existing literature to be outlined subsequently in this thesis and from studies conducted within our own laboratories, it is clear that the cellular and molecular basis of vulnerability to either disease or injury-induced degeneration at the neuromuscular junction (NMJ) remain unknown. In this thesis, I will perform two parallel studies investigating the factors influencing NMJ integrity under degenerative conditions: firstly, in a murine model of the childhood neurodegenerative disease spinal muscular atrophy (SMA) and secondly, in wildtype mice exhibiting an endogenous and developmentally-regulated resistance to injury-induced degeneration. These findings contribute to our understanding of the complex cellular

and molecular cascades influencing the ultimate outcome of the motor neuron in situations of injury and disease.

Hypothesis 1: Neuromuscular junction and molecular correlates of motor neuron degeneration are present in the Smn^{Res} mouse model of SMA at a time of symptomatic onset.

AIM 1: Investigate the extent of cellular and molecular pathology present within the *Smn^{Res}* mouse model at P4, a symptomatic time point within the therapeutic window.

1a. Characterise the typical disease time course of the *Smn^{Res}* mouse model of SMA in our hands, in order to identify the point of symptomatic onset.

1b. Investigate the presence of both pre- and post-synaptic neuromuscular junction pathology in a selection of muscle groups within the *Smn^{Res}* model at an early-symptomatic time point identified in *1a.*

1c. Determine if molecular alterations suggesting an up-regulation of the p53 apoptotic cell death pathway in other mouse models of SMA are present in the *Smn^{Res}* model at early-symptomatic time point outlined in *1a.*

1d. Assess whether select transcriptional alterations identified from large-scale screens of two different early-symptomatic SMA mouse models are also present in the *Smn^{Res}* model at the early-symptomatic time point outlined in *1a*

Hypothesis 2: Postnatal restoration of the pathologically depleted SMN protein at the symptomatic time point outlined in AIM 1, promotes phenotypic improvement that may be attributed to improvements in the cytoarchitecture of the damaged NMJ.

AIM 2: Investigate structural modifications at the neuromuscular junction that accompany rescue of neuromuscular phenotype after conditional re-expression of SMN at an early symptomatic time point in the *Smn^{Res}* model.

2a. Induce re-expression of SMN at the early symptomatic time point identified in *1a* in order to evaluate phenotypic improvement and survival in our hands.

2b. Assess and compare the pathological status of neuromuscular junctions within a variety of muscle groups in rescued versus non-rescued *Smn^{Res}* mice.

2c. Determine whether the differences in pathology between rescued and non-rescued mice reported in *1b* are the result of restored SMN slowing, halting, or reversing pre-synaptic degeneration at the neuromuscular junction.

Hypothesis 3: Molecular alterations in both the nerve and muscle may contribute to the marked increase in neuromuscular junction vulnerability to injury-induced degeneration in wildtype C57BL/J mice over the P12-P24 postnatal period.

AIM 3: Profile molecular alterations occurring in both the pre-synaptic nerve and post-synaptic muscle over a period of increasing NMJ vulnerability in the wildtype C57BL/6 mouse.

3a. Evaluate the efficacy of the TMT10plex™ mass tagging technique, which to date has not been definitively evaluated in whole-tissue studies, as a quantitative proteomics method.

3b. Perform functional annotation analysis on applicably filtered proteomic results to understand what biological processes may be evolving over this critical postnatal period.

3c. Utilise pathway analysis software to generate cellular and molecular predictive networks from the data set to further understand what mechanisms may account for an age-dependant synaptic vulnerability to degeneration.

Chapter TWO: Introduction

2.1 Overview

Spinal muscular atrophy (SMA) is a devastating childhood autosomal recessive disorder resulting from the heritable insufficiency of the ubiquitously expressed SMN (**S**urvival **M**otor **N**euron) protein. With 1 in 40 individuals estimated to be heterozygous carriers of the causative mutation, and an incidence of an estimated 1 in 6-12,000 live births, SMA may be considered the leading genetic cause of childhood and infant mortality worldwide (Farrar, Johnston, Grattan-Smith, Turner, & Kiernan, 2009; Pearn, 1978; Sugarman et al., 2012). Despite the ubiquitous expression of SMN, the archetypal clinical manifestation of this deficit is largely neuromuscular; denervation and death of the lower alpha motor neurons with accompanying atrophy of the proximal skeletal muscles promotes paralysis, respiratory failure, and ultimately, in the majority of cases, death within the first decade of life (Russman, 2007). Within the motor neuron, the neuromuscular junction (NMJ), the point at which the neuron synapses with the skeletal muscle, represents an early and significant pathological target (Dachs et al., 2011; Kariya et al., 2008; Kong et al., 2009; Murray et al., 2008).

An increasingly therapeutics-driven body of research shows promising results in the capacity for systems-wide postnatal restoration of SMN to ameliorate the neuromuscular phenotype and improve lifespan, but only if this is performed at an early symptomatic time point (Foust et al., 2010; Hua et al., 2011; Kariya et al., 2014; Lutz et al., 2011; Robbins, Glascock, Osman, Miller, & Lorson, 2014). The precise cellular and molecular mechanisms underlying this phenotypic rescue, as well as the basis behind the apparent temporal limitations of this approach, also remain poorly

understood. Consequentially, determining the cellular and molecular consequences of SMN restoration upon the motor unit will not only enhance our understanding of the degenerative process, but also highlight which aspects may fail to recover, or conversely, improve, upon re-expression of SMN. These findings may ultimately influence the efficacy of future SMN-based treatments by determining which pathological aspects remain the most vulnerable, and which harbour the capacity for therapeutically-driven repair.

2.1.1 Clinical Background

From its earliest clinical descriptions in the late 19th century by physicians Guido Werdnig and Johann Hoffman, spinal muscular atrophy has been considered a primarily neuromuscular disorder, characterized by its distinctive symptoms of proximal muscle weakness and eventual paralysis; these symptoms paired with SMA's typical manifestation in the first year of life lend it the colloquial term of "floppy infant syndrome" (Farrar et al., 2009). Biomedical advances in the centuries following Werdnig and Hoffman's clinical observations confirmed that this neuromuscular phenotype is the result of the degeneration and death of alpha motor neurons in the ventral horn of spinal cord and lower brainstem, responsible for innervating the muscles of the proximal extremities and abdomen (Markowitz, Tinkle, & Fischbeck, 2004). Electromyographic (EMG) readings in severely affected patients that comprise the majority of diagnoses confirm this profound loss of whole motor units, with remaining motor neurons failing to respond or compensate for neighbouring denervation (Crawford & Pardo, 1996). Conversely, the EMGs of symptomatically milder, juvenile or adult onset SMA cases suggest the presence of overdeveloped motor units that may have responded to neighbouring denervation by compensatory sprouting (Crawford & Pardo, 1996).

Both clinical reports of human patients and the characterisation of animal models of the disease present the phenomenon of differential degrees of pathology between muscles and their respective associated motor units. A stark clinical example exists in the contrast between the marked denervation of the intercostal and axial muscles of the abdomen, and the relative sparing of the neighbouring diaphragm (Farrar et al., 2009). Due to the majority of respiration relying upon the diaphragm during the gradual atrophy of the remaining abdominal musculature, respiration becomes predominantly diaphragmatic; this overdevelopment of the compensatory diaphragm and atrophy of trunk muscles results in many patients developing a characteristic bell-shaped torso (Farrar et al., 2009). This curious selective vulnerability to neurodegeneration between muscle types is mirrored in multiple mouse models of SMA, with select muscles consistently exhibiting significant pathological denervation while others are relatively spared (Mélissa Bowerman, Murray, Beauvais, Pinheiro, & Kothary, 2012; Murray et al., 2008; Thomson et al., 2012). Consequentially, determining why selective proximal muscles and indeed, the motor neuron in general, are especially vulnerable to the depletion of a ubiquitous protein, remains crucial in elucidating the mechanisms underlying the neurodegeneration specifically occurring in SMA.

2.2 Molecular Genetics

2.2.1 The Survival Motor Neuron Gene

The majority of SMA cases are monogenetic disorders exhibiting a classical autosomal recessive inheritance pattern, with patients harbouring the homozygous inheritance of a mutation or deletion in the *Survival Motor Neuron 1 (SMN1)* gene, and resultant null or non-functional production of its ubiquitously expressed translational product, Survival Motor Neuron (SMN) protein. Patients are therefore entirely reliant upon the insufficient compensatory production of SMN by the paralogous *Survival Motor Neuron 2 (SMN2),* which is nearly identical to *SMN1* save for a single C→T base-pair transition within exon 7 (C L Lorson, Hahnen, Androphy, & Wirth, 1999a; U. R. Monani et al., 1999). Nevertheless, this single nucleotide difference generates an exonic splicing silencer or suppresses an exonic splicing enhancer within exon 7; the majority of *SMN2* transcripts produced therefore lack exon 7 and are translated into unstable and rapidly degraded SMN isoforms (Lorson et al. 1999; Lorson & Androphy 2000). *SMN2* exists in varying copy numbers between individuals, with a higher copy number—and therefore higher levels of compensatory bioavailable SMN—correlating to a milder disease severity. Indeed, the inverse correlation between *SMN2* copy number and disease severity is so closely linked that the clinical spectrum of SMA, based on parameters such as age of onset, extent of paralysis and lifespan, is almost inevitably linked to *SMN2* copy number (Lefebvre et al., 1997). However, it should be noted that *SMN2* copy number itself is not the sole disease modifier, as genomic sequencing of several SMA patient cases in which *SMN2* copy number did not directly correlate to clinical phenotype, indicated that splice variations themselves within exon 7 of *SMN2* also hold significant influence upon clinical severity (Prior et al., 2009). Tragically, in the majority of cases, affected individuals possess two or fewer copies of *SMN2* and

accompanying very low production of compensatory SMN, and therefore experience symptomatic onset usually within the first six months of life.

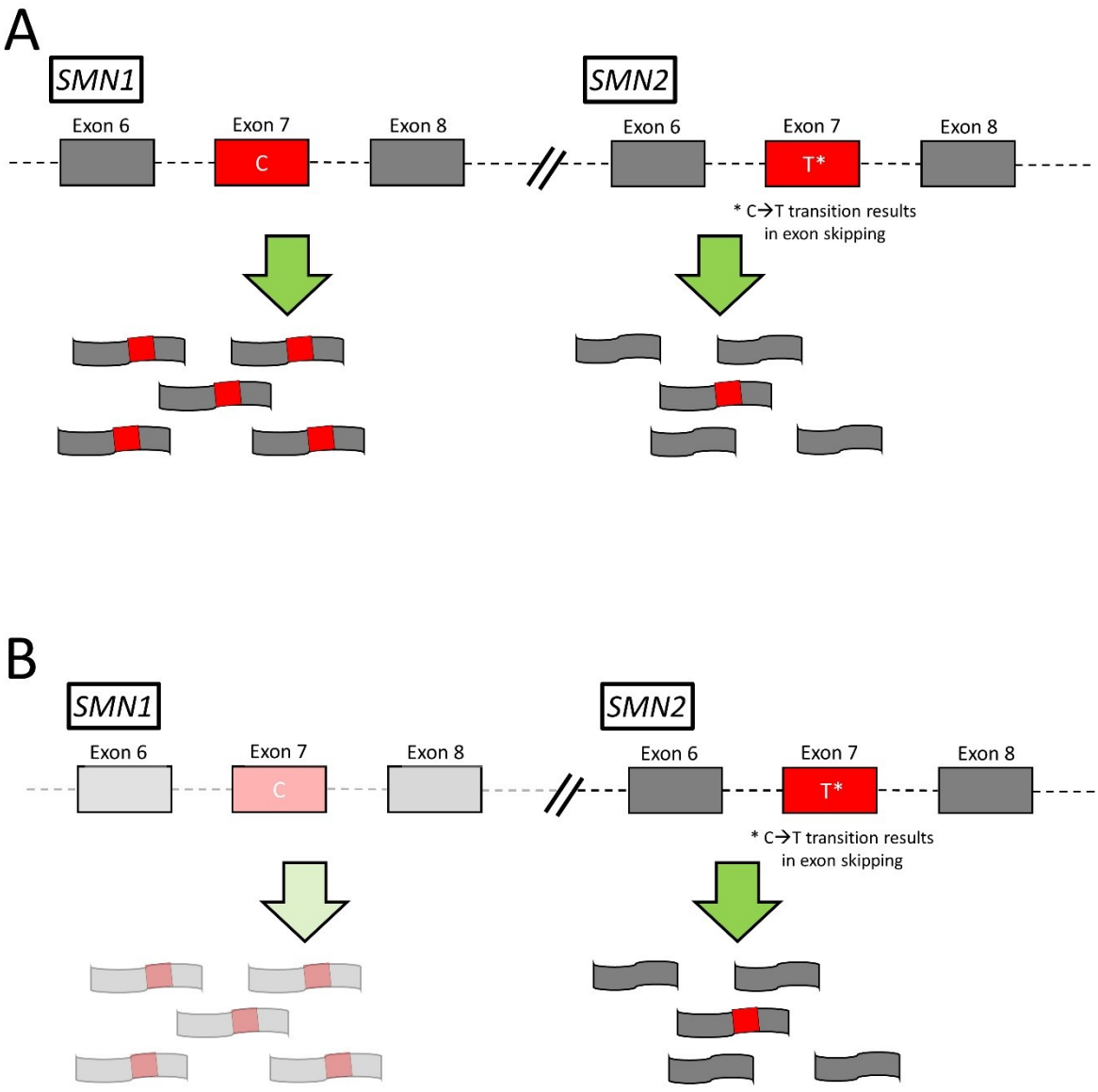

Figure 2.1. Homozygous deletion of *SMN1* results in insufficient compensatory production of Smn by *SMN2.*

A. Normal inheritance of one or two fully-functional copies of *SMN1* results in the physiologically sufficient production of full-length Smn transcripts. **B.** SMA individuals inherit a homozygous mutation or deletion of the *SMN1* gene, resulting in null production of mSmn. Smn transcript levels are therefore reliant upon production by the paralogous *SMN2,* in which a single nucleotide transition within exon 7 promotes aberrant splicing. The majority of transcripts lack exon 7 and are truncated and extremely short-lived, and are translated into equally unstable isoforms. *SMN2* copy number dictates levels of this bioavailable compensatory SMN.

2.2.2 The Survival Motor Neuron Protein

The translational product of *SMN1* and *SMN2,* Survival Motor Neuron (SMN), is a ubiquitously expressed 38kDa protein, with higher levels of expression present in the heart, kidney, and brain (Coovert et al., 1997). Mechanistically, SMN has been implicated in a variety of sub-cellular roles, the most definitive being the biogenesis of the molecular agents responsible for the intronic splicing of pre-mRNA (Chari, Paknia, & Fischer, 2009). Consequentially, one of the more prevalent theories behind the motor neuron-specific degeneration in SMA suggests that dysregulated spliceosomal assembly may impact upon transcripts particularly critical to motor neuron stability. Additionally, SMN has been shown to be involved in axonal mRNA transport, with another hypothesis suggesting that disrupted transport of key transcripts to and from the distal compartments of the lower motor unit promotes the degenerative process (Rossoll et al., 2003). There is also a theorized third mechanism combining the two hypotheses, in which abnormal splice isoforms resulting from aberrant snRNP assembly may perturb molecular pathways involved in the axonal transport of mRNAs. This thesis seeks to provide a subsequent brief summary of SMN's hypothesised endogenous functions and how they may correlate to the neurodegenerative dysfunction present in SMA.

2.2.3 Function of the Survival Motor Neuron Protein

The best-characterised cellular role of the SMN protein is that of the assembly of the SMN complex, a large, ubiquitous molecular structure facilitating the biogenesis and transport of small nuclear ribonucleo proteins (snRNPs) to the nucleus (Chari et al., 2009). These snRNP core complexes form the basis of the pre-mRNA spliceosome, nuclear molecular complexes responsible for intronic splicing of pre-mRNA as well as other post-transcriptional modifications (Chari et al., 2009).

Although the precise stoichiometry of the SMN complex has not been conclusively described, its function appears to rely upon self-association of SMN, with both *in vitro* and *in vivo* complementation assays supporting its oligomeric existence (Christian L. Lorson et al., 1998; Umrao R Monani et al., 2003). In the majority of tissues, the SMN multimer is sequestered in both the cytoplasm and nuclear bodies known as “gems”, which may be identified by immunohistochemical labelling of SMN itself to distinguish complex-enriched spots from other nuclear bodies (Q Liu & Dreyfuss, 1996). An examination of normal cardiac and smooth muscle revealed an absence of these gems, suggesting that these nuclear bodies may serve to collate reserve SMN and other snRNP-associated proteins rather than play a more integral role in Smn’s function (Young et al. 2000).

The currently established structure of the oligomeric SMN complex consists of SMN bound to the gemin proteins (of which Gemins 2-8 are currently best characterized) and the unr-interacting protein (unrip), although interactions with several additional, non-gemin substrates, usually components of various RNP complexes, have also been identified (Battle et al., 2006; Qing Liu, Fischer, Wang, & Dreyfuss, 1997). The SMN-gemin complex, via Gemin 5, binds to small nuclear RNAs (snRNA), termed U1,

U2, U4, U5, U12 and U4atac , which are synthesised in the nucleus as pre-snRNA by RNA polymerase II (RNA polII) and modified prior to export into the cytosol (Yong, Kasim, Bachorik, Wan, & Dreyfuss, 2010). The SMN-gemin associated snRNAs then bind to complementary cytosolic Sm proteins recruited by Gemin 2, to form an intermediate snRNP RNA-protein complex with an Sm core. The SMN assemblyosome then chaperones these snRNPS through the remainder of their biogenesis through their import into the nucleus, where the snRNP core complexes undergo final modifications before oligomerizing as components of either the major (snRNPs U1, U2, U4, U5) or minor (snRNPs U11, U12 and U4atac) spliceosome. Broadly speaking, both the major and minor spliceosome are responsible for the recognition, splicing and removal of intronic sequences of pre-mRNAs, with the minor spliceosome processing a specific subset of low-abundance pre-mRNAs. Additionally, the snRNP U1 appears to hold specialised functions outwith its spliceosomal role in regulating transcript levels by selectively protecting transcripts from premature cleavage or polyadenylation(Berg et al., 2012).

Although a characterisation of the broad range of molecular cascades influenced by snRNPs, whether as part of the SMN assemblyosome or through non-splicing roles, remains largely non-comprehensive, snRNP activity is clearly crucial in the translation from the relatively limited genome to a multifarious proteome spanning diverse tissues and systems. It is therefore natural to consider that elucidating SMN-dependent disruptions in snRNP assembly and their potential influence upon the functional proteome within the lower motor neuron may reveal candidate mechanisms of degeneration in SMA.

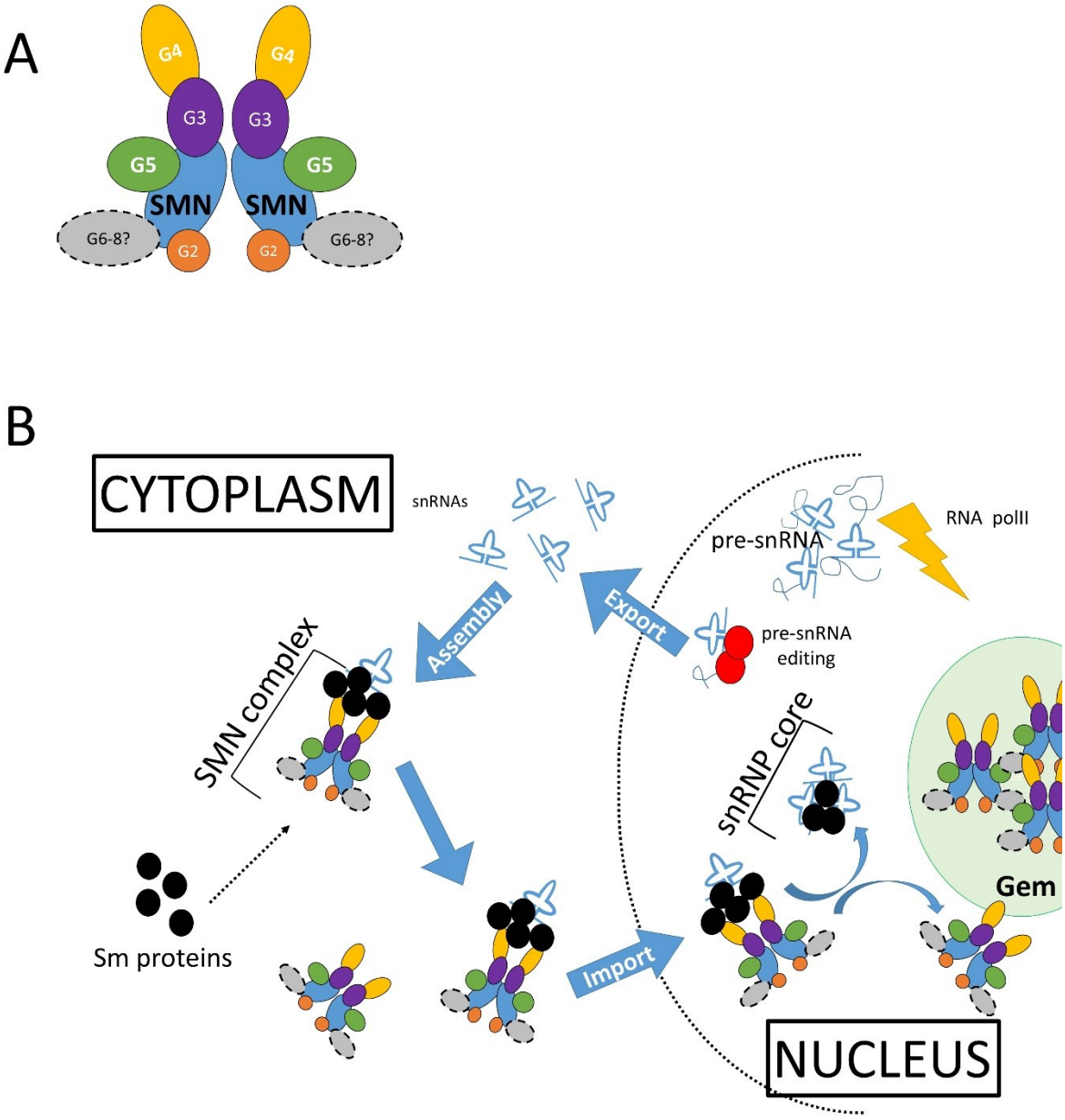

Figure 2.2. The SMN complex

A. Schematic representation of the known structure of the SMN-gemin complex. Complex is representatively shown to be dimeric. Binding sites of Gemin 2 (G2), Gemin 5 (G5) and Gemin 3 (G3) feature direct binding with Smn. Gemin 4 (G4) is indirectly associated with Smn through binding to Gemin 3. To date, the binding sites of Gemins 6-8 (G6-8) have not yet been determined. **B.** Schematic representation of SMN-gemin complex mediated snRNP assembly. Formation of the SMN complex-bound snRNPs occurs in the cytosol through the interactions of snRNAs and a corresponding Sm protein core. The complex is imported back into the nucleus, where the snRNP cores form the basis of either the major or minor spliceosome. Dissociated SMN-gemin complexes are sequestered in nuclear "gems."

2.2.4 The SMN complex and snRNP Assembly in Spinal Muscular Atrophy

While a precise mechanism demonstrating the direct impact of defective snRNP assembly upon the motor neuron-specific degenerative cascade in SMA has not been definitively proven, an increasing body of evidence reveals a marked deficiency in snRNP biogenesis in human patients as well as across multiple animal models of SMA. Prior to a report of these observed defects, it should be noted that the structural characterisation of the SMN protein in its native conformation, as well as the development of several functional assays to evaluate complex-substrate binding, has established a set of parameters evidently integral to the functionality of the SMN assemblyosome (Battle et al., 2006; Berg et al., 2012; Christian L. Lorson et al., 1998; Lutz et al., 2011; Yong et al., 2010). Intrinsic defects in SMN expression impacting upon these parameters may disrupt SMN complex assembly and snRNP biogenesis, spliceosomal formation, and ultimately, mediate potentially degenerative transcriptional and translational perturbations. The parameters for normal SMN-complex associated SMN function may be broadly summarised by the following criteria:

1. The capacity for self-association (oligomerization).
2. In the instance of a mutated SMN isoform, the capacity for association with co-existing full-length SMN (FL-SMN).
3. The capacity to bind gemin proteins.
4. The capacity to bind Sm proteins.

An examination of the structural biology of the SMN protein highlights several motifs and domains that are functionally critical for the execution of the above parameters. **Figure 2.3** outlines the location of several of these key domains within exons 2, 3 and

6 of SMN, and their functional significance upon either substrate binding or self-oligomerization (Burghes & Beattie, 2009).

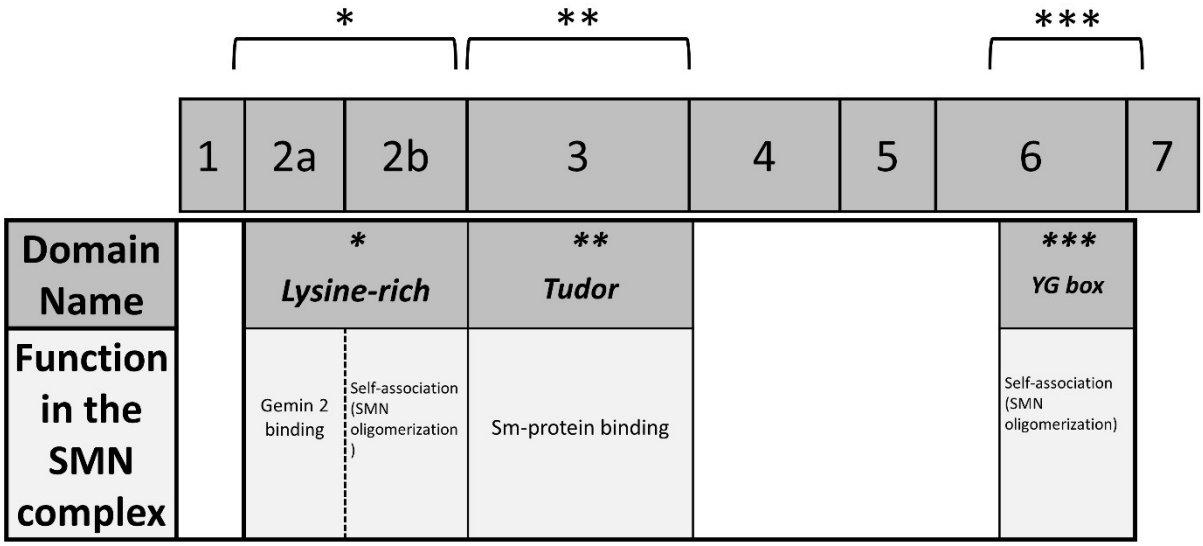

Figure 2.3. Schematic representation of exons 1-7 of Smn and translational domains understood to be key binding sites of the assembled SMN complex. The lysine-rich region within exon 2 contains sequences critical to Gemin 2 binding, responsible for recruitment of Sm proteins to the SMN-gemin complex. The 50 amino acid "Tudor" domain within exon 3 is integral to Sm protein binding and thus the formation of the snRNA-Sm core complex. The "YG-box" within exon 6, so called for its conserved $(Y\text{-}xxx\text{-}G)_3$ motif, contains sequences integral to SMN oligomerization. Mutations within *SMN1* that affect these critical domains therefore influence potentially influence snRNP assembly. Figure adapted from Burghes & Beattie, 2009. Diagram not to scale.

Although 95% of SMA patients exhibit an inherited absence of *SMN1,* the remaining 5% of cases harbour various missense mutations within the gene (Alías et al., 2009). Investigations into the functional outcome of these mutations reveal that a striking majority exist within the aforementioned critical motifs, thereby impairing the native confirmation of SMN and its functional role in snRNP biogenesis (Burghes & Beattie,

2009). Indeed, approximately 50% of *SMN1* missense mutations are mapped to the YG-box motif of exon 6, which is integral for SMN oligomerization (Young et al. 2000). A large remainder of currently identified mutations in *SMN1* are mapped to other domains integral to either oligomerization or SMN complex formation, including binding sites for both gemins and Sm proteins (Burghes & Beattie, 2009).

A large proportion of these mutations have been explored to determine their influence upon snRNP binding, usually in conjunction with a comparably small amount of FL-SMN in order to molecularly recapitulate the *in vivo* situation of an SMA patient expressing very low levels of bioavailable FL-SMN. These mutant isoforms have been subjected to a number of binding assays developed to assess their ability to associate with FL-SMN, oligomerize, or bind Sm proteins. From assaying select variants from the currently identified library of human mutations, it is apparent that different missense sequences within *SMN1* confer differential effects upon substrate and/or SMN binding, suggesting that there is indeed a spectrum of functional outcome to mutations within *SMN1* and that not all mutations are equal in their attenuation of snRNP biogenesis. For a comprehensive list of *SMN1* mutations identified in patients, and their influence upon snRNP assembly when applied *in vitro,* see review by Burghes & Beattie, 2009 (Burghes & Beattie, 2009)

Prior to the development of a viable animal model of the disease, the scarcity of immunohistochemically- labelled SMN-complex enriched nuclear “gems” in primary cultured fibroblasts from severe patients immediately suggests that the a lack of functional machinery required for snRNP assembly may indicate aberrant snRNP biogenesis in SMA (Coovert et al., 1997). Functional defects in patients were finally highlighted when lymphoblasts isolated from a severe SMA case exhibited a decreased capacity for snRNP assembly in culture compared to those obtained from

age-matched controls (Wan et al., 2005). These findings, combined with the aforementioned functional defects in SMN assemblyosome formation from missense mutations in *SMN1*, strongly implicate the "snRNP biogenesis theory" in SMA pathophysiology. Indeed, *SMN2*'s insufficiency as a phenotypic modifier in SMA individuals has been proposed to result from the inability of SMN2 truncated isoforms to oligomerize or effectively bind SMN-complex substrates, thus disrupting snRNP biogenesis and intronic splicing (Workman et al., 2009).

2.2.5 Disrupted snRNP assembly and subsequent splicing alterations in murine models of Spinal Muscular Atrophy.

A greater exploration of the mechanistic relevance of snRNP biogenesis to SMA pathophysiology has arisen from the application of previously outlined human missense mutations into animal, particularly murine, models of the disease

snRNP biogenesis and motor neuron defects in mouse models of SMA

The case for a close relationship between snRNP biogenesis and neuromuscular integrity is perhaps most strongly represented by the application of the *SMN1* missense allele A111G, a mutation demonstrably capable of high snRNP assembly *in vitro*, into *in vivo* models of SMA (Carrel et al., 2006; Shpargel & Matera, 2005; Sun et al., 2005; Workman et al., 2009). The SMN(A111G) mutation, located in the Sm-protein binding Tudor domain of exon 3, exhibits a significantly greater ability *in vitro* than other missense alleles to bind FL-SMN and Sm proteins as well as to assemble snRNPs upon co-transfection with FL-SMN. Upon introduction into the *Smn$^{-/-}$; SMN2* severe mouse model of SMA, SMN(A111G) mediated a robust extension of lifespan corresponding to an up-regulation in spinal cord snRNP assembly and snRNA

expression, notably those pertaining to the minor spliceosome (Workman et al., 2009). Additionally, introduction of SMN(A111G) RNA constructs at high concentrations to Smn-knockdown SMA zebrafish rescued archetypal axonal defects as well as extended lifespan (Workman et al., 2009). However, this phenotypic attenuation was not possible in *Smn* null mice without co-expression of transgenic *SMN2*, nor in zebrafish administered lower concentrations of RNAs (Workman et al., 2009). This suggests that in order to mediate neuromuscular improvement, snRNP assembly operates upon a physiological baseline of oligomerized SMN, from either the association of mutated isoforms to the low levels of FL-SMN endogenously present in mice with an *SMN2* background, or the self-assembly of these isoforms occurring under sufficiently high concentrations. Nevertheless, these results provide convincing implications for SMN's function in snRNP assembly as a potent modulator of the SMA neuromuscular phenotype.

Through an assessment of snRNP assembly activity across various mouse models of SMA varying in phenotypic severity, the link between snRNP assembly and SMA symptomology appears to overlie the established correlation between SMN levels and phenotypic severity. Severe mouse models of SMA exhibit very low levels of snRNP assembly, with assembly levels significantly increasing in milder models of SMA, yet still less than asymptomatic heterozygous or wildtype mice (Gabanella et al., 2007; Zhang et al., 2008). Conversely, the post-symptomatic restoration of SMN into a moderate to severe mouse model spinal muscular atrophy, induced a significant increase in snRNP assembly to complement an improvement motor defects and extension of lifespan (Lutz et al., 2011). Additionally, aberrant snRNP assembly in SMA does not appear to be relegated to the lower motor neuron; Gabanella et al (2007) report widespread defects in snRNP assembly across a variety of neuronal and

non-neuronal tissues in a severe mouse model of the disease. However, although transcriptional dysregulation appeared to be universally present, the most severe defects occurred within the spinal cord, pertaining to transcripts regulated by the minor spliceosome(Gabanella et al., 2007).

Several experiments have attempted to elucidate the mechanism by which defective snRNP assembly may contribute to the degenerative cascade. Administration of pre-assembled snRNPs to a zebrafish model of SMA, exhibiting motor axon defects, rescued axonal morphology and neuromuscular phenotype, strengthening the correlation between reduced snRNP assembly and motor neuron defects (Winkler et al., 2005). The same study also reported that knockdown of Gemin 2, responsible for the recruitment of Sm proteins to the SMN-gemin complex, is also sufficient to promote morphological defects in zebrafish motor axons. However, a novel study suggests that to the interaction between SMN and Gemin-2 may be more broadly involved in RNA metabolism, with potential interactions in a wide variety of RNPs in addition to snRNP assembly (So et al., 2016).

Splicing alterations in mouse models of SMA

Exploration into the downstream consequences of disrupted snRNP activity, particularly that of the minor spliceosome, highlights widespread transcriptional dysregulation hypothesised to contribute to disease pathogenesis. Among the large number of aberrantly spliced transcripts identified in, several have been proposed to harbour a mechanistic influence upon neuronal stability.

Large-scale transcriptional screens of spinal cords or laser-captured motor neurons from a number of murine models report significantly detectable transcriptional changes

at early or even pre-symptomatic stages(Murray, Beauvais, Gibeault, Courtney, & Kothary, 2015; Zhang et al., 2008, 2013). However, transcriptional profiling of the Δ7 mouse model of SMA by Baumer et al (2009) argues that the majority of splicing alterations occurred at P7, a relatively mid- to late-time point in the Δ7 disease time course, and therefore were independent of early pathogenic events (Bäumer et al., 2009).

Consequentially, the timing of transcriptional alterations and their contribution to the ultimate pathophysiology of SMA remains controversial. However, it is clear that, regardless of their timing within the disease time course, a broad degree of transcriptional dysregulation comprises a significant proportion of the molecular pathology characteristic of SMA. Convincingly, postnatal restoration of SMN in a tamoxifen-inducible mouse model of the disease improves snRNP assembly, supporting the implication of snRNP biogenesis and accompanying splicing regulation in the structure and maintenance of the motor unit(Lutz et al., 2011).

2.2.6 The SMN protein, RNA transport and additional substrates

In their evaluation of snRNP assembly across multiple mouse models of SMA, Gabanella et al (2007) report that snRNP assembly, while severely attenuated in the severe Taiwanese model compared to littermate controls, is not significantly less than the longer-lifespan *Δ7* model expressing higher levels of SMN (Gabanella et al., 2007). These findings suggest that SMN may have additional, snRNP-related roles impacting upon the structure and function of the lower motor neuron. Of these proposed alternate mechanisms, SMN has perhaps been most convincingly implicated in a number of non-splicing RNA metabolism roles within the motor neuron axon. For example,

Rossoll et al. (2003) reported that SMN was crucial for axonal transport of β-actin mRNA, thereby implicating both β-actin and additional transcripts that may be required for axonal development and integrity (Rossoll et al., 2003). These findings further invite debate as to whether transcriptional dysregulation resulting from low levels of SMN impact upon critical neuronal pathways in particular, or whether SMN harbours an additional, non-spliceosomal role particular to the motor neuron.

Evidence also exists for other, non-snRNP roles in different tissues. For example, SMN has been suggested to bind to various other CNS proteins, including the quintessential *FMRP* (fragile X-mental retardation protein) protein implicated in Fragile X syndrome, but these associations have not been demonstrated definitively(Meister et al., 2000; Piazzon et al., 2008). Nevertheless, while SMN may be involved in a number of other molecular pathways, these remain to be explored and validated *in vivo* before they may be definitively implicated in motor neuron-specific pathogenesis.

2.2.7 Non-SMN molecular pathways in spinal muscular atrophy

While there appears to be a clear implication for disrupted snRNP assembly in SMA, it remains difficult to determine whether it is the critical molecular pathway promoting disease pathogenesis. A number of studies have outlined alternative molecular candidates capable of modifying disease severity. These include the actin-binding protein plastin-3 and ubiquitination-activating enzyme Uba1, which have both been demonstrated to influence phenotype outcome to varying success upon therapeutic targeting in mouse models of SMA (Ackermann et al., 2013; McGovern et al., 2015; Powis et al., 2016; Wishart et al., 2014).

2.3 Mouse Models of Spinal Muscular Atrophy

The near-duplication of *SMN1* on chromosome 5q13 to yield centromeric copies of the paralogous *SMN2* is a phenomenon conserved to the human species (Rochette, Gilbert, & Simard, 2001). A prominent challenge in the modern SMA research field has therefore been to design an animal model of SMA that effectively recapitulates not only the phenotype, but also the molecular genetics of the disease. Although knockdown or deletion of SMN has been explored in diverse organisms from invertebrate organisms *Schizosaccharomyces pombe*(Qing Liu et al., 1997; Owen, Doe, Mellor, & Davies, 2000; Talbot et al., 1997), *Drosophila melanogaster* (Chan et al., 2003; H. C.-H. Chang et al., 2008), *Caenorhabtidis elegans,* and the zebrafish *Dario renia* (Boon et al., 2009; McWhorter, Monani, Burghes, & Beattie, 2003), the generation of a mammalian model in the mouse has perhaps yielded the most informative insights into SMA pathophysiology.

The first mouse model of SMA, generated by disrupting exon 2 of the murine SMN allele (*Smn)* with a reporter cassette to produce *Smn* null progeny, proved to be embryonically lethal before implantation(Schrank et al., 1997). Analysis of embryonic tissue revealed a large degree of apoptotic cell death at the eight-cell stage post-fertilization, emphasising the critical role of SMN during prenatal development(Schrank et al., 1997). Indeed, complete absence of both *SMN1* and *SMN2* in humans has never been reported, suggesting that a base level of SMN must be required for complete gestation and embryonic viability.

The first breakthrough in the development of a postnatally viable mouse model of SMA was conceived via transgenic expression of *SMN2* on an SMN null murine background (Hsieh-Li et al., 2000; U R Monani et al., 2000). The resultant mice, *$Smn^{-/-}$; SMN2,*

possessing one or two copies of the human transgene, are extremely short-lived and phenotypically representative of the most severe infantile forms of SMA. Mice with two copies of *SMN2* on an *Smn*$^{-/-}$ background die at approximately 4 to 6 days old and exhibit severe motor defects reflective of aggressive motor neuron loss and muscle wasting (U R Monani et al., 2000). However, introducing 8 or more copies of *SMN2* virtually eliminates the SMA phenotype and extends lifespan to a normal duration (U R Monani et al., 2000). A second transgenic *SMN2* model features introduction of *SMN2* on a novel SMN null background generated by homozygous replacement of exon 7 with a reporter cassette (Hsieh-Li et al., 2000). These “Taiwanese” mice with 2 copies of *SMN2* also exhibit a severe phenotype and a lifespan of 8 to 10 days (Hsieh-Li et al., 2000; Lin et al., 2016). Introducing 4 or more copies of *SMN2* extends lifespan to normal duration, again demonstrating that *SMN2* is a potent modulator, albeit not a sole one, of phenotypic severity.

Introduction of a second transgene, consisting of human transgenic SMN cDNA lacking exon 7 (*SMNΔ7*) cDNA onto the severe *Smn*$^{-/-}$*; SMN2* background modestly ameliorates the severe *SMN2; Smn*$^{-/-}$ phenotype (Le et al., 2005). These mice (*SMNΔ7; SMN2; Smn*$^{-/-}$), referred to hereon as the *SMNΔ7* model, survive to a lifespan ranging from 12 to reported 17 days, and exhibit sufficient structural and functional neuromuscular defects to be considered a phenotypically moderate to severe model. Phenotypic attenuation and extension of lifespan has also been reported from the introduction of human transgenic *SMN1* mutations, such as the SMN(A111G) mutation mentioned previously, onto the severe *Smn*$^{-/-}$*; SMN2* model(Workman et al., 2009). Although the precise mechanisms by which the addition of *SMNΔ7* and other SMN mutations to the severe model promote phenotypic improvement, it is hypothesised that the *SMNΔ7* isoform, as well as *SMN1* missense mutations, contribute an increased

capacity to associate with the low levels of FL-SMN produced by *SMN2*. Transgenic addition of the SMN(A2G) mutation to the *Smn*$^{-/-}$*; SMN2* model, which reduces severity and extends lifespan to a greater degree than the *SMNΔ7* transgene, also exhibits a greater binding affinity for FL-SMN *in vitro* than *SMNΔ7,* thereby supporting this theory(Umrao R Monani et al., 2003).

Finally, a recent longer-lifespan, intermediate mouse model of SMA was generated by the knock-in disruption of an exonic splicing enhancer sequence of the murine *Smn* exon 7 allele(Mélissa Bowerman et al., 2012). The resultant *Smn*$^{2B/-}$ mouse, so named for its expression of both the novel knock-in *2B* allele and null allele originally designed by Schrank *et al.,* harbours an intermediate phenotype, with symptomatic onset occurring around 10 days and lifespan extending to a median of 28 days (Mélissa Bowerman et al., 2012).

From the development of diverse mouse models of SMA, ranging in symptomatic severity and lifespan, it has been possible to determine that the lower motor neuron remains an uncontested primary victim of SMN depletion regardless of phenotypic severity, with the distal compartments of these neurons appearing particularly vulnerable. The conservation of structural and functional characteristics between the murine and human motor unit has been vital to enhance our understanding of the mechanisms underlying the degenerative processes in spinal muscular atrophy.

2.3.1 Cellular and Molecular Pathology in the SMA Mouse Motor Neuron

Since Werdnig and Hoffman's original descriptions of the infantile form of the disease, it remains highly evident that the motor neuron is subject to a broad range of morphological and molecular alterations in both patients and in mouse models of

spinal muscular atrophy (Werdnig 1891; Hoffman 1892). On a modern perspective, the contemporary theory of a highly compartmentalized motor neuron, with the cell soma, axon and synapse retaining molecular and metabolic individuality, has lent considerable reconsideration to the SMA field regarding the specificities of motor neuron degeneration. For example, although post-mortem reports of human patients commonly identify a profound loss of motor neuron cell bodies in the ventral horn and brainstem, post-mortem data from mouse models of the disease suggests that this somatic death is actually a pathologically late event in the disease time course (Monani *et al.,* 2000). Indeed, post-mortem analyses of the facial nuclei and ventral horn of *Smn*$^{-/-}$*; SMN2* mice, which exhibit neuromuscular weakness from postnatal day 1, reveals indistinguishable motor neuron counts from age-matched controls until postnatal day 3 or 4, in which approximately 40% and 35% of cell bodies were lost (U R Monani et al., 2000).

By contrast, a broad range of morphological and molecular changes in the distal compartments of the lower motor neuron appear early in the disease time course, often at early symptomatic stages. Neuromuscular junctions (NMJs) from post-mortem analyses of skeletal muscle from end-stage patients indicated a significant degree of structural and functional disruption (Mishra et al., n.d.; Soubrouillard et al., 1995; Swoboda et al., 2005). The generation of mouse models of SMA enabled the ability to profile NMJ pathology throughout the disease time course; subsequent studies therefore conclude that the NMJs are not only definitively altered in mouse models of SMA, but are also amongst the earliest pathological targets (Umrao R Monani et al., 2003; Murray et al., 2008). Significant morphological changes in the integrity of the NMJ, accompanied by multiple abnormalities in presynaptic vesicular distribution, synaptic transmission and intracellular calcium homeostasis, appear to precede the

loss of cell bodies in the ventral horn of the spinal cord (Jablonka, Beck, Lechner, Mayer, & Sendtner, 2007; Kariya et al., 2008; Kong et al., 2009; Lin et al., 2016; Ling, Gibbs, Feng, & Ko, 2012). This thesis seeks to provide a brief summary of the cellular and molecular rather than functional perturbations present in individual compartments compartments of the motor neuron, with a particular emphasis on the synapse or neuromuscular junction.

Cellular aspects of motor neuron pathology.

Consistent with other heritable motor neuron diseases such as ALS, the archetypal classification of motor neuron degeneration in SMA is a “die-back” pathology of pre-synaptic nerve terminals from post-synaptic acetylcholine (AChR) endplates, a conserved process distinct form other mechanisms of neuronal degeneration such as those induced by traumatic injury (Cifuentes-Diaz et al., 2002). Disrupted connectivity at the NMJ remains a consistent feature across multiple mouse models of SMA, albeit to varying extents depending on the phenotypic severity of model.

In addition to disruption of synaptic connectivity, additional morphological defects have been reported across multiple mouse models of SMA and have been subsequently integrated into the canon of pathological hallmarks. Perhaps the most consistently reported is the abnormal accumulation of neurofilament at the presynaptic nerve terminal (Cifuentes-Diaz et al., 2002; Kariya et al., 2008; Murray et al., 2008). These have also been reported in ALS patients and in mouse models in both the somatic body and at the distal nerve terminals of motor axons (Gurney et al., 1994; Mizusawa et al., 1989).

Postsynaptic aspects of the motor neuron also appear to be altered in mouse models of SMA, with a developmental delay in the maturation of the acetylcholine receptor

endplates reported in both the *Δ7* and *Smn*$^{2B/-}$ models of SMA compared to age-matched controls (Mélissa Bowerman et al., 2012; Kariya et al., 2008; Kong et al., 2009).

The aforementioned morphological correlates of NMJ pathology convincingly implicate the distal synapse as a significant cellular target of SMN depletion in mouse models of spinal muscular atrophy. However, an increasing body of evidence suggests that subtle morphological and molecular perturbations are also detectable within the cell soma of pre-symptomatic period of the *Smn*$^{2B/-}$ mouse model of SMA, prior to any manifestation of neuromuscular junction alterations (Murray et al., 2015). It therefore remains to be determined where and when motor neuron pathology, from a molecular to a morphological level, begins. Regardless, cytoarchitectural defects in the NMJ are undoubtedly robust and well-established pathological correlates of SMA, and will serve as the benchmark of the majority of morphological analyses presented in this thesis.

Molecular aspects of motor neuron pathology.

Studies aiming to elucidate the molecular basis of these cellular events have revealed that perturbations may be present at pre-symptomatic time points prior to any evidence of structural or functional changes. An RNAseq analysis of laser-captured motor neurons from the longer-lifespan *Smn*$^{2B/-}$ model suggests that a wide range of molecular perturbations, including an upregulation of transcripts involved in apoptotic signalling, are upregulated in motor neuron cell bodies at pre-symptomatic time points (Murray et al., 2015).

The majority of molecular analyses of the motor units of SMA mice has been performed in post-symptomatic tissue. Several large-scale transcriptional screens of pre- or early-symptomatic SMA tissue, including the spinal cord, reported ubiquitous

and extensive transcriptional dysregulation across multiple tissues, despite the absence of significant neuromuscular symptoms (Murray et al., 2015; Zhang et al., 2008, 2013). Among the transcripts dysregulated in both screens, chondrolectin (Chodl), has been demonstrated to mediate growth cone defects in the motor axons of zebrafish upon knockdown. Conversely, a similar large-scale exon-level time course screen by Baumer et al (2009) claims that majority of splicing alterations, including aberrant splicing of Chodl, occur post-symptomatically in the *Δ7* model of SMA (Bäumer et al., 2009). In a similar paradox to morphological characterisation of the motor neuron in SMA, a greater understanding of the molecular pathways key to initiating and executing the degenerative process in the motor unit is required to conclusively determine which factors represent definitive therapeutic targets. Nevertheless, overlaps in transcriptional changes between mouse models of SMA enables consistently altered transcripts, such as chondrolectin, to represent transcriptional dysregulation occurring on a larger-scale within the motor unit and beyond.

2.3.2 Systemic Pathology in Mouse Models of SMA and Patients

Although the loss of structural and functional integrity of the lower motor neuron appears to be a central defect in the pathogenesis of SMA, histopathological analysis of peripheral organs, as well as various tissue-specific knockout models has revealed a degree of systemic involvement occurring in SMA, suggesting that SMA is a spectrum of pathologies across multiple neuronal and non-neuronal systems. Indeed, the involvement of non-neuronal organs and systems, such as the heart and peripheral vasculature, has never been more greatly implicated than in recent times when our

understanding of the motor neuron degenerative processes has improved, and represent an important consideration for the development of future therapeutics.

In the central nervous system, thalamic degeneration has been reported in severe Type I patients(Shishikura, Hara, Sasaki, & Misugi, 1983). Similarly, a morphological analysis of the brain of *SMN2;Smn*$^{-/-}$ mice reported altered morphology in the hippocampus, a region with higher relative endogenous expression of SMN, attributed to defective neurogenesis, while regions such as the motor cortex, featuring relatively lower expression of SMN, remained structurally unaffected(Wishart et al., 2010). Functional clustering of the widespread transcriptional alterations identified throughout the disease time course of the *Δ7* mouse also revealed potential defects in molecular pathways responsible for cell proliferation within the spinal cord (Bäumer et al., 2009). In the peripheral nervous system, evidence for a disruption in afferent sensory neuron signalling has been cited in both clinical findings and from the study of mouse models (Jablonka et al., 2006; Mentis et al., 2011).

Low levels of SMN also appear to affect non-neuronal tissues. Vascular abnormalities, manifesting as necrosis of the tail and ears, were originally identified within the first transgenic murine models of SMA (Hsieh-Li et al., 2000; U R Monani et al., 2000). Necrotic tails and ears have also been reported in models exhibiting a therapeutically-extended lifespan (Foust et al., 2010; Narver et al., 2008). Similarly, necrosis of the distal digits has also been reported in several severely affected SMA Type 1 patients (Araujo, Araujo, & Swoboda, 2009). Mechanistically, an investigation into the development process of the peripheral vasculature in the severe Taiwanese mouse model reveals widespread developmental defects and accompanying functional hypoxia in the spinal cord (Somers et al., 2016).

Metabolic tissues, such as the pancreas and liver, also appear to suffer structural and functional abnormalities conserved between human patients and mouse models of the disease (Bowerman et al. 2012; Hua et al. 2011).

Cardiac defects appear to be the most notable systemic pathology reported in both a number of mouse models and post-mortem analyses of severely affected patients. These defects range from morphological abnormalities, such as ventricular thinning and atrial-septal malformation, translating to functional deficiencies such as chronic brachycardia (Bevan et al., 2010; Gogliotti, Hammond, Lutz, & DiDonato, 2010; Rudnik-Schöneborn et al., 2010; Shababi et al., 2010). Perhaps most importantly, cardiac defects remain present in several therapeutically-augmented mouse models after amelioration of neuromuscular symptoms. In a notable example, a significant proportion of the phenotypically mild “Burgheron” mice, developed as a mouse model of less severe, SMA Type II and III patients, died suddenly in adulthood without exhibiting any overt neuromuscular deterioration. Post-mortem analysis concluded that cause of death was attributed to gross cardiac deficits (Bogdanik et al., 2015). Likewise, the identification and pharmacological reduction of beta catenin, a downstream target of the SMN-associated ubiquitin factor Uba1, successfully improved neuromuscular junction pathology and motor deficits in severe Taiwanese mice. However, this strategy ultimately failed to modify the lifespan of treated mice; histopathological necropsy implicated gross deficits in both the heart and liver of treated mice as the cause of death. After an analysis of beta catenin levels in both the heart and liver of SMA mice revealed that they were unaffected by ubiquitous depletion of Uba1 levels, it became evident that the Uba1-beta catenin pathway was restricted to the neuromuscular system and therefore therapeutically irrelevant on a systemic level (Wishart et al., 2014).

While the ultimate contribution of each of these tissue-specific deficiencies to the ultimate pathogenesis of SMA remains under considerable debate, it is clear that systemic involvement may significantly influence the severity of the disease time course. Together, this information suggests that future therapies must address systemic factors in addition to motor neuron defects in order to maximise long-term phenotypic outcome. On a relevant sequel to the original Uba1 study, recent findings reported that systemic administration of AAV9-Uba1 promoted a robust rescue of neuromuscular phenotype, extension of lifespan, and amelioration of molecular defects in the ubiquitination pathway in Taiwanese mice. These findings reinforce the concept that a systemic approach to targeting molecular candidates affecting potentially distinct downstream pathways between tissue types harbours the greatest promise in therapeutic efficacy (Powis et al., 2016).

2.4 Therapeutics: Current Studies and Future Implications

As there is currently no commercially available treatment or cure, the only resources available to SMA patients are focussed upon disease management, and in the instances of Type I children, palliative care. However, since the characterisation of the *SMN1* gene in 1995, the overwhelming majority of translational research in SMA has aimed to restore pathologically depleted SMN protein levels. To date, a number of strategies attempting to increase SMN levels have generated excellent promise in basic preclinical studies, enabling several to continue through to early clinical trials. Broadly speaking, these proposed SMN-restoration therapies operate on the basis of either (1) targeting *SMN2* at the gene or protein level in order to enhance endogenous production of full-length, stable SMN protein, or (2) restoring *SMN1* via viral gene

therapy. *SMN2*-targetting compounds may be further subdivided into antisense oligonucleotides designed to inhibit the exonic splicing silencer within exon 7 of *SMN2,* or small molecules either enhancing *SMN2* transcription or stabilising fragile SMN isoforms translated from *SMN2*.

Although the majority of therapeutic developments aim to ameliorate symptoms via direct restoration of SMN levels, a number of non-SMN-based compounds have also been evaluated for their potential to attenuate neuromuscular symptoms in SMA patients, with a number currently in early clinical trials. This thesis seeks to provide a brief summary of both SMN-based and non-SMN based therapeutic strategies, including outlining the factors identified from translational research to be crucial determinants of therapeutic efficacy.

2.4.1 Non-SMN based therapeutics

While the majority of translational research in SMA has, unsurprisingly, focussed upon the restoration of SMN levels, a number of compounds targeting pathways independent of SMN have been championed for their disease-modifying potential. These non-SMN-based therapeutics may be broadly categorised as either (1) neuroprotective agents or (2) muscular agents. Of particular note is the neurotrophic agent olesoxime (TRO19622, Roche, formerly Trophos), which successfully improved motor performance in Phase II clinical trials with Type II and Type III patients, and is currently entering Phase III trials as of June 2016 (CureSMA, 2016). A comprehensive list of non SMN-based compounds registered for clinical trials as of June 2016 has been summarised in a review by Shorrock and Gillingwater, 2016 (Shorrock & Gillingwater, 2016).

2.4.2 SMN-based therapeutics

Promising translational research using animal models of SMA has produced a number of attractive treatment strategies centred around SMN induction, many of which have earned a promising position on the drug pipeline. The earliest attempts to increase SMN levels utilised histone deacetylase (HDAC) inhibitors, with the aim of inhibiting any histone-mediated suppression of the *SMN2* gene (Chang *et al.,* 2001). Application of a host of HDAC inhibitors, including sodium butyrate, valproic acid (VPA), hydroxamic acids, and trichostatin A (TCA), were successful in increasing production of SMN2 transcripts in both patient-derived iPSCs and in phenotypically mild murine models harbouring *SMN2* (Avila et al., 2007; Brichta et al., 2003; J. G. Chang et al., 2001; Narver et al., 2008; Riessland, Brichta, Hahnen, & Wirth, 2006; Somers et al., 2013; Sumner et al., 2003). However, application of these HDACs in both SMA mice and in early cohorts of patient trials produced highly variable phenotypic improvement despite the consistent increase in SMN2 levels (Avila et al., 2007; Kissel et al., 2011; Swoboda et al., 2010). Nevertheless, a comparison of muscular functionality between very young (2-3 years of age) and older (6-8 years of age) treated cohorts suggests that HDAC inhibitors may prove more beneficial in the earlier stages of disease progression, particularly before ambulatory capacity is lost (Kissel et al., 2011; Swoboda et al., 2010). Additionally, application of the HDAC Trichostatin A (TSA) also promoted notable improvement in both lifespan and motor function of the *Smn*$^{2B/-}$ model, which does not harbour transgenic *SMN2* and therefore did not experience an accompanying increase in SMN levels, suggesting that TSA may beneficially impact molecular pathways out with those directly dependent on SMN (H. Liu, Yazdani, Murray, Beauvais, & Kothary, 2014). Other attempts to increase transcription of *SMN2* included identification of a class of compounds, termed quinazolines that inhibit activity of the scavenger enzyme DcpS to increase *SMN2* promoter activity. However,

application of the quinazoline RG3039 to multiple mouse models of SMA ranging in phenotypic severity increased lifespan and motor performance despite only a minimal increase in SMN levels, also suggesting that RG3039 may mediate the majority of its translational activity in non-SMN dependent pathways (Van Meerbeke et al., 2013).

A second class of therapeutic agents have sought to modulate the aberrant splicing pattern of *SMN2,* rather than merely increase its transcriptional output, via antisense oligonucleotide (ASO) technology. ASOs are capable of binding to mRNA sequences to silence their translation or promote degradation, as well as binding to pre-mRNA sequences to promote their splicing into transcriptional and translational variants. Antissense technology has been applied to *SMN2* to either favour splice isoforms inclusive of exon 7, or else to subjugate intronic splicing repressor regions around exon 7. Of particular note is the antisense oligomer targeting the ISS-N1 intronic splicing silencer in *SMN2* intron 7 identified by Singh et al*.,* in 2006; operating under the commercial name Nusinersin (formerly known as ISIS-SMNRx), ASOs targeting ISS-N1 have demonstrated remarkable success through increasing SMN levels in both patient-derived cells and systemic induction in mouse models of SMA (Hua, Vickers, Baker, Bennett, & Krainer, 2007; Hua, Vickers, Okunola, Bennett, & Krainer, 2008; Mitrpant et al., 2013; Porensky et al., 2012; Singh, Singh, Androphy, & Singh, 2006). Phenotypically, this robust induction of SMN upon the ISS-N1 ASO has translated into a profound extension of lifespan and amelioration of neuromuscular phenotype across a number of mouse models ranging in symptomatic severity(Williams et al. 2009; Hua et al. 2011; Porensky et al. 2012)

.

Subsequent clinical trials of Nusinersen in both Type I and later-onset patients have produced similar success in motor improvement, muscular strength, and extension of

lifespan (Ionis Pharmaceuticals, Clinical Trials: NCT02386553, NCT02462759, NCT02594124, NCT02292537, NCT02193074, NCT02052791, NCT01839656, NCT01780246, NCT01703988, NCT01494701). On 1 August 2016, plans were announced to conclude Phase III clinical trials in Type I infants, thereby signifying preparation for the approval process by the Food and Drug Administration (CureSMA, 2016).

Finally, a third class of agents have utilised gene therapy to replace *SMN1*. SMN cDNA was first delivered intravenously via the self-complementary adeno-associated virus serotype 9 AAV9 (scAAV9-SMN), in neonatal one- or two-day old *Δ7* mice, to mediate a robust prevention of in neuromuscular damage and striking extension of lifespan to a near-normal average(Foust et al., 2010). Application of scAAV9-SMN has recapitulated this phenotypic rescue through systemic administration in both nonhuman primates and pigs, while exhibiting similar capacities for efficient blood brain-barrier and systems-wide penetration(Duque et al., 2015; Meyer et al., 2015). As of June 2016, intravenous injection of scAAV9-SMN gene therapy sponsored by AveXis is currently under Phase I clinical trials (AveXis, Clinical Trial: NCT02122952).

Despite extraordinary advancements in the extension of lifespan and improvement of neuromuscular phenotype through SMN-based therapeutics, the precise molecular mechanisms by which postnatally-restored SMN either halts or improves the degenerative process remain poorly characterised. However, from the studies outlined above, it is evident that efficacious SMN-based therapeutic intervention requires must adhere to a set of limitations, which are summarised by the following three criteria:

(1) systemic, rather than a CNS-based, delivery method

(2) sufficient increase in the level and bioavailability of restored SMN

(3) early postnatal administration, at a pre- or early-symptomatic time point

This thesis seeks to briefly discuss these criteria, with a particular emphasis on the crucial need for restoration to occur at an early and pre- or early-symptomatic time point. Indeed, there appears to be a clearly defined therapeutic time window for the induction of SMN, in which attempted restoration out with these early postnatal days results in significantly reduced efficacy. By examining the cellular and molecular factors underlying this apparent temporal "window of opportunity," it may be possible to enhance our understanding of SMN's role in the maintenance and function of the motor unit. It will also be possible to identify what factors are critical for neuromuscular repair, and which aspects may be irreparable despite intervention and therefore represent a target for alternate therapeutic strategies.

Systemic versus CNS-based delivery method

As described previously in this thesis, it has become increasingly evident that the cellular and molecular dysfunction resulting from depleted SMN levels is not restricted to the motor unit. Previous work therapeutically targeting a neural-specific molecular pathway in mice failed to improve overall survival; indeed, these results emphasised the involvement of multi-organ, particularly cardiovascular, pathology in disease prognosis (Wishart et al., 2014). Subsequently, it appears that systemic, rather than previously explored CNS- or neural-specific delivery methods harbour the greatest potential in improving not only motor neuron pathology, but also overall survival. These findings are effectively represented in comparison studies with an equivalent dose of ASO administered introcerebroventricularly (ICV) versus systemically in severe, Taiwanese pups at P10. While pups receiving systemic injection of the ASO survived

to a median of 108 days, pups receiving an identical ICV dose of the ASO limited to the CNS only survived to a mean of 16 days (Hua et al., 2011).

Threshold requirement for SMN

Due to the long-established correlation between SMN levels and disease severity, it is perhaps natural to conclude that therapies promoting only a minimal increase in SMN level prove largely inefficient in attenuating neuromuscular or systemic pathology alike upon application in mouse models and clinical trials. Indeed, the overall minimal impact of quinazoline compounds upon phenotypic outcome in mouse models has been attributed to its failure to increase in SMN levels sufficiently *in vivo* (Van Meerbeke et al., 2013). From an understanding of the molecular genetics behind the disease as well as aforementioned studies restoring SMN by exogenous agents, there is an evident physiological threshold dictating the onset, or conversely, amelioration, of an SMA phenotype. Bowerman et al. (2012) utilised the novel *2B* allele, which produces approximately 15% of SMN compared to the wildtype Smn allele, to explore the point at which an SMA phenotype becomes evident. Their findings concluded that the "switch" from asymptomatic status to an SMA phenotype must occur upon depletion of SMN to below 30% of normal levels, thereby supporting the existence of a rigid threshold requirement for SMN (Bowerman et al. 2012). This physiological threshold must be considered in ensuring high bioavailability of postnatally-restored SMN, with only delivery methods capable of exceeding this threshold considered to be clinically relevant. With consideration to the increasing implications of multi-organ involvement in SMA, this threshold must also therefore be considered on a systems-wide level.

Timing of postnatal administration: "the earlier the better"

Finally, mounting evidence highlights the existence of a “therapeutic time window” for SMN-based treatments. From both gene therapy and ASO studies in multiple animal models of SMA, it is clear that early treatment, at either a pre-symptomatic time point or at initiation of phenotypic onset, profoundly attenuates pre-existing neuromuscular weakness and prevents the neuromuscular junction denervation and muscle wasting characteristic of the normal disease course. Most importantly, early intervention has been demonstrated to robustly prolong survival, often to a duration comparable with a normal murine lifespan (Foust et al., 2010; Hua et al., 2011; Passini et al., 2011; Porensky et al., 2012). However, efficacy of this phenotypic rescue drops accordingly with a temporal delay in administration; indeed, of survival capacity has been shown to be significantly reduced when administration is delayed by as little as 48 hours (Foust et al., 2010; Hua et al., 2011; Kariya et al., 2014; Lutz et al., 2011; Robbins et al., 2014). The mechanisms underpinning this limited window of opportunity remain poorly understood, but must be elucidated in order to ensure the accessibility of SMN-based therapeutics to all patients. As prenatal screening of SMA is not currently available, the indisputable majority of SMA patients are diagnosed after neuromuscular symptoms—and therefore neuronal and systemic pathology—have already manifested. If indeed, as the animal data to be discussed below has suggested, the therapeutic benefit of SMN restoration is significantly hindered by the presence of existing pathology, there is therefore an utmost urgency to understand what cellular or molecular factors comprise this therapeutic window and how they may be pharmacologically manipulated in order to extend it.

2.4.3 The therapeutic window: from the perspective of the NMJ

In addition to the robust evidence detailing the temporal limitations of SMN-based therapies via scAAV9-SMN and ASO targeting techniques, a study generating a conditional model of SMN restoration in a mouse model of SMA further reaffirmed the existence of an SMN-dependent therapeutic window (Lutz et al., 2011). By engineering a floxed murine allele, termed *Res,* in which murine Smn exon 7 was replaced by a sequence containing *SMN2* exon 7 (inclusive of exonic splicing silencer) and inverted murine Smn exon 7, the so-called Smn^{Res} mouse served as, in absence of Cre-mediated recombination at the loxP sites, an mouse model of SMA exhibiting a similar disease course to the *Δ7* model of SMA. Phenotypic onset occurred at approximately 4 days old and reached end-stage at approximately 14 to 16 days (Lutz et al., 2011). Administration of tamoxifen activated the expression of the oestrogen receptor-fused *Cre* recombinase, which in turn promoted recombination of the *Res* allele and therefore re-expression of full-length SMN inclusive of exon 7 (Lutz et al., 2011). By providing an elegant system for the conditional postnatal induction of SMN, Lutz et al. (2011) generated an efficient model in which it was possible to examine neuromuscular and systems-wide pathology after SMN was restored at different postnatal time points.

Initial experiments administering tamoxifen at different postnatal time points within the Smn^{Res} model recapitulated the therapeutic window outlined by previous studies utilising gene therapy or ASOs; maximal rescue was achieved with treatment at P2 and P4, with efficacy dropping by treatment at P6 (Lutz et al., 2011). Strikingly, administration of tamoxifen at P8, by which neuromuscular symptoms had advanced significantly, was virtually ineffective in attenuating neuromuscular symptoms or prolonging lifespan beyond that of the untreated *Δ7* model (Lutz et al., 2011).

From this study and others, there is therefore a clearly defined therapeutic window in which postnatal restoration of SMN is effective, but the mechanisms behind this temporal limitation are poorly understood. Importantly, the in-depth characterisation of this therapeutic window by Lutz et al. (2011) highlights that phenotypic outcome systematically decreases in direct correlation delays in treatment. This gradual decrease in therapeutic efficacy invites the suggestion of a number of dynamic processes occurring within the motor unit and beyond, that evolve over this period to produce differential outcomes following SMN treatment. It is perhaps natural to assume that these dynamic alterations are merely the progression of motor neuron pathology to a late-symptomatic "point of no return" after which treatment with SMN is futile. By this hypothesis, it would be possible to infer that postnatally-restored SMN produces no unique effect upon the motor unit beyond halting subsequent degeneration. In other words: *Does induction of SMN merely maintain the* status quo *of the motor unit at time of rescue, and therefore must be performed at an early time point, before degeneration has progressed to a lethal extent?*

However, it is not unreasonable to hypothesise that intervention with SMN-dependant therapeutics may enable repair mechanisms to occur within the motor unit. Regeneration of the peripheral nervous system, including reinnervation of neuromuscular junctions following traumatic injury has been reported, albeit never investigated in a model of SMA (Barry & Ribchester, 1995). In examining the muscles of successfully rescued Smn^{Res} mice (ie. those treated from P2-P6), Lutz et al. (2011) observed a marked absence of neuromuscular junction pathology, a finding concurrent with other reports of SMN-mediated phenotypic rescue. However, in both the Lutz study and in other studies to date, it is unclear whether the lack of NMJ pathology in phenotypically improved mice is attributed to a mere halting of any degeneration

present at time of rescue, or whether early intervention with SMN enables regenerative mechanisms to repair pre-existing damage, the capacity for which is lost at later time points? In other words: *Is postnatal induction of SMN capable of mediating processes capable of repairing pre-existing damage? If so, what aspects of the motor neuron are successfully corrected, and which remain damaged beyond repair?*

By determining what cellular events may occur at the highly vulnerable neuromuscular junction in the event of early versus late-symptomatic SMN restoration—promoting successful versus failed phenotypic rescue, respectively—it will be possible to understand the mechanisms dictating the therapeutic window. After first profiling the extent of cellular and molecular disruption present within a mouse model of SMA at a point of early symptomatic onset, it will then be possible to utilise these findings to conclude whether restoration of SMN to the early-symptomatic motor unit merely halts or truly reverses degeneration.

Defining the neuromuscular junction response to postnatally restored SMN at different symptomatic phases will not only enhance our understanding of SMN's role in the maintenance and function of the motor unit, but will also be critical in providing the most efficacious treatment for SMA patients. At the moment, there is no postnatal screening for SMA available; consequentially, patients are usually diagnosed because they are exhibiting neuromuscular abnormalities or missing developmental motor milestones. Understanding what cellular and molecular events limit the therapeutic window may enable us to develop a means of manipulating and extending these limitations with other methods, thereby rendering SMN-based treatments an accessible and realistic option for all patients, regardless of time of diagnosis.

2.5 Aims of this chapter

2.5.1 Summary

To summarise, spinal muscular atrophy is a heritable neurodegenerative disease caused by insufficient production of SMN protein. The archetypal pathological hallmark of SMA remains definitively neuromuscular, with a series of pre- and post-synaptic perturbations promoting a loss of cytoarchitectural integrity at the neuromuscular junction. These morphological deficits are accompanied by a broad range of dysregulated molecular cascades within the motor unit and beyond. Recent therapeutic advances in the SMA field demonstrate a remarkable amelioration of disease phenotype and extension of lifespan through postnatal restoration of SMN. However, the success of this SMN-based rescue phenomenon appears to be temporally limited; maximal rescue is achieved when SMN is restored at an early postnatal time point, but efficacy of rescue drops with later restoration of SMN. There is therefore an apparent "therapeutic window" of opportunity for effective SMN treatment, the mechanisms behind which are currently poorly understood. Additionally, it has become evident that the fate of pathological correlates within the motor unit, particularly at the neuromuscular junction, remain uncharacterised in situations of successful improvement versus failed amelioration of gross phenotype. We hypothesise that an understanding of the cellular and molecular factors comprising successful SMN-based recovery versus deterioration may provide a mechanistic explanation of the temporal limitations of SMN-based therapies.

We have established a conditional mouse model of SMN restoration designed by Lutz *et al.*, the *Smn*^{Res} model, in our own facilities, to address the key question of this chapter:

"Which pathological features present in the motor unit, particularly the neuromuscular junction, at time of SMN restoration are irreparable, and which harbour the capacity for recovery?"

In this thesis, I perform an extensive cellular and molecular characterisation of the *Smn^{Res}* mouse model of SMA with a particular emphasis on synaptic pathology, pre- and post-restoration of SMN, to address the following aims:

2.5.2 Aims

AIM 1: Investigate the extent of cellular and molecular pathology present within the *Smn^{Res}* mouse model at P4, a symptomatic time point within the therapeutic window.

1a. Characterise the typical disease time course of the *Smn^{Res}* mouse model of SMA in our hands, in order to identify the point of symptomatic onset.

1b. Investigate the presence of both pre- and post-synaptic neuromuscular junction pathology in a selection of muscle groups within the *Smn^{Res}* model at an early-symptomatic time point identified in *1a.*

1c. Determine if molecular alterations suggesting an up-regulation of the p53 apoptotic cell death pathway in other mouse models of SMA are present in the *Smn^{Res}* model at early-symptomatic time point outlined in *1a.*

1d. Assess whether select transcriptional alterations identified from large-scale screens of two different early-symptomatic SMA mouse models are also present in the *Smn^{Res}* model at the early-symptomatic time point outlined in *1a*

AIM 2: Investigate structural modifications at the neuromuscular junction that accompany rescue of neuromuscular phenotype after conditional re-expression of SMN at an early symptomatic time point in the *Smn^{Res}* model.

2a. Induce re-expression of SMN at the early symptomatic time point identified in *1a* in order to evaluate phenotypic improvement and survival in our hands.

2b. Assess and compare the pathological status of neuromuscular junctions within a variety of muscle groups in rescued versus non-rescued *Smn^{Res}* mice.

2c. Determine whether the differences in pathology between rescued and non-rescued mice reported in *1b* are the result of restored SMN slowing, halting, or reversing pre-synaptic degeneration at the neuromuscular junction.

Chapter TWO: Methods

2.6 The *Cre-ER; SMN2; Δ7; Smn^{Res}* Mouse

Design of the "Res" allele. The tamoxifen-inducible *Cre-ER; SMN2; Δ7; Smn^{Res}* mouse model used in this thesis was generated by Lutz et al, (2011) and established in our own facilities. In addition to expressing both *SMN2* and *SMNΔ7* (see et al), the *Cre-ER; SMN2; Δ7; Smn^{Res}* mouse harbours a novel, rescuable *Smn* allele designed by Lutz et al (2011), hereforth referred to as the "rescue" or *Res* allele. BAC clones containing human *SMN2* (BAC 939i7) and murine *Smn* (BAC 148d4) were used as the starting sequences to target endogenous murine *Smn.* A BAC-based targeting vector was designed (Valenzuela et al., 2003) via homologous recombination to replace endogenous *Smn* exons 7 and 8 with a donor cassette, containing the following in order: a short upstream region (homogology upstream [HU]), homologous to mouse BAC, a lox71 site, a 380bp sequence containing exon 7 and flanking intronic sequences of human *SMN2*, a 387bp fragment containing, in an inverted orientation, the sequences of murine *Smn* exon 7 and flanking introns, a lox66 site in inverted orientation to lox71, a hygromycin resistance gene under both prokaryotic and eurkaroytic promoters flanked by FRT sites, a 928bp fragment containing exon 8 of human *SMN2*, and a short downstream region (homology downstream [HD]) homologous to the mouse BAC (see **Figure 2.4**). This vector, comprising endogenous *Smn* exons 1-6 fused to the hybrid sequence outlined above, was linearized and electroporated into VGF1 ES cells. A LONA assay was used to isolate hygromycin-resistant ES colonies (Osoegawa et al., 2000). After FLP-mediated removal of the hygromycin resistance gene, cells were microinjected into donor 8-cell embryos to

generate mice on an FVB background (Poueymirou et al., 2007). Mice heterozygous for this novel rescue allele (*Smn*$^{Res/+}$*);* (stock no. 007249, Jackson Laboratory) formed the basis of breeding to generate the *Cre-ER; SMN2; Δ7; Smn*^{Res} line.

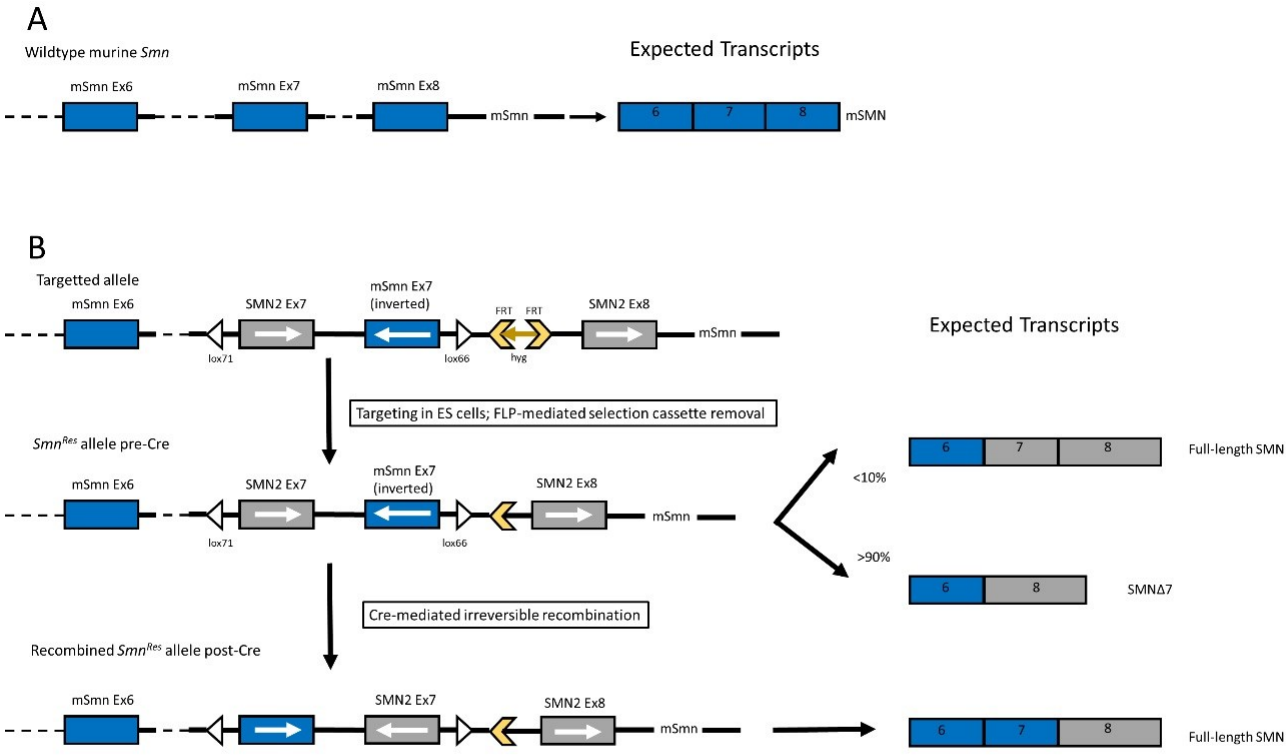

Figure 2.4 Construction of the *Res* allele with corresponding transcriptional products. A. Wildtype murine Smn (exons 6, 7 and 8) shown for reference, with transcriptional outcome being production of full-length murine Smn transcript. **B.** The *Res* allele designed by Lutz *et al* comprises a BAC-based targeting vector containing endogenous murine *Smn* exons 1-6 fused to the following hybrid sequence: intronic-inclusive sequences of *SMN2* Exon 7 and inverted intron-inclusive sequences of murine *Smn* Exon 8 is floxed by two loxP sites in opposing orientations, as well as a FRT-flanked hygromycin resistance gene and exon 8 of human SMN2. This vector was introduced into VGF1 ES cells, which were then selected for hygromycin resistance. After FLP-mediated removal of the hygromycin resistance gene, the inverted orientation of murine *Smn* Exon 7 within the *Smn*^{Res} allele results in the majority of transcripts produced to be truncated and unstable due to their lack of exon 7 (SmnΔ7). **C.** Following administration of tamoxifen, Cre-mediated recombination at loxP sites results in restoration of normal orientation of murine exon 7, and therefore production of full-length Smn transcripts, inclusive of exon 7.

Generation of the EIIa-Cre; SMN2; Δ7; Smn$^{Res/+}$ mouse. *Smn$^{Res/+}$* mice were then crossed to heterozygous Δ7 SMA carriers (Jax stock no. 007951; Jackson Laboratory). These progeny, termed *SMN2; Δ7*; *Smn$^{Res/+}$* were then crossed to TM-inducible (Cre-ER) carriers (Jax stock no. 004682; Jackson Laboratory) to generate heterozygous *Smn$^{Res/+}$* progeny either carrying (*EIIa-Cre; SMN2; Δ7*; *Smn$^{Res/+}$*) or lacking (*SMN2; Δ7*; *Smn$^{Res/+}$*) the *EIIa-Cre* allele, ie. the capacity for tamoxifen-induced recombination. The *Cre-ER; SMN2; Δ7; Smn^{Res}* line was imported, bred and maintained in our own facilities at the University of Edinburgh.

Generation of tamoxifen-inducible SMN2; Δ7; Smn$^{Res/Res}$ mice. The *SMN2; Δ7*; *Smn$^{Res/+}$* carriers, either carrying or lacking the *EIIa-Cre* allele outlined above were intercrossed to generate the experimental cohorts used in this project. *EIIa-Cre; SMN2; Δ7; Smn$^{Res/+}$* mice were crossed to *SMN2; Δ7; Smn$^{Res/+}$* mice to yield litters with approximately 25% SMA pups. Of these *SMN2; Δ7; Smn$^{Res/Res}$* offspring, approximately 50% harboured the *EIIa-Cre* allele and were therefore tamoxifen-rescuable, with the other approximate 50% not expressing *EIIa-Cre* to serve as unrescuable SMA controls.

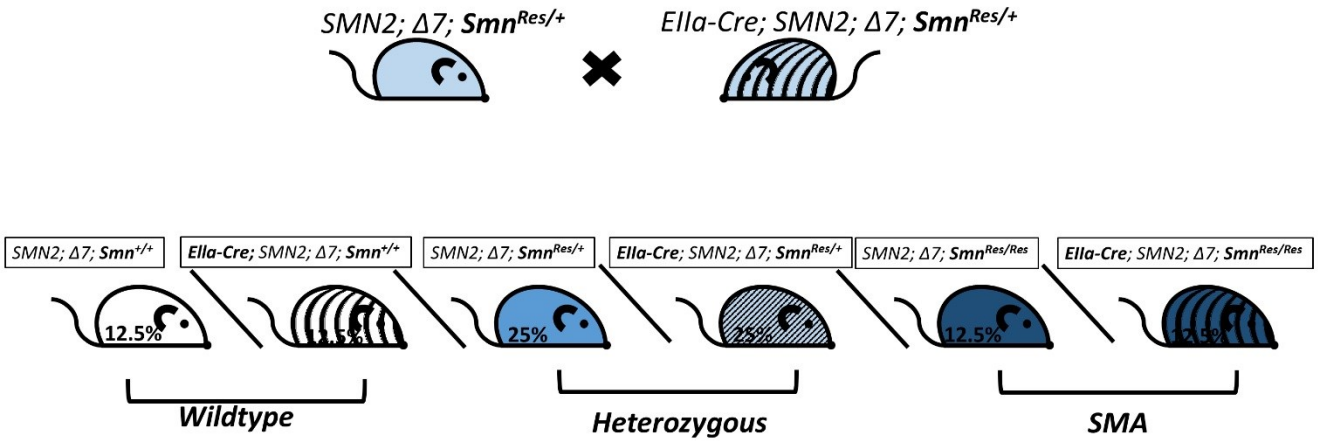

Figure 2.5. Schematic of breeding to generate experimental cohort.

Crossing *Ella-Cre; SMN2; Δ7; Smn$^{Res/+}$* mice to *SMN2; Δ7; Smn$^{Res/+}$* produced litters of which approximately 25% were homozygous for the *Smn^{Res}* allele, ie. *SMN2; Δ7; Smn$^{Res/Res}$;* homozygosity of the *Res* allele ensured majority production of truncated Smn transcripts, and therefore molecularly to phenotypically recapitulated SMA. Of these SMA pups, approximately 50% (ie. 12.5% of the total litter) also carried the *Ella-Cre* allele, and therefore the capacity to undergo Cre-mediated recombination of the *Res* allele upon administration of tamoxifen.

2.7 Animal Breeding and Maintenance

All mice used in this project were treated in accordance with the guidelines outlined by the UK Animal Scientific Procedures Act (1986), following the three principles of Reduction, Refinement and Replacement. The *Cre-ER; SMN2; Δ7; Smn^{Res}* colony was maintained under Specific and Opportunistic Pathogen-Free conditions in individually ventilated cages (IVC) in breeding facilities at the University of Edinburgh.

All mice were sacrificed by an overdose of anaesthetic (IsoFlo, Abbott, Quebec, Canada). All procedures were performed in accordance with the guidelines outlined by the Home Office, United Kingdom. For molecular and morphological characterisation of the postnatal time point at which tamoxifen-inducible recombination and phenotypic rescue was reported to be maximally effective by Lutz et al (2011), pups were sacrificed at an early symptomatic timepoint (P4). For molecular and morphological characterisation of post-phenotypic rescue, pups were sacrificed at P10 by which unrescued pups exhibited a significant neuromuscular phenotype.

2.8 Genotyping

DNA was extracted from ear notches (weaned) or tail tips (sacrificed pups) by digesting the tissue in Tail Tip Lysis Buffer (TTLB); 0.5M EDTA, 1M Tris-HCl, 1M NaCl, 10% SDS, ddH2O) and Proteinase K (1mg/ml) overnight at 55°C. DNA was precipitated in isopropanol and washed in 70% ethanol before suspension in 200µl of ddH2O to yield a concentration of approximately 200ng/µl.

Smn^{Res} genotyping. To determine the presence of the non-inverted *Res* allele, polymerase chain reaction (PCR) was performed using a Kapa2G Robust PCR kit with dNTPs (Kapa Biosystems Ltd). Oligos (Sigma-Aldrich) were designed for specific binding to the noninverted, native *Res* allele based on the forward (5'-GGCAGTTTTAGACTCATCATGTATCTG-3') and reverse (5′-ACTTATGGAGATCCCTCGAGATAAC-3′) primer sequences published by Lutz *et al*. Amplification was performed in a CFX Connect™ Real-Time PCR Detection System to the following temperature cycling protocol:

Table 2.1 *Smn*^{Res} genotyping thermocycling conditions

Thermocycling Conditions		
Step	Temperature (°C)	Duration
1	94	2 m
2	94	20 s
3	65	15 s
4	68	10 s
5	Steps 2-4 x10	--
6	94	15 s
7	60	10 s
8	72	10 s
9	Steps 6-8 x10	--
10	72	2 m
11	10	hold

Amplified product was separated by gel electrophoresis; product was run in 1x TAE buffer on a 1.5% agarose gel containing 0.01% SYBRSafe© DNA stain (Invitrogen) at 100V for 40 minutes. Gel was imaged on a UV transilluminator and identity of PCR product was distinguished based on band size. The product of the wildtype reaction produced a band of approximately 150bp and the transgenic reaction of 103bp.

Cre-ER genotyping. To determine the presence of the *CreER* allele, PCR was performed using an Invitrogen Taq polymerase kit (Promega) and primers were designed based on publication by Lutz et al. Primers were designed according to the forward: (5' – GCGCTCTCCCAGTAAAAACTATC – 3') and reverse (5' – GTGAAACAGCATTGCTGTCACTT – 3') primer sequences published by The Jackson Lab's Cre-transgenic genotyping protocol. Amplification was performed in a T1 Thermoblock thermal cycler (Biometra) to the following temperature cycling protocol:

Table 2.2 *Ella-Cre* genotyping thermocycling conditions.

Thermocycling Conditions		
Step	Temperature (°C)	Duration
1	94	3 m
2	94	30 s
3	51.7	1 m
4	72	2 m
5	Steps 2-4 x35	--
6	72	2 m
7	10	hold

Amplified product was separated by gel electrophoresis; product was run in 1x TAE buffer on a 1.5% agarose gel containing 0.01% SYBRSafe© DNA stain (Invitrogen) at 100V for 40 minutes. Gel was imaged on a UV transilluminator and identity of PCR product was distinguished based on band size. The product of the wildtype reaction produced a band of approximately 324bp and the transgenic reaction of 100bp.

2.9 Phenotypic Assessment of Mice

Weight/righting reflex. Litters from *Smn*$^{Res/+}$*; Smn*$^{Res/+}$ breed pairs were monitored daily for SMA-like phenotypes. At P4, pups were weighed and righting reflex was tested to evaluate muscle strength. Pups were turned over on their back on a flat bench top with all four paws in the air, and the time for them to right and stably place all four paws on the bench top was recorded. Cut-off time for righting was set at 30 seconds. All pups were righted twice, with a minimum of two minutes rest in nests between tests to minimise the possibility of hypothermia-induced fatigue. For experiments characterising pups at an early symptomatic time point, pups and littermate controls were sacrificed by overdose of inhalational isoflurane and decapitation at P4. For experiments characterising restoration of SMN at an early symptomatic time point, pups were dosed at P4 with a 75mg/kg solution of tamoxifen in corn oil and monitored closely in the following days for signs of musculoskeletal weakness. Pups were weighed and subjected to time to right test at P6, P8 and P10, at which they were sacrificed at P10 by overdose of inhalational isoflurane and decapitation.

2.10 Tamoxifen Dosing

A tamoxifen solution of 40mg/ml TM (Sigma-Aldrich) was prepared in corn oil (Sigma-Alrdich) by 3x15 minutes dissolution in a sonicating water bath at 37.5°C. P4 pups from $Smn^{Res/+}$; $Cre\text{-}ER^{+/-}$ and $Smn^{Res/+}$; $Cre\text{-}ER^{-/-}$ crosses phenotypically identified to be SMA were administered a 75 mg/kg dose of this solution by oral gavage. Following dosing, pups were closely monitored, and weight and motor performance were noted at P6, P8 and P10, before sacrifice by overdose of inhalational isoflurane and decapitation at P10. n=3 mice exhibiting phenotypic rescue were continually monitored, weighed and motor performance tested through weaning into adulthood. 1-2cm tail tips were taken from sacrificed pups for DNA extraction and retrospective genotyping, while ear notches from weaned mice were used for DNA extraction and genotyping.

2.11 Quantitative Fluorescent Western Blotting

Extraction and sample preparation. Spinal cords were freshly dissected and halved at the dorsiventral midline, and immediately snap-frozen on dry ice and stored at -80°C. Tissue was homogenized using a handheld motorized pestle (VWR International) in 100µl RIPA buffer (Fisher Scientific) with 1% Halt protease inhibitor cocktail (Sigma Aldrich). Homogenate was cooled on ice for 10 minutes, then centrifuged at 4°C at 14000rpm for 10 minutes. Centrifuged samples were immediately re-transferred to ice and supernatant was removed by pipetting, while pellet was discarded. Concentration of extracted protein was determined by micro-BCA kit (Pierce Biosystems).

Quantitative fluorescent western blotting. Samples were prepared to load between 10 and 25µg of protein in 10 µl deionised water and 5µl of NuPage® LDS Sample buffer 4X (Invitrogen, UK). Samples were denatured at 98°C for 2 minutes and were loaded in a NuPAGE™ Novex™ 4-12% Bis-Tris protein gel (Invitrogen, UK) alongside 5µl of Novex® Sharp Pre-stained Protein Standard (Thermo Fisher). Gels were run at 80mV for 5 minutes to ensure equal stacking, then 150mV for 50 minutes. Gels were excised, removed to a pre-prepared i-Blot2® transfer stack (Invitrogen, UK) and transferred using an 8.5 minute transfer cycle in the i-Blot2® transfer system (Invitrogen, UK).

After transfer, membranes were excised and transferred to 20ml Falcon tubes containing 5ml of Ponceau S solution; 0.1% Ponceau S (Sigma-Aldrich), 0.5% acetic acid (Sigma-Aldrich) in ddH2O. Membranes were stained for 20 minutes, rolling, at room temperature then washed in ddH2O until bands were visible. Membranes were scanned in greyscale using a CanoScan LiDE220 digital scanner (Canon) and saved as a TIFF image for total protein analysis. Membranes were washed in ddH2O and

blocked in 5ml Odyssey® Blocking Buffer (Li-COR Biosciences) at room temperature for 30 minutes.

Membranes were incubated in primary antibody solution containing primary antibodies at the following concentration (Fas 1:1000, Abcam) in a solution of 1% tween-20 (Sigma) in 5ml Odyssey® Blocking Buffer (Li-COR Biosystems) at 4°C overnight.

The following day, membranes were washed 6x 5 minutes in PBS, rolling, at room temperature. Membranes were incubated in secondary antibody solution containing IRDye® 680RD donkey anti-rabbit IgG (H+L) (Li-COR Biosciences) at a concentration of 1:5000 (0.02%) in a solution of 1% tween-20 (Sigma) in 5ml Odyssey® Blocking Buffer (Li-COR Biosciences). Membranes were incubated for 90 minutes at room temperature and covered to prevent photobleaching.

After secondary antibody incubation, membranes were washed 2x 5 minutes, then 3x 10 minutes in PBS, rolling, at room temperature. Membranes were dried and stored at 4°C prior to imaging and analysis.

Measurement and analysis. TIFF images of Ponceau-stained blots were imported into Odyssey® ImageStudio Lite software (Version 5.2). ImageStudio Lite (Version 5.2) was used to analyse the intensity of identical sections of total protein banding against background. Readouts of the intensity of total protein banding relative to background were imported into Microsoft Excel (Windows 2013) to calculate loading consistency and normalisation factors. Western blots were imaged on the 700nm channel using the Odyssey® Infrared Imaging System at a resolution of 169μm. All quantification was performed on the 700nm channel, with the intensity of bands normalised using the factors generated from total protein analysis. All statistical analysis and generation of graphs was performed in GraphPad Prism7 (Windows). All data are presented as a

scatter plot of individual *n* with mean ± SE unless otherwise noted. Individual statistical tests used are noted in figure legends. Statistical significance was considered to be $p \leq 0.05$. Figures were created using GNU Image Manipulation Program (GIMP) for Windows.

2.12 RT-qPCR

Dorsiventrally halved spinal cords of freshly dissected mice were snap-frozen on dry ice and stored at -80°C. RNA was extracted from thawed tissue using a microRNeasy kit (Qiagen) according to manufacturer's instructions and concentration was determined using NanoDrop (Thermo Scientific). Reverse transcription was performed using an RT^2 First Strand Kit (Qiagen) using 1µg of RNA per reaction to generate cDNA.

SYBR Green Assays. For SYBR-Green compatible primer-designed assays to determine relative expression of Fas, Phorbol-12-Myristate-13-Acetate-Induced Protein 1 (PMAIP) and (Cyclin-Dependent Kinase Inhibitor 1A) CDKN1a, RT-qPCR was performed using KAPA2G Robust PCR Master Mix with dNTPs (KAPA Biosystems) in a CFX Connect™ Real-Time PCR Detection System according to the following temperature cycling protocol compatible with KAPA2G Robust PCR Master Mix with dNTPs:

Table 2.3 KAPA2G Robust PCR Master Mix Thermocycling Conditions

Thermocycling Conditions		
Step	Temperature (°C)	Duration
1	95	3 m
2	95	3 s
3	60	20 s
4	Repeat steps 2-3 x39	--
5	95	10 s
6	65	5 s
7	95	5s

Three housekeeping genes (GAPDH, YWHAZ, β-actin) were used in each assay. All samples were run in technical triplicate.

TaqMan Assays. To determine relative expression of chondrolectin (Chodl), ETS Variant 1 (Etv1) and Ubiquitin specific peptidase-like 1 (Uspl1), pre-optimised Taqman® gene expression assays were used in combination with TaqMan® Gene Expression Master Mix according to manufacturer's instructions. RT-qPCR was performed in a CFX Connect™ Real-Time PCR Detection System according to temperature cycling protocol compatible with TaqMan® Gene Expression Master Mix:

Table 2.4 TaqMan® Gene Expression Master Mix Thermocycling Conditions

Thermocycling Conditions		
Step	Temperature (°C)	Duration
1	50	2 m
2	95	10 m
3	95	15 s
4	60	1 m
5	Repeat steps 2-4 x40	--

Four housekeeping genes (β-actin, Gusb, Hprt and GAPDH) were used in each assay. All samples were run in technical triplicate.

For all RT-qPCR assays, graphs were generated and statistical analyses were performed using Bio-Rad CFX Manager™ software. Data are presented as a bar chart of mean ± SE unless otherwise noted. Individual statistical tests used are noted in figure legends. Statistical significance was considered to be $p \leq 0.05$. Figures were created using GNU Image Manipulation Program (GIMP) for Windows.

2.13 Whole-mount immunofluorescence

Dissection and immunocytochemical labelling. Gross preparation of cranial and abdominal muscles were freshly dissected, pinned and fixed in 4% paraformaldehyde in phosphate buffered saline, rocking, for 15 minutes. Fixed preparations were finely dissected under a microscope (Leica) to isolate muscles of interest. Refer to **Figure 2.6** for a schematic detailing the anatomical location of muscles isolated; the cranial muscles (rostral and caudal levator auris longus (LALr/LALc), abductor auris longus (AAL) and auricularis superior (AS)) and the transversus abdominis (TVA) were utilised in all whole-mount immunofluorescence experiments. Muscles were permeabilised for 1 hour in 2% Triton-PBS, followed by blocking in 4% bovine serum albumin, 1% Triton-PBS. Muscles were incubated for a minimum of 48 hours at 4°C in primary antibody solution at the following concentrations: synaptic vesicle protein 2 (Developmental Studies Hybridoma Bank, Iowa) 1:100; neurofilament 2H3 (Developmental Studies Hybridoma Bank, Iowa) 1:50, in 4% bovine serum albumin, 1% Triton-PBS. Preparations were washed 3x10 minutes in PBS and incubated for a minimum of 24 hours in 488-conjugated IgG secondary antibody solution (Jackson ImmunoResearch) at a concentration of 1:250 in phosphate buffered saline, and covered to prevent photobleaching. Preparations were washed 3x 10 minutes and incubated for 90 minutes in tetramethylrhodamine-conjugated α-bungarotoxin (TRITC-α-BTX) (Life Technologies) at a concentration of 1:250 in phosphate buffered saline.

Preparations were washed 3x 10 minutes in phosphate buffered saline and mounted on slides (Menzel-Glasser) in Mowiol Mounting Medium® (Sigma-Aldrich) and coverslipped (VWR). Slides were stored covered to prevent photobleaching.

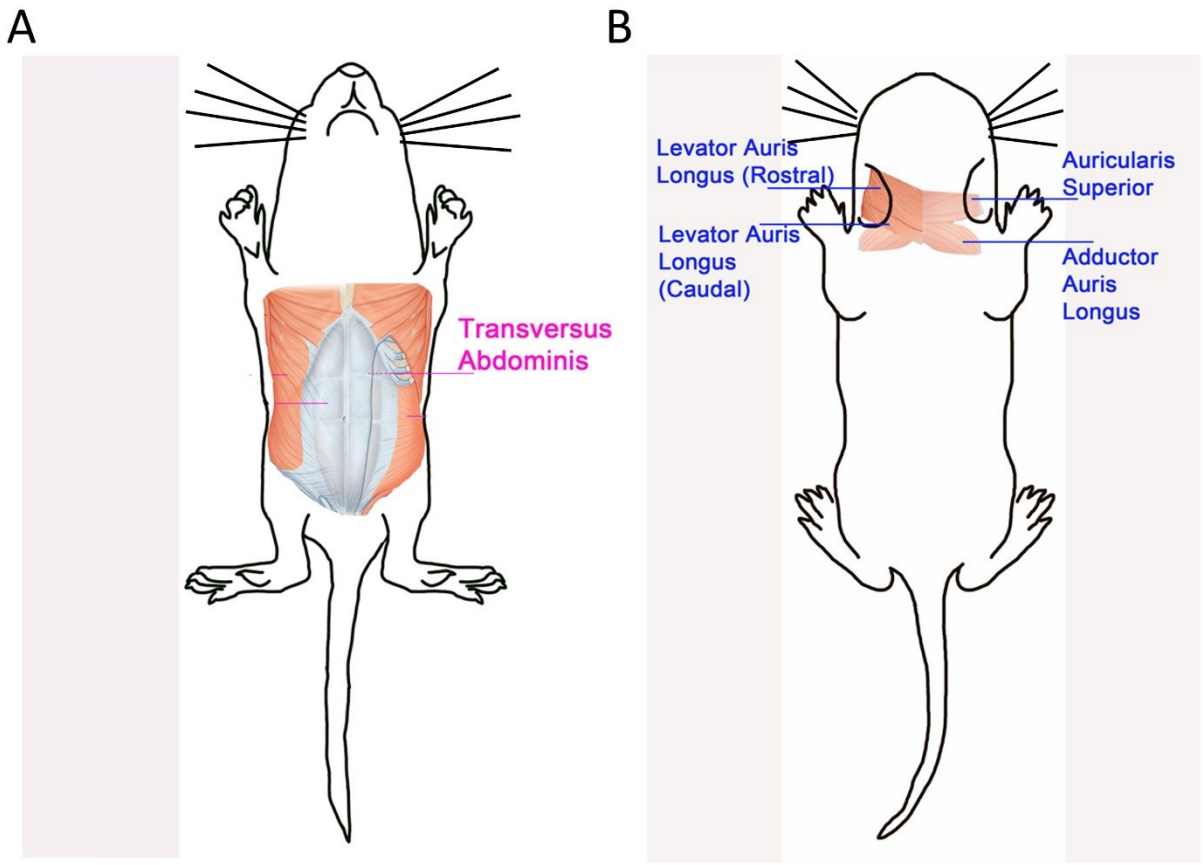

Figure 2.6. Schematic illustrating anatomical positioning of abdominal and cranial muscles utilised for whole-mount immunocytochemistry and neuromuscular junction (NMJ) analysis.
(A) The transversus abdominis (TVA) is a thin, flat abdominal muscle located deep to the external oblique and rectus abdominis, and is partially covered by the internal oblique. Access to the TVA is obtained by removing the skin and fat from the torso to expose the abdominal musculature, then peeling away the overlying external oblique and rectus abdominis, aided by a dissection microscope. The perpendicular striations of the internal oblique are identified and cleared away, and the isolated TVA is detached from the inferiormost rib. **(B)** The cranial muscles: caudal and rostral bands of the levator auris longus (LALc and LALr respectively), auricularis superior (AS) and abductor auris longus (AAL) are responsible for moving the pinnae (ears) of the mouse. They exist in two layers, with the left and right LALc and LALr forming the superficial layer, above the layer comprising the left and right AS and AAL. The cranial muscles offer an elegant preparation for whole-mount immunocytochemistry when isolated as a pair of complete sets, ie. left and right preparations with superficial (LALr and LALc) and deep (AAL and AS) layers attached at the midline.
Figure adapted from illustration by LM Murray, unpublished.

Imaging and analysis. Quantification of endplate occupancy and neurofilament accumulation, was performed using a Leica DMi8 inverted epifluorescent microscope (Leica Microsystems) (10x, 20x and 40x objectives; 0.53, 0.55 and 0.9NA; Leica DMi8 microscope; Leica DFC7000-T camera). Labelled pre-synaptic nerve terminals were visualised using 488nm excitation and 520nm emission optics, while TRITC-α-BTX-labelled endplates were visualised using 543nm excitation and 590nm emission optics. Quantification of endplate occupancy and neurofilament accumulation was performed blind, and incorporated a minimum of 50 neuromuscular junctions (NMJs) from at least three distinct fields of view per muscle (*n*=number of muscles muscle*, N*= number of mice; *n=2* muscles, ie. one pair per muscle type, per *N)*. Endplate occupancy was quantified to the following criteria: fully occupied, ie. complete coverage of the post-synaptic endplate by the branches of the nerve terminal; partially occupied, ie. partial withdrawal of the pre-synaptic nerve terminal from the post-synaptic endplate, or vacant, ie. complete withdrawal of the pre-synaptic nerve terminal from the post-synaptic endplate. Neurofilament accumulation was quantified to the following criteria: *Stage 1*: no accumulation visible; *Stage 2*: individual nerve terminal branches swollen, complexity of nerve terminal branching retained; *Stage 3*: severe accumulation, complexity of nerve terminal branching largely lost, underlying post-synaptic endplate largely obscured; *Stage 4*: complete and absolute obscurity of the post-synaptic endplate by the neurofilament-engorged nerve terminal. To measure endplate size TRITC-α-BTX-labelled endplates were imaged using 543 nm excitation and 590 nm emission optics, and images were exported from Leica Application Suite LASX software (Leica Microsystems) as a TIFF file and analysed in greyscale using Fiji ImageJ software. Individual endplate measurements were determined using the "freehand draw" tool in Fiji ImageJ software; a minimum of from at least three distinct

fields of view per muscle (*n=2* muscles, ie. one pair per muscle type, per *N).* All quantification was performed blinded to ensure there was no knowledge of genotype. Images were blinded to ensure there was no knowledge of genotype. Individual statistical tests and *n* numbers used are noted in figure legends. Statistical significance was considered to be $p \leq 0.05$.

Confocal microscopy was performed using a Nikon A1R$^+$ Resonant Scanning System (Nikon) (10x and 40x objectives; 0.3 and 1.3 oil NA; Nikon A1R$^+$ microscope; simultaneous image acquisition). 488 and 543 nm laser lines were used for excitation. The resultant confocal Z-series produced in NIS Elements 2D Analysis software were exported and merged using Fiji ImageJ software.

Figures were created using GNU Image Manipulation Program (GIMP) for Windows.

Chapter TWO: Results

2.14. Cellular and molecular characterisation of the motor unit in the early symptomatic *Cre-ER; SMN2; Δ7; Smn^{Res}* mouse

The initial aim of this study was to identify and characterise what cellular and molecular perturbations may exist in the *Cre-ER; SMN2; Δ7; Smn^{Res}* (*Smn^{Res})* mouse model, newly established in our breeding facilities, at a designated early symptomatic time point. I selected postnatal day 4 (P4), a time point near the limits of the therapeutic window, as the age at which I would perform this pathological investigation. Published findings by Lutz et al (2011) and our own phenotypic observations (unpublished) identified P4 as a point within the disease time course at which a neuromuscular phenotype was significantly distinguishable. Characterisation of pathology present in the early-symptomatic P4 *Smn^{Res}* mouse would serve as a baseline for the ultimate aim of determining what pathological features are capable of recovery upon postnatal restoration of SMN.

2.14.1. Pre-synaptic nerve terminal loss and abnormal accumulation of neurofilament in the Smn^{Res} mouse at P4.

In order to evaluate the pathological status of the motor neuron at P4, I examined morphological correlates of both pre- and post-synaptic pathology at the neuromuscular junction (NMJ) in a range of muscles from the abdomen and head of the mouse, selected for their differential exhibition of NMJ pathology in other mouse models of SMA. The transversus abdominis (TVA; an abdominal muscle from the anterior abdominal wall), the levator auris longus (LAL; a cranial muscle comprised of two distinct bands, rostral (LALr) and caudal (LALc)), the auricularis superior (AS; a

cranial muscle), and abductor auris longus (AAL; a cranial muscle) were isolated as whole-mount muscle preparations for the visualisation and analysis of complete pre-synaptic nerve terminals and associated acetylcholine receptor (AChR) endplates. Aforementioned muscles examined have been previously characterised to be differentially affected in several mouse models of SMA (Mélissa Bowerman et al., 2012; Murray et al., 2008; Thomson et al., 2012). In particular, the TVA has been reported to be highly vulnerable in other murine models of SMA as well as in other mouse models of motor neuron degeneration (Mélissa Bowerman et al., 2012; Murray et al., 2008; Newbery et al., 2005).

The TVA and the cranial muscles (LALc, LALr, AS and AAL) were dissected from early-symptomatic P4 *Smn*^{Res} mice. Dissections were performed to isolate the TVA from the surrounding abdominal muscles, while the superficial layer (LALc and LALr), and deep layer (AS and adjacent AAL) of the cranial muscles were kept attached at the midline (refer to **Figure 2.6)** and subsequently processed as a flat "quadrant," with all four individual muscles remaining highly distinct. Care was taken in all dissections to maintain the integrity of the muscle along with the respective nerve supply. Pre-synaptic axons and nerve terminals were labelled with antibodies directed against total neurofilament (NF) and synaptic vesicle protein 2 (SV2) (green; see Methods), while post-synaptic AChR endplates were labelled with tetramethylrhodamine-conjugated α-bungarotoxin (BTX) (red; see Methods).

Almost 100% of endplates examined within muscles belonging to wildtype or heterozygous P4 animals were fully innervated by the pre-synaptic nerve terminal. Full innervation was defined as complete coverage of the post-synaptic endplate by the branches of the nerve terminal; a representative confocal micrograph highlighting a cluster of fully innervated endplates within the LALc of a P4 control mouse is visible

as the top-left image of Figure 1A. However, a striking proportion of endplates across all muscles in the *Smn*^{Res} animals featured either partial or complete withdrawal of the pre-synaptic endplate (depicted in **Figure 2.7A** by arrowhead and arrow, respectively). Statistical analysis of the percentages of fully innervated, partially innervated, or vacant endplates in the TVA, LALc, LALr, AS and AAL of *Smn*^{Res} mice compared to respective muscles in littermate controls revealed a significant decrease in the percentage of fully occupied endplates and a significant increase in the percentage of partially occupied or vacant endplates across all muscles of the P4 *Smn*^{Res} mouse (**Figure 2.7B**). A comparison of the mean percentage of vacant endplates within individual *Smn*^{Res} muscles highlighted an intermuscular spectrum of vulnerability to denervation, with the AAL featuring the relatively smallest percentage of partially innervated or vacant endplates; endplates within the LALr, AS, TVA and LALc suffered increasingly severe losses of the pre-synaptic nerve terminal, respectively (**Figure 2.7B**).

An abnormal presence of aggregated neurofilament (NF) infiltrating the pre-synaptic terminal is a pathological hallmark consistently reported across a number of mouse models of SMA (Mélissa Bowerman et al., 2012; Cifuentes-Diaz et al., 2002; Kariya et al., 2008; Kong et al., 2009; Murray et al., 2008). Marked NF accumulation was immediately evident within the NMJs of P4 *Smn*^{Res} muscles compared to those of littermate controls. Severity of accumulation was quantified based on an independently-devised scoring criteria. Individual endplates across all muscles were categorised as one of the following: *Stage 1*: no accumulation visible; *Stage 2*: individual nerve terminal branches swollen, complexity of nerve terminal branching retained; *Stage 3*: severe accumulation, complexity of nerve terminal branching largely lost, underlying post-synaptic endplate largely obscured; *Stage 4*: complete and

absolute obscurity of the post-synaptic endplate by the neurofilament-engorged nerve terminal. Statistical analyses confirmed the significant presence of severely accumulated neurofilament (Stages 3 & 4) across the AAL, LALr, AS, TVA and LALc of P4 *Smn*^{Res} mice compared to the equivalent muscles of P4 littermate controls (**Figure 2.7C**). Comparison of the mean rank of percentages of endplates within all *Smn*^{Res} muscles scored as being affected by Stage 4-type accumulation also produced an intermuscular spectrum of pathology in the same order as the spectrum of denervation, with the AAL and the LALc being the least and most affected, respectively.

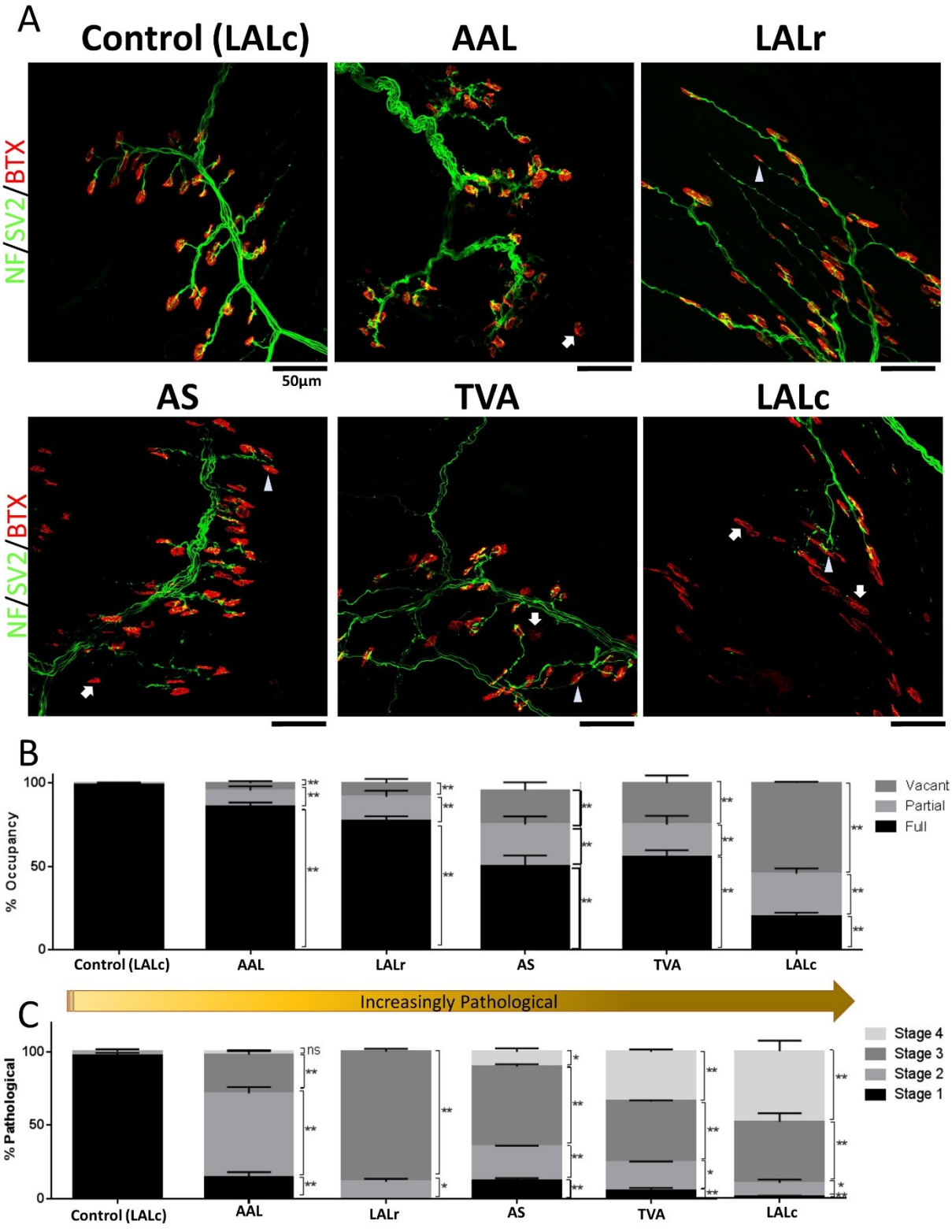
A
Control (LALc)
AAL
LALr
NF/SV2/BTX
50µm
AS
TVA
LALc
NF/SV2/BTX
B
% Occupancy
100
50
0
Vacant
Partial
Full
Control (LALc)
AAL
LALr
AS
TVA
LALc
Increasingly Pathological
C
% Pathological
100
50
0
ns
Stage 4
Stage 3
Stage 2
Stage 1
Control (LALc)
AAL
LALr
AS
TVA
LALc

Figure 2.7. A spectrum of severity in pre-synaptic morphological defects exists within cranial and abdominal muscles of the P4 *Smn^{Res}* mouse.

(A) Representative confocal micrographs depicting neuromuscular junctions from the caudal band of the levator auris longus (LALc) of a P4 littermate control compared to, in order of increasing pathology, the abductor auris longus (AAL), rostral band of the levator auris longus (LALr), auricularis superior (AS), transversus abdominis (TVA) and caudal band of the levator auris longus (LALc) of P4 *Smn^{Res}* mice. Note the presence of completely (arrow) and partially denervated (arrowhead) motor endplates in all *Smn^{Res}* muscles, in particular the LALc as evidenced by AChR labelling (red) in the absence of a pre-synaptic terminal (green). (Green- neurofilament (NF)/ synaptic vesicle protein (SV2); red- tetramethylrhodamine-conjugated bungarotoxin (BTX)). Scale bar=20µm. **(B)** Quantification of the percentage of fully innervated (black), partially innervated (light grey) and vacant (dark grey) endplates across the AAL, LALr, AS, TVA and LALc of P4 *Smn^{Res}* mice compared to equivalent muscles in P4 littermate controls. Only quantification of the control LALc is depicted in this figure. Significant denervation was observed in all muscles, with the overall greatest percentage of denervation occurring in the LALc. **(C)** Quantification of the percentage of endplates exhibiting presence of accumulated neurofilament from non-presence (Stage 1) to severe accumulation (Stage 4) across the AAL, LALr, AS, TVA and LALc of P4 *Smn^{Res}* mice compared to the LALc of a P4 littermate control. Presence of severe (Stages 3 and 4) NF accumulation was observed in all muscles, with the overall greatest percentage of severe accumulation occurring in the LALc. (n=3 *Smn^{Res}*/control mice, respectively; data are mean ± SE)

(**p*>0.05; ***p*>0.01, according to Mann-Whitney *U* test of each category respectively, eg. % vacant endplates in *Smn^{Res}* versus control for each muscle.)

2.14.2. Shrinkage of post-synaptic endplates in the P4 Smn^{Res} mouse.

In addition to assessing the extent of denervation and NF infiltration of the pre-synaptic nerve terminal at P4 in the *Smn^{Res}* mouse, the size of post-synaptic AChR densities were quantified independently to determine whether any morphological alterations were detectable. A statistical comparison of endplate size measured in the AAL, LALr, AS, TVA and LALc of P4 *Smn^{Res}* mice compared to equivalent muscles in P4 littermate controls revealed a consistent and significant shrinkage of post-synaptic endplate area across all muscle groups (**Figure 2.8A, 2.8B)**. There was no significant variability in endplate size between muscles (data not shown).

In contrast to the apparent intermuscular spectrum of vulnerability to pre-synaptic nerve terminal loss and NF accumulation, the mean endplate area within all muscles characterised (AAL, LALr, AS, TVA and LALc) did not vary significantly between muscle type, suggesting that these post-synaptic alterations may be occurring independently and are not influenced by the status of their associated pre-synaptic inputs (**Figure 2.8B**).

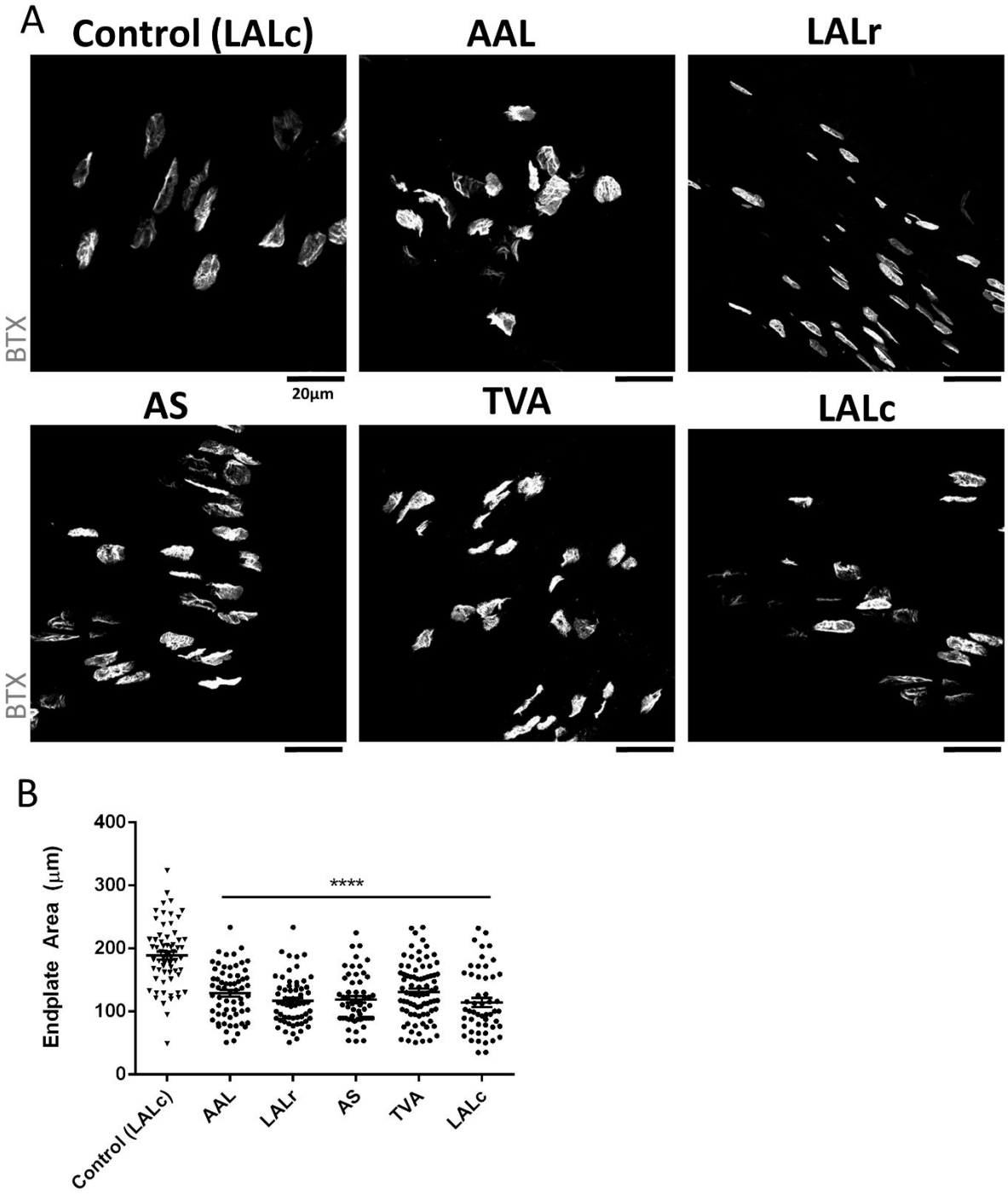

Figure 2.8. Post-synaptic AChR endplates within the cranial and abdominal musculature are significantly smaller at P4 in the *Smn^{Res}* mouse. (A) Representative confocal micrographs showing tetramethylrhodamine-conjugated α-bungarotoxin-labelled AChRs (BTX/red) from the LALc of a P4 control mouse compared to those of the AAL, LALr, AS, TVA and LALc from a P4 *Smn^{Res}* mouse. Scale bar=20µm. **(B)** Quantification of endplate size within the AAL, LALr, AS, TVA and LALc of P4 *Smn^{Res}* mice compared to equivalent muscles in P4 littermate controls. There was no significant variability in endplate size between control muscles; consequentially, endplates within the control LALc only are depicted. A significant reduction in mean endplate size compared to control muscles exists within all muscles analysed (AAL, LALr, AS, TVA and LALc). (n=3 *Smn^{Res}*/control mice per muscle respectively; data are mean ± SE) (****p<0.0001 according to one-way ANOVA with Dunnett's multiple comparisons test).

2.14.3. Upregulation of components of the p53 apoptotic cell death pathway at the transcriptional and protein level at P4 in the Smn^{Res} mouse.

Structural disruption of motor neuron synaptic compartments accompanies a multifarious body of molecular dysregulation in multiple mouse models of SMA, occurring either as a direct result of SMN depletion, or as part of secondary cascades triggered by the degenerative process. It is of crucial interest in the SMA research field to elucidate which specific molecular events precede—and thereby potentially initiate—the degenerative process, and whether these perturbations also occur in a compartmentalised manner to mirror the apparent dissociation between the timing of synaptic and somatic structural changes.

A recent transcriptional screen of laser-captured motor neurons from pre-symptomatic $Smn^{2B/-}$ mice by Murray *et al.* detected an upregulation of transcripts involved in the p53 signalling pathway, despite a lack of phenotype or structural alterations at the neuromuscular junction (Murray et al*.,* 2015). Transcriptional analysis of spinal cords containing motor neuron cell bodies from pre-symptomatic severe "Taiwanese" mice confirmed a similar phenomenon, implicating an upregulation of the p53 apoptosis pathway as a potential modulator of subsequent disturbances in the rest of the motor neuron (Murray et al*.,* 2015).

It was therefore of interest to determine whether apoptotic cell death-associated transcripts would continue be upregulated after onset of neuromuscular phenotype and synaptic pathology. RT-qPCR confirmed that the transcripts of three separate components of the p53 pathway, Cdkn1a, Fas, and PMAIP, were all significantly upregulated at P4 within the spinal cord of the Smn^{Res} mouse (**Figure 2.9A)**.

Quantitative fluorescent western blotting (QFWB) to measure relative levels of Fas in P4 *Smn*^{Res} spinal cords confirmed that this robust upregulation was also translated at the protein level (**Figure 2.9B, 2.9C**).

The combined data suggests that a pre-symptomatic upregulation of p53 transcripts continues through the onset of morphological alterations at the distal compartments of SMA motor neurons and accompanying neuromuscular symptoms. In addition to serving as a future molecular criterion upon which to assess the efficacy of SMN restoration, these findings suggest that aberrant p53 signalling may be intrinsically involved in the degenerative process.

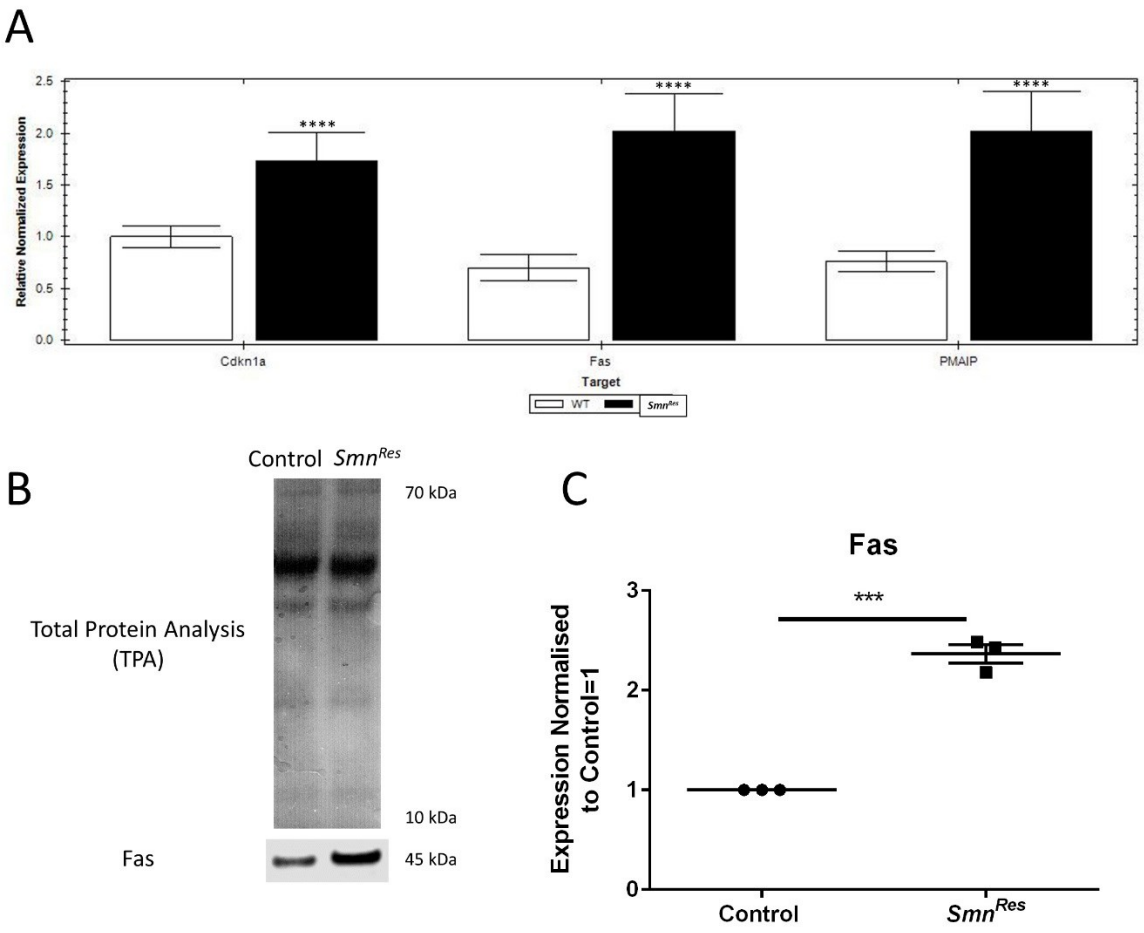

Figure 2.9. Upregulation of factors associated with p53 apoptotic cell death at both the transcriptional and protein level occurs at early symptomatic timepoint P4 in the *Smn^{Res}* mouse.
(A) Bar charts (mean ± SEM) depicting a significant transcriptional upregulation of Fas, CDKN1a and PMAIP, components of the p53 apoptotic signalling pathway, in dorsoventrally halved spinal cords of P4 *Smn^{Res}* mice compared to wild-type controls. Note that this is the third mouse SMA mouse model in which upregulation of programmed cell death-associated transcripts may be observed at an early symptomatic timepoint (please refer to Murray *et al.,* 2015) (n=3; ****$P < 0.0001$, by Mann Whitney *U* test). **(B)** Representative examples of western blot bands used for the quantification of total protein load (TPA) and Fas. Expression of Fas was normalised to total protein load (Ponceau S stain) in order to reliably determine expression changes. **(C)** Scatter plot (mean ± SE) of relative expression of Fas in n=3 *Smn^{Res}* dorsoventral spinal cord halves in relation to wildtype controls. Upregulated expression of Fas at the protein level was statistically significant in relation to wildtype controls. (***$p<0.001$ by unpaired two-tailed *t*-test).

2.14.4. Conservation of select aspects of SMA-specific early-symptomatic transcriptional dysregulation in the Smn^{Res} model.

In addition to the RNAseq screen of motor neurons from pre-symptomatic $Smn^{2B/-}$ mice performed by Murray *et al.,* numerous transcriptional screens of SMA neural tissue (i.e. laser-captured motor neurons or spinal cords) at either pre- or early-symptomatic time points in both the *Δ7* and $SMN2;Smn^{-/-}$ models have identified a subset of transcripts implicated in the SMA degenerative process. Chondrolectin (Chodl), reported to be downregulated in three separate studies of two different mouse models of SMA, promotes defects in motor axonogenesis upon knockdown in zebrafish. The SUMOlyation enzyme ubiquitin specific peptidase-like 1 (Uspl1) and transcription factor Etv1 were also both consistently downregulated across all three screens and have been implicated in aberrant neurodevelopment (Murray *et al.,* 2008; Zhang *et al.,* 2011; Zhang *et al.,* 2013).

In order to assess whether aberrant expression of Chodl, Uspl1 and Etv1 transcripts was similarly conserved in the Smn^{Res} model, TaqMan® probe-based gene expression RT-qPCR assays were performed to measure the relative level of transcriptional expression in Smn^{Res} spinal cords compared to wildtype controls. Relative levels of Chodl (**Figure 2.10A**) and Uspl1 (**Figure 2.10B**) were significantly and robustly downregulated and upregulated respectively, in accordance with trends reported by both the Murray and Zhang screens. There was no significant difference in the relative levels of Etv1 between Smn^{Res} and wildtype spinal cord replicates (**Figure 2.10C**). However, alterations in the expression of Etv1 transcripts in the Smn^{Res} mouse may be of a magnitude requiring a greater sensitivity for detection, such as the transcriptional analysis of laser-capture motor neurons rather than the spinal cord, which includes additional neuronal and non-neuronal cells.

In providing a preliminary characterisation of the molecular dysfunction present at P4 in the *Smn*^{Res} model, these experiments demonstrate that similar transcriptional disturbances occurring at early symptomatic time points in more commonly used mouse models of SMA are also present in the *Smn*^{Res} mouse. Although both Lutz et. al (2011) and our own observations indicate that symptomatic onset only occurs at P4, these findings suggest that a significant degree of both structural and molecular alterations have already occurred within the motor unit of the *Smn*^{Res} mouse.

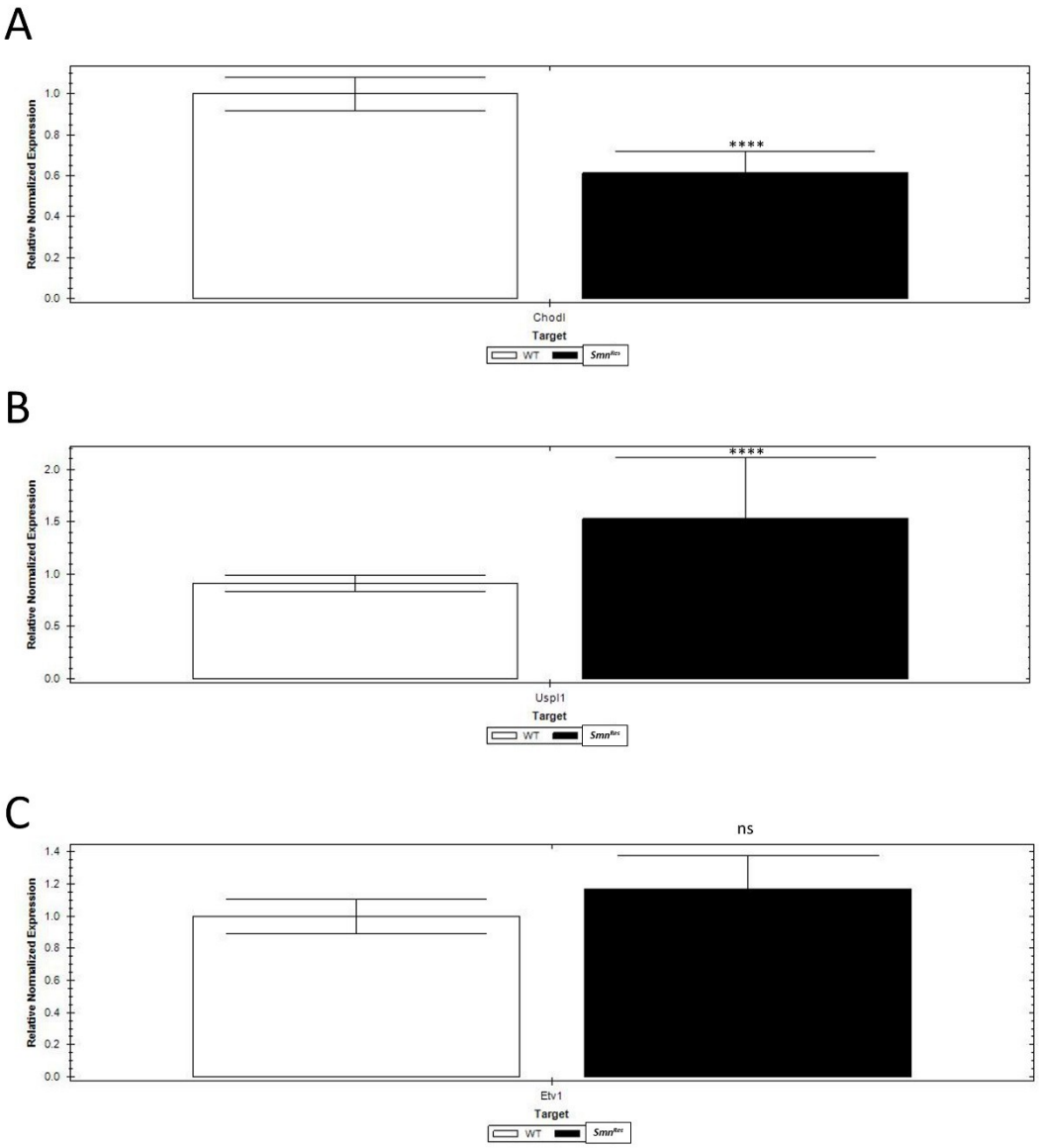

Figure 2.10. The early symptomatic P4 *Smn*^{Res} mouse exhibits similar transcriptional dysregulation reported in three separate studies of two different mouse models at pre- or early-symptomatic timepoints .

(A-C) Bar charts (mean ± SEM) showing relative transcriptional expression of three identified across three separate RNAseq screens of pre- or early-symptomatic SMA spinal cords in dorsoventrally halved spinal cords of P4 *Smn*^{Res} mice compared to wild-type controls. **(A)** Relative levels of the motor axon-growth implicated protein chondrolectin (Chodl) are significantly downregulated at the transcriptional level in the P4 *Smn*^{Res} mouse spinal cord. This observation is in accordance with previous studies conducted in both spinal cords and in laser-captured motor neurons at pre- or early-symptomatic timepoints in two different mouse models of SMA (please refer to Discussion). **(B)** Relative levels of the SUMOlyation enzyme ubiquitin Specific Peptidase Like 1 (Uspl1) are significantly upregulated at the transcriptional level in the P4 *Smn*^{Res} mouse spinal cord. This observation is in accordance with previous studies conducted in both spinal cords and in laser-captured motor neurons at pre- or early-symptomatic timepoints in two different mouse models of SMA (please refer to Discussion). **(C)** There is no significant difference in relative levels of expression of the transcription factor Etv1, another transcript implicated in motor neuron circuitry, in the P4 *Smn*^{Res} mouse spinal cord. (n=3; ****$P < 0.0001$, by Mann Whitney *U* test).

2.15 Characterisation of phenotypic rescue mediated by induction of SMN at P4

The second aim of this study was to determine what cellular and molecular aspects of SMA-specific motor neuron damage may be reversible. Having demonstrated the presence of a broad range of morphological and molecular deficits at the early-symptomatic time point P4, all litters including *Smn^{Res}* pups were gavaged at P4 with 75mg/kg tamoxifen (TM) according to methodology outlined by Lutz et al. in order to promote *Cre*-mediated recombination of the floxed, inverted *Res* allele (see Methods for details of allelic construct). *Smn^{Res}* pups harbouring one copy of the *Cre-ER* allele (*Cre-ER; SMN2; Δ7; Smn^{Res}* mice; hereby referred to as *Smn^{Res} + TM* mice) were capable of *Cre*-mediated recombination of the inverted *Res* allele, and therefore underwent re-expression of full-length SMN. *Smn^{Res}* pups lacking the *Cre-ER* allele (*SMN2; Δ7; Smn^{Res}* mice; hereby referred to still as *Smn^{Res}* mice) do not harbour the capacity for *Cre*-mediated recombination, and therefore continue to follow the typical disease time course. Regardless of *Cre-ER* expression status, heterozygous or wildtype pups were simultaneously treated with tamoxifen to serve as littermate controls. To compare the phenotypic profile of recombined (*Smn^{Res}* + TM) mice versus non-recombined *Smn^{Res}* mice, all treated litters were weighed and subjected to a motor test to assess muscular strength at day of treatment (P4) and every two days thereafter. Mice were then sacrificed at P10, a normal end-stage in the disease time course of the *Smn^{Res}* mouse, and tissues were processed as detailed previously. Whole-mount muscle preparations and spinal cords were utilised as the basis of cellular and molecular analyses to determine what aspects of motor neuron pathology were capable of recovery after the postnatal restoration of SMN.

2.15.1. Phenotypic correction of the Smn^{Res} mouse following re-expression of full-length SMN at P4.

At time of treatment with tamoxifen at P4, both *Smn^{Res}* and *Smn^{Res}* + TM pups were markedly smaller and lighter than wildtype or heterozygous littermate controls (**Figure 2.11A**). Following a single administration of 75mg/kg tamoxifen (TM) via oral gavage at P4, *Smn^{Res}* mice, which do not harbour the *Cre-ER* allele, followed the typical phenotypic time course of SMA mice, failing to thrive and remaining significantly smaller than littermate controls at time of sacrifice at P10. Conversely, *Cre-ER* mice (*Smn^{Res} + TM)* mice gained weight over the 6 days following treatment, at a magnitude and rate comparable to that of treated littermates. By sacrifice at P10, the mean weight of *Smn^{Res}* + TM pups was nearly indistinguishable from that of littermate controls (**Figure 2.11A).**

Prior to treatment with tamoxifen at P4, the performance of all *Smn^{Res}* (non-*Cre* expressing), *Smn^{Res}* + TM (*Cre*- expressing), and control pups in a time-to-right test was noted (see Methods for a detailed description of the time-to-right assay). While P4 control mice were able to right themselves well within the 30 second cut-off time, both P4 *Smn^{Res}* and *Smn^{Res}* + TM pups exhibited an obvious difficulty in turning themselves over, with the majority assessed completely unable to right themselves within the cut-off period (**Figure 2.11B**). After tamoxifen treatment, all mice were subjected to further time-to-right tests at P6, P8 and P10. The *Smn^{Res}* mouse, which does not harbour the *Cre-ER* allele and therefore does not undergo re-expression of full-length SMN, continued to perform poorly in the time-to-right assay, and was still unable to right itself within 30 seconds at any assessed time point. In contrast, *Smn^{Res}* + TM animals, which re-express full-length SMN upon metabolism of tamoxifen, exhibited a rapid and robust improvement in motor performance at all time points

assessed (**Figure 2.11B**). By time of sacrifice at P10, the righting ability of *Smn*^{Res} + TM animals was virtually indistinguishable from littermate controls, with all pups assayed able to right themselves within 10 seconds. Perhaps most strikingly, an improvement in righting ability was immediately evident by P6, only 48 hours after treatment, in three of the four *Smn*^{Res} + TM mice. The fourth *Smn*^{Res} mouse, which failed to right itself within the 30 second cut-off in one of two trials, was highly active during both trials despite poor righting ability. This atypical activity distinguished it from the age-matched *Smn*^{Res} pup which exhibited a marked decrease in movement and ceased its struggle to right, remaining immobile within the 30 second period.

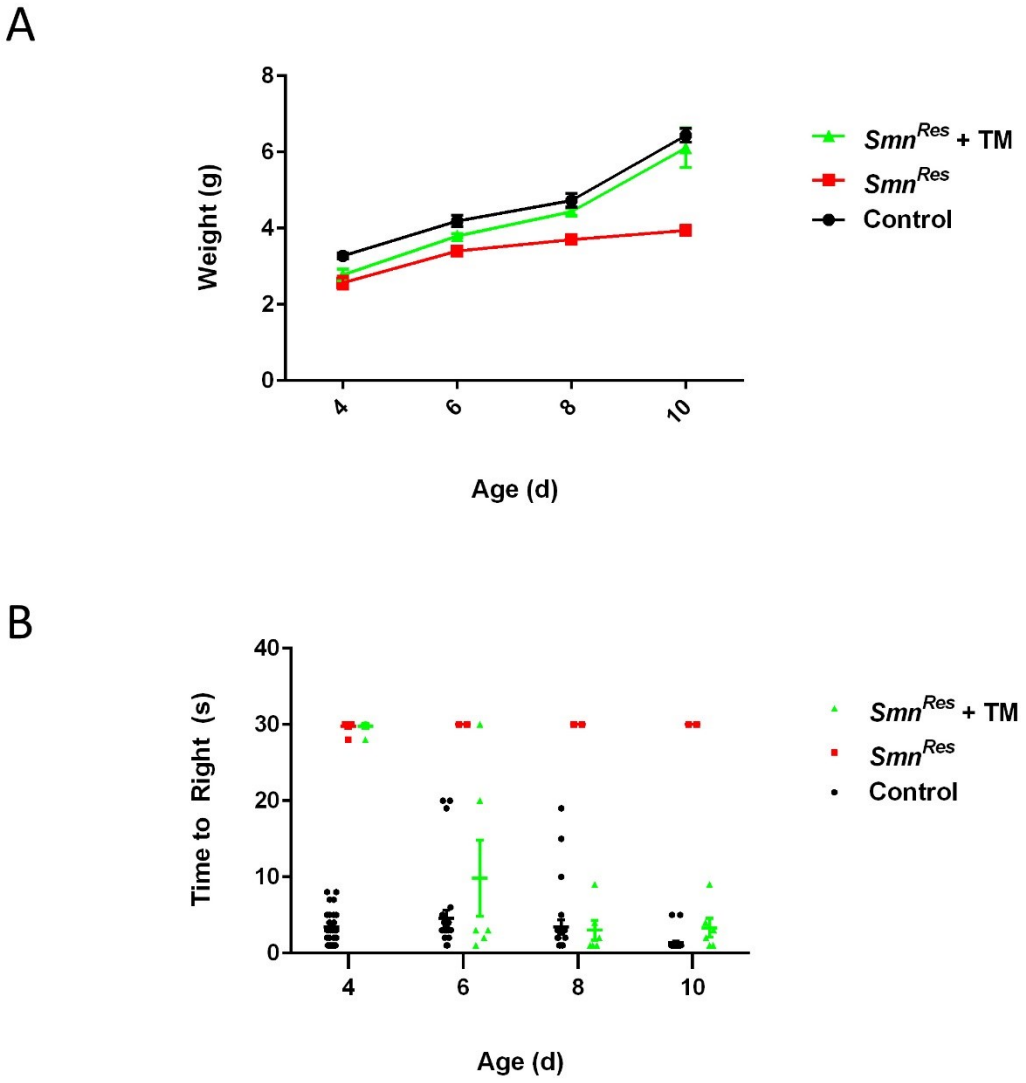

Figure 2.11. Re-expression of full-length SMN via tamoxifen-mediated recombination of the *Res* allele at P4 promotes improvements in weight gain and motor performance.
(A) Weight curve comparing growth profiles of SMN recombined (*Smn^{Res} + TM)* and non-recombined (*Smn^{Res})* mice compared to littermate controls over time. The *Smn^{Res}* mouse that did not undergo tamoxifen-mediated recombination failed to thrive and gain weight from P4 onwards, and was noticeably smaller than littermate controls at P10. *Cre-ER; Smn^{Res}* animals are capable of tamoxifen-induced recombination *(Smn^{Res} +TM)* and exhibit a more robust weight gain after dosage with tamoxifen at P4. Body weight was measured every two days from P4. (n=4 *Smn^{Res} +TM*; n=4 *Smn^{Res}* at P4, n=1 for subsequent time points; n>12 control). **(B)** Scatter plot comparing performance of *Smn^{Res} + TM* and *Smn^{Res}* mice in time-to-right assay. Immediately prior to tamoxifen dosage at P4, both *Smn^{Res}* and *Smn^{Res} + TM* animals exhibited a marked difficulty in righting ability compared to littermate controls. *Cre-ER; Smn^{Res} (Smn^{Res}+ TM)* animals gavaged at P4 are capable of SMN recombination and showed a robust improvement in motor performance within 48 hours from time of dosing. The *Smn^{Res}* mouse, which did not express *Cre-ER,* did not undergo recombination of SMN upon dosing at P4 and continued to perform poorly in the time-to-right test until sacrifice at P10. Time to right performance was assessed every two days from P4, with two trials per animal per session. For each test, animals were placed on their backs on a flat bench top with all four paws in the air, and the time for them to return to the standard anatomical position with all four paws stably to the bench surface was recorded. Cutoff for all tests was set at 30 seconds. Animals were returned to their nests for a minimum of two minutes between trials to minimise hypothermia-induced fatigue (n=4 *Smn^{Res} +TM*; n=4 *Smn^{Res}* at P4, n=1 for subsequent time points; n>12 control).

A

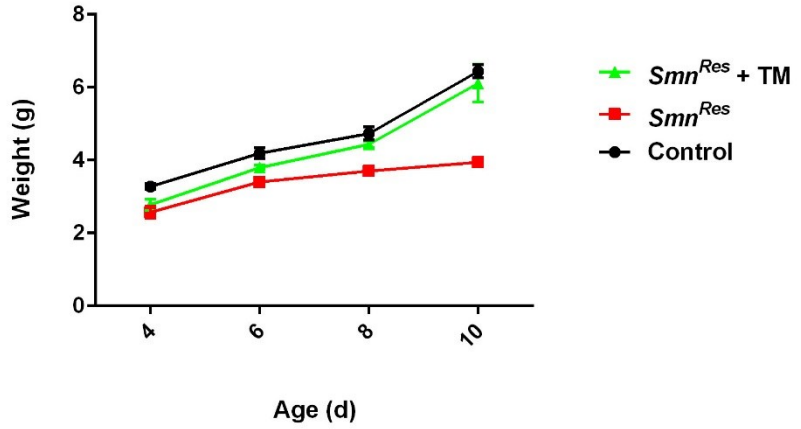

B

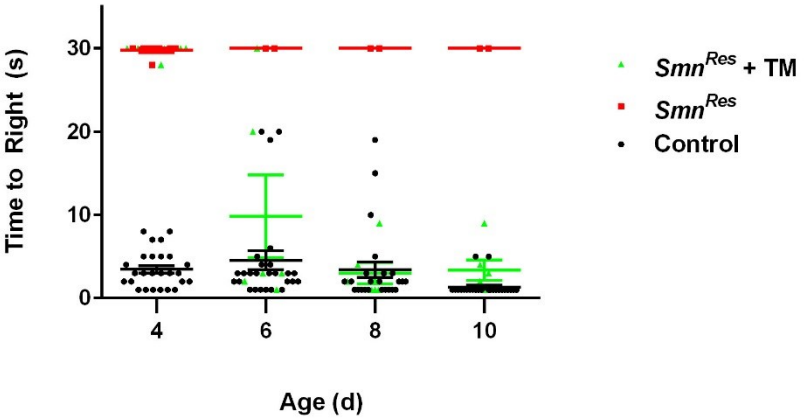

Figure X.X. Re-expression of full-length SMN via tamoxifen-mediated recombination of the *Res* allele at postnatal day 4 promotes improvements in weight gain and motor performance.
(A) Graphical representation of the weights of SMN recombined (*Smn^{Res} + TM)* and non-recombined (*Smn^{Res})* mice compared to littermate controls over time. *Smn^{Res}* mice that do not undergo tamoxifen-mediated recombination fail to thrive and gain weight from P4 onwards, and are noticeably smaller than littermate controls at P10. *Cre-ER; Smn^{Res}* animals are capable of tamoxifen-induced recombination *(Smn^{Res} +TM)* and exhibit a more robust weight gain after dosage with tamoxifen at P4. Body weight was measured every two days from P4. (n=4 *Smn^{Res} +TM*; n=4 *Smn^{Res}* at P4, n=1 for subsequent time points; n>12 control). **(B)** Scatter plot of performance in time-to-right assay. All *Smn^{Res}* animals regardless of *Cre-ER* expression prior to tamoxifen dosage exhibited a marked difficulty in righting at P4 compared to littermate controls. *Cre-ER; Smn^{Res} (Smn^{Res}+ TM)* animals gavaged at P4 are capable of SMN recombination and showed a robust improvement in motor performance within 48 hours from time of dosing. *Smn^{Res}* animals not expressing *Cre-ER* do not undergo recombination of SMN upon dosing at P4 and continued to perform poorly in the time-to-right test until sacrifice at P10. Time to right performance was assessed every two days from P4, with two trials per animal per session. For each test, animals were placed on their backs on a flat bench top with all four paws in the air, and the time for them to return to the standard anatomical position with all four paws stably to the bench surface was recorded. Cutoff for all tests was set at 30 seconds. Animals were returned to their nests for a minimum of two minutes between trials to minimise hypothermia-induced fatigue (n=4 *Smn^{Res} +TM*; n=4 *Smn^{Res}* at P4, n=1 for subsequent time points; n>12 control).

2.15.2. Amelioration of pre-synaptic terminal loss and neurofilament accumulation across all muscle groups in the P10 Smn^{Res} + TM *mouse after tamoxifen-mediated re-expression of full-length SMN at P4.*

Whole-mount preparations of the tamoxifen-treated P10 TVA, AAL, LALr, AS, and LALc muscles from *Smn^{Res}* mice, *Smn^{Res}*+ TM mice, and littermate controls were immunocytochemically labelled for imaging and analysis of their neuromuscular junctions. As these muscles had been characterised within the P4 *Smn^{Res}* mouse to be differentially vulnerable to cellular correlates of pre-synaptic pathology, it was of interest to evaluate not only whether pathology had worsened in the P10 *Smn^{Res}* mouse, but also to determine whether any morphological abnormalities were altered within muscles belonging to *Smn^{Res}*+ TM mice.

At P4, prior to dosage with tamoxifen, the AS, TVA and LALc of *Smn^{Res}* mice exhibited the greatest extent of pre-synaptic nerve terminal loss and accumulation of phosphorylated neurofilament at P4 in the untreated *Smn^{Res}* mouse (see **Figure 2.7**). Upon examination of the AS, TVA and LALc of P10 *Smn^{Res}* mice, which lack the *Cre-ER* allele, it was immediately evident that their highly pathological status at P4 was predictably retained at P10 (**Figure 2.12A, B, C: middle column**). Quantification of the percentage of fully occupied, partially occupied, or vacant endplates within the P10 *Smn^{Res}* AS, TVA and LALc confirmed that a significant percentage of endplates within all muscles were either only partially innervated or complete vacant of any innervation by the pre-synaptic nerve terminal. (**Figure 2.12D**). Similarly, quantification of neurofilament infiltration of the pre-synaptic nerve terminal, using an identical staging criteria as applied to P4 *Smn^{Res}* muscles, revealed the significant accumulation of phosphorylated neurofilament to a severe extent (Stages 3 and 4) at the neuromuscular junction of P10 *Smn^{Res}* mice. (**Figure 2.12E).**

Remarkably, the structural integrity of neuromuscular junctions within the AS, TVA and LALc of *Smn*^{Res} + TM P10 mice appeared strikingly unimpaired, even under high confocal resolution (**Figure 2.12A, B, C: right column**). Indeed, quantification of the percentage of vacant AChR endplates confirmed that there was no significant difference in the percentage of vacant endplates within the AS, TVA and LALc of P10 *Smn*^{Res} mice compared to those within equivalent muscles from P10 littermate controls. However, within the AS and TVA of *Smn*^{Res} + TM mice, a small but significant percentage of endplates remained only partially innervated, suggesting that while re-expression of full-length SMN at P10 mediates a clear improvement in pre-synaptic terminal loss, the stability of the synaptic interface may not be entirely restored.

Quantification of NF accumulation within the AS, TVA and LALc of P10 *Smn*^{Res} + TM mice confirmed that there was no longer a statistically relevant presence of NMJs exhibiting the most severe degree of infiltration (Stage 4) compared to littermate controls (**Figure 2.12E**). However, both the AS and TVA still exhibited a significant percentage of endplates harbouring severe Stage 3-type accumulation, again suggesting that while restoration of SMN at P4 rescues defects in synaptic innervation, it may not be sufficient to promote an absolute recovery of neuromuscular junction disturbances in the *Smn*^{Res} mouse.

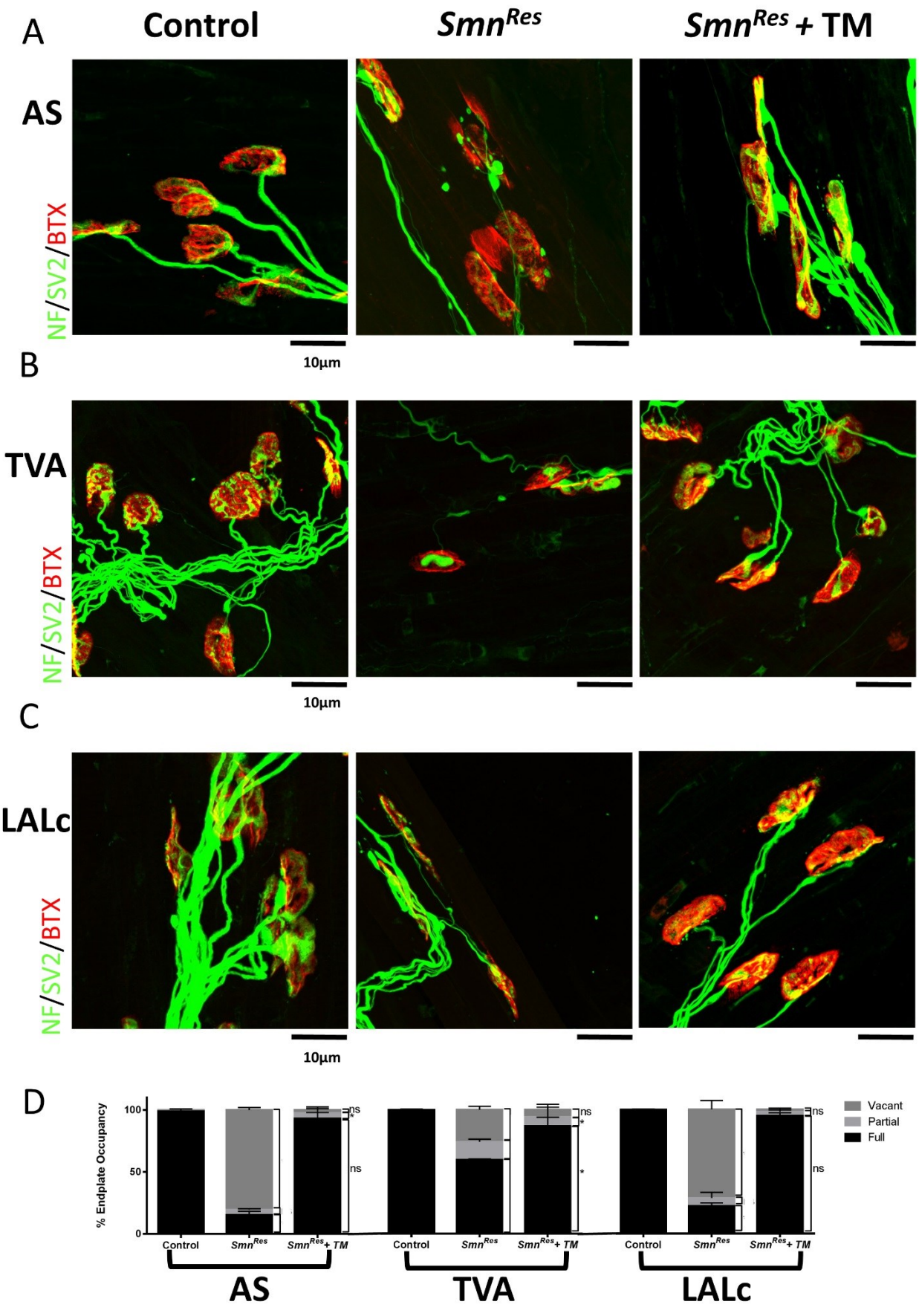
A
Control
Smn^Res
Smn^Res + TM
AS
NF/SV2/BTX
10µm
B
TVA
NF/SV2/BTX
10µm
C
LALc
NF/SV2/BTX
10µm
D
% Endplate Occupancy
100
50
0
ns
*
ns
ns
*
*
ns
ns
Vacant
Partial
Full
Control
Smn^Res
Smn^Res+ TM
AS
TVA
LALc

E

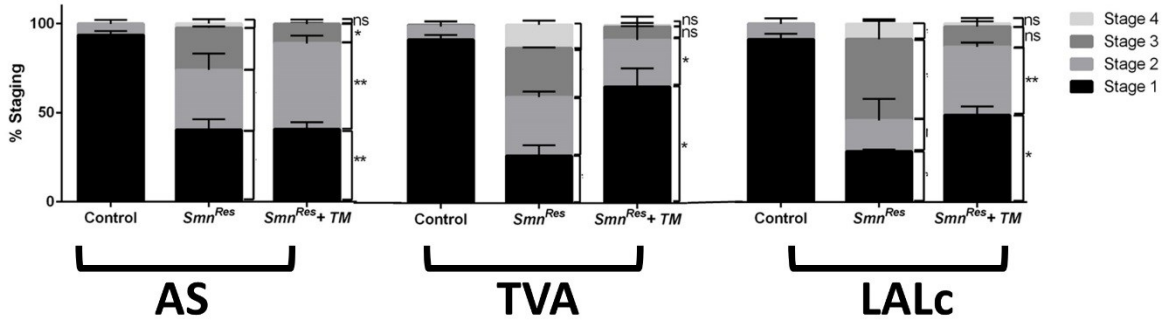

Figure 2.12. Tamoxifen-mediated re-expression of full-length SMN at P4 ameliorates but does not eliminate pre-synaptic terminal loss and pathological morphology at the neuromuscular junction in the most vulnerable muscles at P10.

(A-C) Representative confocal micrographs depicting neuromuscular junctions in the **(A)** auricularis superior (AS), **(B)** transversus abdominis (TVA) and **(C)** caudal band of the levator auris longus (LALc) of a non-*Cre-ER* expressing *Smn^{Res}* mouse at P10 and a *Cre-ER; Smn^{Res} (Cre-ER; Smn^{Res}+ TM)* mouse at P10 compared to a littermate control. All control and experimental mice were gavaged with 75mg/kg tamoxifen at P4; *Cre-ER; Smn^{Res} (Smn^{Res}+ TM)* mice undergo recombination of the *Res* allele and re-expression of full-length SMN. (Green/NF/SV2: neurofilament/synaptic vesicle protein 2; red/BTX: tetramethylrhodamine-conjugated bungarotoxin). Scale bar= 10µm **(D)** Quantification of the percentage of fully innervated (black), partially innervated (light grey), or vacant (dark grey) endplates at P10 within the AS, TVA and LALc, depicted in **(A-C)** respectively. By P10, a marked percentage of endplates within the AS, TVA and LALc of the *Smn^{Res}* mouse are either only partially innervated by the pre-synaptic nerve terminal or completely denervated. Statistical analysis of the percentage of fully innervated, partially innervated, and vacant endplates within the *Smn^{Res}+ TM* mice that undergo tamoxifen-mediated recombination upon dosage at P4 demonstrates that by P10, the percentage of vacant endplates within the AS, TVA and LALc of the *Smn^{Res}+ TM* mice is insignificant from those of controls across these three muscles. **(E)** Quantification of the percentage of endplates exhibiting presence of accumulated neurofilament from non-presence (Stage 1) to severe accumulation (Stage 4) across the AS, TVA and LALc depicted in **(A-C)** respectively. By P10, a marked percentage of endplates within the AS, TVA and LALc of the *Smn^{Res}* mouse exhibit a severe (Stages 3 and 4) accumulation of phosphorylated neurofilament of P4 mice compared to endplates within the respective muscles of a P10 littermate control. In comparison, although the respective muscles of *Smn^{Res}+ TM* mice that undergo tamoxifen-mediated recombination still exhibit a significant presence of phosphorylated neurofilament to a milder degree (ie. Stage 2) compared to littermate controls, the most severe degree of pre-synaptic neurofilament accumulation (ie. Stage 4) is no longer significantly present within the AS, TVA and LALc.

(n=6 *Smn^{Res}+* TM/control; n=2 *Smn^{Res}* muscles, respectively; data are mean ± SE)

(*p<0.05*; **p<0.01* by Kruskaw-Wallis test with Dunn's *post-hoc* multiple comparisons of each criteria within each muscle separately, eg. Kruskaw-Wallis test of the % of fully occupied endplates within the AS; Kruskaw-Wallis test of the % of NMJs exhibiting Stage 3-type severity of accumulated phosphorylated neurofilament within the TVA).

Quantification of pre-synaptic nerve terminal loss and accumulation of phosphorylated neurofilament within the cranial muscles relatively resistant to NMJ pathology at P4 (AAL and LALr) between *Smn*^{Res} and *Smn*^{Res} + TM P10 mice compared to littermate controls confirmed a similar phenomenon of pathological amelioration (**Figure 2.13**). While the AAL and LALr of P10 *Smn*^{Res} mice still harboured a small percentage of partially or entirely denervated post-synaptic endplates, the percentage of partially innervated or vacant endplates within the AAL and LALr of *Smn*^{Res} + TM mice at P10 was negligible and not statistically significant from that of muscles from P10 littermate controls. The statistical analysis of the percentage of endplates exhibiting abnormally accumulated neurofilament also confirmed that there was no longer a significant presence of severe NF infiltration (Stage 3 or 4) within the AAL or LALr of P10 *Smn*^{Res}+ *TM* mice, while the AAL and LALr of non-*Cre-ER* expressing P10 *Smn*^{Res} mice still contained a significant percentage of NMJs scored as being severely affected compared to littermate controls.

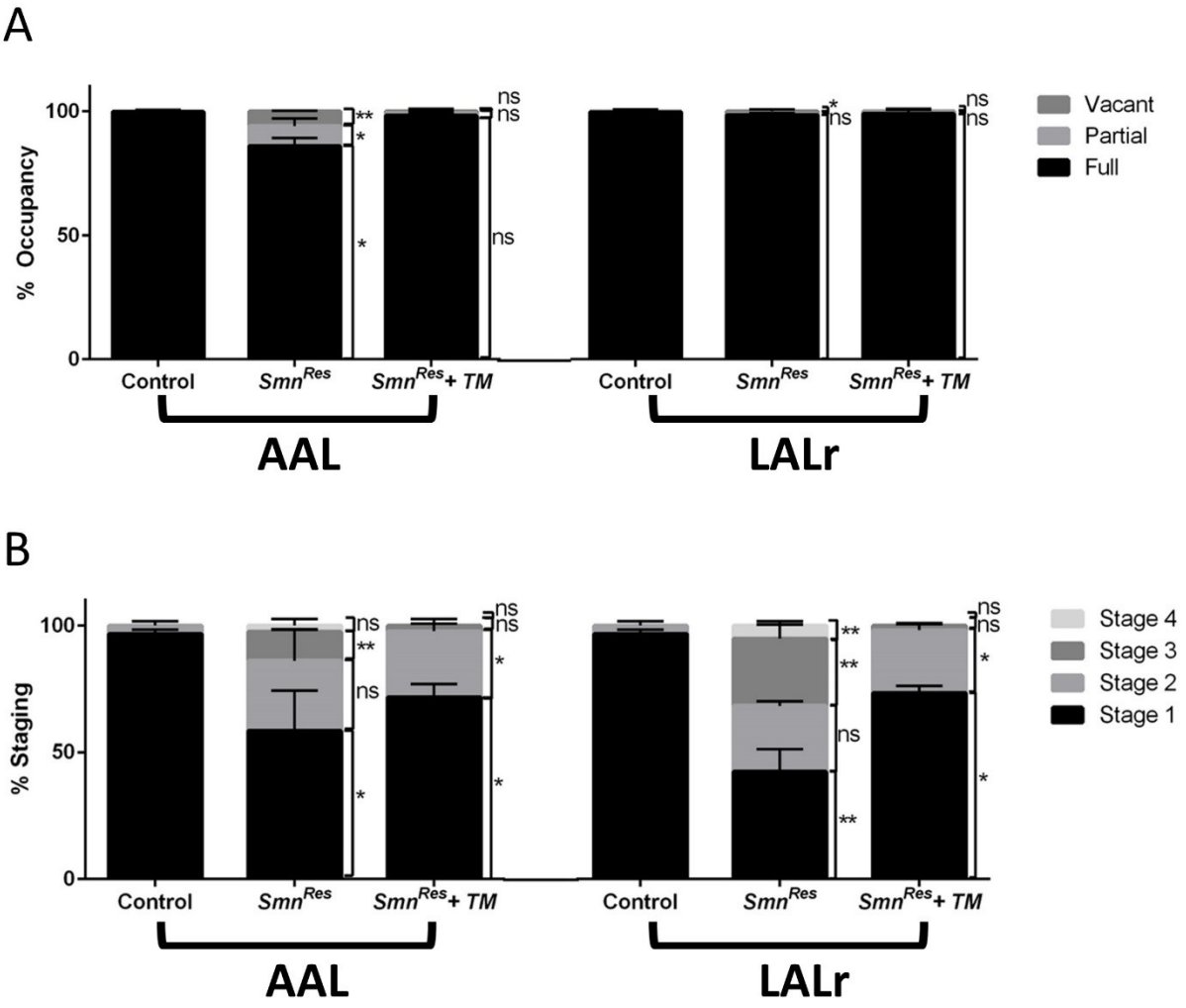

Figure 2.13. Tamoxifen-mediated re-expression of full-length SMN at P4 also ameliorates but does not eliminate pre-synaptic terminal loss and pathological morphology at the neuromuscular junction in the less vulnerable cranial muscles at P10.

(A) Quantification of the percentage of fully innervated (black), partially innervated (light grey), or vacant (dark grey) endplates at P10 within the abductor auris longus (AAL) and rostral band of the levator auris longus (LALr), two cranial muscles exhibiting a comparatively milder pathology at P4 than the AS, TVA or LALc (refer to Figure 1). By P10, a small but significant percentage of endplates within the AAL and LALr are completely vacant of any innervation by the pre-synaptic nerve terminal in the *Smn^{Res}* mouse. Statistical analysis of the percentage of vacant endplates within the *Smn^{Res}+ TM* mice that undergo tamoxifen-mediated recombination upon dosage at P4 demonstrates that by P10, the percentage of vacant endplates within the AAL and LALr of the *Smn^{Res}+ TM* mice is insignificant from those of controls across these three muscles. **(B)** Quantification of the percentage of endplates exhibiting presence of accumulated neurofilament from non-presence (Stage 1) to severe accumulation (Stage 4) across the AAL and LALr. By P10, a marked percentage of endplates within the AAL and LALr of the *Smn^{Res}* mouse exhibit a severe (Stages 3 and 4) accumulation of phosphorylated neurofilament of P4 mice compared to endplates within the respective muscles of a P10 littermate control. In comparison, although the respective muscles of *Smn^{Res}+ TM* mice that undergo tamoxifen-mediated recombination still exhibit a significant presence of phosphorylated neurofilament to a milder degree (ie. Stage 2) compared to littermate controls, the most severe degree of pre-synaptic neurofilament accumulation (ie. Stage 3 and 4) is no longer significantly present within the AAL and LALr.

(n=6 *Smn^{Res}+* TM/control; n=2 *Smn^{Res}* muscles, respectively; data are mean ± SE)

(**p*<0.05*; **p*<0.01 by Kruskaw-Wallis test with Dunn's *post-hoc* multiple comparisons of each criteria within each muscle separately, eg. Kruskaw-Wallis test of the % of fully occupied endplates within the AAL; Kruskaw-Wallis test of the % of NMJs exhibiting Stage 3-type severity of accumulated phosphorylated neurofilament within the LALr).

2.15.3. Preservation of post-synaptic endplates and reinnervation by the previously withdrawn pre-synaptic nerve terminal within the cranial musculature of the P10 Smn^{Res} + TM *mouse.*

The previous data demonstrate that tamoxifen-induced re-expression of full-length SMN promotes a robust improvement in the proportion of fully innervated neuromuscular junctions in both highly vulnerable muscles (eg. LALc) and relatively resistant muscles (eg. LALr). It remained unknown as to whether the high percentage of fully innervated endplates present in the muscles of P10 Smn^{Res+} TM mouse were due to either one of two situations:

(1) intervention with SMN at P4 merely preserves synapses still intact at point of treatment, while denervated endplates remain vacant and fade by P10, or

(2) previously withdrawn pre-synaptic nerve terminals undergo reinnervation of the post-synaptic endplate upon restored expression of full-length SMN

In order to elucidate whether re-expression of SMN merely preserved intact NMJs or promoted reinnervaton of vacant post-synaptic endplates, individual epifluorescent micrographs of the LAL (both caudal and rostral bands) were montaged to reconstruct the entire innervation pattern of the LAL. Nerve terminals and motor axons were labelled with antibodies against neurofilament (NF) and synaptic vesicle protein 2 (SV2) and AChR endplates were labelled with TRITC-conjugated α-bungarotoxin. A representative montage of the LALc and LALr from a P10 control mouse is visible in **Figure 2.14A.** Note the distinct presence of five endplate regions within the rostral band (identified as R1-R5) and two endplate regions within the caudal band (C1 and C2), first identified by Murray *et. al.,* 2009.

C2 and R3-R5 were selected as regions highly unlikely to be damaged or lost from variability in dissection between muscles due to their proximity to the midline. The total

number of TRITC-BTX labelled endplates within the C2 region of the LALc and within the R3-R5 region of the LALr, were counted and subjected to statistical analyses. The C2 region in the LALc of P10 *Smn*^{Res} mice suffered a marked and significant loss of endplates compared to littermate controls. However, analysis of the number of endplates remaining in the C2 region of the LALc of P10 *Smn*$^{Res+}$ TM mice revealed no significant variability from littermate controls, suggesting that no perceptible loss of endplates had occurred between treatment at P4 and analysis at P10 (**Figure 2.14C**).

A comparison of the number of endplates remaining within the R3-R5 region of the LALr highlighted no significant difference in the number of endplates in muscles from *Smn*^{Res} mice nor in *Smn*$^{Res+}$ TM mice compared to littermate controls (**Figure 2.14D**).

Together with the remarkable improvement in neuromuscular junction integrity across all muscles reported in **Figures 2.12 and 2.13**, these data suggest that tamoxifen-mediated re-expression of SMN at P4 promotes neuronal regeneration to enable the pre-synaptic terminal to reinnervate vacant AChR endplates. This phenomenon is most striking in muscles exhibiting a high degree of pathology at time of treatment.

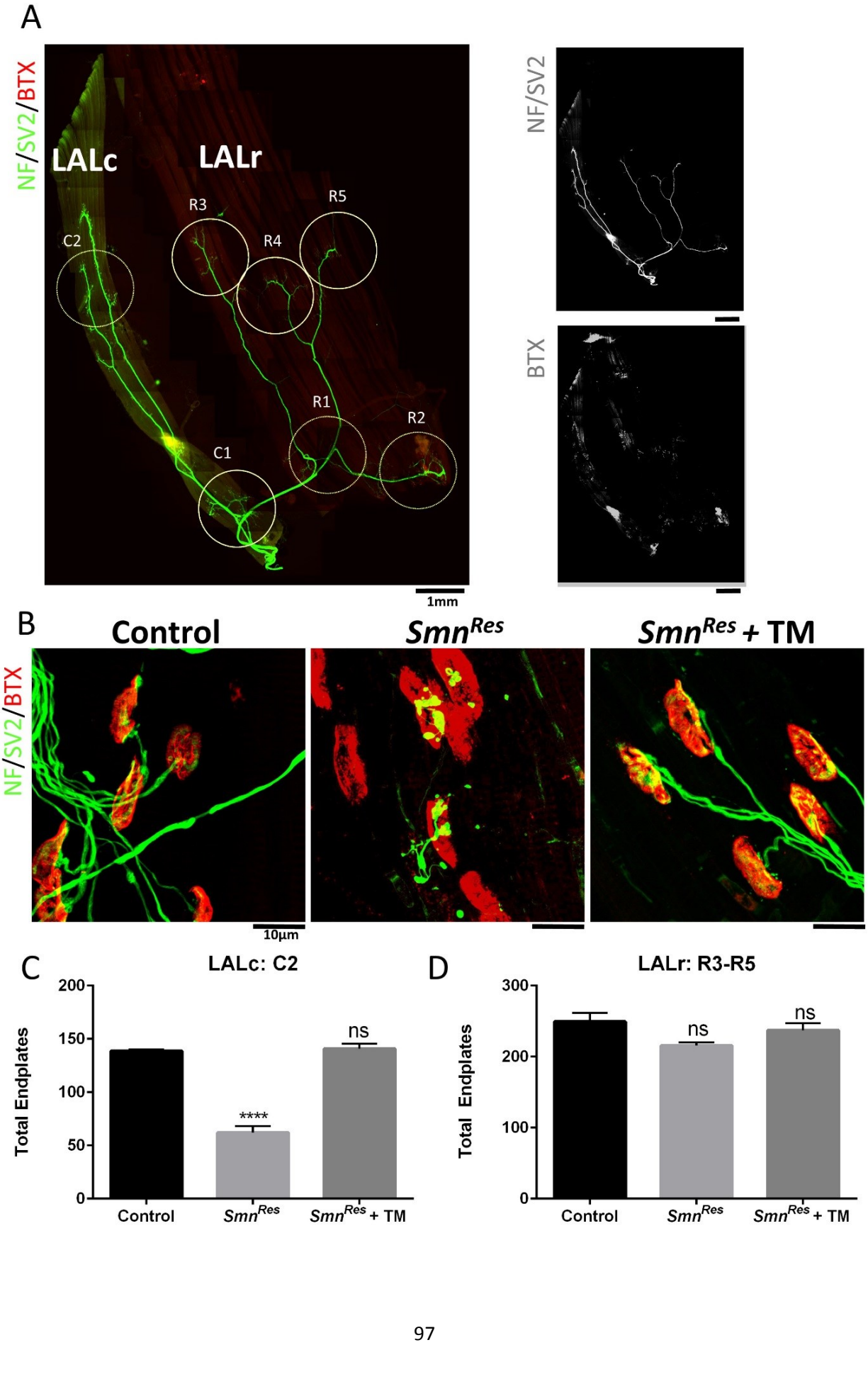
A
NF/SV2/BTX
LALc
LALr
R3
R5
C2
R4
R1
R2
C1
1mm
NF/SV2
BTX
B
Control
Smn^Res
Smn^Res + TM
NF/SV2/BTX
10µm
C
LALc: C2
Total Endplates
200
150
100
50
0
ns
****
Control
Smn^Res
Smn^Res + TM
D
LALr: R3-R5
Total Endplates
300
200
100
0
ns
ns
Control
Smn^Res
Smn^Res + TM

Figure 2.14. Tamoxifen-mediated re-expression of full-length SMN at P4 promotes preservation of existing AChR endplates and reinnervation by the previously withdrawn pre-synaptic nerve terminal

(A) Montaged fluorescent micrographs of a neurofilament (green)/synaptic vesicle protein 2 (green) and tetramethylrhodamine-conjugated α-bungarotoxin (red) labelled LAL muscle. Note the distinct innervation patterns of the caudal (LALc) and rostral (LALr) bands. The LALc contains two distinct endplate regions (C1 and C2) while the rostral band hosts five endplate regions (R1-R5). In this analysis, C2 of the caudal band and R3-R5 of the rostral band were used due to their consistency eliminating dissection. Scale bar= 1mm. **(B)** Representative confocal micrographs depicting neuromuscular junctions in the caudal band of the levator auris longus (LALc) of a non-*Cre-ER* expressing Smn^{Res} mouse at P10 and a *Cre-ER;* Smn^{Res} *(Cre-ER;* Smn^{Res}*+ TM)* mouse at P10 compared to a littermate control. All control and experimental mice were gavaged with 75mg/kg tamoxifen at P4; *Cre-ER;* Smn^{Res} *(*Smn^{Res}*+ TM)* mice undergo recombination of the *Res* allele and re-expression of full-length SMN. (Green/NF/SV2: neurofilament/synaptic vesicle protein 2; red/BTX: tetramethylrhodamine-conjugated bungarotoxin). Scale bar= 10μm **(C)** Quantification of the number of visible endplates in the C2 region of the LALc. By P10, the Smn^{Res} mouse has lost a significant number of AChR endplates to accompany pathological denervation and neurofilament accumulation (refer to Figure 6 & 7). Conversely, the total number of endplates in C2 of the *Cre-ER;* Smn^{Res} *(*Smn^{Res}*+ TM)* mouse is insignificantly affected. As a significant proportion of endplates in the Smn^{Res} mouse were denervated at P4 (refer to Figure 1) compared to a dramatic improvement in endplate occupancy at P10 in the *Cre-ER;* Smn^{Res} *(*Smn^{Res}*+ TM),* this suggests that re-expression of full-length SMN at P4 promotes the regeneration of the pre-synaptic nerve terminal and reinnervation of previously denervated endplates, rather than mere preservation of those still occupied at P4. **(D)** Quantification of the number of visible endplates in the R3-R5 region of the LALr. There is no significant difference in the number of AChR endplates remaining in the R3-R5 region of either the Smn^{Res} or *Cre-ER;* Smn^{Res} *(*Smn^{Res}*+ TM)* mouse at P10 compared to littermate controls. This observation is in accordance with data suggesting that the LALr is only mildly affected in the *Res* model (refer to Figures 1-2 and 7). (n=6 Smn^{Res}+ TM/control; n=2 Smn^{Res} muscles, respectively; data are mean ± SE) *(****p*<0.0001, according to one-way ANOVA with Dunnett's multiple comparisons test.)

Chapter TWO: Discussion

2.16 Overview of Results

The results presented in this chapter firstly reveal that a significant degree of morphological and molecular alterations are evident within the motor unit of the *Smn*^{Res} mouse model of SMA at an early symptomatic time point of P4. Within both the cranial and abdominal musculature, neuromuscular junctions (NMJs) of P4 *Smn*^{Res} mice exhibit cytoarchitectural defects ranging from abnormally accumulated neurofilament at the pre-synaptic nerve terminal and shrinkage of the post-synaptic endplate, to perhaps most notably, a significant loss of synaptic integrity between the pre-synaptic nerve terminal and post-synaptic endplate. These morphological abnormalities at the synapse are accompanied by transcriptional and protein changes within the spinal cord, in which a number of molecular factors, including those associated with apoptotic cell death and other degenerative cascades implicated in SMA, are aberrantly expressed

Secondly, I report a robust rescue of neuromuscular phenotype, as indicated by weight gain and motor performance, following induction of full-length SMN at P4 in the *Smn*^{Res} mouse. Thirdly, and perhaps most importantly, I have demonstrated that intervention with SMN at P4, a time point I have characterised by marked cellular and molecular pathology, results in a striking amelioration of aforementioned pathological correlates at the NMJ, including denervation and neurofilament accumulation. Moreover, I have determined that these improvements in NMJ integrity following restoration of SMN may be attributed to the reinnervation of vacant endplates by the previously withdrawn pre-synaptic nerve terminal. Overall, these results suggest that while NMJ is indeed a

highly vulnerable pathological target in SMA, it is not without the capacity for profound structural regeneration following therapeutic intervention with SMN.

2.17. Correlates of cellular and molecular pathology are present at P4 in the *Smn^{Res}* mouse model of SMA.

Mounting evidence from a number of SMN-based gene therapy and ASO studies suggests that maximal efficacy in therapeutic intervention may only be achieved when SMN is restored at a pre- or early-symptomatic time point, thereby highlighting the existence of a "therapeutic window of opportunity" (Foust et al., 2010; Hua et al., 2011; Passini et al., 2011; Porensky et al., 2012). In order to evaluate the pathological status of the NMJ prior to and following therapeutic intervention with SMN, I selected a time point near the limits of this "window", at which phenotypic rescue would still be possible. Lutz et. al. (2011) observed that the *Smn^{Res}* mouse exhibited deficits in muscular strength by P4; this observation was recapitulated in our hands (Lutz et al., 2011; **Figure 2.11**).

Although both Lutz et. al (2011) and our own observations identified P4 as an early symptomatic time point in the *Smn^{Res}* disease course, the results from these experiments reveal, surprisingly, the marked presence of pre- and post-synaptic pathological hallmarks within all muscles analysed, particularly in the TVA and in the LALc and AS of the cranial muscles. These structural defects at the synapse were accompanied by a significant degree of molecular dysregulation at both the transcriptional and protein level within the spinal cord. These findings, highlighting the extensive disruption of NMJ cytoarchitecture in the *Smn^{Res}* mouse at the start of symptomatic onset, support the popular idea that the synapse is an early and

significant pathological target in SMA. Similarly, these results highlighting a significant disruption of multiple molecular pathways at the time of symptomatic onset in the *Smn*^{Res} mouse also support the theory that degenerative cascades are initiated prior to severe phenotypic decline (Bäumer et al., 2009). Together, these findings suggest that effective therapeutic intervention in patients presenting at time of diagnosis with neuromuscular symptoms must take into account the potential morphological and molecular deficits that may already have manifested at the synapse and beyond.

2.18. Postnatal restoration of SMN at P4 in the Smn^{Res} mouse promotes correction of structural defects and reinnervation of the NMJ

Remarkably, intervention with full-length SMN in the P4 *Smn*^{Res} mouse results in a robust correction of the numerous structural deficits outlined above, including the denervation of NMJs, across all muscles analysed. By montaging epifluorescent micrographs of the *Smn*^{Res} LALc and LALr in order to assess the number of post-synaptic endplates remaining within the musculature, I have revealed that this phenomenon may be attributed to the regeneration of the pre-synaptic nerve terminal input rather than a mere retention of synapses intact at time of restoration.

2.18.1 Implications of neuronal regeneration: therapeutic relevance and a new perspective from reports of clinical trials of Nusinersen (formerly ISIS-SMNRx)

Unlike within the CNS, synapses within the PNS have been widely reported to be capable of regeneration from injury-induced Wallerian degeneration (Barry & Ribchester, 1995; Comley et al., 2011). However, these regenerative capacities have

not been explored in NMJs denervated as a result of disease-induced, “die-back” mechanisms. A number of studies in mouse models of SMA have reported the absence of gross structural defects in NMJs following early therapeutic intervention with SMN; however, restoration of SMN was performed extremely early within the disease course, often at a pre-symptomatic time point, and thus appeared to merely prevent, rather than correct, NMJ damage (Foust et al., 2010; Hua et al., 2011; Passini et al., 2011). While Lutz et. al (2011) reported an improvement in NMJ integrity following restoration of SMN after onset of symptoms, it was unknown whether SMN-based intervention merely halted degeneration at the time of treatment, or whether postnatal restoration of SMN was capable of enabling the damaged motor neuron to regenerate and thereby repair degeneration at the synapse (Lutz et al., 2011). In this thesis, I have presented promising evidence that the SMA NMJ is indeed capable of regenerating itself following therapeutic intervention with SMN. This phenomenon is evident not only in muscles exhibiting comparably mild pathology at P4, but also in the highly vulnerable LALc, AS, and TVA. To date, these results represent the first indication of neuronal regeneration present within a mouse model of SMA following postnatal restoration of SMN.

In a clinical context, these findings suggest that the NMJs of SMA patients harbour a similar regenerative capacity following treatment with the number of SMN-based therapies currently under clinical trial. As there is no current prenatal screening for SMA, patients are typically diagnosed because they are exhibiting neuromuscular abnormalities or failing to meet developmental milestones. As my results from P4 *Smn*^{Res} mice have suggested, a marked degree of structural damage to the synapse may have already occurred by the time neuromuscular symptoms have manifested. By demonstrating that damaged synapses from early symptomatic mice are capable

of structural repair following SMN-based intervention, these findings indicate that SMN-based therapeutics may be a realistic and efficacious option for the vast majority of patients diagnosed after neuromuscular symptoms have begun.

Although the functional implications of these findings are currently outwith the scope of this study, an interesting body of unpublished electromyographical results from recent Nusinersen (formerly ISIS-SMNRx) trials have reported a marked improvement in compound muscle action potential-motor unit estimation (CMAP-MUNE) scores in Type 1 patients treated at an early symptomatic time point (unpublished results presented by Stephen Kolb*,* 2016). In conjunction with the findings presented in this thesis, these clinical results from Type 1 cohorts suggest that synaptic function, as well as structure, harbours the capacity for repair following postnatal restoration of SMN.

2.18.2 Systemic involvement in therapeutic outcome

The results presented in this thesis reveal that tissue-wide restoration of SMN in the *Smn*^{Res} mouse at P4 promoted a robust improvement in neuromuscular phenotype, as evidenced by improvement in motor performance. However, a remarkable aspect of this phenotypic improvement lay in the fact that several treated mice, exhibiting a marked difficulty in righting at P4, were subsequently able to completely and rapidly right themselves within 48 hours of tamoxifen administration. While the findings presented in this chapter indicate a profound degree of regeneration and repair occurring within damaged NMJs in the abdominal musculature following SMN restoration, the increasing implication of systemic defects in SMA must be considered. In other words, is this improvement in motor performance purely the result of

reinnervation of denervated muscles by the pre-synaptic nerve terminal, or does restoration of SMN also correct systemic defects present in the P4 *Smn*^{Res} mouse? It would therefore be of interest to not only investigate the timing of this reinnervation phenomenon following induction of SMN at P4, but also to perform a histopathological analysis of the *Smn*^{Res} mouse, pre- and post-rescue, to determine whether any systemic defects present at P4 also recover.

2.19. On a future perspective

2.19.1 Further characterisation of the rescue phenomenon

From the results presented in this chapter, it may be suggested that cytoarchitectural defects present at the NMJ in the P4 *Smn*^{Res} mouse harbour undergo an exceptional degree of repair following re-expression of SMN. Naturally, future work is needed to determine whether the molecular dysregulation identified in the P4 *Smn*^{Res} mouse is similarly ameliorated. Lutz et. al (2011) reported an improvement in snRNP assembly following induction of SMN at P4; it would be of interest to determine whether other molecular correlates of SMA similarly improve following SMN-based intervention (Lutz et al., 2011). As discussed in the introduction to this thesis, effective therapeutic intervention must consider the widespread histological and molecular implications of SMN depletion. It would therefore be of interest to determine whether molecular cascades downstream of SMN, such as components of the ubiquitin proteasome system, are altered following re-expression of SMN at P4, within the motor unit and beyond.

Finally, this study provide a basis for the further characterisation of the SMN-based therapeutic window. The results presented in this chapter demonstrate that phenotypic

recovery following restoration of SMN at a point “within” the therapeutic window is accompanied by a striking amelioration of pathological correlates at the NMJ; the pathological status of NMJs in a model of late intervention outwith this window, in which we do not expect phenotypic improvement, remain unknown. By analysing NMJ pathology from *Smn^{Res}* mice in which SMN has been restored at different time points, both within and outwith the therapeutic window, it may be possible to determine which aspects of NMJ pathology fail versus successfully recover upon re-expression of SMN. Ultimately, deciphering which cellular aspects of synaptic pathology must be corrected in order to mediate successful phenotypic improvement will provide a mechanistic insight into the temporal limitations of SMN-based therapeutic intervention.

2.19.2 Manipulation of the therapeutic window with combinational therapeutics

By understanding the cellular and molecular events that occur following restoration of SMN at either pre- or post-symptomatic phases of the disease, it will then be possible to develop targeted methods, such as administration of previously identified non-SMN based candidate drugs, to pharmacologically manipulate and extend this therapeutic time window. This work will not only significantly enhance our understanding of what cellular and molecular factors constitute successful clinical outcome, but also maximise the benefit of SMN-based therapies for all SMA patients, regardless of time of diagnosis.

Chapter THREE: Introduction

3.1. Overview

The distal compartments of the lower motor neuron are vulnerable to degenerate in response to a broad range of disease, injury and toxin-induced insults. A number of genetic factors have been identified to influence the response of the axon and synapse to degeneration, most prominently from studies of the protective properties conferred by the spontaneous mouse mutation, Wld^S (Ferri, Sanes, Coleman, Cunningham, & Kato, 2003; Thomas H Gillingwater et al., 2006; Mack et al., 2001; Wang et al., 2001; Wang, Davis, Culver, & Glass, 2002) A growing body of evidence suggests that developmental maturity may also significantly regulate the vulnerability of synaptic compartments of the motor neuron in response to traumatic injury. A study profiling the synaptic response to injury over the postnatal developmental period in mice determined that neuromuscular junctions (NMJs) of very young mice appear to exhibit a reduced rate of degeneration, which is steadily lost through subsequent developmental maturation (Murray, Comley, Gillingwater, & Parson, 2011).

3.2. Age-dependent vulnerability in the motor neuron soma

Since Waller's experiments in the mid-19th century describing a systematic process of anterograde degeneration in severed frog cranial nerves, the mechanisms regulating neurodegeneration following the application of a traumatic stimulus have been extensively studied (Waller, 1850). From a number of these studies, it appears that the degenerative response of the motor neuron cell body, or soma, is markedly

influenced by age-dependant mechanisms. For example, following the crush or transection of the motor neuron axon, neonatal soma have been reported to undergo rapid death, whereas adult soma appear comparably more resilient (Kapoukranidou et al., 2005; L. Li et al., 1998; Pollin, McHanwell, & Slater, 1991). In modern neuroscience, the neuron is considered a highly subdivided structure, with soma, axon and synapses harbouring highly distinct and independent metabolic processes. This theory resulted from observations that degeneration following disease or injury-mediated trauma also occurs in a compartmentalized manner (Gillingwater & Ribchester, 2001). In consideration of this apparent compartmentalized response to degeneration, and the observation that response to injury is developmentally regulated at the cell body, a number of studies have sought to elucidate whether the distal synapses of motor neurons from very young versus older mice may also harbour distinct responses to nefarious stimuli.

3.3. Age-dependant vulnerability at the neuromuscular junction

3.3.1 Age-dependent synaptic response to injury in the Wld(s) mouse

As described in the general introduction to this thesis, the Wld^S mutation confers axonal protection from a number of injury, toxic, and disease-induced insults (Ferri et al., 2003; Gillingwater et al., 2006; Mi et al., 2005; M S Wang et al., 2001; Wang, Wu, Culver, & Glass, 2001; Wang et al., 2002). Although early reports by Perry (1992) and Ribchester (1995) initially suggested that the protective axonal phenotype faded after six months of age, subsequent morphological and biochemical comparisons of young adult versus mice older than 7 months revealed that neither the expression of Wld at the protein level nor the degenerative response to axotomy appears to differ between

young and mature adult Wld^S mice (Perry, Brown, & Tsao, 1992; Ribchester et al., 1995 Gillingwater et al., 2002). However, the study by Gillingwater et al. (2002) identified a notable discrepancy in the rate of degeneration at the neuromuscular junction between young and older adult Wld^s mice. In contrast to the robust axonal protection exhibited in Wld^s mice of all ages, axotomy in nerves from 7 month old Wld^s mice initiated a rapid and near-immediate dissolution of nerve terminal integrity at the neuromuscular junction, although minimally slowly than wildtype age-matched controls. Interestingly, similar traumatic procedures in the nerves of 2 month old Wld^s mice promoted a marked delay in the degeneration of the neuromuscular junction; indeed, at approximately 120 hours post-axotomy, up to up to 90% of post-synaptic densities were still innervated by the pre-synaptic nerve terminal (Gillingwater et al., 2002). These data were supplemented by electrophysiological recordings revealing a rapid decline in endplate potential (EPP) recordings from neuromuscular junctions in the 7 month old mice compared to the relatively resilient recordings from 2 month old mice, suggesting that loss of synaptic function as well as a breakdown of synaptic cytoarchitecture was a comparably accelerated event in older Wld^s mice compared to younger Wld^s mice (Gillingwater et al., 2002) In addition to providing further evidence supporting a significant degree of compartmentalization in the neurodegenerative process, these findings served as an early indication that age-dependant factors may influence the vulnerability of the distal synapse in the murine motor neuron.

3.3.2 Age-dependent synaptic response to injury in the wildtype mouse

The major quandary resulting from experiments performed exclusively in Wld^s mice concerned whether this phenomenon of age-dependant vulnerability was relevant to normal processes of motor neuron degeneration, or whether it was merely an extension of Wld interacting with additional, possibly developmentally regulated,

endogenous factors within the neuron. In a surprising discovery, similar nerve injury experiments performed in wildtype mice revealed an astonishing degree of age-dependant protection at the neuromuscular junction (Murray *et al.,* 2011). Fascinatingly, these results were recapitulated in two distinct models of motor neuron damage, suggesting that age-dependent regulation of synaptic vulnerability may be a ubiquitous phenomenon in the wildtype mouse motor neuron (Murray et al., 2011).

3.3.3. The wildtype neuromuscular junction in hypoxia-reperfusion injury

In addition to the wide range of disease and injury-induced stimuli mentioned previously, nerve cells within both the CNS and PNS, including motor neurons, have been shown to be highly vulnerable to damage from hypoxia-reperfusion injury (Baxter et al., 2008; Watzlawik et al., 2015). A study by Baxter et al (2008) elegantly characterised this hypoxia-reperfusion damage on a morphological level through devising a novel *ex vivo* murine muscle preparation, containing both pre-synaptic nerve terminals and post-synaptic densities, that was capable of being maintained in oxygenated physiological solution (Baxter et al., 2008). By depleting the O2 concentration of the solution to hypoxic levels, Baxter et al. (2008) were then able to generate significant damage to neuromuscular junction connectivity by initiating reperfusion with normal O2 concentrations (Baxter et al., 2008). By demonstrating the marked vulnerability of NMJs to hypoxia-reperfusion damage, this *ex vivo* model is clinically relevant to surgical situations, in which extended tourniquet application has been suspected of promoting chronic damage to peripheral nerves (Saunders, Louis, Weingarden, & Waylonis, 1979). These findings are also of particular interest in conjunction with the growing implication for defective vasculature and accompanying

hypoxia of the PNS and skeletal muscle in a number of neurodegenerative diseases, including ALS and SMA (Moreau et al., 2006; Somers et al., 2016).

Murray et al. (2011) applied this *ex-vivo* hypoxia-reperfusion technique in a variety of cranial and abdominal muscles isolated from P2-P28 wildtype C57BL/6 mice in order to generate a time course analysis of the NMJ response to hypoxic stress. Strikingly, it was immediately evident that preservation of synaptic integrity post-injury diminished in a systematic manner in line with the age of the mice (Murray et al., 2011). Indeed, it was possible to visualise a nearly linear drop-off in NMJ integrity as measured 6 hours post-reperfusion. From P2 to P10, NMJs appeared robustly resistant to hypoxia-reperfusion-induced degeneration, with minimal denervation of the pre-synaptic terminal detectable in injured muscles of P2 to P10 mice 24 hours after the procedure. After P10, NMJ integrity, as measured by the number of fully occupied endplates present 24 hours after reperfusion, dropped steadily in line with the age of the mouse until P21 and older, by which virtually no endplates remained fully innervated 6 hours after injury (Murray *et al.,* 2011). Muscles previously characterised to be differentially vulnerable to degeneration in mouse models of the motor neuron disease spinal muscular atrophy (SMA) (Mélissa Bowerman et al., 2012; Murray et al., 2008; Thomson et al., 2012) exhibited very little variability in their response to hypoxia-reperfusion injury; neuromuscular junctions within the TVA, LAL, AS, and AAL all adhered to this phenomenon of an age-dependant drop-off in resistance to degeneration, with only subtle differences reported between muscle types (Murray et al., 2011). These findings suggest that this apparent developmentally-regulated vulnerability is ubiquitous to all synapses within in the murine skeletal musculature.

Functional assessment of NMJs identified as robustly resistant to hypoxia-reperfusion injury, ie. those from neonatal mice P10 and younger, revealed that these synapses

appear to be functionally as well as structurally preserved 24 hours after injury (Murray et al., 2011). Application of the styryl dye FM1-43FX, which is only taken up by synapses actively undergoing vesicular uptake, robustly labelled all visible endplates within P10 muscles to an extent comparable with non-hypoxic controls, suggesting that synaptic functionality is also retained in the muscles of very young mice (Murray et al., 2011).

3.3.4. The wildtype neuromuscular junction in axotomy

In an attempt to determine whether this phenomenon of an age-dependant increase in neuromuscular junction vulnerability was reproducible in a separate model of peripheral nerve injury, Murray et al. (2011) performed similar time course analyses of neuromuscular junctions in the deep lumbrical muscles 24 hours after axotomy of their nerve supply, the tibial nerve. Remarkably, these experiments revealed a striking conservation of the age-dependant increase in vulnerability identified by the hypoxia-perfusion experiments; NMJs appeared robustly protected from nerve cut-induced Wallerian degeneration up until P21, after which virtually all synaptic integrity appeared to be lost (Murray et al., 2011).

This age-dependant increase in neuromuscular junction vulnerability to injury is illustrated in **Figure 3.1.,** which depicts the steady decline in neuromuscular junction integrity in conjunction with chronological age of the mouse. This phenomenon was demonstrated to be conserved in the levator auris longus (LAL), auricularis superior (AS) and abductor auris longus (AAL) as well as in the abdominal transversus abdominis (TVA) subjected to hypoxia-reperfusion damage, and in the deep lumbrical muscles following tibial nerve crush (Murray et al., 2011). From these experiments, it is therefore evident that a robust protection of neuromuscular junctions following

traumatic injury occurs until approximately 10-12 days of age, after which the extent of the protective phenomenon decreases steadily until it is virtually non-existent by P21.

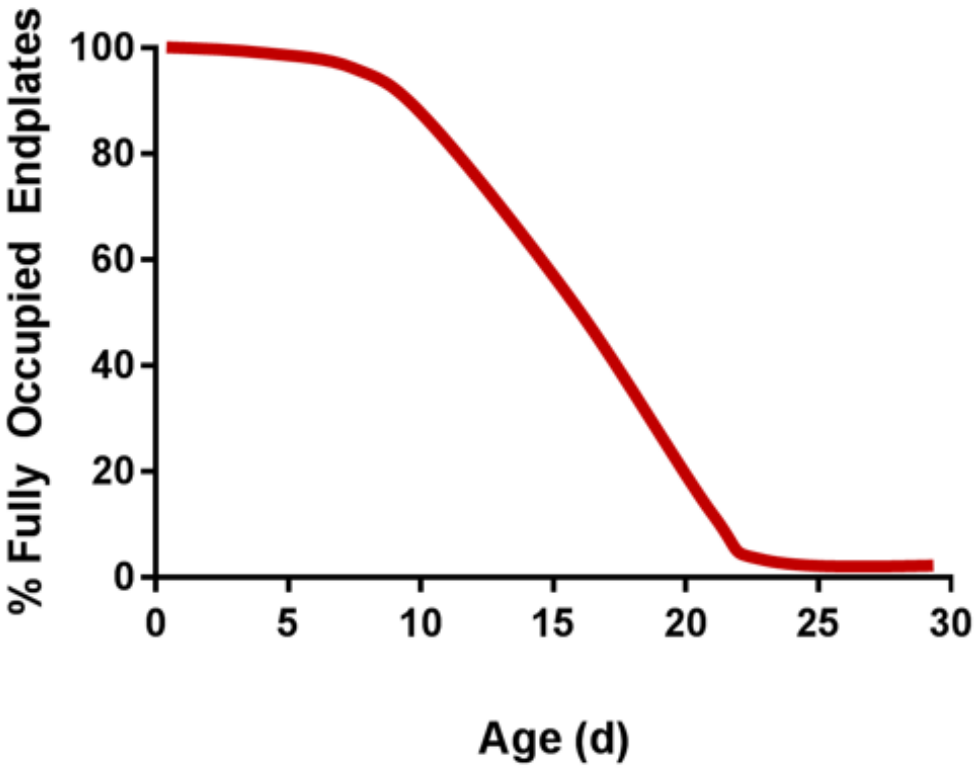

Figure 3.1. Schematic diagram illustrating the progressive, age-dependant decline in neuromuscular junction resistance to both axotomy and hypoxia-reperfusion induced injury produced by both physical trauma and hypoxia-reperfusion. This phenomenon was evident in multiple cranial and abdominal muscles subjected to hypoxia-reperfusion injury, as well as in the deep lumbrical muscles following tibial nerve crush, suggesting the existence of a conserved and ubiquitous response mechanism regulating the degenerative response that is applicable to different types of injurious stimuli.

3.3.5. Differential responses to neuromuscular junction degeneration: an intrinsic synaptic factor or ubiquitous developmental regulation?

The data reported by Murray *et al.* (2011) strongly suggested that a number of mechanisms intrinsic to the developing mouse may regulate NMJ integrity in response to multiple degenerative insults. However, Murray et al. (2011) additionally sought to determine whether this endogenous preservation of NMJ integrity in neonatal mice was determined by the age of the animal, rather than the developmental "age" of the synapse. Regeneration of the neuromuscular junction following either physical or toxin-induced motor neuron injury has been consistently reported to produce developmentally immature, polyinnervated synapses (Barry & Ribchester, 1995; Brown & Ironton, 1978; Fawcett & Keynes, 1990; Werle & Herrera, 1991). Murray et al. (2011) generated "neonatal" synapses in adult mice via the introduction of a preconditioning lesion in the tibial nerve (Murray et al., 2011). Surprisingly, the regenerated NMJs analysed within the lumbrical muscles of older mice appeared to degenerate as rapidly as non-conditioned synapses after a tibial nerve cut was performed. Indeed, the significant degree of denervation reported within these "immature" synapses 24 hours post-procedure was indistinguishable from the percentage of degeneration suffered by their "mature" counterparts (Murray et al., 2011). These findings suggested that the surrounding neonatal environment, or indeed, the age of the entire motor neuron, rather than the synapse itself, dictates the developmental regulation of NMJ vulnerability.

3.4. Aims of this chapter

3.4.1 Summary

To summarise, the neuromuscular junction has been demonstrated to be an early and critical pathological target in not only a range of heritable and spontaneous motor neuron diseases, but also in following injury. For this reason, determining the mechanisms that influence synaptic vulnerability may provide relevant insight on the neurodegenerative process. Studies of the spontaneous Wld^S mutation, which confers a significant delay in axonal degeneration following injury in mice of all ages, revealed that NMJs within the muscles of older adult mice were not protected from synaptic fragmentation after axotomy, compared to the relative resilience exhibited in NMJs from young adult Wld^S mice undergoing identical injury (Gillingwater et al., 2002). Similar studies investigating the synaptic response to both nerve crush and hypoxia-reperfusion injury revealed, surprisingly, that this age-dependent phenomenon was also present in wildtype mice (Murray et al., 2011). NMJs of neonatal mice until approximately P10 appeared robustly resistant degeneration, with a large majority remaining structurally and functionally intact 24 hours after either hypoxia-reperfusion or transection injury (Murray et al*.,* 2011). Conversely, identical procedures in mice of increasing chronological age produced a progressive decline in NMJ protection until approximately P21, by which the vast majority of NMJs underwent rapid and near-complete denervation (Murray et al., 2011). Experiments utilising a preconditioning lesion to generate immature neuromuscular junctions in adult mice failed to mitigate this rapid degeneration of NMJs post axotomy, suggesting that the molecular factors responsible for this period of protection do not originate from the neuromuscular junction itself, but rather are a product of the neonatal environment (Murray et al., 2011). It is therefore possible to hypothesise that a series of dynamic molecular

changes are occurring in the wildtype mouse over this postnatal period that account for this dramatic decrease in NMJ protection.

I have performed an extensive time-course proteomic analysis of the molecular changes occurring over this critical period of increasing synaptic vulnerability, in tissues comprising the immediate environment of the neuromuscular junction: namely, the nerve and post-synaptic muscle. I have then utilised both functional enrichment analysis and predictive pathway analysis to gain further insight into the cellular processes evolving over this period in the wildtype mouse that may account for an increase in rate of axonal and synaptic degeneration.

3.4.2 Aims

AIM 3: Profile molecular alterations occurring in both the pre-synaptic nerve and post-synaptic muscle over the period of increasing NMJ vulnerability in the wildtype C57BL/6 mouse.

3a. Evaluate the efficacy of the TMT10plex™ mass tagging technique, which to date has not been definitively evaluated in whole-tissue studies, as a quantitative proteomics method.

3b. Perform functional annotation enrichment analysis on applicably filtered proteomic results to understand what biological processes may be evolving over this critical postnatal period.

3c. Utilise pathway analysis software to generate cellular and molecular predictive networks from the data set to further understand what mechanisms may account for an age-dependant synaptic vulnerability to degeneration.

Chapter THREE: Methods

3.5 Postnatal nerve and muscle time course proteomics study

3.5.1 Extraction and sample preparation.

Murine nerves (distal portion of the sciatic nerve) and lumbrical muscles (*n*=5 mice per timepoint; each *n* consists of left and right set of nerves/muscle respectively) from wildtype C57BL/6J mice were freshly dissected, snap frozen on dry ice and stored at -80°C **(Figure 3.2).** Tissue was thawed at room temperature, and dissociated in 150µl (muscle) or 250µl (nerve) of label-free buffer containing 1% Halt protease inhibitor cocktail (Sigma-Aldrich); 1.21g Tris hydroxyl methylamine in 80ml ultra-pure dH2O, pH to 7.6 using HCl, made up to 100ml using dH2O, 0.4g SDS added for every 10ml. Dissociation was performed using 2x cycles of the following: (1) 1 minute of a pre-programmed "M-tube protein" dissocation in a gentleMacs tissue dissociator (Millentyl Biotech), followed by (2) centrifugation at 300g for 2 minutes at room temperature. Homogenate was cooled on ice for 20 minutes to allow foam to dissipate. Homogenate was then centrifuged at 20000rpm for 20 minutes at 4°C, and protein concentration of isolated supernatant was determined by microBCA Assay kit (Pierce). Extracted protein samples were stored at -80°C until processing for TMT labelling.

Total protein concentration was determined by loading 7.5µg of protein per timepoint on a NuPAGE™ Novex™ 4-12% Bis-Tris protein gel (Invitrogen, UK) alongside 3µl of SeeBlue® Plus2 Protein Standard (Thermo Fisher). Gel was run at 80V for 5 minutes to ensure equal running, then 150V for 50 minutes. Gel was excised and incubated for 2 hours at room temperature in InstaBlue Coomassie Brilliant Blue pre-mixed solution (Expedeon). Gel was washed 3x 5 minutes in ddH2O. The intensity of total protein

bands was determined by scanning in the 700nm channel with the Li-COR Odyssey® infrared imaging system (Li-COR Biosciences) at a resolution of 169µm and analysing the intensity of identical sections of total protein banding in the 700nm with the Odyssey® ImageStudio Lite software (Version 5.2).

3.5.2 Tandem mass tag (TMT) labelling and fractionation of extracted samples.

Tandem mass tagging and fractionation of extracted samples was performed by the FingerPrints Proteomics facilities at the University of Dundee, to the following protocol:

Protein samples were thawed, trypsinised and desalted at room temperature. 100µg of desalted tryptic peptides per sample were dissolved in 100µl of 100mM tetraethylammonium bromide (TEAB). The 10 different tandem mass tag (TMT) labels comprising the TMT10plex™ kit (Thermo Fisher Scientific) were dissolved in 41µL anhydrous acetonitrile. Each dissolved label was added to a different sample; see **Figure 3.2** for the specificities of which label corresponded to which sample. The sample-label mixture was incubated for 1 hour at room temperature. Labelling reaction was stopped by adding 8µl of 5% hydroxylamine per sample.

Following labelling with TMT, samples were mixed, desalted, and dried in a speed-vac at 30°C. Samples were re-dissolved in 200µl ammonium formate (NH_4HCO_2) (10mM, pH 10) and peptides were fractionated using an Ultimate 3000 RP-High pH High Performance Liquid Chromatography column (Thermo-Scientific) containing an XBridge C18 column (XBridge peptide BEH, 130Å, 3.5 µm, 2.1 X 150 mm) (Waters, Ireland) with an XBridge guard column (XBridge, C18, 3.5 µm, 2.1X10mm) (Waters, Ireland). Buffers A and B used for fractionation consist, respectively, of (A) 10mM ammonium formate in milliQ water and (B) 10mM ammonium formate with 90%

acetonitrile. Before use, both buffers were adjusted to pH10 with ammonia. Fractions were collected using a WPS-3000FC auto-sampler (Thermo-Scientific) at 1 minute intervals. Column and guard column were equilibrated with 2% Buffer B for twenty minutes at a constant flow rate of 0.2ml/min. 175µl per sample was loaded onto the column at a rate of 0.2ml/min, and the separation gradient was started 1 minute after sample was loaded onto the column. Peptides were eluted from the column with a gradient of 2% Buffer B to 5% Buffer B in 6 minutes, and then from 5% Buffer B to 60% Buffer B in 50 minutes. Column was washed for 16 minutes in 100% Buffer B and equilibrated at 2% Buffer B for 20 minutes as mentioned previously. The fraction collection started 1 minute after injection and stopped after 80 minutes (total 80 fractions, 200µl each). The total number of fractions concatenated was set to 15 and the content of the fractions was dried and suspended in 50µl of 1% fomic acid prior to analysis with LC-MS.

3.5.3 LC-MS/MS Analysis

Liquid chromatography- tandem mass spectrometry was performed by FingerPrints Proteomics Facilities at the University of Dundee, to the following protocol:

Analysis of peptide readout was performed on a Q Exactive™ HF Hybrid Quadrupole-Orbitrap™ Mass Spectrometer (Thermo Scientific) coupled with a Dionex Ultimate 3000 RS (Thermo Scientific). LC buffers were made up to the following: Buffer A (2% acetonitrile and 0.1% formic acid in Milli-Q water (v/v)) and Buffer B (80% acetonitrile and 0.08% formic acid in Milli-Q water (v/v). Aliquots of 15µl per sample were loaded at a rate of 5µL/minute onto a trap column (100 µm × 2 cm, PepMap nanoViper C18 column, 5 µm, 100 Å, Thermo Scientific) which was equilibrated with 98% Buffer A.

The trap column was washed for 6 minutes at the same flow rate and then the trap column was switched in-line with a resolving C18 column (Thermo Scientific) (75 µm × 50 cm, PepMap RSLC C18 column, 2 µm, 100 Å). Peptides were eluted from the column at a constant flow rate of 300 nl/min with a linear gradient from 95% Buffer A to 40% Buffer B in 122 min, and then to 98% Buffer B by 132 min. The resolving column was then washed with 95% Buffer B for 15 min and re-equilibrated in 98% Buffer A for 32 min. Q Exactive™ HF was used in data dependent mode. A scan cycle was comprised of a MS1 scan (m/z range from 335-1800, with a maximum ion injection time of 50 ms, a resolution of 120 000 and automatic gain control (AGC) value of 3x106) followed by 15 sequential-dependant MS2 scans (with an isolation window set to 0.4 Da, resolution at 60000, maximum ion injection time at 200 ms and AGC 1x105. To ensure mass accuracy, the mass spectrometer was calibrated on the first day that the runs were performed.

3.5.4 Database search and protein identifications

Raw MS data from the 15 fractions were searched against mouse (*Mus musculus)* protein sequences from UniProtKB/Swiss-Prot using the MASCOT search engine (Matrix Science, Version 2.2) through Proteome Discoverer™ software (Version 1.4, Thermo Fisher). Parameters for database search were as follows: MS1 Tolerance: 10ppm; MS2 Tolerance: 0.06da; fixed modification: Carbamidomethyl (C) Variable Modification: Oxidation (M), Dioxidation (M), Acetyl (N-term), Gln->pyro-Glu (N-term Q), TMT 10(N-term and K); maximum missed cleavage: 2; and target FDR 0.01.

All identifications were quantified as relative ratios of expression compared to the first time point (P12) through Proteome Discoverer™ software (Thermo Fisher, Version

1.4). Relative ratios along with UnitProtKB/Swiss-Prot identifications were exported into Microsoft Excel as a raw data file containing ID, ratio of change in expression at each time point (P15, P18, P21, P24) compared to P12=1.

3.5.5 Filtering of raw data.

Raw proteomic identifications (5628 proteins identified in nerve time course; 4414 proteins identified in muscle time course), were further filtered to exclude any proteins with altered expression less than 20% in either direction at P24 compared to P12. The 20% cut-off has been demonstrated successfully in previous label-free and isobaric mass-tagged experiments in neural tissue and skeletal muscle as an ideal threshold to obtain a stringent data set (Comley et al., 2011; Fuller, Hurtado, Wishart, & Gates, 2014; Mutsaers et al., 2011; Mutsaers, Lamont, Hunter, Wishart, & Gillingwater, 2013; Wishart et al., 2012, 2014).

3.5.6 Selection of relevant expression clusters from filtered data in BioLayout Express^{3D}

Filtering raw proteomic data by an expression change of >20% at P24 than at P12 in produced a separate filtered list of proteins in nerve and muscle. These lists were imported separately into BioLayout *Express^{3D}* and clustered based on relative expression profile from P12 to P24. Algorithms in BioLayout *Express^{3D}* generate a visual network to represent each data set, utilising special proximity to represent the similarity in expression profile of individual proteins over time. The resultant visual networks were utilised to distinguish expression clusters that followed either a general upward or downward trend in expression from P12 to P24. These “upregulated” and

“downregulated” clusters in nerve and muscle respectively were analysed on an individual basis to exclude clusters that did not follow an experimentally relevant expression profile from P12 to P24. For example, clusters containing proteins that exhibited a consistent increase or decrease in expression over were selected, while clusters consisting of proteins that exhibited an overall upregulation or downregulation but oscillated in expression during middle time points were excluded. Manual selection of experimentally desirable clusters yielded 1734 proteins in the nerve and 1874 proteins the muscle, respectively, that were suitable for functional clustering and pathway analysis.

3.5.7 DAVID Analysis.

In two separate analyses, first with raw protein identifications, and later with filtered data sets, relative expression ratios compared to the first time point (P12) were sorted by consistency in change in expression over all five time points in Microsoft Excel. Proteins exhibiting a consistent upregulation or downregulation in nerve or muscle from P12 through all four subsequent time points to P24, regardless of magnitude of change, were submitted as a gene list and converted into DAVID IDs against the DAVID 6.7 *Mus musculus* database. Four separate analyses were performed from the following lists of proteins, grouped as: (1) Consistent upregulated expression in nerve, (2) Consistent downregulated expression in nerve, (3) Consistent upregulated expression in muscle, and (4) Consistent downregulated expression in muscle. These lists were analysed using the Functional Annotation Clustering tool in DAVID Bioinformatics Resources (Version 6.7) to produce a list of functional annotations. Functional annotations are ranked by a DAVID enrichment score. An enrichment score

greater than 1.3 in DAVID is equivalent to $p<0.05$, and considered to be statistically significant. As with many gene ontological methods, these functional annotations provide an indication of which biological functions may be upregulated within the data set over time, but are often subject to a number of sampling- and database-based biases, and are therefore are imperfect indicators of biological validity. For this reason, I performed a more precise functional analysis utilising Ingenuity Pathway Analysis (IPA) software, which utilises an “expert-curated” database.

3.6 In Silico Protein Pathway Analysis

The Ingenuity Pathway Analysis (IPA) application (Ingenuity Systems, Silicon Valley, CA) was used to visualise and explore the cellular and molecular pathways that may have been altered as a result of expression changes over time, IPA generates networks of gene and protein interactions and disease associations, amongst other results, based on *in silico* predicted or experimentally reported interactions stored within the “hand-curated” Ingenuity Knowledge database. The majority (90%) of data comprising the Ingenuity Knowledge database are derived from peer-reviewed publications; the remaining 10% of stored interactions have been identified by other *in silico* techniques. Networks generated by IPA were set to a maximum of 35 member molecules, and were ranked according to a score calculated by a right-tailed Fisher’s exact test, which takes into account total protein input and size of the produced network. Network scores represent the relevance of the particular network to the overall analysis (ie. proteomic alterations in nerve or muscle between P12 and P24). In this study, networks generated by IPA were limited to those producing the top 25 scores. For more information on the computational methodology underpinning IPA, please refer to http://www.ingenuity.com/.

Separate pathway analyses were performed on the filtered nerve and muscle data sets, which produced 25 predictive molecular networks each. A third, combined analysis, which consolidated nerve and muscle results, enabled the identification of molecular overlap within networks generated from nerve and muscle data. Extrapolation of this overlap through the Pathway Designer function generated a combined network in which molecular interactions conserved between both nerve and muscle data sets were explored.

3.7 Image Processing

Figures were created using GNU Image Manipulation Program (GIMP) for Windows.

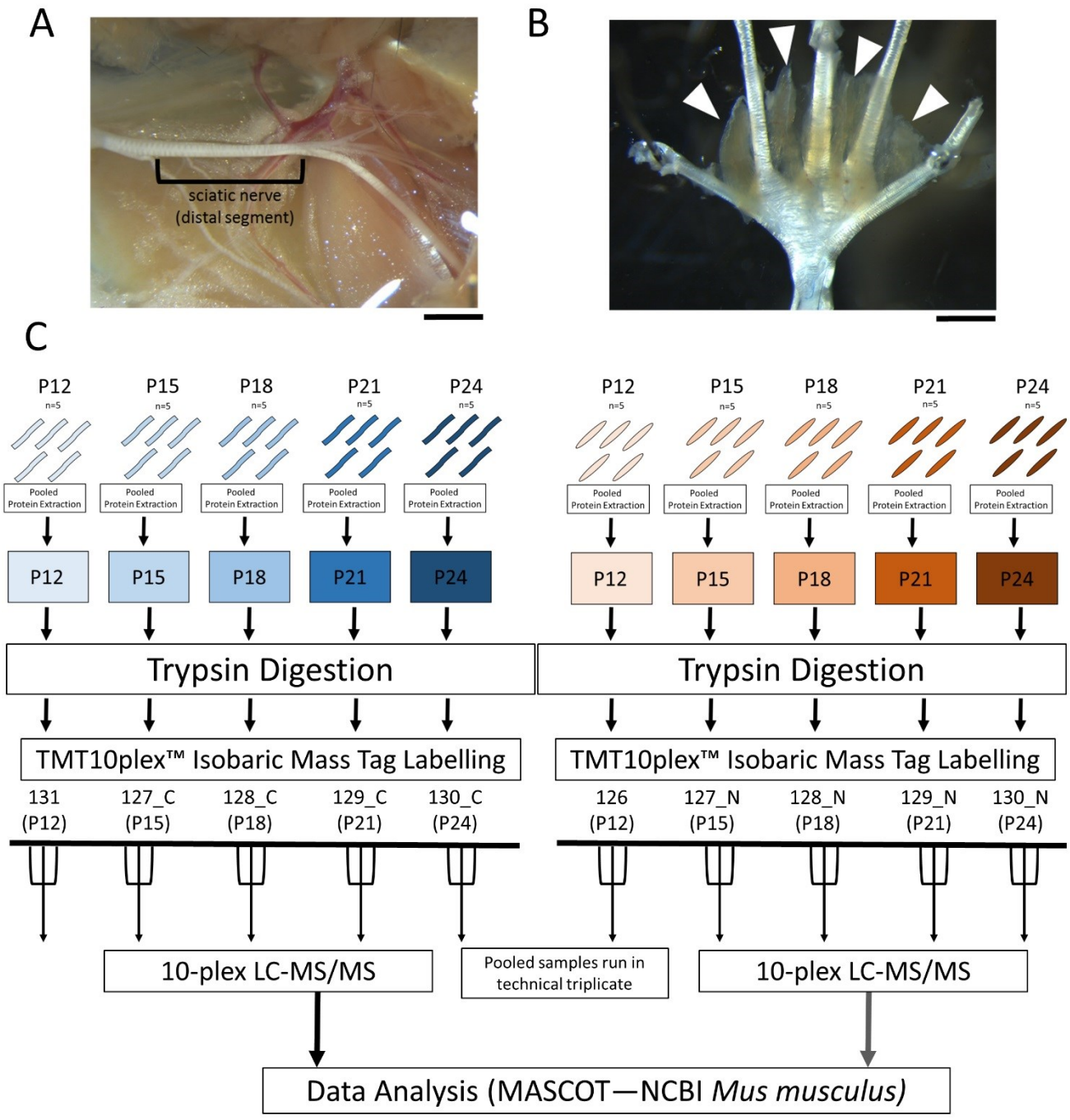

Figure 3.2. Schematic of sample preparation, TMT 10plex™ Tandem Mass Tag labelling, and quantitative LC-MS/MS workflow. (A) High magnification photograph of the exposed sciatic nerve in a wildtype C57BL/6 adult mouse leg. Brackets indicate region that was isolated for experiment (2 nerves per *n;* 1 nerve per hind limb per mouse). Care was taken to isolate anatomically identical regions of sciatic nerve, as an investigation by Eaton et al (2013) revealed a significant discrepancy in endogenous expression levels of the abundant proteins neurofilament and β-actin, commonly used as a "loading control," between proximal and distal regions of the mouse sciatic nerve. **(B)** High magnification photograph of a clean hind-limb lumbrical muscle preparation from a wildtype C57BL/6 adult mouse. Microdissection of the skinned hind limb is used to isolate the four lumbrical muscles (indicated by arrowheads) attached to the FDL tendon. After clearing away connective tissue, the four lumbricals per hind limb attached to the tendon were excised (8 lumbricals per *n*; 4 muscles per hind limb per mouse) for this experiment. **(C)** Schematic of sample preparation workflow for TMT 10plex™ labelling and subsequent LC-MS/MS. Sciatic nerves (2 nerves per *n*) and lumbrical muscles (8 muscles per *n*) from n=5 mice per timepoint were banked and pooled for a single extraction in label-free buffer per timepoint. Pooled samples were labelled using all 10 isobaric mass tags from a TMT 10plex™ kit (Thermo Fisher). Labelled samples were prepared for LC-MS/MS and run in technical triplicate.

3.8 Quantitative fluorescent western blotting (QFWB)

3.8.1 Extraction and sample preparation.

Anatomically consistent segments of nerve (sciatic nerve, intercostal nerve, brachial plexus) were freshly dissected, snap-frozen on dry ice and stored at -80°C. Tissue was homogenized using a handheld motorized pestle (VWR International) in 100µl RIPA buffer (Fisher Scientific) with 1% Halt protease inhibitor cocktail (Sigma Aldrich). Homogenate was cooled on ice for 10 minutes, then centrifuged at 4°C at 14000rpm for 10 minutes. Centrifuged samples were immediately re-transferred to ice and supernatant was removed by pipetting, while pellet was discarded. Concentration of extracted protein was determined by micro-BCA kit (Pierce Biosystems).

3.8.2 Quantitative fluorescent western blotting.

Samples were prepared to load between 10 and 25µg of protein in 10 µl deionised water and 5µl of NuPage® LDS Sample buffer 4X (Invitrogen, UK). Samples were denatured at 98°C for 2 minutes and were loaded in a NuPAGE™ Novex™ 4-12% Bis-Tris protein gel (Invitrogen, UK) alongside 5µl of Novex® Sharp Pre-stained Protein Standard (Thermo Fisher). Gels were run at 80mV for 5 minutes to ensure equal stacking, then 150mV for 50 minutes. Gels were excised, removed to a pre-prepared i-Blot2® transfer stack (Invitrogen, UK) and transferred using an 8.5 minute transfer cycle in the i-Blot2® transfer system (Invitrogen, UK).

After transfer, membranes were excised and transferred to 20ml Falcon tubes containing 5ml of Ponceau S solution; 0.1% Ponceau S (Sigma-Aldrich), 0.5% acetic acid (Sigma-Aldrich) in ddH2O. Membranes were stained for 20 minutes, rolling, at room temperature then washed in ddH2O until bands were visible. Membranes were

scanned in greyscale using a CanoScan LiDE220 digital scanner (Canon) and saved as a TIFF image for total protein analysis. Membranes were washed in ddH2O and blocked in 5ml Odyssey® Blocking Buffer (Li-COR Biosciences) at room temperature for 30 minutes.

Membranes were incubated in primary antibody solution containing primary antibodies at the following concentrations (ROCK2 1:200, Abcam; SIRT2 1: 500, Abcam; calretinin 1:1000, Swant) in a solution of 1% tween-20 (Sigma) in 5ml Odyssey® Blocking Buffer (Li-COR Biosystems) at 4°C overnight. Antibodies to SIRT2 and calretinin were generously provided by members of the Gillingwater laboratory.

The following day, membranes were washed 6x 5 minutes in PBS, rolling, at room temperature. Membranes were incubated in secondary antibody solution containing either IRDye® 680RD donkey anti-mouse IgG (H+L) or IRDye® 680RD donkey anti-rabbit IgG (H+L) antibodies (Li-COR Biosciences) at a concentration of 1:5000 (0.02%) in a solution of 1% tween-20 (Sigma) in 5ml Odyssey® Blocking Buffer (Li-COR Biosciences). Membranes were incubated for 90 minutes at room temperature and covered to prevent photobleaching.

After secondary antibody incubation, membranes were washed 2x 5 minutes, then 3x 10 minutes in PBS, rolling, at room temperature. Membranes were dried and stored at 4°C prior to imaging and analysis.

3.8.3 Measurement and analysis.

TIFF images of Ponceau-stained blots were imported into Odyssey® ImageStudio Lite software (Version 5.2). ImageStudio Lite (Version 5.2) was used to analyse the intensity of identical sections of total protein banding against background. Readouts of the intensity of total protein banding relative to background were imported into

Microsoft Excel (Windows 2013) to calculate loading consistency and normalisation factors. Western blots were imaged on the 700nm channel using the Odyssey® Infrared Imaging System at a resolution of 169µm. All quantification was performed on the 700nm channel, with the intensity of bands normalised using the factors generated from total protein analysis. All statistical analysis and generation of graphs was performed in GraphPad Prism7 (Windows). All data are presented as a scatter plot of individual *n* with mean ± SE unless otherwise noted. Individual statistical tests used are noted in figure legends. Statistical significance was considered to be $p \leq 0.05$. Figures were created using GNU Image Manipulation Program (GIMP) for Windows.

Chapter THREE: Results

3.9 TMT10plex™ isobaric mass tag labelling yields powerful mass spectrometry throughput and comprehensive identification of the nerve and muscle proteome.

The preliminary aim of this study was to evaluate the efficacy of the novel TMT10plex™ reporter ion kit as a labelling technique for quantitative mass spectrometry. Previous work has demonstrated how iTRAQ isobaric labelling and label-free methods can be used for proteomic analysis of murine peripheral nerves and skeletal muscles (Comley et al., 2011; Mutsaers et al., 2011; Mutsaers et al., 2013). Recent advances in the structural design of isobaric tagging reagents have enabled the development of “multiplex” tandem mass-tag reporter ion kits, which enable the concurrent quantitative analysis of multiple samples, in contrast to the limitations of earlier duplex methods. I designed a time-course study to analyse five distinct time points spanning the decline in NMJ protection by Murray et. al (2011), within both the sciatic nerve and lumbrical muscles, with the aim of determining the coverage potential of the 10plex™ reporter ion kit.

Consolidation of raw peptide outputs across all five time points within sciatic nerve and muscle samples respectively were translated into protein identifications by searching against human protein sequences using the MASCOT protein database (Matrix Science, Version 2.2) and quantified as relative ratios of expression compared to the first time point (P12) through Proteome Discovery software (Thermo Fisher, Version 1.4). This produced a list of raw muscle and nerve output respectively; within these lists, only proteins identified by a >95% total ion score confidence interval and 2 or more unique peptides were deemed reliable for analysis. Within the sciatic nerve

samples, 7440 total proteins were identified by a >95% total ion score confidence interval, of which 5628 were identifiable by 2 or more unique peptides (**Supplementary Table 1**). Within the lumbrical muscle samples, 6079 total proteins were identified by a >95% total ion score confidence interval, of which 4414 were identifiable by more than 2 unique peptides (**Supplementary Table 2**). These results, which provided a comparably greater coverage of both the nerve and muscle proteome than previous isobaric or label-free studies, implicate TMT10plex™ as a robust and powerful labelling technique.

3.10 Validation of expression profiles reported in TMT10plex™ proteomics study by quantitative fluorescent western blotting (QFWB) of select candidate proteins in peripheral nerves.

In order to confirm the veracity of expression trends identified by the proteomics study, I selected individual protein candidates for validation by quantitative fluorescent western blotting. Candidates were selected from the unfiltered nerve data set based on their magnitude of change over the experimental period, implicated modulation of injury-induced neuronal degeneration based on the published literature, and availability of quality antibodies suitable for fluorescence-based western blotting. Of particular interest was calretinin (CALB2), identified in a comparative proteomics study to be consistently up-regulated across two mouse models of neurodegenerative disease and a model of injury-induced stroke. Translationally, CALB2 knockdown has been demonstrated to potently delay degeneration of the olfactory receptor neuron in *Drosophila* (Wishart et al., 2012). The raw proteomic output of this study reported a change in expression of CALB2 of nearly 750% from P12 to P24 (7.488 P24/P12 ratio). NAD-dependent deacetylase sirtuin-2 (SIRT2) exhibited more modest increases in

expression in the raw proteomic data (1.330 P24/P12 ratio) but has been similarly up-regulated across a number of neurodegenerative disease and injury models (Amorim et al., 2015; Wishart et al., 2012). Finally, the raw data reported that rho-associated kinase 2 (ROCK2) underwent negligible changes in expression at P24 compared to P12. It was therefore selected as another validation candidate as an internal control. All signals from western blots were quantified against total protein load (Ponceau S stain) in order to reliably determine expression changes (**Figure 3.3A).** SIRT2 exhibited a significant increase in expression (1.423 ± 0.06; P24/P12 ratio of mean ± SEM) (**Figure 3.3C)**, thus confirming the direction and magnitude of expression change reported in the TMT data. Similarly, expression of CALB2 by QFWB reported an increase in expression significant at P21 (3.107 ± 0.09; P21/P12 ratio of mean ± SEM), which profiled expression changes reported by the proteomic data, albeit to a lesser magnitude (**Figure 3.3D)**. Despite a slight trend towards an increase in relative expression over time, overall, there was no significant difference in expression levels of ROCK2 between P12-P24, in concurrence with the TMT data (**Figure 3.3B**). The QFWB data therefore indicate that TMT10plex™ proteomic analysis is likely to accurately profile molecular alterations occurring over the P12-P24 postnatal period, albeit not to a precise magnitude. While several quantitative labelling strategies such as iTRAQ appear to modestly compress expression ratios, thus resulting in an underreporting of protein expression changes, very little is known about such phenomena in the relatively novel TMT10plex™ technology (Karp et al., 2010). For this reason, future work is required to gauge the precision of TMT output versus more traditional quantitation methods.

*Antibodies to calretinin and SIRT2 were generously provided by the Gillingwater Laboratory.

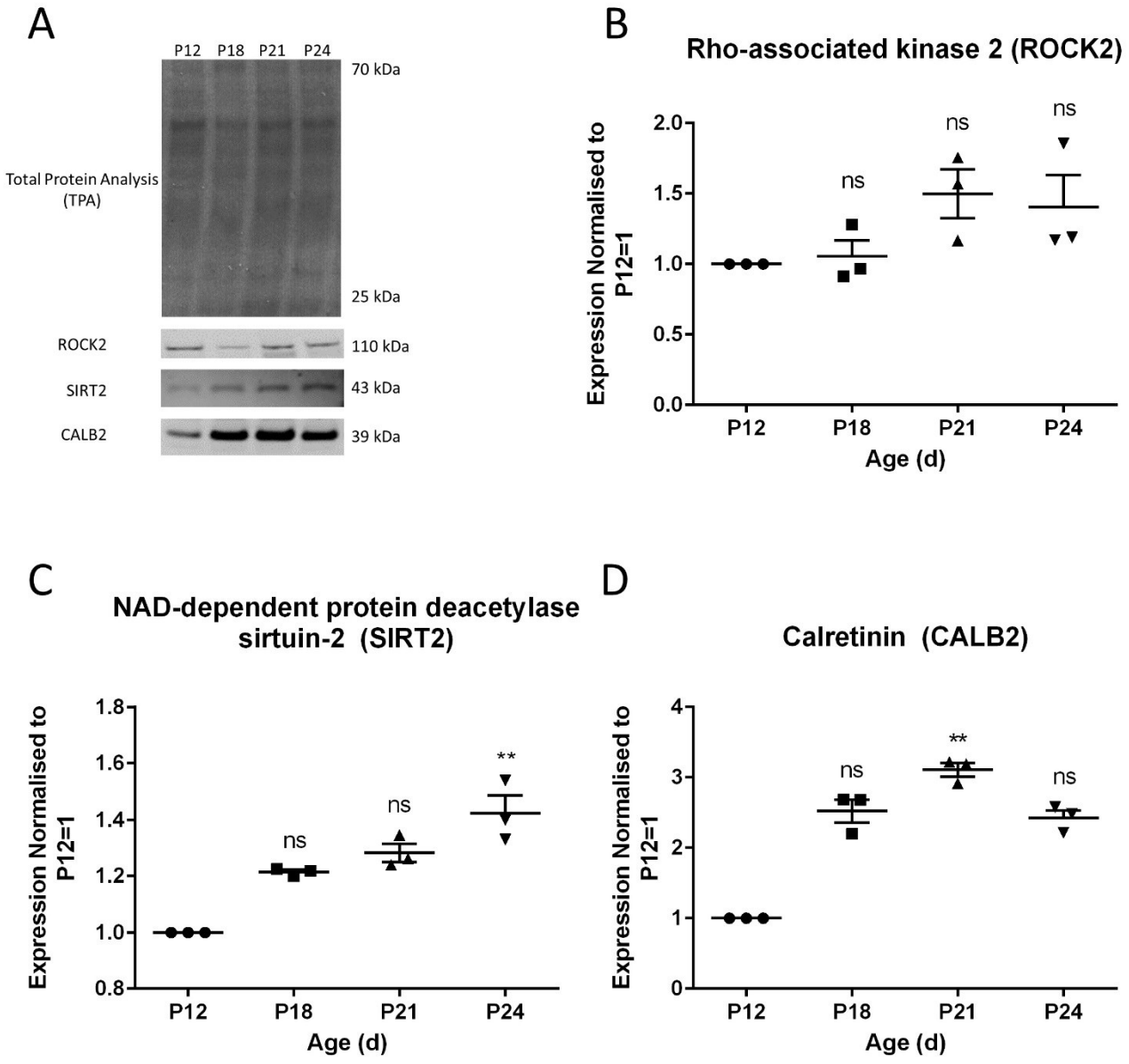

Figure 3.3. Candidate validation of proteomic data by quantitative fluorescent Western blotting
(A) Representative examples of bands used for the quantification of total protein load (TPA), rho-associated kinase 2 (ROCK2), NAD-dependent deacetylase sirtuin-2 (SIRT2) and calretinin (CALB2). All candidate blots were normalised to total protein load (Ponceau S stain) in order to reliably determine expression changes. **(B-D)** Scatter plots (individual data points; mean ± SE) of relative expression of **(B)** ROCK2, **(C)** SIRT2 and **(D)** CALB2 in relation to the first time point (P12) =1. Direction and magnitude of change is consistent with TMT data. Upregulated expression of CALB2 at P21 and SIRT2 at P24 was statistically significant in relation to P12. In accordance with the magnitude of expression changes reported by TMT data, changes in expression of ROCK2 in relation to P12 was not statistically significant. (n=3 pairs of nerves per time point; Kruskaw-Wallis test with Dunn's *post-hoc* multiple comparisons, where $^{**}p<0.01$).

3.11 Filtering and expression cluster selection of raw proteomic output produces a comprehensive yet concentrated list of proteins suitable for additional functional clustering and pathway analysis

3.11.1 Filtering of raw proteomic output.

Raw proteomic output (5628 proteins identified in nerve time course; 4414 proteins identified in muscle time course), was further filtered to exclude any proteins with altered expression less than 20% in either direction at P24 compared to P12. Previous studies have demonstrated that the 20% cut-off threshold produces a reliable and stringently consolidated data set (Wishart et al*.,* 2010; Comley et al*.,* 2011; Mutsaers et al., 2011; Wishart et al., 2012; Wishart et al., 2014; Fuller et al., 2014).

Selection of relevant expression clusters generated in BioLayout Express^{3D}

A list of proteins with altered expression >20% at P24 compared to P12 in sciatic nerve, and a list of proteins with altered expression >20% at P24 than at P12 in lumbrical muscles, were imported separately into BioLayout *Express^{3D}* and clustered based on relative expression profile from P12 to P24. A separate visual network for each data set was generated, utilising special proximity to represent the similarity in expression profile of individual proteins over time (**Figure 3.4A; Figure 3.5A).** Utilising these visual networks, it was possible, in both nerve and muscle datasets, to distinguish a large body of proteins, comprising numerous specific expression profiles, that followed either a general upward or downward trend in expression from P12 to P24 (**Figure 3.4B&F; Figure 3.5B&F**). Consolidating these generally “upregulated” or “downregulated” set of proteins into their respective expression clusters provided an elegant graphical representation of the specific expression pattern of each cluster of

proteins generated by the software. This made it possible to select groups of proteins comprising a cluster that followed an the predicted relevant expression profile from P12 to P24. Clusters containing proteins that exhibited a consistent increase or decrease in expression over time (**Figure 3.4C&G; Figure 3.5C&G**) were selected, while clusters consisting of proteins that exhibited an overall up-regulation or down-regulation but oscillated in expression during middle time points were excluded (**Figure 3.4D&H; Figure 3.5D&H)**.

Individual selection of experimentally desirable clusters further narrowed the pool of nerve and muscle protein identifications to a total of 1734 proteins in nerve samples and 1874 proteins in muscle samples, respectively. (**Figure 3.4J & 3.5J**).

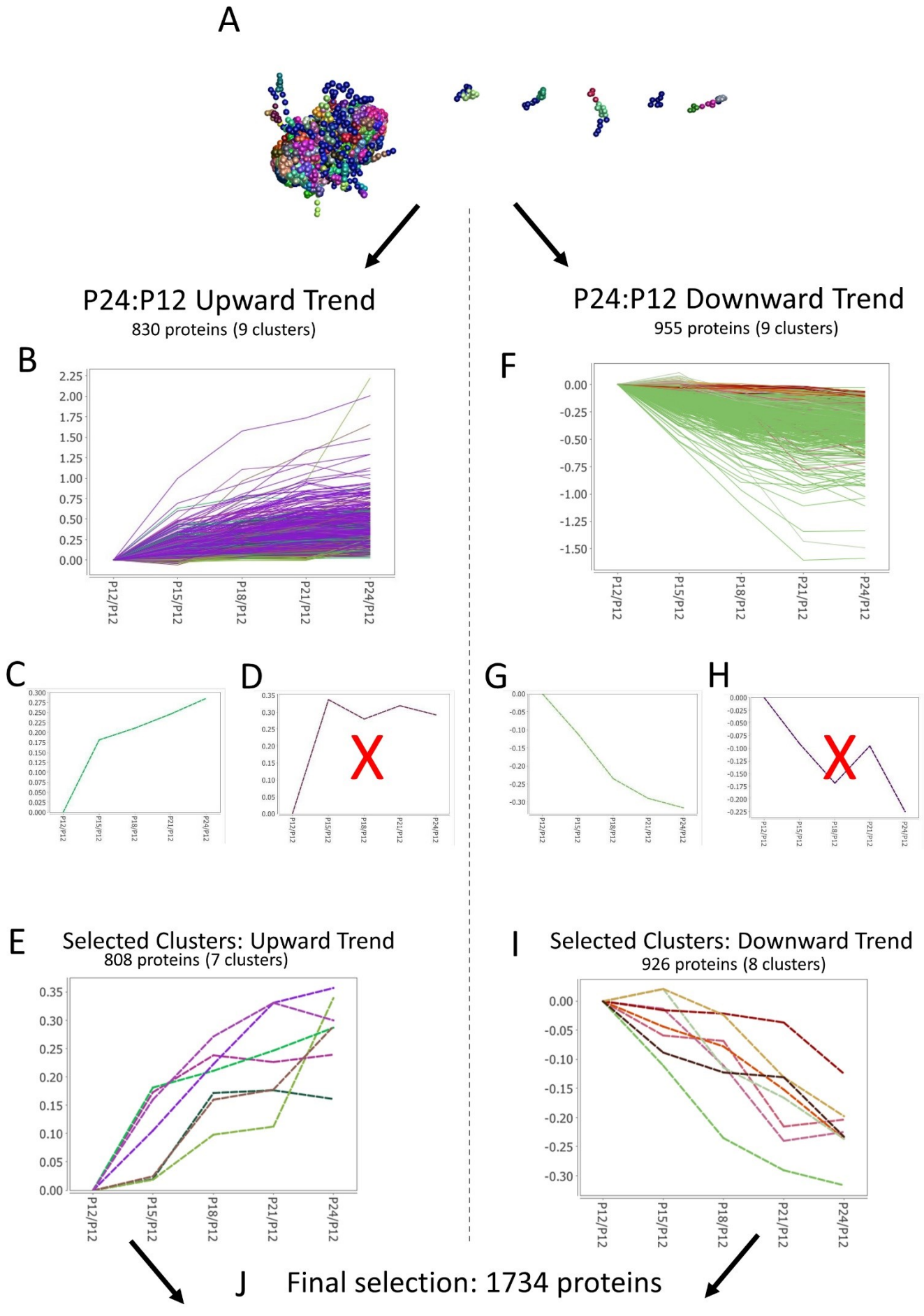
A
P24:P12 Upward Trend
830 proteins (9 clusters)
B
P24:P12 Downward Trend
955 proteins (9 clusters)
F
C
D
G
H
X
X
E
Selected Clusters: Upward Trend
808 proteins (7 clusters)
I
Selected Clusters: Downward Trend
926 proteins (8 clusters)
J
Final selection: 1734 proteins
P12/P12
P15/P12
P18/P12
P21/P12
P24/P12

Figure 3.4. BioLayout *Express^{3D}* enables selection of proteins exhibiting desirable and experimentally relevant expression profile within the filtered nerve dataset.

(A) A visual network generated in BioLayout *Express^{3D}* depicting relative expression patterns of proteins within the filtered nerve dataset (exhibiting a >20% change in relative expression at P24 from P12). Each ball or "node" represents an individual protein; spacial proximity between nodes represents similarity in expression behaviour over the P12 to P24 period. Multiple nodes comprise an expression "cluster," denoted by the same colour; clusters are generated by BioLayout *Express^{3D}* software by grouping proteins within the data set that exhibit similar relative expression patterns. Individual clusters may be explored to view the identities of proteins grouped by expression profile. Note the dominance of two hemispheres beginning to become visible within the largest "bundle" of the visual network; these hemispheres represent clustered proteins exhibiting either an overall increase (B) or decrease (F) in expression over the experimental period. **(B)** 9 clusters, incorporating 830 proteins, exhibit an upward trend in relative expression over the experimental time period. Each solid coloured line represents the relative expression of an individual protein over time.

(C) Example of a cluster exhibiting a desirable expression profile over the experimental period. Proteins within this cluster feature a relative increase over two different rates of change in expression over the P12-P24 time period, and were therefore selected for future analysis. **(D)** Example of a cluster excluded from final selection for analysis. Although it trends toward overall upregulated expression, with greater relative expression at P24 than at P12, its relative "level" expression profile from P15 excludes it from experimental relevance. **(E)** A final pool of 808 proteins across 7 clusters, all exhibiting a relative increase in expression over time, was selected for pathway analysis. Individual clusters are represented by dotted lines. **(F)** 9 clusters compromised of 955 proteins exhibited a downward trend in relative expression from P12 to P24. Solid coloured lines represent the relative expression of an individual protein over time. **(G)** Example of a cluster exhibiting a desirable expression profile over the experimental period. Proteins within this cluster feature a steady relative decrease in expression over the P12-P24 time period, and were therefore selected for future analysis. **(H)** Example of a cluster excluded from final selection for analysis. Although final expression at P24 is relatively less than that at P12, its relative increase in expression from P18 to P21 exclude it from experimental relevance. **(I)** A final pool of 926 proteins across 8 clusters, all exhibiting a relative decrease in expression over time, was selected for pathway analysis. **(J)** Combining the pools of selected clusters exhibiting upward or downward trends over the P12 to P24 time period **(E&I,** respectively**)** generated a final yield of 1734 proteins within the nerve dataset to be subjected to pathway analysis.

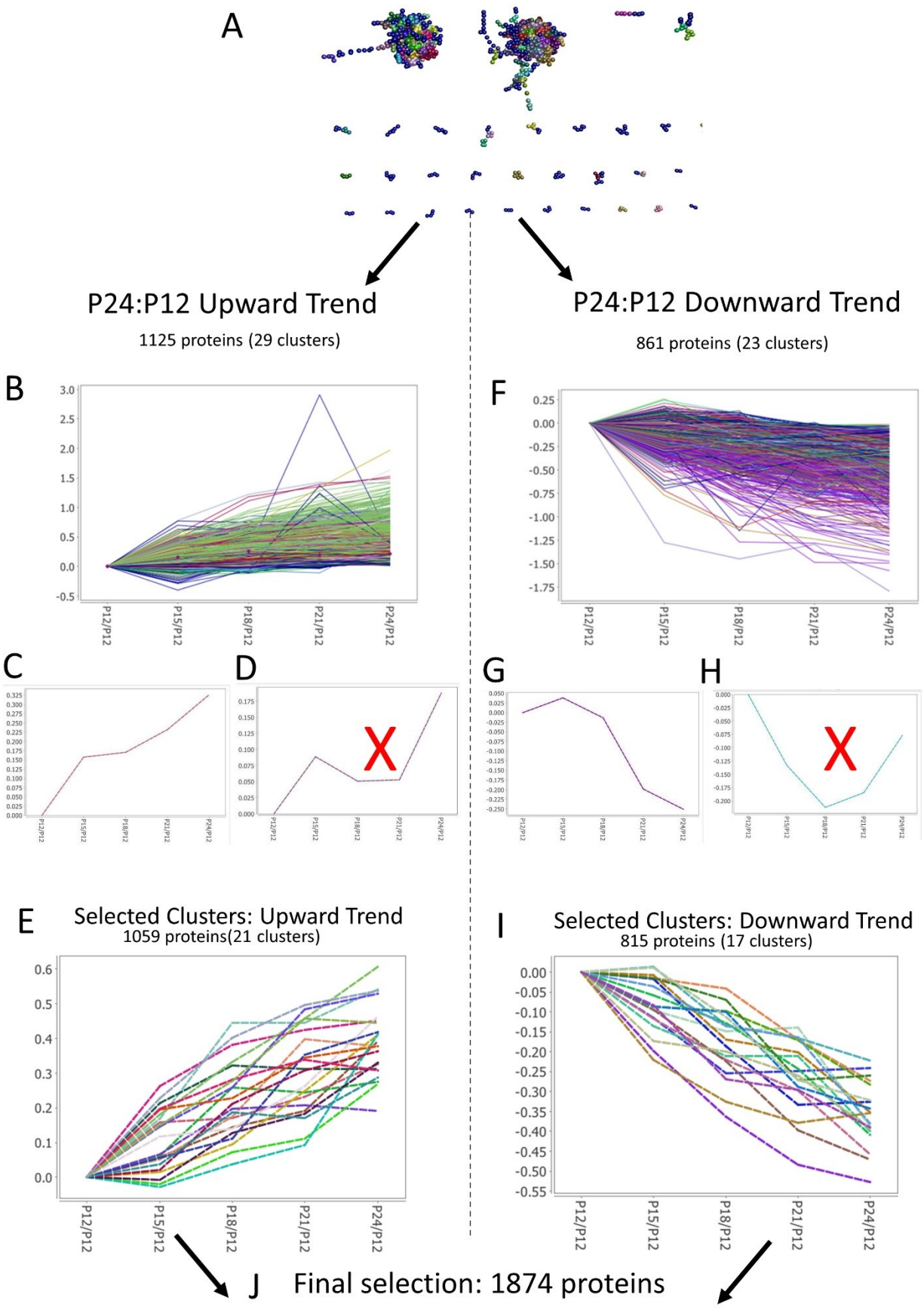
A
P24:P12 Upward Trend
1125 proteins (29 clusters)
P24:P12 Downward Trend
861 proteins (23 clusters)
B
F
C
D
G
H
X
X
E
Selected Clusters: Upward Trend
1059 proteins(21 clusters)
I
Selected Clusters: Downward Trend
815 proteins (17 clusters)
P12/P12
P15/P12
P18/P12
P21/P12
P24/P12
J
Final selection: 1874 proteins

Figure 3.5. BioLayout *Express^{3D}* enables selection of proteins exhibiting desirable and experimentally relevant expression profile within the filtered muscle dataset.

(A) A visual network generated in BioLayout *Express^{3D}* depicting relative expression patterns of proteins within the filtered muscle dataset (exhibiting a >20% change in relative expression at P24 from P12). Each ball or "node" represents an individual protein; spacial proximity between nodes represents similarity in expression behaviour over the P12 to P24 period. Multiple nodes comprise an expression "cluster," denoted by the same colour; clusters are generated by BioLayout *Express^{3D}* software by grouping proteins within the data set that exhibit similar relative expression patterns. Individual clusters may be explored to view the identities of proteins grouped by expression profile. Note the dominance of two large, distinct bundles within the visual network; these bundles represent clustered proteins exhibiting either an overall increase (B) or decrease (F) in expression over the experimental period. **(B)** 29 clusters, incorporating 1125 proteins, exhibit an upward trend in relative expression over the experimental time period. Each solid coloured line represents the expression profile over time of an individual protein.

(C) Example of a cluster exhibiting a desirable expression profile over the experimental period. Proteins within this cluster feature a steady relative increase in expression over the P12-P24 time period, and were therefore selected for future analysis. **(D)** Example of a cluster excluded from final selection for analysis. Although it trends toward overall upregulated expression, with greater relative expression at P24 than at P12, its expression profile at middle time points P18 and P21 exclude it from experimental relevance. **(E)** A final pool of 1059 proteins across 21 clusters, all exhibiting a relative increase in expression over time, was selected for pathway analysis. Individual clusters are represented by dotted lines. **(F)** 23 clusters compromised of 861 proteins exhibited a downward trend in relative expression from P12 to P24. Solid coloured lines represent the expression profile of an individual protein over time. **(G)** Example of a cluster exhibiting a desirable expression profile over the experimental period. Proteins within this cluster feature a steady relative decrease in expression over the P12-P24 time period, and were therefore selected for future analysis. **(H)** Example of a cluster excluded from final selection for analysis. Although final expression at P24 is relatively less than that at P12, its relative increase in expression from P18 to P24 exclude it from experimental relevance. **(I)** A final pool of 815 proteins across 17 clusters, all exhibiting a relative decrease in expression over time, was selected for pathway analysis. **(J)** Combining the pools of selected clusters exhibiting upward or downward trends over the P12 to P24 time period **(E&I,** respectively**)** generated a final yield of 1874 proteins within the muscle dataset to be subjected to pathway analysis.

Graphical representation of the filtering process, first by magnitude (ie. >20% change threshold) then by direction of change (ie. selection of relevant *BioLayout* profiles) reveals the extent of data refinement performed to transform raw LC-MS/MS protein identifications to a reliable data set suitable for pathway analysis and further functional clustering (**Figure 3.6; Figure 3.7**).

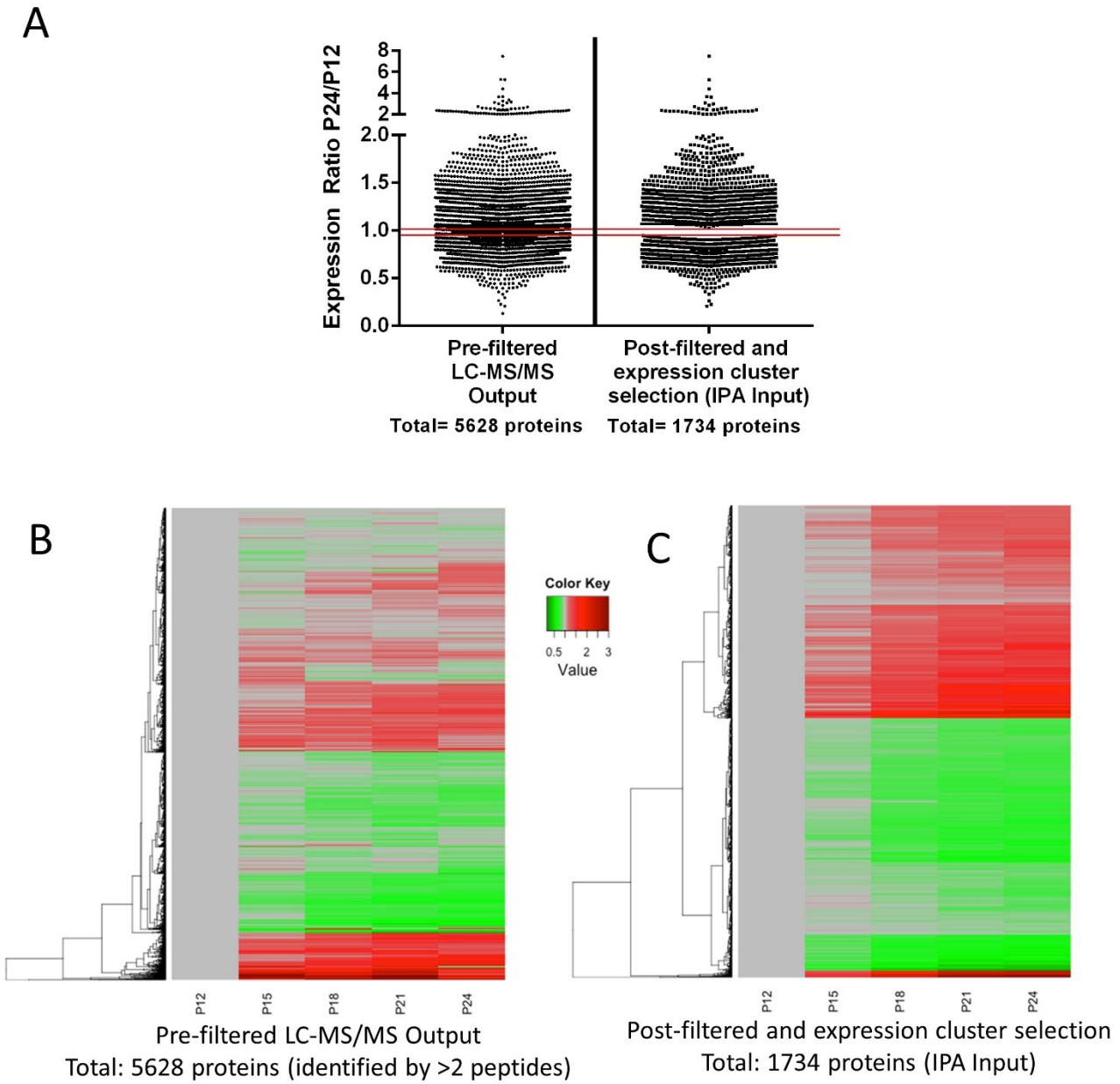

Figure 3.6. Filtering of raw proteomics data and selection for experimentally relative expression patterns yields a final nerve dataset enriched for proteins exhibiting an experimentally relevant increase or decrease in expression from P12 to P24.

(A) Scatter plot depicting the filtering process undertaken on raw proteomics data (LC-MS/MS output identified by 2 or more unique peptides) through selection of relevant expression clusters to generate a final list of 1734 proteins exhibiting consistent increases or decreases in expression in murine sciatic nerve from P12 to P24. 5628 proteins were identified by 2 or more unique peptides from LC-MS/MS and subjected to a cutoff of 20% minimum change at P24 compared to P12; proteins exhibiting a relative expression change below this threshold (demarcated by zone in between red lines) were excluded from the filtered list and subsequent expression clustering. Selection of proteins exhibiting experimentally relevant expression patterns in BioLayout *Express*^{3D} (refer to Figure **X.2**) yielded a final list of 1734 proteins consistently altered across the experimental period. Data are presented as expression ratios (P24/P12) and each datum point represents an individual protein. See Materials and Methods for further information on data filtering and expression cluster selection. **(B)** Heat map depicting changes in expression of the 5628 proteins in the unfiltered raw proteomics dataset relative to expression at the first time point, P12. Data were inputted as relative expression ratios. **(C)** Heat map depicting changes in expression of the 1734 proteins remaining after filtering by the 20% cutoff and selection in BioLayout *Express*^{3D} for consistent relative increase or decrease in expression from P12 to P24. Data were inputted as relative expression ratios. Note the clear enrichment for proteins exhibiting experimentally relevant expression profiles only, ie. a consistent increase or decrease from P12 to P24.

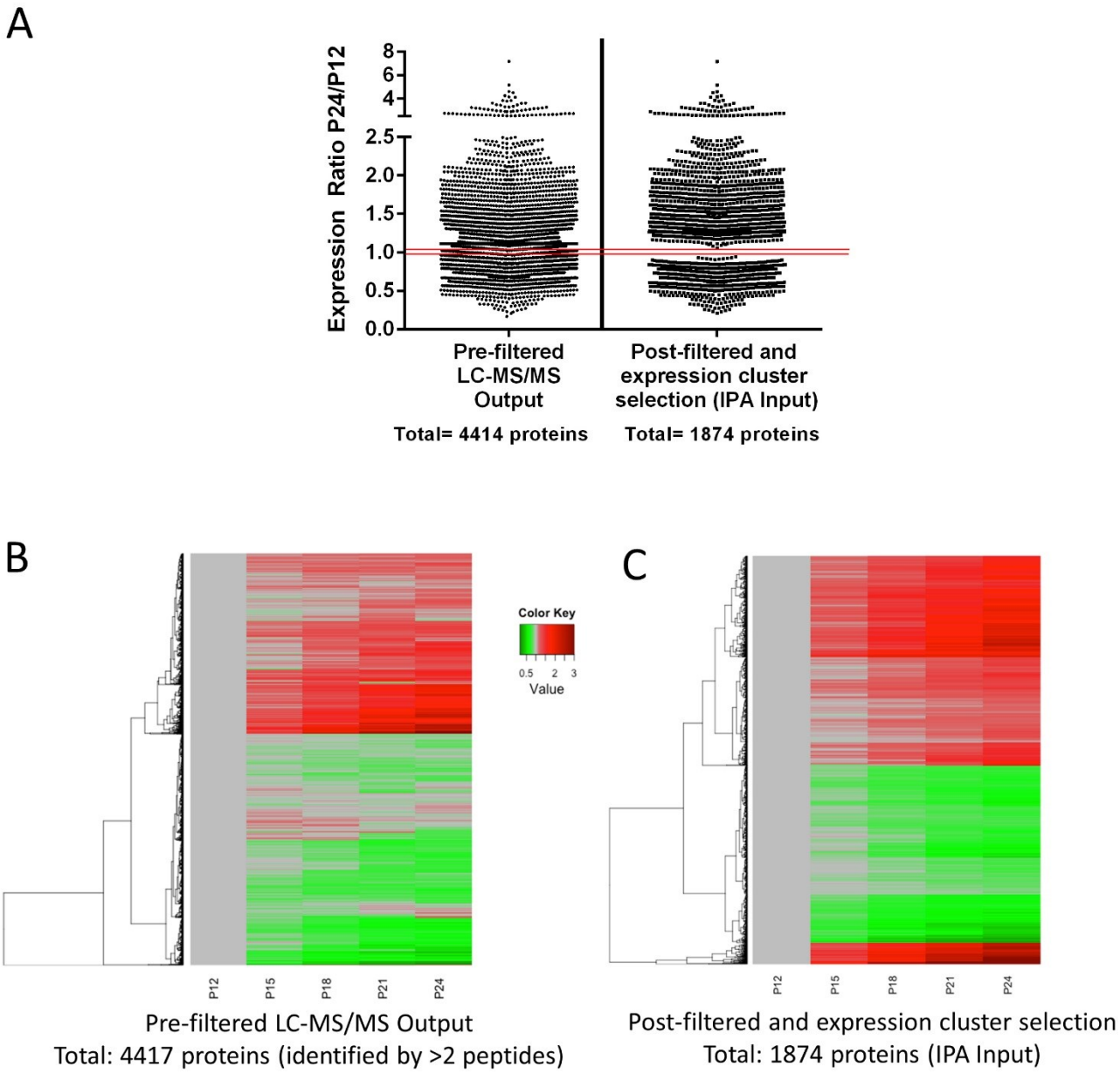

Figure 3.7. Filtering of raw proteomics data and selection for experimentally relative expression patterns yields a final muscle dataset enriched for proteins exhibiting an experimentally relevant increase or decrease in expression from P12 to P24.

(A) Scatter plot depicting the filtering process undertaken on raw proteomics data (LC-MS/MS output identified by 2 or more unique peptides) through selection of relevant expression clusters to generate a final list of 1734 proteins exhibiting consistent increases or decreases in expression in murine lumbrical muscles from P12 to P24. 4417 proteins were identified by 2 or more unique peptides from LC-MS/MS and subjected to a cutoff of 20% minimum change at P24 compared to P12; proteins exhibiting a relative expression change below this threshold (demarcated by zone in between red lines) were excluded from the filtered list and subsequent expression clustering. Selection of proteins exhibiting experimentally relevant expression patterns in BioLayout *Express*^{3D} (refer to Figure **X.2**) yielded a final list of 1874 proteins consistently altered across the experimental period. Data are presented as expression ratios (P24/P12) and each datum point represents an individual protein. See Materials and Methods for further information on data filtering and expression cluster selection. **(B)** Heat map depicting changes in expression of the 4417 proteins in the unfiltered raw proteomics dataset relative to expression at the first time point, P12. Data were inputted as relative expression ratios. **(C)** Heat map depicting changes in expression of the 1874 proteins remaining after filtering by the 20% cutoff and selection in BioLayout *Express*^{3D} for consistent relative increase or decrease in expression from P12 to P24. Data were inputted as relative expression ratios. Note the clear enrichment for proteins exhibiting experimentally relevant expression profiles only, ie. a consistent increase or decrease from P12 to P24.

3.12 Functional annotation analysis of filtered proteomics output enhances enrichment in both nerve and muscle for mitochondrial and oxidative phosphorylation pathway components in upregulated proteins, and RNA binding and processing pathways in downregulated proteins.

The refined nerve and muscle datasets were sorted into four lists: (1) Consistent upregulated expression in nerve, (2) Consistent downregulated expression in nerve, (3) Consistent upregulated expression in muscle, and (4) Consistent downregulated expression in muscle. These lists were analysed using the Functional Annotation Clustering tool in DAVID Bioinformatics Resources (Version 6.7) to produce a list of functional annotations of filtered proteins. **Table 3.1** lists the 10 most significantly enriched biological clusters generated from functional annotations either consistently upregulated or consistently downregulated between P12 and P24 in nerve. **Table 3.2** lists the 10 most significantly enriched biological groups generated from functional annotations either consistently upregulated or consistently downregulated between P12 and P24 in muscle. An enrichment score greater than 1.3 in DAVID is considered loosely equivalent to $p<0.05$.

Table 3.1: Statistically altered functional clusters of sciatic nerve dataset filtered by magnitude and direction of expression from P12 to P24.

Filtered: Up from P12-P24 in Nerve		**Filtered: Down from P12-P24 in Nerve**	
Cluster Name	Enrichment Score	Cluster Name	Enrichment Score
Mitochondrial oxidation reduction; NAD-dependant	8.44	mRNA processing/ Spliceosome	25.24
Cell fraction	4.61	RNP complex/ribosome	23.19
Cytoskeletal actin binding	4.53	RNA binding	16.1
Membrane lipoproteins	4.26	Intracellular organelle lumen	12.54
Magnesium binding	4.06	Endoplasmic reticulum	11.87
Cofactor metabolism	3.95	Translation initiation	9.73
Cytoplasmic vesicles	3.81	Endoplasmic reticulum	9.03
Nucleotide binding	3.7	Protein transport (Golgi)	6.54
Endocytosis	3.3	Endoplasmic reticulum membrane	5.41
Nucleotide binding	2.98	mRNA transport/RNA localization	5.05

Functional annotation analysis of proteins consistently upregulated within the sciatic nerve between P12 and P24 from the final refined dataset revealed a marked enrichment for biological groups implicated in oxidative phosphorylation and mitochondrial respiration. The most significant cluster was comprised of proteins involved in NAD-dependent “redox” processes. The majority of the remaining top-10 biological groups produced by this analysis included clusters comprised of proteins

involved in magnesium binding, nucleotide binding, endocytosis, and cytoskeletal actin binding.

Functional annotation analysis of proteins consistently down-regulated within the sciatic nerve between P12 and P24 from the final refined dataset yielded the dominant presence of biological groups comprised of proteins involved in mRNA processing and binding, as well as RNA-editing machinery such as the RNP complex and spliceosome. Other top groups contained proteins pertaining to endoplasmic reticulum and Golgi interactions.

Table 3.4: Statistically altered functional clusters of lumbrical muscle dataset filtered by magnitude and direction of expression from P12 to P24.

Filtered: Up from P12-P24 in Muscle		Filtered: Down from P12-P24 in Muscle	
Cluster Name	Enrichment Score	Cluster Name	Enrichment Score
Mitochondria	134.15	Endoplasmic reticulum	12.26
Mitochondrial membrane	82.63	Protein transport	10.38
Oxidation reduction/electron transport chain (ETC)	43.65	Membrane-bound vesicle	9.81
Electron transport/ oxioreductase/NADH dehydrogenase activity	25.4	Actin binding/actin cytoskeleton	8.89
Cellular respiration/electron transport chain	22.5	Actin cytoskeleton organisation	8.52
Mitochondrial lumen	21.82	Non-membrane bound organelle	7.83
Myofibril contraction	20.61	RNA processing/RNA splicing/spliceosome	6.17
Cellular respiration/cofactor metabolism	12.27	Lysosome	5.26
Glucose metabolism/glycolysis	12.2	Endoplasmic reticulum	5.21
Respiratory ETC/ Oxidative phosphorylation/mitochondrial electron transport (NADH)	8.91	Intracellular organelle lumen	5.15

Functional annotation analysis of proteins consistently up-regulated within the lumbrical muscles between P12 and P24 from the final refined dataset similarly suggested an overwhelming dominance of clusters implicated in mitochondrial—specifically, electron transport chain—activity. Indeed, 9 of the 10 most significantly enriched functional clusters identified pertained to mitochondrial metabolic activity.

The top cluster identified comprised of mitochondrial proteins, with an enrichment score of 134.15.

Functional annotation analysis of proteins consistently down-regulated in within the musculature between P12 and P24 from the final refined dataset produced several biological groups enriched for proteins implicated in endoplasmic reticulum activity, RNA processing and RNA splicing. Of additional interest were groups comprised of proteins involved in actin binding and cytoskeletal dynamics.

While by no means an in-depth representation of the biological events occurring over this developmental period, the functional annotation analysis of the filtered data suggests an interesting parallel between nerve and muscle datasets. It is evident that clusters pertaining to mitochondrial and redox functions from up-regulated proteins, and to RNA binding and splicing machinery from down-regulated proteins, dominate both the muscle and nerve data sets. These data invite the considerations of parallel mechanistic changes occurring within both the nerve and muscle from P12 to P24, that may influence the vulnerability of their physical interface—the neuromuscular junction.

3.13 *In silico* pathway analysis of refined muscle and nerve data sets identifies comprehensive networks implicated in oxidative phosphorylation, redox sensitivity, and RNA and protein binding.

In order to explore any potential cellular or molecular pathways that may be modified as a result of the expression alterations present in the refined proteomic data, I performed a systems level analysis using Ingenuity Pathway Analysis software. Through performing a separate analysis on nerve and muscle data sets independently, it was possible to generate a visual representation of molecular networks comprised of interactions between proteins in each respective data set, on the basis of experimentally observed interactions reported in the literature. Combining IPA-generated nerve and muscle output to produce a parallel analysis then enabled the identification of any molecular overlaps between the functional networks proposed to be altered in both nerve and muscle between P12 and P24.

For the nerve analysis, the filtered list of 1734 proteins was imported into Ingenuity Pathway Analysis (IPA); of these, 1713 were mappable by the software and therefore suitable for data mining of the published literature to generate interaction networks. All networks were scored by a unique value, based on total protein input and network size, that represents the relevance of the particular network to the overall analysis (i.e. proteomic alterations in nerve between P12 and P24). Networks generated by IPA were limited to 25 networks comprising a maximum of 35 members per network.

For the muscle analysis, the filtered list of 1874 proteins imported produced 1862 mappable proteins suitable for network generation. The combined analysis of nerve and muscle included all mappable proteins from both nerve and muscle data sets (1713 and 1862, respectively) analysed in parallel, before utilisation of a “combined pathways” function to pinpoint potential conserved molecular pathways. Expression

of all proteins comprising imported nerve and muscle lists had been reported as a ratio in relation to expression at P12; IPA converted all ratios into fold-change in relation to P12. Pathway analysis of nerve, muscle, and combined data sets only included proteins exhibiting a >1.2 fold change at P24 from P12.

3.13.1 The top molecular network generated by IPA-based pathway analysis of sciatic nerve proteins with altered expression over the experimental period implicates RNA metabolism as a key process evolving between P12 and P24.

The top network generated by pathway-based analysis of nerve proteomic data comprised functions involved in RNA post-transcriptional modification. The 34 molecules comprising this top network were not only all present within our data set, but were also almost entirely down-regulated over the experimental time period. Additionally, the interactions between proteins constituting this network were almost entirely direct interactions and therefore had been reported in the published literature as experimentally observed. Upon visualisation of the network, it is evident that the majority of these molecular interactions from a core, or “hub”; molecules comprising this centre “hub” include MCM2, a component of the minichromosome-maintenance protein complex, Synaptotagmin-binding cytoplasmic RNA-interacting protein (SYNCRIP), and various other ribonucleoproteins (RNPs). The implications of decreasing RNA-binding and post-transcriptional modification activity over time elegantly parallel the functional annotation analysis of the filtered nerve data, which demonstrated an overwhelming enrichment for processes of RNA metabolism, particularly the post-transcriptional functions of spliceosome assembly and processing, within proteins down-regulated over time.

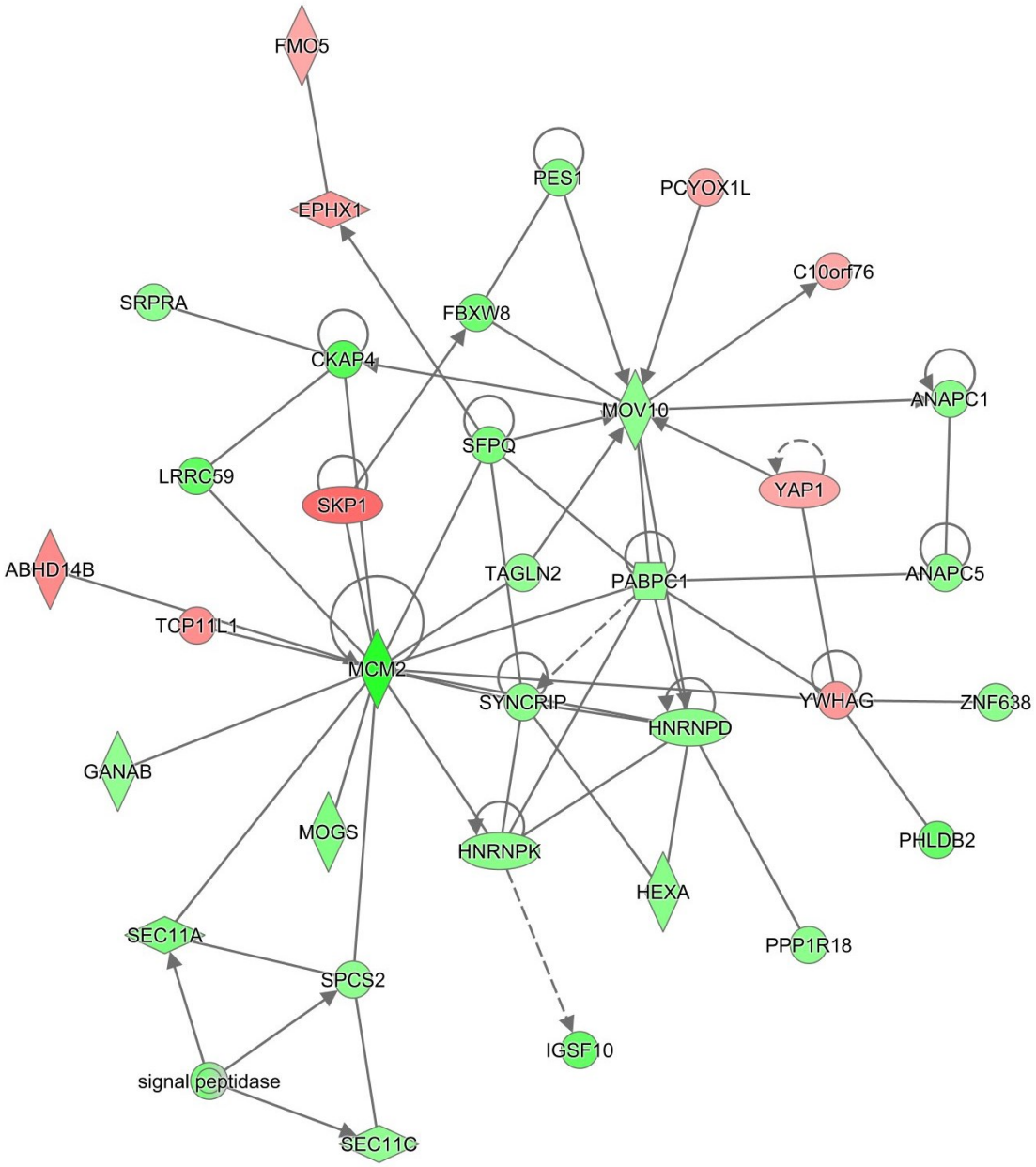

Figure 3.8. Pathway analysis of filtered molecular changes in the nerve over the postnatal developmental period highlights a molecular network comprised of proteins involved in RNA binding and RNA metabolism.
(A) The top identified interaction network in nerve features proteins involved in RNA metabolism, specifically components of the RNA-binding ribonucleoprotein complex. Proteins within these networks with modified expression over the postnatal P12-P24 time-course in the nerve are represented with red (up-regulated over postnatal period) or green (down-regulated over postnatal period); intensity of colour corresponds with magnitude of expression change. Note the dominance of proteins exhibiting a >1.2 fold downregulation in expression (green) between P12 and P24 within our samples. All molecules comprising this network were present within the nerve data set. Solid connecting lines represent a direct interaction experimentally reported in the published literature, while dashed connecting lines indicate an indirect interaction. All suggested indirect interactions were confirmed manually using the Ingenuity Pathway Analysis software to identify publications indicating an interaction between two components of the network.

3.13.2 Additional pathway analysis of sciatic nerve proteins with altered expression over the experimental period highlights a network involved in sodium channel localisation and redox sensitivity.

Another network generated by pathway-based analysis of nerve proteomic data included functions broadly divided into sodium channel localisation and, perhaps more interestingly, sensitivity to redox activity (**Figure 3.9.A)**. Hierarchical reordering of this network by number of interactions (**Figure 3.9.B)** revealed the dominance of Parkinsonism-Associated Declygase 7(PARK7) as a senior molecular hub of this network, including three direct interactions with proteins such as the NADH-dependent redox enzyme malate dehydrogenase 1 (MDH1), the mitochondrial enzyme Pyrroline-5-carboxylate reductase 1 (PYCR1), and glutathione peroxidase, a major enzyme involved in response to oxidative damage. Additionally, PARK7 was shown to indirectly interact with the oxidative-stress protein superoxide dismutase (Sod), linked to ALS. The redox sensitivity functions of this molecular network serve as an interesting potential correlate to the apparent up-regulation in mitochondrial and redox activity between P12 and P24 reported by the functional clustering data.

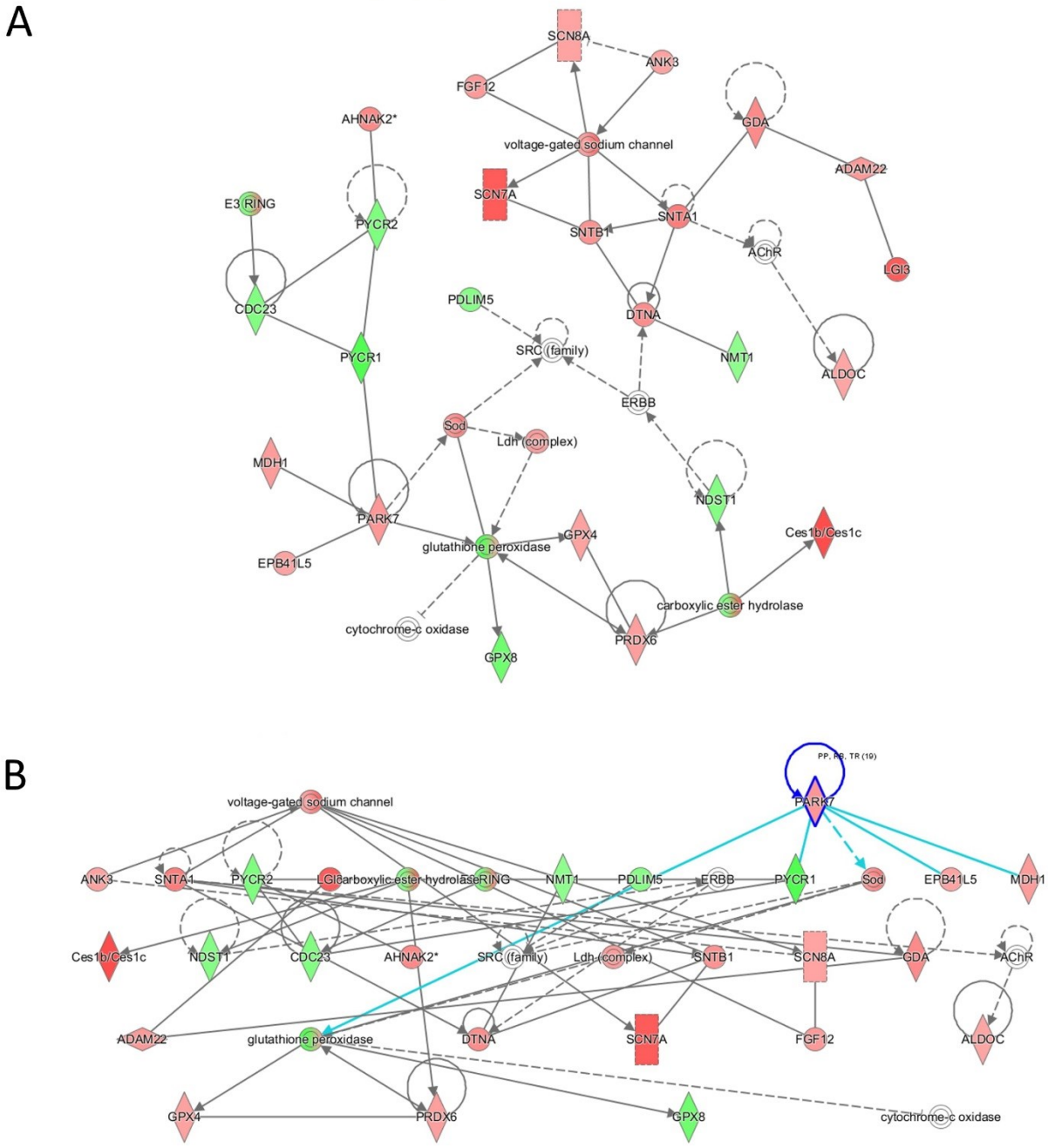

Figure 3.9. Pathway analysis of filtered molecular changes in nerve over the postnatal developmental period identifies networks involved in ion channel localisation and the protective response to oxidative stress and redox sensitivity.

(A) A top-25 identified interaction network in nerve features proteins involved in ion channel localisation and the cellular response to oxidative stress. **(B)** Re-organisation of the same network based on hierarchy of interactions highlights the role of the mitochondrial-implicated protein PARK7 within this network. Proteins within these networks with modified expression over the postnatal P12-P24 time-course in the nerve are represented with red (up-regulated over postnatal period) or green (down-regulated over postnatal period); intensity of colour corresponds with magnitude of expression change. White represents a molecule that is absent from both datasets but an important component of the network. Blue connecting lines represent the highlighted interactions of PARK7. Solid connecting lines represent a direct interaction, while dashed connecting lines indicate an indirect interaction. All suggested indirect interactions were confirmed manually using the Ingenuity Pathway Analysis software to identify publications indicating an interaction between two components

3.13.3 The top molecular network generated by IPA-based pathway analysis of lumbrical muscle proteins with altered expression over the experimental period implicates RNA binding and ribonucleoprotein activity as a key process evolving between P12 and P24.

In a remarkable parallel to the results produced by pathway analysis of the nerve data, the top network generated by pathway-based analysis of lumbrical muscle proteomic data also comprised functions involved in RNA binding and ribonucleoprotein activity. This network consisted of 35 molecules, which were all present within our data set. Additionally, the interactions between proteins constituting this network were all direct and therefore experimentally observed according to reports in the published literature. Although this network appears to lack a single molecular hub, central molecules comprising this radiating network are overwhelmingly components of ribonucleoprotein complexes, responsible for binding RNA for post-transcriptional modification; all of these RNP components appear to exhibit a consistent decrease in expression between P12 and P24. These results, again suggesting a marked decrease in RNA-binding, spliceosomal assembly and post-transcriptional modification activity over the experimental period, not only recapitulate results produced by the functional clustering analysis of filtered muscle data, but also parallel both network-based and functional clustering-generated suggestions of a similar phenomenon occurring in the postnatal murine nerve.

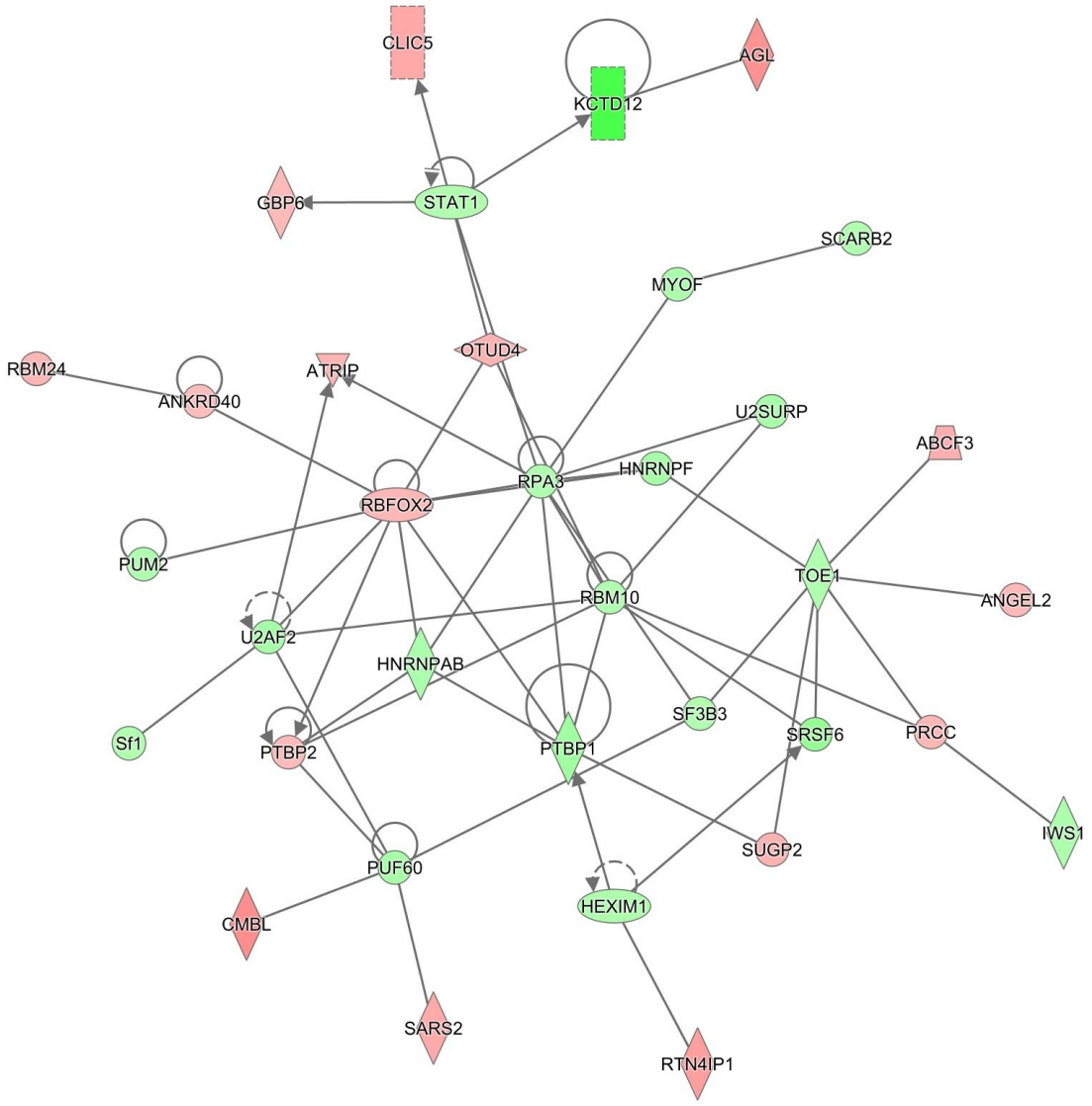

Figure 3.10. Pathway analysis of filtered molecular changes in the musculature over the postnatal developmental period highlights a molecular network comprised of proteins involved in RNA binding ribonucleoprotein assembly.

(A) The top identified interaction network in lumbrical muscle based on expression changes between P12 and P24 features proteins involved in RNA metabolism, specifically components of the RNA-binding ribonucleoprotein complex. The central "hub" comprising this interaction network consists predominantly of members of the pre-mRNA processing ribonucleoproteins (RNPS). Proteins within these networks with modified expression over the postnatal P12-P24 time-course in the nerve are represented with red (up-regulated over postnatal period) or green (down-regulated over postnatal period); intensity of colour corresponds with magnitude of expression change. Note the dominance of proteins exhibiting a >1.2 fold downregulation in expression (green) between P12 and P24 within our samples. All molecules comprising this network were present within the muscle data set. Solid connecting lines represent a direct interaction experimentally reported in the published literature, while dashed connecting lines indicate an indirect interaction. All suggested indirect interactions were confirmed manually using the Ingenuity Pathway Analysis software to identify publications indicating an interaction between two components

3.13.4 Multiple networks generated by IPA-based pathway analysis of lumbrical muscle proteins with altered expression over the experimental time period implicate a marked increase in mitochondrial membrane and oxidative phosphorylation activity between P12 and P24.

Perhaps unsurprisingly with consideration to the results produced by functional clustering analysis of the filtered muscle dataset, a large majority of the remaining top 25 networks produced by pathway analysis of the muscle data comprise mitochondrial respiratory components; specifically, components of the electron transport chain. Two such networks are presented as **Figure 3.11A** and **Figure 3.11B.** In the Figure **3.11A,** note the presence of a dominant subnetwork comprised entirely of direct interactions between proteins identified to be consistently up-regulated within the dataset; investigation into the functional characterisation of these proteins using information stored within the Ingenuity Knowledge Base reveals that they are all components of complexes I and IV of the electron transport chain, located within the inner mitochondrial membrane. Within this subnetwork, the ubiquitous enzymatic complex NADH dehydrogenase, or complex I, serves as the clear hub; direct interactions with NADH dehydrogenase are highlighted in blue.

A separate network visible in **Figure 3.11B** also reveals the robust direct interconnectivity of subunits of complexes I and III of the electron transport chain. A clear subsection of the generated network is based entirely on direct interactions between proteins identified to be consistently up-regulated within the dataset.

These findings, which recapitulate molecular trends identified to be significantly enriched through functional clustering analysis via an easily discernible visual network, invite the consideration of an escalating involvement of oxidative phosphorylation pathways over the P12 to P24 period.

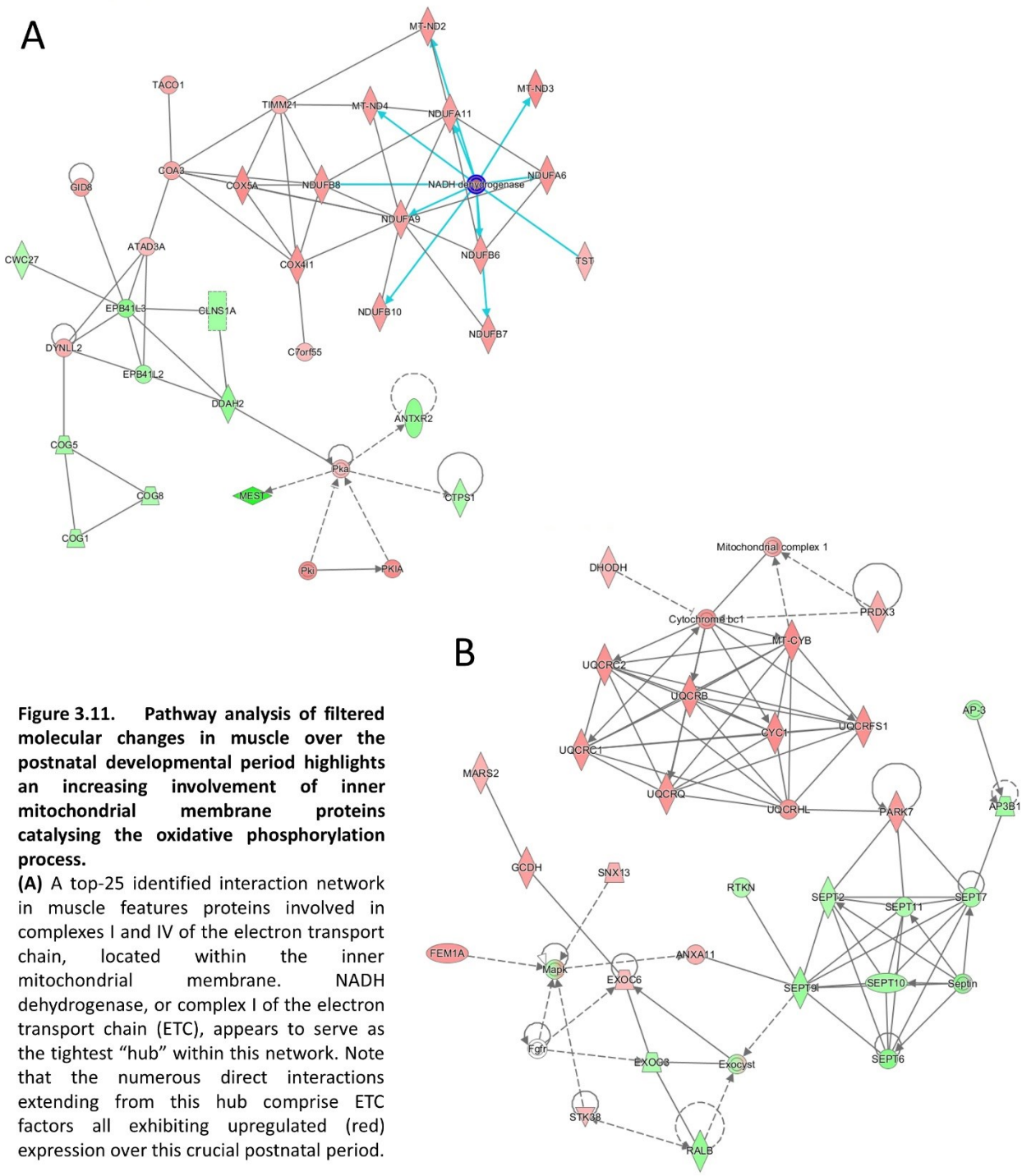

Figure 3.11. Pathway analysis of filtered molecular changes in muscle over the postnatal developmental period highlights an increasing involvement of inner mitochondrial membrane proteins catalysing the oxidative phosphorylation process.

(A) A top-25 identified interaction network in muscle features proteins involved in complexes I and IV of the electron transport chain, located within the inner mitochondrial membrane. NADH dehydrogenase, or complex I of the electron transport chain (ETC), appears to serve as the tightest "hub" within this network. Note that the numerous direct interactions extending from this hub comprise ETC factors all exhibiting upregulated (red) expression over this crucial postnatal period.

(B) Another top-25 identified interaction network in muscle features proteins involved in cytoskeletal organisation, vesicular trafficking, and most strikingly, complex I of the electron transport chain. Note the tightness of interactions within the top "cluster" of this network. The multifarious interactions comprising this complex I network all feature ETC components with consistently upregulated (red) expression over the crucial postnatal period. Proteins within these networks with modified expression over the postnatal P12-P24 time-course in either nerve or muscle are represented with red (up-regulated over postnatal period) or green (down-regulated over postnatal period); intensity of colour corresponds with magnitude of expression change. White represents a molecule that is absent from both datasets but an important component of the network. Blue connecting lines represent the highlighted interactions of NADH dehydrogenase. Solid connecting lines represent a direct interaction, while dashed connecting lines indicate an indirect interaction. All suggested indirect interactions were confirmed manually using the Ingenuity Pathway Analysis software to identify publications indicating an interaction between two components.

3.14 Convergence of pathway analysis-generated networks from nerve and muscle data sets highlights multiple conserved direct interactions between components of the oxidative phosphorylation pathway.

Using the Path Designer function in Ingenuity Pathway Analysis, it was possible to identify a molecular overlap between a predictive network generated from the previous independent nerve analysis, and a network generated from the previous muscle analysis. Extrapolation of this convergence into a visual network, organised by cellular location, revealed the conservation of multiple direct interactions between components of the electron transport chain in both nerve and muscle data sets (**Figure 3.12**). In adherence with the previous functional clustering analyses of nerve and muscle data sets, these results demonstrated an increased expression in proteins involved in the mitochondrial electron transport chain over the P12-P24 period. This predicted mechanistic overlap in functional pathways occurring in both the sciatic nerve and the innervated lumbrical muscles implicated mitochondrial electron transport chain activity as a candidate pathway potentially modulating the vulnerability status of the neuromuscular junction.

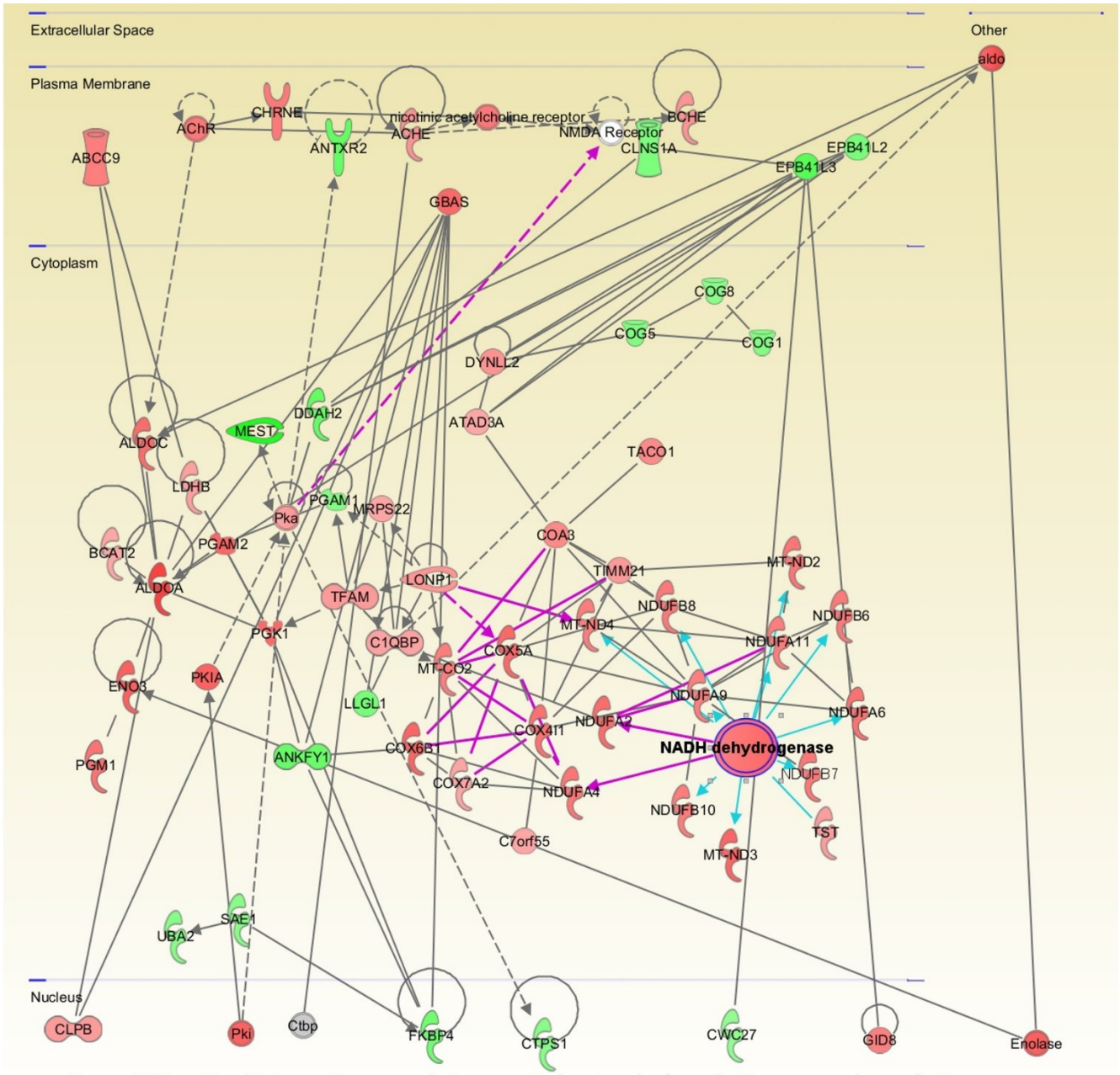

Figure 3.12. Combining pathway analysis-generated networks from both nerve and muscle time-course data sets highlights a conserved escalation in the involvement of mitochondrial oxidative phosphorylation pathways over the key postnatal developmental period.

The Path Designer function in Ingenuity Pathway Analysis software was used to identify overlaps in top-25 networks between nerve and muscle. The resultant combined interaction network reveals an overlap in molecular interactions pertaining to the mitochondrial oxidative phosphorylation process; in particular, candidates identified as components of mitochondrial complex I (NADH dehydrogenase) and complex IV (cytochrome c oxidase) exhibit conserved expression changes in both nerve and muscle data sets. In combination with the functional annotation analysis of data filtered by expression profile **(see Tables 3.1 and 3.2)** it is increasingly evident that oxidative phosphorylation, in particular the first step of the electron transport chain (NADH dehydrogenase), serves as a crucial "hub" linking the molecular changes present in both nerve and muscle over this crucial time period. Proteins within this network with modified expression over the postnatal P12-P24 time-course in either nerve or muscle are represented with red (up-regulated over postnatal period) or green (down-regulated over postnatal period); intensity of colour corresponds with magnitude of expression change. Grey represents a molecule that is absent from both datasets but an important component of the network. Solid connecting lines represent a direct interaction, while dashed connecting lines indicate an indirect interaction. Interactions conserved between nerve and muscle data sets are highlighted as purple connecting lines. Blue connecting lines represent the highlighted interactions of NADH dehydrogenase. All suggested indirect interactions were confirmed manually using the Ingenuity Pathway Analysis software to identify publications indicating an interaction between the two components.

Chapter THREE: Discussion

3.15 Overview of Results

In this chapter, I utilise TMT10plex™ tandem mass-tagging proteomics in order to profile the molecular changes occurring in the sciatic nerve and lumbrical muscles over a time course corresponding to a reported escalation in neuromuscular junction vulnerability to injury. Firstly, these results demonstrate a robust and comprehensive coverage of the nerve and muscle proteome with TMT10plex™ technology, yielding a protein abundance profoundly exceeding those produced by label-free studies of peripheral nerves or skeletal muscle. To date, this study is one of the first applications of TMT10plex™ in the quantitative proteomic study of whole tissues. Secondly, functional enrichment analyses of filtered proteomic output, refined by both magnitude of change and expression pattern over time, reveals a significant and conserved enrichment for an increase in the processes of oxidative phosphorylation (OXPHOS) and mitochondrial respiration over time in both the nerve and muscle. Similarly, functional enrichment analyses of filtered nerve and muscle data sets protein suggests a significant decrease in the processes of RNA binding and post-transcriptional modification over time in both tissues. These findings are supplemented by multiple pathway analysis-generated molecular networks strongly implicating an escalation in OXPHOS activity and cellular responses to oxidative stress over this period of increasing neuronal vulnerability. Finally, comparative pathway analyses combining nerve and muscle time course data sets identifies an overlap in interactive networks suggesting a conserved increase in mitochondrial bioenergetics, particularly in expression of components comprising complex I of the electron transport chain.

3.16 TMT10plex™ mass tagging is a powerful tool enabling a comprehensive exploration of the murine nerve and muscle proteome.

Previous studies utilising quantitative proteomics in the molecular characterisation of murine nerves and skeletal muscles have successfully obtained a modest proteome coverage through both iTRAQ isobaric labelling and label-free techniques (Comley et al., 2011; Mutsaers et al. 2011; Mutsaers et al., 2013). In particular, a label-free proteomic approach to elucidating the molecular perturbations present in mouse models of spinal muscular atrophy (SMA) have resulted in the successful identification of peripheral biomarkers and therapeutically targetable candidates (Mutsaers et al. 2011; Mutsaers et al., 2013; Wishart et al., 2014; Powis et al., 2016). Several studies have sought to assess the efficacy of label-free versus chemical labelling (including iTRAQ and tandem mass tagging) techniques; in studies utilising whole tissues, label-free methods have traditionally been favoured as a more powerful and reliable quantification method (Latosinska et al., 2015; Trinh et al., 2013; X. Wang, Anderson, Smith, & Dabney, 2012). However, recent modifications to the labelling reagents used in multiplexed quantitation have been anticipated to produce a greater coverage capacity compared to previously available chemical labelling methods(Braun et al., 2015; Edwards & Haas, 2016). In this study, I have demonstrated that the recently developed TMT10plex™ tandem mass tagging system is not only a robustly viable technique in the time course molecular analysis of both nerve and muscle, but that it also produces a prolific coverage of the mouse proteome, exemplified by the markedly greater abundance attained than previously reported label-free studies of the murine musculature utilising the same identification criteria (Mutsaers et al., 2011; Mutsaers, et al., 2013).

It should also be noted that this proteomic analysis was performed under consideration of recent evidence suggesting that the proteomic composition of different segments of the same tissue varies significantly. Eaton et al. (2013) demonstrated a marked discrepancy in the expression levels of β-actin and neurofilament-light between proximal and distal regions of the sciatic nerve, inviting speculation that a similar inconsistency may also exist throughout the proteome (Eaton et al., 2013). Consequentially, care was taken to ensure that all tissue samples used in this study were anatomically consistent. These conditions, in conjunction with the validation of select candidates within the data set by quantitative fluorescent western blotting (**Figure 3.2)**, suggest that the robust coverage generated in this TMT10plex™ study is truly representative of global changes in the nerve and muscle proteome over the postnatal developmental period.

3.17 Conserved molecular changes occur in both nerve and muscle over the time course.

After establishing that “immature,” regenerated NMJs in adult mice failed to exhibit the marked resistance to Wallerian degeneration observed in the NMJs of neonatal “immature” mice, Murray et al. (2011) reasoned that the molecular factors potentially regulating this age-based vulnerability to degeneration were not intrinsic to the NMJ itself, but rather originated from either the rest of the motor neuron, or else in the surrounding synaptic environment (Murray et al., 2011). Consequentially, this study therefore sought to profile molecular changes occurring in both the sciatic nerve and in the deep lumbrical muscles over the period corresponding to a steady drop in neuroprotection. Functional annotation analysis of proteins exhibiting a steady upregulation over this P12-P24 period revealed a striking enrichment for the processes

of OXPHOS and associated mitochondrial functions, in both the nerve and the muscle (**Table 3.1, Table 3.2**). Indeed, the most enriched biological group identified from the nerve data, comprised of proteins involved in mitochondrial redox reactions, earned an enrichment score of 8.44, while the top biological group in muscle, comprised of proteins involved in mitochondrial activity, earned an enrichment score of 134.15; for context, a DAVID enrichment score of >1.3 is considered to be loosely equivalent to $p<0.05$ (Huang, Sherman, & Lempicki, 2009). While the biological relevance of these findings will be discussed subsequently, this apparent synchronicity in heightened mitochondrial activity between the motor neuron and muscle are particularly compelling in consideration of the hypothesis that the developmental age of the motor neuron and surrounding environment may regulate synaptic vulnerability to injury-induced degeneration.

3.17.1. Elevated mitochondrial biodynamics are conserved between both nerve and muscle.

Pathway analysis of proteomic alterations occurring in both the nerve and the muscle further suggested a conserved escalation in mitochondrial OXPHOS activity. For example, a number of molecular networks generated from analysis of the filtered muscle data set feature proteins involved in mitochondrial activity, particularly involving electron I of transport chain (**Figure 3.11A; Figure 3.11B**). It should noted that these networks were predominantly comprised of direct interactions between proteins present within the data set, rather than predicted or indirect interactions.

Interestingly, a top nerve network, comprising proteins involved in the cellular response to oxidative stress, highlighted a hierarchal role for PARK7, a major neuronal oxidative stress sensor in which mutations cause autosomal recessive early-onset

Parkinson's disease (H. M. Li, Niki, Taira, Iguchi-Ariga, & Ariga, 2005; Niki, Takahashi-Niki, Taira, Iguchi-Ariga, & Ariga, 2003; Shendelman, Jonason, Martinat, Leete, & Abeliovich, 2004; Takahashi et al., 2001; Yokota et al., 2003). PARK7 has also been identified to be markedly upregulated in both iPSC motor neurons from Type 1 SMA patients as well as in hippocampal synaptosomes from severe Taiwanese SMA mice; accordingly, SMA has been recently added to the list of neurodegenerative conditions in which oxidative stress may impart a major pathological influence (Fuller et al., 2015; Miller, Shi, Zelikovich, & Ma, 2016; Wishart et al., 2014).

Taken together, these findings invite consideration of a concurrent increase in OXPHOS activity and oxidative stress response mechanisms, in both the nerve and muscle. A possible explanation linking these findings is that the apparent rise in oxidative stress response capacity within the nerve homeostatically accompanies a developmental escalation in electron transport chain activity, which is a major source of reactive oxygen species (Hamanaka & Chandel, 2010).

3.18 Mitochondrial bioenergetics and neurodegeneration.

3.18.1. Mitochondria in heritable and spontaneous neurodegenerative disease

Due to the high metabolic demand of neuronal tissues, it is perhaps unsurprising that defective mitochondrial activity appears to be a major pathological candidate –and subsequently, an attractive therapeutic target—in a number of neurodegenerative disorders (Fernández-Vizarra, Enríquez, Pérez-Martos, Montoya, & Fernández-Silva, 2011). Within the central nervous system (CNS), the most definitive association between aberrant mitochondrial dysfunction and neurodegeneration originates from studies of Parkinson's disease patients and animal models alike; indeed, rotenone-induced inhibition of complex I of the electron transport chain in rodents is considered

a robust replication of the Parkinsonian disease course (Schapira et al., 1989; Cannon et al., 2009; Park et al., 2006). Defects in mitochondrial motility, trafficking and basal respiration capacity, coupled with morphological abnormalities, have been widely reported in both patient tissues and in animal models of Alzheimer's disease, Huntington's disease, Batten Disease, and other heritable and spontaneous CNS conditions, as well as in the non-demented aging brain (Blass, Sheu & Gibson, 2000; Bobba et al., 2013; Goebel, Heipertz, Scholz, Iqbal, & Tellez-Nagel, 1978; Hamilton, Pellman, Brustovetsky, Harris, & Brustovetsky, 2016; Hauptmann et al., 2009; Kondziella, Hammer, Sletvold, & Sonnewald, 2003; Yao et al., 2009; Luiro et al., 2006; Yin, Manczak, & Reddy, 2016).

Altered mitochondrial dynamics, including alterations in OXPHOS activity and accompanying production of reactive oxygen species are similarly implicated in heritable and spontaneous diseases of the peripheral nervous system, including ALS. Specifically, the production of reactive oxygen species via defects in the mitochondrial electron transport chain appear to be major pathological candidates in degenerative diseases of the motor neuron. For example, it has recently been suggested that the mechanism by which TAR DNA-binding protein 43 (TDP-43), the quintessential ALS mutation, exerts its toxic gain-of-function is by binding to mRNAs encoding subunits of complex I of the electron transport chain; the subsequent disassembly of complex I appears to promote a rise in oxidative stress *in vitro* (Wang et al., 2016). Aberrant mitochondrial dynamics have also been implicated in SMA, with significant levels of oxidative stress within the motor neuron cell body and axon, accompanying structural mitochondrial abnormalities and OXPHOS defects, reported in the *Δ7* mouse model of SMA (Miller et al., 2016).

3.18.2 Mitochondria in Wld^S-senstitive and archetypal Wallerian Degeneration

Although recent evidence has suggested that mitochondria are not crucial in the execution of injury-induced Wallerian degeneration, mitochondrial biodynamics have been widely reported to be capable of modestly influencing the rate and extent of Wallerian degeneration (Barrientos et al., 2011; Kitay, McCormack, Wang, Tsoulfas, & Zhai, 2013; Loreto, Di Stefano, Gering, & Conforti, 2015; Villegas et al., 2014).

The mechanistic contribution of mitochondria to the injury-induced degenerative process have been investigated in both the protective Wld^S model (Kitay et al., 2013), and in wildtype mice alike (Barrientos et al., 2011; Villegas et al., 2014). From these studies, it has become evident that neuronal mitochondria regulate a number of molecular processes within the distal compartments of the neuron that harbour a marked influence upon degenerative outcome following injury, such as the regulation of axoplasmic Ca^{2+} levels, production of reactive oxygen species, and maintenance of electron transport chain integrity (Avery et al., 2012; Barrientos et al., 2011). For example, the capacity for mitochondria to open a mitochondrial permeability transition pore (mPTP) within their inner membrane in response to cellular stresses enables them to dictate the activation of cell death signalling pathways. In the context of injurious axotomy, the rise in intracellular Ca^{2+} levels following injury-induced loss of neuronal membrane integrity promotes the opening of mPTPs which in turn appear to activate subsequent axonal degeneration (George, Glass, & Griffin, 1995; Villegas et al., 2014).

3.18.3 Elevated mitochondrial bioenergetics as a preconditioning contributor to neuronal vulnerability

However, the findings presented in this chapter are the result of proteomic experiments performed on tissues in which no disease- nor injury-induced degenerative perturbations have occurred. Rather, I present evidence for the dynamic molecular changes occurring throughout this postnatal developmental period, such as an escalation in mitochondrial bioenergetics, to "pre-condition" the distal compartments of the motor neuron to degenerate following injury. In other words, while increased OXPHOS activity itself is not inherently pro-degenerative, do increased mitochondrial bioenergetics in the motor axon and musculature of the mature wildtype mouse pre-condition the distal synapse to degenerate more rapidly upon traumatic insult?

While the majority of studies correlating OXPHOS activity to neurodegeneration disease or injury models report the consequences of dysregulated mitochondrial respiration as mentioned previously, a small but growing body of evidence has presented a correlation of elevated basal levels of healthy bioenergetic activity to neuronal vulnerability. A study of differential vulnerability to Parkinsonian degeneration between populations of dopaminergic neurons in the brain proposed that the leading discrepancy between otherwise functionally similar neuronal populations lay in the elevated basal OXPHOS levels of the vulnerable group (Pacelli *et al.,* 2015).

While the mechanisms by which endogenously elevated OXPHOS activity may pre-condition the neuron to increased vulnerability remain unknown, a potential explanation may be that increased basal mitochondrial bioenergetics produce overall higher levels of reactive oxygen species, which may promote more aggressive

degeneration upon loss of axonal integrity following traumatic insult. Indeed, the results from this chapter indicating an upregulation of molecular networks responsible for oxidative stress response over the P12-P24 period provide compelling support for this theory. Based on the current understanding that mitochondria dynamically regulate the axoplasmic Ca^{2+} levels required for the initiation of the degenerative cascade, it is also possible that alterations in mitochondrial demand over this developmental maturation period also invoke differential, age-dependant capacities for this homeostatic regulation (Avery et al., 2012).

3.19. On a future perspective

In order to support my hypothesis, it would firstly be of utmost interest to assess basal OXPHOS activity within both the nerve and musculature over this P12-P24 period in order to identify any age-dependant differences. Subsequently, it would also be of interest to investigate whether manipulation of basal OXPHOS activity within the motor neuron and surrounding musculature, with a number of readily available pharmacological compounds, is capable of attenuating the phenomenon of an age-dependant synaptic response to injury. The *ex-vivo* whole-mount culture model provides an attractive platform upon which to test these compounds, as it circumvents potential difficulties in mechanism of delivery and pharmacodynamics that often accompany investigation in *in vivo* model.

Chapter FOUR: General Discussion

4.1 Overview of Results

In this study, I have examined two distinct situations of neuromuscular junction vulnerability: firstly, in a mouse model of spinal muscular atrophy, in muscles exhibiting a marked presence of structural pathology; remarkably, therapeutic intervention with SMN promoted a robust improvement in these cytoarchitectural defects, suggesting that the PNS may be able to regenerate from die-back neuropathies as well as it can from injury-induced Wallerian degeneration. Secondly, I have profiled a number of molecular changes occurring in the nerve and muscle of wildtype mice over a time period in which NMJ resistance to injury-induced degeneration drops dramatically. My findings implicate an escalation in OXPHOS activity and similar mitochondrial bioenergetics over this period of increasing vulnerability, inviting the consideration of elevated mitochondrial bioenergetics as a determinant of accelerated injury-induced degeneration at the NMJ.

4.2 The changing molecular profile of the neonatal mouse: implications for mouse models of disease and beyond

Although the results presented in this thesis highlight several cellular and molecular events potentially impacting upon NMJ vulnerability to degeneration, it is difficult to draw an extensive conclusion between two highly distinct situations. Indeed, it remains unknown whether any commonality exists between the degenerative process in SMA, and Wld^S-sensitive pathways (Kariya et al., 2009). However, my results highlighting a broad range of molecular changes evolving over postnatal development in the wildtype

mouse inevitably invite a reconsideration of molecular experiments performed in mouse models across a diverse age spectrum. If the murine proteome indeed evolves dramatically over developmental maturation as suggested by my results, this suggests that a broad array of molecular pathways, including those potentially impacting upon pathogenic cascades, may be markedly influenced by the age of the mouse. For example, it is tempting to consider what implications these findings may have in the comparison of traditional, shorter-lived mouse models of SMA, which exhibit a lifespan typically less than 20 days, to newer, therapeutically-manipulated mouse models which often live for up to a year. Future investigations evaluating whether age-dependant changes within the wildtype proteome alter pathogenic pathways therefore be of great interest.

4.3 Conclusions

The work described in this thesis details several cellular and molecular factors that may determine motor neuron vulnerability to both degenerative disease and injury. In summary, I have shown that:

1. A significant degree of cellular and molecular pathology is present within the motor unit at time of symptomatic onset in a mouse model of SMA.
2. Therapeutic intervention with full-length SMN at this symptomatic time point not only promotes a robust rescue of neuromuscular phenotype and extension of lifespan, but also results in the marked repair of several pathological correlates at the NMJ, including regeneration of the pre-synaptic nerve terminal.
3. Proteomic analysis of the wildtype mouse nerve and muscle over P12-P24, a time period previously characterised by a marked rise in NMJ vulnerability to axotomy- and hypoxia-reperfusion-induced degeneration, highlights a number of altered molecular pathways occurring over postnatal development, including pathways involved in OXPHOS and RNA-binding.

References

Ackermann, B., Kröber, S., Torres-Benito, L., Borgmann, A., Peters, M., Hosseini Barkooie, S. M., … Wirth, B. (2013). Plastin 3 ameliorates spinal muscular atrophy via delayed axon pruning and improves neuromuscular junction functionality. *Human Molecular Genetics*, *22*(7), 1328–47. http://doi.org/10.1093/hmg/dds540

Alías, L., Bernal, S., Fuentes-Prior, P., Barceló, M. J., Also, E., Martínez-Hernández, R., … Tizzano, E. F. (2009). Mutation update of spinal muscular atrophy in Spain: molecular characterization of 745 unrelated patients and identification of four novel mutations in the SMN1 gene. *Human Genetics*, *125*(1), 29–39. http://doi.org/10.1007/s00439-008-0598-1

Araujo, A. prufer de Q. C., Araujo, M., & Swoboda, K. J. (2009). Vascular Perfusion Abnormalities in Infants with Spinal Muscular Atrophy. *The Journal of Pediatrics*, *155*(2), 292–294. http://doi.org/10.1016/j.jpeds.2009.01.071

Avery, M. A., Rooney, T. M., Pandya, J. D., Wishart, T. M., Gillingwater, T. H., Geddes, J. W., … Freeman, M. R. (2012). *WldS Prevents Axon Degeneration through Increased Mitochondrial Flux and Enhanced Mitochondrial Ca2+ Buffering*. *Current Biology* (Vol. 22). http://doi.org/10.1016/j.cub.2012.02.043

Avila, A. M., Burnett, B. G., Taye, A. A., Gabanella, F., Knight, M. A., Hartenstein, P., … Sumner, C. J. (2007). Trichostatin A increases SMN expression and survival in a mouse model of spinal muscular atrophy. *The Journal of Clinical Investigation*, *117*(3), 659–71. http://doi.org/10.1172/JCI29562

Barrientos, S. A., Martinez, N. W., Yoo, S., Jara, J. S., Zamorano, S., Hetz, C., … Court, F. A. (2011). Axonal Degeneration Is Mediated by the Mitochondrial Permeability Transition Pore. *Journal of Neuroscience*, *31*(3), 966–978. http://doi.org/10.1523/JNEUROSCI.4065-10.2011

Barry, J. A., & Ribchester, R. R. (1995). Persistent polyneuronal innervation in partially denervated rat muscle after reinnervation and recovery from prolonged nerve conduction block. *The Journal of Neuroscience : The Official Journal of the Society for Neuroscience*, *15*(10), 6327–39. Retrieved from http://www.ncbi.nlm.nih.gov/pubmed/7472398

Battle, D. J., Lau, C.-K., Wan, L., Deng, H., Lotti, F., & Dreyfuss, G. (2006). *The Gemin5 Protein of the SMN Complex Identifies snRNAs*. *Molecular Cell* (Vol. 23). http://doi.org/10.1016/j.molcel.2006.05.036

Bäumer, D., Lee, S., Nicholson, G., Davies, J. L., Parkinson, N. J., Murray, L. M., … Talbot, K. (2009). Alternative Splicing Events Are a Late Feature of Pathology in a Mouse Model of Spinal Muscular Atrophy. *PLoS Genetics*, *5*(12), e1000773. http://doi.org/10.1371/journal.pgen.1000773

Baxter, B., Gillingwater, T. H., & Parson, S. H. (2008). Rapid loss of motor nerve terminals following hypoxia-reperfusion injury occurs via mechanisms distinct from classic Wallerian degeneration. *Journal of Anatomy*, *212*(6), 827–35. http://doi.org/10.1111/j.1469-7580.2008.00909.x

Berg, M. G., Singh, L. N., Younis, I., Liu, Q., Pinto, A. M., Kaida, D., … Dreyfuss, G. (2012). U1 snRNP Determines mRNA Length and Regulates Isoform Expression. *Cell*, *150*(1), 53–64. http://doi.org/10.1016/j.cell.2012.05.029

Bevan, A. K., Hutchinson, K. R., Foust, K. D., Braun, L., McGovern, V. L., Schmelzer, L., … Kaspar, B. K. (2010). Early heart failure in the SMNDelta7 model of spinal muscular atrophy and correction by postnatal scAAV9-SMN delivery. *Human Molecular Genetics*, *19*(20), 3895–905. http://doi.org/10.1093/hmg/ddq300

Blass, J.P., Sheu, K.F., & Gibson, G.E. (2000). Inherent Abnormalities in Energy Metabolism in Alzheimer Disease: Interaction with Cerebrovascular Compromise. *Annals of the New York Academy of Sciences*, *903*(1 VASCULAR FACT), 204–221. http://doi.org/10.1111/j.1749-6632.2000.tb06370.x

Bobba, A., Amadoro, G., Valenti, D., Corsetti, V., Lassandro, R., & Atlante, A. (2013). Mitochondrial respiratory chain Complexes I and IV are impaired by β-amyloid via direct interaction and through Complex I-dependent ROS production, respectively. *MITOCH*, *13*, 298–311. http://doi.org/10.1016/j.mito.2013.03.008

Bogdanik, L. P., Osborne, M. A., Davis, C., Martin, W. P., Austin, A., Rigo, F., … Lutz, C. M. (2015). Systemic, postsymptomatic antisense oligonucleotide rescues motor unit maturation delay in a new mouse model for type II/III spinal muscular atrophy. *Proceedings of the National Academy of Sciences of the United States of America*, *112*(43), E5863–72. http://doi.org/10.1073/pnas.1509758112

Boon, K.-L., Xiao, S., McWhorter, M. L., Donn, T., Wolf-Saxon, E., Bohnsack, M. T., … Beattie, C. E. (2009). Zebrafish survival motor neuron mutants exhibit presynaptic neuromuscular junction defects. *Human Molecular Genetics*, *18*(19), 3615–25. http://doi.org/10.1093/hmg/ddp310

Bowerman, M., Murray, L. M., Beauvais, A., Pinheiro, B., & Kothary, R. (2012). A critical smn threshold in mice dictates onset of an intermediate spinal muscular atrophy phenotype associated with a distinct neuromuscular junction pathology. http://doi.org/10.1016/j.nmd.2011.09.007

Bowerman, M., Swoboda, K. J., Michalski, J.-P., Wang, G.-S., Reeks, C., Beauvais, A., … Kothary, R. (2012). Glucose metabolism and pancreatic defects in spinal muscular atrophy. *Annals of Neurology*, *72*(2), 256–268. http://doi.org/10.1002/ana.23582

Braun, C. R., Bird, G. H., Wü Hr, M., Erickson, B. K., Rad, R., Walensky, L. D., … Haas, W. (n.d.). Generation of Multiple Reporter Ions from a Single Isobaric Reagent Increases Multiplexing Capacity for Quantitative Proteomics. http://doi.org/10.1021/acs.analchem.5b02307

Brichta, L., Hofmann, Y., Hahnen, E., Siebzehnrubl, F. A., Raschke, H., Blumcke, I., … Wirth, B. (2003). Valproic acid increases the SMN2 protein level: a well-known drug as a potential therapy for spinal muscular atrophy. *Human Molecular Genetics*, *12*(19), 2481–9. http://doi.org/10.1093/hmg/ddg256

Brown, M. C., & Ironton, R. (1978). Sprouting and regression of neuromuscular synapses in partially denervated mammalian muscles. *The Journal of Physiology*, *278*, 325–48. Retrieved from http://www.ncbi.nlm.nih.gov/pubmed/671308

Burghes, A. H. M., & Beattie, C. E. (2009). Spinal muscular atrophy: why do low levels of survival motor neuron protein make motor neurons sick? *Nature Reviews. Neuroscience*, *10*(8), 597–609. http://doi.org/10.1038/nrn2670

Cannon, J. R., Tapias, V., Na, H. M., Honick, A. S., Drolet, R. E., & Greenamyre, J. T. (2009). A highly reproducible rotenone model of Parkinson's disease. *Neurobiology of Disease*, *34*(2), 279–90. Retrieved from http://www.ncbi.nlm.nih.gov/pubmed/19385059

Carrel, T. L., McWhorter, M. L., Workman, E., Zhang, H., Wolstencroft, E. C., Lorson, C., … Beattie, C. E. (2006). Survival motor neuron function in motor axons is independent of functions required for small nuclear ribonucleoprotein biogenesis. *The Journal of Neuroscience : The Official Journal of the Society for Neuroscience*, *26*(43), 11014–22. http://doi.org/10.1523/JNEUROSCI.1637-06.2006

Chan, Y. B., Miguel-Aliaga, I., Franks, C., Thomas, N., Trülzsch, B., Sattelle, D. B., … van den Heuvel, M. (2003). Neuromuscular defects in a Drosophila survival motor neuron gene mutant. *Human Molecular Genetics*, *12*(12), 1367–76. Retrieved from http://www.ncbi.nlm.nih.gov/pubmed/12783845

Chang, H. C.-H., Dimlich, D. N., Yokokura, T., Mukherjee, A., Kankel, M. W., Sen, A., … Artavanis-Tsakonas, S. (2008). Modeling spinal muscular atrophy in Drosophila. *PloS One*, *3*(9), e3209. http://doi.org/10.1371/journal.pone.0003209

Chang, J. G., Hsieh-Li, H. M., Jong, Y. J., Wang, N. M., Tsai, C. H., & Li, H. (2001). Treatment of spinal muscular atrophy by sodium butyrate. *Proceedings of the National Academy of Sciences of the United States of America*, *98*(17), 9808–13. http://doi.org/10.1073/pnas.171105098

Chari, A., Paknia, E., & Fischer, U. (2009). The role of RNP biogenesis in spinal muscular atrophy. *Current Opinion in Cell Biology*, *21*(3), 387–393. http://doi.org/10.1016/j.ceb.2009.02.004

Cifuentes-Diaz, C., Nicole, S., Velasco, M. E., Borra-Cebrian, C., Panozzo, C., Frugier, T., … Melki, J. (2002). Neurofilament accumulation at the motor endplate and lack of axonal sprouting in a spinal muscular atrophy mouse model. *Human Molecular Genetics*, *11*(12), 1439–47. Retrieved from http://www.ncbi.nlm.nih.gov/pubmed/12023986

Comley, L. H., Fuller, H. R., Wishart, T. M., Mutsaers, C. A., Thomson, D., Wright, A. K., … Gillingwater, T. H. (2011). ApoE isoform-specific regulation of regeneration in the peripheral nervous system. *Human Molecular Genetics*, *20*(12), 2406–21. http://doi.org/10.1093/hmg/ddr147

Coovert, D. D., Le, T. T., McAndrew, P. E., Strasswimmer, J., Crawford, T. O., Mendell, J. R., … Burghes, A. H. (1997). The survival motor neuron protein in spinal muscular atrophy. *Human Molecular Genetics*, *6*(8), 1205–14. Retrieved from http://www.ncbi.nlm.nih.gov/pubmed/9259265

Crawford, T. O., & Pardo, C. A. (1996). The Neurobiology of Childhood Spinal Muscular Atrophy.

Dachs, E., Hereu, M., Piedrafita, L., Casanovas, A., Calderó, J., & Esquerda, J. E. (2011). Defective neuromuscular junction organization and postnatal myogenesis in mice with severe spinal muscular atrophy. *Journal of Neuropathology and Experimental Neurology*, *70*(6), 444–61. http://doi.org/10.1097/NEN.0b013e31821cbd8b

Duque, S. I., Arnold, W. D., Odermatt, P., Li, X., Porensky, P. N., Schmelzer, L., … Burghes, A. H. M. (2015). A large animal model of spinal muscular atrophy and correction of phenotype. *Annals of Neurology*, *77*(3), 399–414. http://doi.org/10.1002/ana.24332

Eaton, S. L., Roche, S. L., Llavero Hurtado, M., Oldknow, K. J., Farquharson, C., Gillingwater, T. H., & Wishart, T. M. (2013). Total protein analysis as a reliable loading control for quantitative fluorescent Western blotting. *PloS One*, *8*(8), e72457. http://doi.org/10.1371/journal.pone.0072457

Edwards, A., & Haas, W. (2016). Multiplexed Quantitative Proteomics for High-Throughput Comprehensive Proteome Comparisons of Human Cell Lines. *Methods in Molecular Biology (Clifton, N.J.)*, *1394*, 1–13. http://doi.org/10.1007/978-1-4939-3341-9_1

Farrar, M. A., Johnston, H. M., Grattan-Smith, P., Turner, A., & Kiernan, M. C. (2009). Spinal muscular atrophy: molecular mechanisms. *Current Molecular Medicine*, *9*(7), 851–62. Retrieved from http://www.ncbi.nlm.nih.gov/pubmed/19860664

Fawcett, J. W., & Keynes, R. J. (1990). Peripheral nerve regeneration. *Annual Review of Neuroscience*, *13*, 43–60. http://doi.org/10.1146/annurev.ne.13.030190.000355

Fernández-Vizarra, E., Enríquez, J. A., Pérez-Martos, A., Montoya, J., & Fernández-Silva, P. (2011). Tissue-specific differences in mitochondrial activity and biogenesis. *Mitochondrion*, *11*(1), 207–213. http://doi.org/10.1016/j.mito.2010.09.011

Ferri, A., Sanes, J. R., Coleman, M. P., Cunningham, J. M., & Kato, A. C. (2003). *Inhibiting Axon Degeneration and Synapse Loss Attenuates Apoptosis and Disease Progression in a Mouse Model of Motoneuron Disease*. *Current Biology* (Vol. 13). http://doi.org/10.1016/S0960-9822(03)00206-9

Foust, K. D., Wang, X., McGovern, V. L., Braun, L., Bevan, A. K., Haidet, A. M., … Kaspar, B. K. (2010). Rescue of the spinal muscular atrophy phenotype in a mouse model by early postnatal delivery of SMN. *Nature Biotechnology*, *28*(3), 271–4. http://doi.org/10.1038/nbt.1610

Fuller, H. R., Hurtado, M. L., Wishart, T. M., & Gates, M. A. (2014). The rat striatum responds to nigro-striatal degeneration via the increased expression of proteins associated with growth and regeneration of neuronal circuitry. *Proteome Science*, *12*, 20. http://doi.org/10.1186/1477-5956-12-20

Fuller, H. R., Mandefro, B., Shirran, S. L., Gross, A. R., Kaus, A. S., Botting, C. H., … Sareen, D. (2015). Spinal Muscular Atrophy Patient iPSC-Derived Motor Neurons Have Reduced Expression of Proteins Important in Neuronal Development. *Frontiers in Cellular Neuroscience*, *9*, 506. http://doi.org/10.3389/fncel.2015.00506

Gabanella, F., Butchbach, M. E. R., Saieva, L., Carissimi, C., Burghes, A. H. M., & Pellizzoni, L. (2007). Ribonucleoprotein assembly defects correlate with spinal muscular atrophy severity and preferentially affect a subset of spliceosomal snRNPs. *PloS One*, *2*(9), e921. http://doi.org/10.1371/journal.pone.0000921

George, E. B., Glass, J. D., & Griffin, J. W. (1995). Axotomy-induced axonal degeneration is mediated by calcium influx through ion-specific channels. *The Journal of Neuroscience : The Official Journal of the Society for Neuroscience*, *15*(10), 6445–52. Retrieved from http://www.ncbi.nlm.nih.gov/pubmed/7472407

Gillingwater, T. H., Ingham, C. A., Parry, K. E., Wright, A. K., Haley, J. E., Wishart, T. M., … Ribchester, R. R. (2006). Delayed synaptic degeneration in the CNS of Wlds mice after cortical lesion. *Brain : A Journal of Neurology*, *129*(Pt 6), 1546–56. http://doi.org/10.1093/brain/awl101

Gillingwater, T. H., & Ribchester, R. R. (2001). Compartmental neurodegeneration and synaptic plasticity in the Wld(s) mutant mouse. *The Journal of Physiology*, *534*(Pt 3), 627–39. Retrieved from http://www.ncbi.nlm.nih.gov/pubmed/11483696

Gillingwater, T. H., Thomson, D., Mack, T. G. A., Soffin, E. M., Mattison, R. J., Coleman, M. P., & Ribchester, R. R. (2002). Age-dependent synapse withdrawal at axotomised neuromuscular junctions in Wld(s) mutant and Ube4b/Nmnat transgenic mice. *The Journal of Physiology*, *543*(Pt 3), 739–55. Retrieved from http://www.ncbi.nlm.nih.gov/pubmed/12231635

Goebel, H. H., Heipertz, R., Scholz, W., Iqbal, K., & Tellez-Nagel, I. (1978). Juvenile Huntington chorea: clinical, ultrastructural, and biochemical studies. *Neurology*, *28*(1), 23–31. Retrieved from http://www.ncbi.nlm.nih.gov/pubmed/145549

Gogliotti, R. G., Hammond, S. M., Lutz, C., & DiDonato, C. J. (2010). *Molecular and phenotypic reassessment of an infrequently used mouse model for spinal muscular atrophy*. *Biochemical and Biophysical Research Communications* (Vol. 391). http://doi.org/10.1016/j.bbrc.2009.11.090

Gurney, M. E., Pu, H., Chiu, A. Y., Dal Canto, M. C., Polchow, C. Y., Alexander, D. D., … Deng, H. X. (1994). Motor neuron degeneration in mice that express a human Cu,Zn superoxide dismutase mutation. *Science (New York, N.Y.)*, *264*(5166), 1772–5. Retrieved from http://www.ncbi.nlm.nih.gov/pubmed/8209258

Hamanaka, R. B., & Chandel, N. S. (2010). Mitochondrial reactive oxygen species regulate cellular signaling and dictate biological outcomes. *Trends in Biochemical Sciences*, *35*(9), 505–513. http://doi.org/10.1016/j.tibs.2010.04.002

Hamilton, J., Pellman, J. J., Brustovetsky, T., Harris, R. A., & Brustovetsky, N. (2016). Oxidative metabolism and Ca2+ handling in isolated brain mitochondria and striatal neurons from R6/2 mice, a model of Huntington's disease. *Human Molecular Genetics*. http://doi.org/10.1093/hmg/ddw133

Hauptmann, S., Scherping, I., Dröse, S., Brandt, U., Schulz, K. L., Jendrach, M., … Müller, W. E. (2009). Mitochondrial dysfunction: An early event in Alzheimer pathology accumulates with age in AD transgenic mice. *Neurobiology of Aging*, *30*, 1574–1586. http://doi.org/10.1016/j.neurobiolaging.2007.12.005

Hsieh-Li, H. M., Chang, J. G., Jong, Y. J., Wu, M. H., Wang, N. M., Tsai, C. H., & Li, H. (2000). A mouse model for spinal muscular atrophy. *Nature Genetics*, *24*(1), 66–70. http://doi.org/10.1038/71709

Hua, Y., Sahashi, K., Rigo, F., Hung, G., Horev, G., Bennett, C. F., & Krainer, A. R. (2011). Peripheral SMN restoration is essential for long-term rescue of a severe spinal muscular atrophy mouse model. *Nature*, *478*(7367), 123–6. http://doi.org/10.1038/nature10485

Hua, Y., Vickers, T. A., Baker, B. F., Bennett, C. F., & Krainer, A. R. (2007). Enhancement of SMN2 exon 7 inclusion by antisense oligonucleotides targeting the exon. *PLoS Biology*, *5*(4), e73. http://doi.org/10.1371/journal.pbio.0050073

Hua, Y., Vickers, T. A., Okunola, H. L., Bennett, C. F., & Krainer, A. R. (2008). Antisense Masking of an hnRNP A1/A2 Intronic Splicing Silencer Corrects SMN2 Splicing in Transgenic Mice. *The American Journal of Human Genetics*, *82*(4), 834–848. http://doi.org/10.1016/j.ajhg.2008.01.014

Huang, D. W., Sherman, B. T., & Lempicki, R. A. (2009). Systematic and integrative analysis of large gene lists using DAVID bioinformatics resources. *Nature Protocols*, *4*(1), 44–57. http://doi.org/10.1038/nprot.2008.211

Jablonka, S., Beck, M., Lechner, B. D., Mayer, C., & Sendtner, M. (2007). Defective Ca2+ channel clustering in axon terminals disturbs excitability in motoneurons in spinal muscular atrophy. *The Journal of Cell Biology*, *179*(1), 139–49. http://doi.org/10.1083/jcb.200703187

Jablonka, S., Karle, K., Sandner, B., Andreassi, C., von Au, K., & Sendtner, M. (2006). Distinct and overlapping alterations in motor and sensory neurons in a mouse model of spinal muscular atrophy. *Human Molecular Genetics*, *15*(3), 511–8. http://doi.org/10.1093/hmg/ddi467

Kapoukranidou, D., Gougoulias, N., Hatzisotiriou, A., Fardi, D., Albani, M., & Kalpidis, I. (2005). Assessment of motoneuron death during development following neonatal nerve crush and Mg2+ treatment. *Medical Science Monitor : International Medical Journal of Experimental and Clinical Research*, *11*(10), BR373–9. Retrieved from http://www.ncbi.nlm.nih.gov/pubmed/16192895

Kariya, S., Obis, T., Garone, C., Akay, T., Sera, F., Iwata, S., … Monani, U. R. (2014). Requirement of enhanced Survival Motoneuron protein imposed during neuromuscular junction maturation. *The Journal of Clinical Investigation*, *124*(2), 785–800. http://doi.org/10.1172/JCI72017

Kariya, S., Park, G.-H., Maeno-Hikichi, Y., Leykekhman, O., Lutz, C., Arkovitz, M. S., … Monani, U. R. (2008). Reduced SMN protein impairs maturation of the neuromuscular junctions in mouse models of spinal muscular atrophy. *Human Molecular Genetics*, *17*(16), 2552–69. http://doi.org/10.1093/hmg/ddn156

Kissel, J. T., Scott, C. B., Reyna, S. P., Crawford, T. O., Simard, L. R., Krosschell, K. J., … Project Cure Spinal Muscular Atrophy Investigators' Network. (2011). SMA CARNIVAL TRIAL PART II: a prospective, single-armed trial of L-carnitine and valproic acid in ambulatory children with spinal muscular atrophy. *PloS One*, *6*(7), e21296. http://doi.org/10.1371/journal.pone.0021296

Kitay, B. M., McCormack, R., Wang, Y., Tsoulfas, P., & Zhai, R. G. (2013). Mislocalization of neuronal mitochondria reveals regulation of Wallerian degeneration and NMNAT/WLD(S)-mediated axon protection independent of axonal mitochondria. *Human Molecular Genetics*, *22*(8), 1601–14. http://doi.org/10.1093/hmg/ddt009

Kondziella, D., Hammer, J., Sletvold, O., & Sonnewald, U. (2003). The pentylenetetrazole-kindling model of epilepsy in SAMP8 mice: glial–neuronal metabolic interactions. *Neurochemistry International*, *43*, 629–637. http://doi.org/10.1016/S0197-0186(03)00093-7

Kong, L., Wang, X., Choe, D. W., Polley, M., Burnett, B. G., Bosch-Marcé, M., … Sumner, C. J. (2009). Impaired synaptic vesicle release and immaturity of neuromuscular junctions in spinal muscular atrophy mice. *The Journal of Neuroscience : The Official Journal of the Society for Neuroscience*, *29*(3), 842–51. http://doi.org/10.1523/JNEUROSCI.4434-08.2009

Latosinska, A., Vougas, K., Makridakis, M., Klein, J., Mullen, W., Abbas, M., … Jankowski, V. (2015). Comparative Analysis of Label-Free and 8-Plex iTRAQ Approach for Quantitative Tissue Proteomic Analysis. *PloS One*, *10*(9), e0137048. http://doi.org/10.1371/journal.pone.0137048

Le, T. T., Pham, L. T., Butchbach, M. E. R., Zhang, H. L., Monani, U. R., Coovert, D. D., … Burghes, A. H. M. (2005). SMNDelta7, the major product of the centromeric survival motor neuron (SMN2) gene, extends survival in mice with spinal muscular atrophy and associates with full-length SMN. *Human Molecular Genetics*, *14*(6), 845–57. http://doi.org/10.1093/hmg/ddi078

Lefebvre, S., Burlet, P., Liu, Q., Bertrandy, S., Clermont, O., Munnich, A., … Melki, J. (1997). Correlation between severity and SMN protein level in spinal muscular atrophy. *Nature Genetics*, *16*(3), 265–269. http://doi.org/10.1038/ng0797-265

Li, H. M., Niki, T., Taira, T., Iguchi-Ariga, S. M. M., & Ariga, H. (2005). Association of DJ-1 with chaperones and enhanced association and colocalization with mitochondrial Hsp70 by oxidative stress. *Free Radical Research*, *39*(10), 1091–9. http://doi.org/10.1080/10715760500260348

Li, L., Houenou, L. J., Wu, W., Lei, M., Prevette, D. M., & Oppenheim, R. W. (1998). Characterization of spinal motoneuron degeneration following different types of peripheral nerve injury in neonatal and adult mice. *The Journal of Comparative Neurology*, *396*(2), 158–168. http://doi.org/10.1002/(SICI)1096-9861(19980629)396:2<158::AID-CNE2>3.0.CO;2-#

Lin, T.-L., Chen, T.-H., Hsu, Y.-Y., Cheng, Y.-H., Juang, B.-T., Jong, Y.-J., … Sumner, C. (2016). Selective Neuromuscular Denervation in Taiwanese Severe SMA Mouse Can Be Reversed by Morpholino Antisense Oligonucleotides. *PLOS ONE*, *11*(4), e0154723. http://doi.org/10.1371/journal.pone.0154723

Ling, K. K. Y., Gibbs, R. M., Feng, Z., & Ko, C.-P. (2012). Severe neuromuscular denervation of clinically relevant muscles in a mouse model of spinal muscular atrophy. *Human Molecular Genetics*, *21*(1), 185–95. http://doi.org/10.1093/hmg/ddr453

Liu, H., Yazdani, A., Murray, L. M., Beauvais, A., & Kothary, R. (2014). The Smn-independent beneficial effects of trichostatin A on an intermediate mouse model of spinal muscular atrophy. *PloS One*, *9*(7), e101225. http://doi.org/10.1371/journal.pone.0101225

Liu, Q., & Dreyfuss, G. (1996). A novel nuclear structure containing the survival of motor neurons protein. *The EMBO Journal*, *15*(14), 3555–65. Retrieved from http://www.ncbi.nlm.nih.gov/pubmed/8670859

Liu, Q., Fischer, U., Wang, F., & Dreyfuss, G. (1997). The Spinal Muscular Atrophy Disease Gene Product, SMN, and Its Associated Protein SIP1 Are in a Complex with Spliceosomal snRNP Proteins. *Cell*, *90*(6), 1013–1021. http://doi.org/10.1016/S0092-8674(00)80367-0

Loreto, A., Di Stefano, M., Gering, M., & Conforti, L. (2015). Wallerian Degeneration Is Executed by an NMN-SARM1-Dependent Late Ca2+ Influx but Only Modestly Influenced by Mitochondria. *Cell Reports*, *13*(11), 2539–2552. http://doi.org/10.1016/j.celrep.2015.11.032

Lorson, C. L., & Androphy, E. J. (2000). An exonic enhancer is required for inclusion of an essential exon in the SMA-determining gene SMN. *Human Molecular Genetics*, *9*(2), 259–65. Retrieved from http://www.ncbi.nlm.nih.gov/pubmed/10607836

Lorson, C. L., Hahnen, E., Androphy, E. J., & Wirth, B. (1999a). A single nucleotide in the SMN gene regulates splicing and is responsible for spinal muscular atrophy. *Proceedings of the National Academy of Sciences of the United States of America*, *96*(11), 6307–11. http://doi.org/10.1073/pnas.96.11.6307

Lorson, C. L., Hahnen, E., Androphy, E. J., & Wirth, B. (1999b). A single nucleotide in the SMN gene regulates splicing and is responsible for spinal muscular atrophy. *Proceedings of the National Academy of Sciences of the United States of America*, *96*(11), 6307–11. Retrieved from http://www.ncbi.nlm.nih.gov/pubmed/10339583

Lorson, C. L., Strasswimmer, J., Yao, J.-M., Baleja, J. D., Hahnen, E., Wirth, B., … Androphy, E. J. (1998). SMN oligomerization defect correlates with spinal muscular atrophy severity. *Nature Genetics*, *19*(1), 63–66. http://doi.org/10.1038/ng0598-63

Lutz, C. M., Kariya, S., Patruni, S., Osborne, M. A., Liu, D., Henderson, C. E., … Monani, U. R. (2011). Postsymptomatic restoration of SMN rescues the disease phenotype in a mouse model of severe spinal muscular atrophy. *The Journal of Clinical Investigation*, *121*(8), 3029–41. http://doi.org/10.1172/JCI57291

Mack, T. G., Reiner, M., Beirowski, B., Mi, W., Emanuelli, M., Wagner, D., … Coleman, M. P. (2001). Wallerian degeneration of injured axons and synapses is delayed by a Ube4b/Nmnat chimeric gene. *Nature Neuroscience*, *4*(12), 1199–206. http://doi.org/10.1038/nn770

Markowitz, J. A., Tinkle, M. B., & Fischbeck, K. H. (2004). *Spinal Muscular Atrophy in the Neonate*. *Journal of Obstetric, Gynecologic & Neonatal Nursing* (Vol. 33). http://doi.org/10.1177/0884217503261125

McGovern, V. L., Massoni-Laporte, A., Wang, X., Le, T. T., Le, H. T., Beattie, C. E., … Burghes, A. H. M. (2015). Plastin 3 Expression Does Not Modify Spinal Muscular Atrophy Severity in the ∆7 SMA Mouse. *PloS One*, *10*(7), e0132364. http://doi.org/10.1371/journal.pone.0132364

McWhorter, M. L., Monani, U. R., Burghes, A. H. M., & Beattie, C. E. (2003). Knockdown of the survival motor neuron (Smn) protein in zebrafish causes defects in motor axon outgrowth and pathfinding. *The Journal of Cell Biology*, *162*(5), 919–31. http://doi.org/10.1083/jcb.200303168

Meister, G., Bühler, D., Laggerbauer, B., Zobawa, M., Lottspeich, F., & Fischer, U. (2000). Characterization of a nuclear 20S complex containing the survival of motor neurons (SMN) protein and a specific subset of spliceosomal Sm proteins. *Human Molecular Genetics*, *9*(13), 1977–86. Retrieved from http://www.ncbi.nlm.nih.gov/pubmed/10942426

Mentis, G. Z., Blivis, D., Liu, W., Drobac, E., Crowder, M. E., Kong, L., … O'Donovan, M. J. (2011). Early Functional Impairment of Sensory-Motor Connectivity in a Mouse Model of Spinal Muscular Atrophy. *Neuron*, *69*(3), 453–467. http://doi.org/10.1016/j.neuron.2010.12.032

Meyer, K., Ferraiuolo, L., Schmelzer, L., Braun, L., McGovern, V., Likhite, S., … Kaspar, B. K. (2015). Improving single injection CSF delivery of AAV9-mediated gene therapy for SMA: a dose-response study in mice and nonhuman primates. *Molecular Therapy : The Journal of the American Society of Gene Therapy*, *23*(3), 477–87. http://doi.org/10.1038/mt.2014.210

Mi, W., Beirowski, B., Gillingwater, T. H., Adalbert, R., Wagner, D., Grumme, D., … Coleman, M. P. (2005). The slow Wallerian degeneration gene, WldS, inhibits axonal spheroid pathology in gracile axonal dystrophy mice. *Brain : A Journal of Neurology*, *128*(Pt 2), 405–16. http://doi.org/10.1093/brain/awh368

Miller, N., Shi, H., Zelikovich, A. S., & Ma, Y.-C. (2016). Motor Neuron Mitochondrial Dysfunction in Spinal Muscular Atrophy. *Human Molecular Genetics*. http://doi.org/10.1093/hmg/ddw262

Mishra, V. N., Kalita, J., Kesari, A., Mitta, B., Shankar, S. K., & Misra, U. K. (n.d.). A clinical and genetic study of spinal muscular atrophy. *Electromyography and Clinical Neurophysiology*, *44*(5), 307–12. Retrieved from http://www.ncbi.nlm.nih.gov/pubmed/15378871

Mitrpant, C., Porensky, P., Zhou, H., Price, L., Muntoni, F., Fletcher, S., … Burghes, A. H. M. (2013). Improved antisense oligonucleotide design to suppress aberrant SMN2 gene transcript processing: towards a treatment for spinal muscular atrophy. *PloS One*, *8*(4), e62114. http://doi.org/10.1371/journal.pone.0062114

Mizusawa, H., Matsumoto, S., Yen, S. H., Hirano, A., Rojas-Corona, R. R., & Donnenfeld, H. (1989). Focal accumulation of phosphorylated neurofilaments within anterior horn cell in familial amyotrophic lateral sclerosis. *Acta Neuropathologica*, *79*(1), 37–43. Retrieved from http://www.ncbi.nlm.nih.gov/pubmed/2511732

Monani, U. R., Lorson, C. L., Parsons, D. W., Prior, T. W., Androphy, E. J., Burghes, A. H. M., & McPherson, J. D. (1999). A single nucleotide difference that alters splicing patterns distinguishes the SMA gene SMN1 from the copy gene SMN2. *Human Molecular Genetics*, *8*(7), 1177–1183. http://doi.org/10.1093/hmg/8.7.1177

Monani, U. R., Pastore, M. T., Gavrilina, T. O., Jablonka, S., Le, T. T., Andreassi, C., … Burghes, A. H. M. (2003). A transgene carrying an A2G missense mutation in the SMN gene modulates phenotypic severity in mice with severe (type I) spinal muscular atrophy. *The Journal of Cell Biology*, *160*(1), 41–52. http://doi.org/10.1083/jcb.200208079

Monani, U. R., Sendtner, M., Coovert, D. D., Parsons, D. W., Andreassi, C., Le, T. T., … Burghes, A. H. (2000). The human centromeric survival motor neuron gene (SMN2) rescues embryonic lethality in Smn(-/-) mice and results in a mouse with spinal muscular atrophy. *Human Molecular Genetics*, *9*(3), 333–9. Retrieved from http://www.ncbi.nlm.nih.gov/pubmed/10655541

Moreau, C., Devos, D., Brunaud-Danel, V., Defebvre, L., Perez, T., Destée, A., … Just, N. (2006). Paradoxical response of VEGF expression to hypoxia in CSF of patients with ALS. *Journal of Neurology, Neurosurgery, and Psychiatry*, *77*(2), 255–7. http://doi.org/10.1136/jnnp.2005.070904

Murray, L. M., Beauvais, A., Gibeault, S., Courtney, N. L., & Kothary, R. (2015). Transcriptional profiling of differentially vulnerable motor neurons at pre-symptomatic stage in the Smn (2b/-) mouse model of spinal muscular atrophy. *Acta Neuropathologica Communications*, *3*, 55. http://doi.org/10.1186/s40478-015-0231-1

Murray, L. M., Comley, L. H., Gillingwater, T. H., & Parson, S. H. (2011). The response of neuromuscular junctions to injury is developmentally regulated. *FASEB Journal : Official Publication of the Federation of American Societies for Experimental Biology*, *25*(4), 1306–13. http://doi.org/10.1096/fj.10-171934

Murray, L. M., Comley, L. H., Thomson, D., Parkinson, N., Talbot, K., & Gillingwater, T. H. (2008). Selective vulnerability of motor neurons and dissociation of pre- and post-synaptic pathology at the neuromuscular junction in mouse models of spinal muscular atrophy. *Human Molecular Genetics*, *17*(7), 949–62. http://doi.org/10.1093/hmg/ddm367

Mutsaers, C. A., Lamont, D. J., Hunter, G., Wishart, T. M., & Gillingwater, T. H. (2013). Label-free proteomics identifies Calreticulin and GRP75/Mortalin as peripherally accessible protein biomarkers for spinal muscular atrophy. *Genome Medicine*, *5*(10), 95. http://doi.org/10.1186/gm498

Mutsaers, C. A., Wishart, T. M., Lamont, D. J., Riessland, M., Schreml, J., Comley, L. H., … Gillingwater, T. H. (2011). Reversible molecular pathology of skeletal muscle in spinal muscular atrophy. *Human Molecular Genetics*, *20*(22), 4334–44. http://doi.org/10.1093/hmg/ddr360

Narver, H. L., Kong, L., Burnett, B. G., Choe, D. W., Bosch-Marcé, M., Taye, A. A., … Sumner, C. J. (2008). Sustained improvement of spinal muscular atrophy mice treated with trichostatin A plus nutrition. *Annals of Neurology*, *64*(4), 465–70. http://doi.org/10.1002/ana.21449

Newbery, H. J., Gillingwater, T. H., Dharmasaroja, P., Peters, J., Wharton, S. B., Thomson, D., … Abbott, C. M. (2005). Progressive loss of motor neuron function in wasted mice: effects of a spontaneous null mutation in the gene for the eEF1 A2 translation factor. *Journal of Neuropathology and Experimental Neurology*, *64*(4), 295–303. Retrieved from http://www.ncbi.nlm.nih.gov/pubmed/15835265

Niki, T., Takahashi-Niki, K., Taira, T., Iguchi-Ariga, S. M. M., & Ariga, H. (2003). DJBP: a novel DJ-1-binding protein, negatively regulates the androgen receptor by recruiting histone deacetylase complex, and DJ-1 antagonizes this inhibition by abrogation of this complex. *Molecular Cancer Research : MCR*, *1*(4), 247–61. Retrieved from http://www.ncbi.nlm.nih.gov/pubmed/12612053

Osoegawa, K., Tateno, M., Woon, P. Y., Frengen, E., Mammoser, A. G., Catanese, J. J., … de Jong, P. J. (2000). Bacterial artificial chromosome libraries for mouse sequencing and functional analysis. *Genome Research*, *10*(1), 116–28. Retrieved from http://www.ncbi.nlm.nih.gov/pubmed/10645956

Owen, N., Doe, C. L., Mellor, J., & Davies, K. E. (2000). Characterization of the Schizosaccharomyces pombe orthologue of the human survival motor neuron (SMN) protein. *Human Molecular Genetics*, *9*(5), 675–84. Retrieved from http://www.ncbi.nlm.nih.gov/pubmed/10749974

Park, J., Lee, S. B., Lee, S., Kim, Y., Song, S., Kim, S., … Chung, J. (2006). Mitochondrial dysfunction in Drosophila PINK1 mutants is complemented by parkin. *Nature*, *441*(7097), 1157–61. http://doi.org/10.1038/nature04788

Passini, M. A., Bu, J., Richards, A. M., Kinnecom, C., Sardi, S. P., Stanek, L. M., … Cheng, S. H. (2011). Antisense oligonucleotides delivered to the mouse CNS ameliorate symptoms of severe spinal muscular atrophy. *Science Translational Medicine*, *3*(72), 72ra18. http://doi.org/10.1126/scitranslmed.3001777

Pearn, J. (1978). Incidence, prevalence, and gene frequency studies of chronic childhood spinal muscular atrophy. *Journal of Medical Genetics*, *15*(6), 409–13. Retrieved from http://www.ncbi.nlm.nih.gov/pubmed/745211

Perry, V. H., Brown, M. C., & Tsao, J. W. (1992). The Effectiveness of the Gene Which Slows the Rate of Wallerian Degeneration in C57BL/Ola Mice Declines With Age. *The European Journal of Neuroscience*, *4*(10), 1000–2. Retrieved from http://www.ncbi.nlm.nih.gov/pubmed/12106435

Piazzon, N., Rage, F., Schlotter, F., Moine, H., Branlant, C., & Massenet, S. (2008). In vitro and in cellulo evidences for association of the survival of motor neuron complex with the fragile X mental retardation protein. *The Journal of Biological Chemistry*, *283*(9), 5598–610. http://doi.org/10.1074/jbc.M707304200

Pollin, M. M., McHanwell, S., & Slater, C. R. (1991). The effect of age on motor neurone death following axotomy in the mouse. *Development (Cambridge, England)*, *112*(1), 83–9. Retrieved from http://www.ncbi.nlm.nih.gov/pubmed/1769343

Porensky, P. N., Mitrpant, C., McGovern, V. L., Bevan, A. K., Foust, K. D., Kaspar, B. K., … Burghes, A. H. M. (2012). A single administration of morpholino antisense oligomer rescues spinal muscular atrophy in mouse. *Human Molecular Genetics*, *21*(7), 1625–38. http://doi.org/10.1093/hmg/ddr600

Poueymirou, W. T., Auerbach, W., Frendewey, D., Hickey, J. F., Escaravage, J. M., Esau, L., … Valenzuela, D. M. (2007). F0 generation mice fully derived from gene-targeted embryonic stem cells allowing immediate phenotypic analyses. *Nature Biotechnology*, *25*(1), 91–9. http://doi.org/10.1038/nbt1263

Powis, R. A., Karyka, E., Boyd, P., Côme, J., Jones, R. A., Zheng, Y., … Hua, Y. (2016). Systemic restoration of UBA1 ameliorates disease in spinal muscular atrophy. *JCI Insight*, *1*(11), 409–413. http://doi.org/10.1172/jci.insight.87908

Prior, T. W., Krainer, A. R., Hua, Y., Swoboda, K. J., Snyder, P. C., Bridgeman, S. J., … Kissel, J. T. (2009). *A Positive Modifier of Spinal Muscular Atrophy in the SMN2 Gene*. *The American Journal of Human Genetics* (Vol. 85). http://doi.org/10.1016/j.ajhg.2009.08.002

Ribchester, R. R., Tsao ', J. W., Barry, J. A., Asgari-Jirhandeh, N., Perry ', V. H., & Brown2, M. C. (1995). Persistence of Neuromuscular Junctions after Axotomy in Mice with Slow Wallerian Degeneration (C57BLM/ldS). *European Journal of Neuroscience*, *7*, 1641–1650.

Riessland, M., Brichta, L., Hahnen, E., & Wirth, B. (2006). The benzamide M344, a novel histone deacetylase inhibitor, significantly increases SMN2 RNA/protein levels in spinal muscular atrophy cells. *Human Genetics*, *120*(1), 101–10. http://doi.org/10.1007/s00439-006-0186-1

Robbins, K. L., Glascock, J. J., Osman, E. Y., Miller, M. R., & Lorson, C. L. (2014). Defining the therapeutic window in a severe animal model of spinal muscular atrophy. *Human Molecular Genetics*, *23*(17), 4559–68. http://doi.org/10.1093/hmg/ddu169

Rochette, C. F., Gilbert, N., & Simard, L. R. (2001). SMN gene duplication and the emergence of the SMN2 gene occurred in distinct hominids: SMN2 is unique to Homo sapiens. *Human Genetics*, *108*(3), 255–66. Retrieved from http://www.ncbi.nlm.nih.gov/pubmed/11354640

Rossoll, W., Jablonka, S., Andreassi, C., Kröning, A.-K., Karle, K., Monani, U. R., & Sendtner, M. (2003). Smn, the spinal muscular atrophy-determining gene product, modulates axon growth and localization of beta-actin mRNA in growth cones of motoneurons. *The Journal of Cell Biology*, *163*(4), 801–12. http://doi.org/10.1083/jcb.200304128

Rudnik-Schöneborn, S., Vogelgesang, S., Armbrust, S., Graul-Neumann, L., Fusch, C., & Zerres, K. (2010). Digital necroses and vascular thrombosis in severe spinal muscular atrophy. *Muscle & Nerve*, *42*(1), 144–7. http://doi.org/10.1002/mus.21654

Russman, B. S. (2007). Spinal muscular atrophy: clinical classification and disease heterogeneity. *Journal of Child Neurology*, *22*(8), 946–51. http://doi.org/10.1177/0883073807305673

Saunders, K. C., Louis, D. L., Weingarden, S. I., & Waylonis, G. W. (1979). Effect of tourniquet time on postoperative quadriceps function. *Clinical Orthopaedics and Related Research*, (143), 194–9. Retrieved from http://www.ncbi.nlm.nih.gov/pubmed/509826

Schapira, A., Cooper, J. M., Dexter, D., Jenner, P., Clark, J. B., & Marsden, C. D. (1989). MITOCHONDRIAL COMPLEX I DEFICIENCY IN PARKINSON'S DISEASE. *The Lancet*, *333*(8649), 1269. http://doi.org/10.1016/S0140-6736(89)92366-0

Schrank, B., Götz, R., Gunnersen, J. M., Ure, J. M., Toyka, K. V, Smith, A. G., & Sendtner, M. (1997). Inactivation of the survival motor neuron gene, a candidate gene for human spinal muscular atrophy, leads to massive cell death in early mouse embryos. *Proceedings of the National Academy of Sciences of the United States of America*, *94*(18), 9920–5. Retrieved from http://www.ncbi.nlm.nih.gov/pubmed/9275227

Shababi, M., Habibi, J., Yang, H. T., Vale, S. M., Sewell, W. A., & Lorson, C. L. (2010). Cardiac defects contribute to the pathology of spinal muscular atrophy models. *Human Molecular Genetics*, *19*(20), 4059–71. http://doi.org/10.1093/hmg/ddq329

Shendelman, S., Jonason, A., Martinat, C., Leete, T., & Abeliovich, A. (2004). DJ-1 is a redox-dependent molecular chaperone that inhibits alpha-synuclein aggregate formation. *PLoS Biology*, *2*(11), e362. http://doi.org/10.1371/journal.pbio.0020362

Shishikura, K., Hara, M., Sasaki, Y., & Misugi, K. (1983). A neuropathologic study of Werdnig-Hoffmann disease with special reference to the thalamus and posterior roots. *Acta Neuropathologica*, *60*(1-2), 99–106. Retrieved from http://www.ncbi.nlm.nih.gov/pubmed/6880628

Shorrock, H. K., & Gillingwater, T. H. (2016). Development and translation of therapies for spinal muscular atrophy. *Citation: EMJ Neurol*, *4*(1), 64–73.

Shpargel, K. B., & Matera, A. G. (2005). Gemin proteins are required for efficient assembly of Sm-class ribonucleoproteins. *Proceedings of the National Academy of Sciences of the United States of America*, *102*(48), 17372–7. http://doi.org/10.1073/pnas.0508947102

Singh, N. K., Singh, N. N., Androphy, E. J., & Singh, R. N. (2006). Splicing of a critical exon of human Survival Motor Neuron is regulated by a unique silencer element located in the last intron. *Molecular and Cellular Biology*, *26*(4), 1333–46. http://doi.org/10.1128/MCB.26.4.1333-1346.2006

So, B. R., Wan, L., Zhang, Z., Li, P., Babiash, E., Duan, J., … Dreyfuss, G. (2016). A U1 snRNP-specific assembly pathway reveals the SMN complex as a versatile hub for RNP exchange. *Nature Structural & Molecular Biology*, *23*(3), 225–30. http://doi.org/10.1038/nsmb.3167

Somers, E., Lees, R. D., Hoban, K., Sleigh, J. N., Zhou, H., Muntoni, F., … Parson, S. H. (2016). Vascular Defects and Spinal Cord Hypoxia in Spinal Muscular Atrophy. *Annals of Neurology*, *79*(2), 217–30. http://doi.org/10.1002/ana.24549

Somers, E., Riessland, M., Schreml, J., Wirth, B., Gillingwater, T. H., & Parson, S. H. (2013). *Increasing SMN levels using the histone deacetylase inhibitor SAHA ameliorates defects in skeletal muscle microvasculature in a mouse model of severe spinal muscular atrophy*. *Neuroscience Letters* (Vol. 544). http://doi.org/10.1016/j.neulet.2013.03.052

Soubrouillard, C., Pellissier, J. F., Lepidi, H., Mancini, J., Rougon, G., & Figarella-Branger, D. (1995). Expression of developmentally regulated cytoskeleton and cell surface proteins in childhood spinal muscular atrophies. *Journal of the Neurological Sciences*, *133*(1), 155–163. http://doi.org/10.1016/0022-510X(95)00182-2

Sugarman, E. A., Nagan, N., Zhu, H., Akmaev, V. R., Zhou, Z., Rohlfs, E. M., … Allitto, B. A. (2012). Pan-ethnic carrier screening and prenatal diagnosis for spinal muscular atrophy: clinical laboratory analysis of >72,400 specimens. *European Journal of Human Genetics : EJHG*, *20*(1), 27–32. http://doi.org/10.1038/ejhg.2011.134

Sumner, C. J., Huynh, T. N., Markowitz, J. A., Perhac, J. S., Hill, B., Coovert, D. D., … Fischbeck, K. H. (2003). Valproic acid increases SMN levels in spinal muscular atrophy patient cells. *Annals of Neurology*, *54*(5), 647–54. http://doi.org/10.1002/ana.10743

Sun, Y., Grimmler, M., Schwarzer, V., Schoenen, F., Fischer, U., & Wirth, B. (2005). Molecular and functional analysis of intragenic SMN1 mutations in patients with spinal muscular atrophy. *Human Mutation*, *25*(1), 64–71. http://doi.org/10.1002/humu.20111

Swoboda, K. J., Prior, T. W., Scott, C. B., McNaught, T. P., Wride, M. C., Reyna, S. P., & Bromberg, M. B. (2005). Natural history of denervation in SMA: relation to age, SMN2 copy number, and function. *Annals of Neurology*, *57*(5), 704–12. http://doi.org/10.1002/ana.20473

Swoboda, K. J., Scott, C. B., Crawford, T. O., Simard, L. R., Reyna, S. P., Krosschell, K. J., … Network, for the P. C. S. M. A. I. (2010). SMA CARNI-VAL Trial Part I: Double-Blind, Randomized, Placebo-Controlled Trial of L-Carnitine and Valproic Acid in Spinal Muscular Atrophy. *PLoS ONE*, *5*(8), e12140. http://doi.org/10.1371/journal.pone.0012140

Takahashi, K., Taira, T., Niki, T., Seino, C., Iguchi-Ariga, S. M., & Ariga, H. (2001). DJ-1 positively regulates the androgen receptor by impairing the binding of PIASx alpha to the receptor. *The Journal of Biological Chemistry*, *276*(40), 37556–63. http://doi.org/10.1074/jbc.M101730200

Talbot, K., Ponting, C. P., Theodosiou, A. M., Rodrigues, N. R., Surtees, R., Mountford, R., & Davies, K. E. (1997). Missense mutation clustering in the survival motor neuron gene: a role for a conserved tyrosine and glycine rich region of the protein in RNA metabolism? *Human Molecular Genetics*, *6*(3), 497–500. Retrieved from http://www.ncbi.nlm.nih.gov/pubmed/9147655

Thomson, S. R., Nahon, J. E., Mutsaers, C. A., Thomson, D., Hamilton, G., Parson, S. H., & Gillingwater, T. H. (2012). Morphological characteristics of motor neurons do not determine their relative susceptibility to degeneration in a mouse model of severe spinal muscular atrophy. *PloS One*, *7*(12), e52605. http://doi.org/10.1371/journal.pone.0052605

Trinh, H. V, Grossmann, J., Gehrig, P., Roschitzki, B., Schlapbach, R., Greber, U. F., & Hemmi, S. (2013). iTRAQ-Based and Label-Free Proteomics Approaches for Studies of Human Adenovirus Infections. *International Journal of Proteomics*, *2013*, 581862. http://doi.org/10.1155/2013/581862

Valenzuela, D. M., Murphy, A. J., Frendewey, D., Gale, N. W., Economides, A. N., Auerbach, W., … Yancopoulos, G. D. (2003). High-throughput engineering of the mouse genome coupled with high-resolution expression analysis. *Nature Biotechnology*, *21*(6), 652–9. http://doi.org/10.1038/nbt822

Van Meerbeke, J. P., Gibbs, R. M., Plasterer, H. L., Miao, W., Feng, Z., Lin, M.-Y., … Sumner, C. J. (2013). The DcpS inhibitor RG3039 improves motor function in SMA mice. *Human Molecular Genetics*, *22*(20), 4074–83. http://doi.org/10.1093/hmg/ddt257

Villegas, R., Martinez, N. W., Lillo, J., Pihan, P., Hernandez, D., Twiss, J. L., & Court, F. A. (2014). Calcium Release from Intra-Axonal Endoplasmic Reticulum Leads to Axon Degeneration through Mitochondrial Dysfunction. *Journal of Neuroscience*, *34*(21), 7179–7189. http://doi.org/10.1523/JNEUROSCI.4784-13.2014

Waller, A. (1850). Experiments on the Section of the Glossopharyngeal and Hypoglossal Nerves of the Frog, and Observations of the Alterations Produced Thereby in the Structure of Their Primitive Fibres. *Philosophical Transactions of the Royal Society of London*, *140*(0), 423–429. http://doi.org/10.1098/rstl.1850.0021

Wan, L., Battle, D. J., Yong, J., Gubitz, A. K., Kolb, S. J., Wang, J., & Dreyfuss, G. (2005). The survival of motor neurons protein determines the capacity for snRNP assembly: biochemical deficiency in spinal muscular atrophy. *Molecular and Cellular Biology*, *25*(13), 5543–51. http://doi.org/10.1128/MCB.25.13.5543-5551.2005

Wang, M. S., Davis, A. A., Culver, D. G., & Glass, J. D. (2002). WldS mice are resistant to paclitaxel (taxol) neuropathy. *Annals of Neurology*, *52*(4), 442–7. http://doi.org/10.1002/ana.10300

Wang, M. S., Fang, G., Culver, D. G., Davis, A. A., Rich, M. M., & Glass, J. D. (2001). The WldS protein protects against axonal degeneration: a model of gene therapy for peripheral neuropathy. *Annals of Neurology*, *50*(6), 773–9. Retrieved from http://www.ncbi.nlm.nih.gov/pubmed/11761475

Wang, M.-S., Wu, Y., Culver, D. G., & Glass, J. D. (2001). The Gene for Slow Wallerian Degeneration (Wlds) Is Also Protective against Vincristine Neuropathy. *Neurobiology of Disease*, *8*(1), 155–161. http://doi.org/10.1006/nbdi.2000.0334

Wang, W., Wang, L., Lu, J., Siedlak, S. L., Fujioka, H., Liang, J., … Wang, X. (2016). The inhibition of TDP-43 mitochondrial localization blocks its neuronal toxicity. *Nature Medicine*, *22*(8), 869–878. http://doi.org/10.1038/nm.4130

Wang, X., Anderson, G. A., Smith, R. D., & Dabney, A. R. (2012). A hybrid approach to protein differential expression in mass spectrometry-based proteomics. *Bioinformatics (Oxford, England)*, *28*(12), 1586–91. http://doi.org/10.1093/bioinformatics/bts193

Watzlawik, J. O., Kahoud, R. J., O'Toole, R. J., White, K. A. M., Ogden, A. R., Painter, M. M., … Rodriguez, M. (2015). Abbreviated exposure to hypoxia is sufficient to induce CNS dysmyelination, modulate spinal motor neuron composition, and impair motor development in neonatal mice. *PloS One*, *10*(5), e0128007. http://doi.org/10.1371/journal.pone.0128007

Werle, M. J., & Herrera, A. A. (1991). Elevated levels of polyneuronal innervation persist for as long as two years in reinnervated frog neuromuscular junctions. *Journal of Neurobiology*, *22*(1), 97–103. http://doi.org/10.1002/neu.480220110

Williams, J. H., Schray, R. C., Patterson, C. A., Ayitey, S. O., Tallent, M. K., & Lutz, G. J. (2009). Oligonucleotide-mediated survival of motor neuron protein expression in CNS improves phenotype in a mouse model of spinal muscular atrophy. *The Journal of Neuroscience : The Official Journal of the Society for Neuroscience*, *29*(24), 7633–8. http://doi.org/10.1523/JNEUROSCI.0950-09.2009

Winkler, C., Eggert, C., Gradl, D., Meister, G., Giegerich, M., Wedlich, D., … Fischer, U. (2005). Reduced U snRNP assembly causes motor axon degeneration in an animal model for spinal muscular atrophy. *Genes & Development*, *19*(19), 2320–30. http://doi.org/10.1101/gad.342005

Wishart, T. M., Huang, J. P.-W., Murray, L. M., Lamont, D. J., Mutsaers, C. A., Ross, J., … Gillingwater, T. H. (2010). SMN deficiency disrupts brain development in a mouse model of severe spinal muscular atrophy. *Human Molecular Genetics*, *19*(21), 4216–28. http://doi.org/10.1093/hmg/ddq340

Wishart, T. M., Mutsaers, C. A., Riessland, M., Reimer, M. M., Hunter, G., Hannam, M. L., … Gillingwater, T. H. (2014). Dysregulation of ubiquitin homeostasis and β-catenin signaling promote spinal muscular atrophy. *The Journal of Clinical Investigation*, *124*(4), 1821–34. http://doi.org/10.1172/JCI71318

Wishart, T. M., Rooney, T. M., Lamont, D. J., Wright, A. K., Morton, A. J., Jackson, M., … Gillingwater, T. H. (2012). Combining comparative proteomics and molecular genetics uncovers regulators of synaptic and axonal stability and degeneration in vivo. *PLoS Genetics*, *8*(8), e1002936. http://doi.org/10.1371/journal.pgen.1002936

Workman, E., Saieva, L., Carrel, T. L., Crawford, T. O., Liu, D., Lutz, C., … Burghes, A. H. M. (2009). A SMN missense mutation complements SMN2 restoring snRNPs and rescuing SMA mice. *Human Molecular Genetics*, *18*(12), 2215–29. http://doi.org/10.1093/hmg/ddp157

Yao, J., Irwin, R. W., Zhao, L., Nilsen, J., Hamilton, R. T., & Brinton, R. D. (2009). Mitochondrial bioenergetic deficit precedes Alzheimer's pathology in female mouse model of Alzheimer's disease. *Proceedings of the National Academy of Sciences*, *106*(34), 14670–14675. http://doi.org/10.1073/pnas.0903563106

Yin, X., Manczak, M., & Reddy, P. H. (2016). Mitochondria-targeted molecules MitoQ and SS31 reduce mutant huntingtin-induced mitochondrial toxicity and synaptic damage in Huntington's disease. *Human Molecular Genetics*, *25*(9), 1739–53. http://doi.org/10.1093/hmg/ddw045

Yokota, T., Sugawara, K., Ito, K., Takahashi, R., Ariga, H., & Mizusawa, H. (2003). Down regulation of DJ-1 enhances cell death by oxidative stress, ER stress, and proteasome inhibition. *Biochemical and Biophysical Research Communications*, *312*(4), 1342–1348. http://doi.org/10.1016/j.bbrc.2003.11.056

Yong, J., Kasim, M., Bachorik, J. L., Wan, L., & Dreyfuss, G. (2010). Gemin5 Delivers snRNA Precursors to the SMN Complex for snRNP Biogenesis. *Molecular Cell*, *38*(4), 551–562. http://doi.org/10.1016/j.molcel.2010.03.014

Young, P. J., Le, T. T., thi Man, N., Burghes, A. H. M., & Morris, G. E. (2000). The Relationship between SMN, the Spinal Muscular Atrophy Protein, and Nuclear Coiled Bodies in Differentiated Tissues and Cultured Cells. *Experimental Cell Research*, *256*(2), 365–374. http://doi.org/10.1006/excr.2000.4858

Young, P. J., Man, N. T., Lorson, C. L., Le, T. T., Androphy, E. J., Burghes, A. H., & Morris, G. E. (2000). The exon 2b region of the spinal muscular atrophy protein, SMN, is involved in self-association and SIP1 binding. *Human Molecular Genetics*, *9*(19), 2869–77. Retrieved from http://www.ncbi.nlm.nih.gov/pubmed/11092763

Zhang, Z., Lotti, F., Dittmar, K., Younis, I., Wan, L., Kasim, M., & Dreyfuss, G. (2008). SMN Deficiency Causes Tissue-Specific Perturbations in the Repertoire of snRNAs and Widespread Defects in Splicing. *Cell*, *133*(4), 585–600. http://doi.org/10.1016/j.cell.2008.03.031

Zhang, Z., Pinto, A. M., Wan, L., Wang, W., Berg, M. G., Oliva, I., … Dreyfuss, G. (2013). Dysregulation of synaptogenesis genes antecedes motor neuron pathology in spinal muscular atrophy. *Proceedings of the National Academy of Sciences of the United States of America*, *110*(48), 19348–53. http://doi.org/10.1073/pnas.1319280110

Appendix 1

Supplementary Table 1a: Top 50 proteins exhibiting increased expression between P12-P24 in the sciatic nerve

	Description	P24/P12 ratio
P07759	Serine protease inhibitor A3K OS=Mus musculus GN=Serpina3k PE=1 SV=2 - [SPA3K_MOUSE]	9.230
Q08331	Calretinin OS=Mus musculus GN=Calb2 PE=1 SV=3 - [CALB2_MOUSE]	7.448
Q8VCT4	Carboxylesterase 1D OS=Mus musculus GN=Ces1d PE=1 SV=1 - [CES1D_MOUSE]	5.279
P28665	Murinoglobulin-1 OS=Mus musculus GN=Mug1 PE=1 SV=3 - [MUG1_MOUSE]	5.244
P31428	Dipeptidase 1 OS=Mus musculus GN=Dpep1 PE=1 SV=2 - [DPEP1_MOUSE]	4.385
O54786-2	Isoform ICAD-S of DNA fragmentation factor subunit alpha OS=Mus musculus GN=Dffa - [DFFA_MOUSE]	3.647
Q9WU63	Heme-binding protein 2 OS=Mus musculus GN=Hebp2 PE=1 SV=1 - [HEBP2_MOUSE]	3.632
P00329	Alcohol dehydrogenase 1 OS=Mus musculus GN=Adh1 PE=2 SV=2 - [ADH1_MOUSE]	3.073
P47880	Insulin-like growth factor-binding protein 6 OS=Mus musculus GN=Igfbp6 PE=2 SV=2 - [IBP6_MOUSE]	2.986
P24549	Retinal dehydrogenase 1 OS=Mus musculus GN=Aldh1a1 PE=1 SV=5 - [AL1A1_MOUSE]	2.835
Q91V77	Protein S100-A1 OS=Mus musculus GN=S100a1 PE=4 SV=1 - [Q91V77_MOUSE]	2.566
P50114	Protein S100-B OS=Mus musculus GN=S100b PE=2 SV=2 - [S100B_MOUSE]	2.557
P09470	Angiotensin-converting enzyme OS=Mus musculus GN=Ace PE=1 SV=3 - [ACE_MOUSE]	2.525
A2AG50	MAP7 domain-containing protein 2 OS=Mus musculus GN=Map7d2 PE=1 SV=1 - [MA7D2_MOUSE]	2.507
P23953	Carboxylesterase 1C OS=Mus musculus GN=Ces1c PE=1 SV=4 - [EST1C_MOUSE]	2.452
P0C7M9	C-type lectin domain family 2 member L OS=Mus musculus GN=Clec2l PE=2 SV=1 - [CLC2L_MOUSE]	2.412
Q05AA6	Dystrophin-related protein 2 OS=Mus musculus GN=Drp2 PE=1 SV=1 - [DRP2_MOUSE]	2.391

P21447	Multidrug resistance protein 1A OS=Mus musculus GN=Abcb1a PE=1 SV=3 - [MDR1A_MOUSE]	2.378
D3YXJ9	MCG51871 OS=Mus musculus GN=Cldn24 PE=4 SV=1 - [D3YXJ9_MOUSE]	2.313
P19246	Neurofilament heavy polypeptide OS=Mus musculus GN=Nefh PE=1 SV=3 - [NFH_MOUSE]	2.310
P51910	Apolipoprotein D OS=Mus musculus GN=Apod PE=2 SV=1 - [APOD_MOUSE]	2.300
Q00519	Xanthine dehydrogenase/oxidase OS=Mus musculus GN=Xdh PE=1 SV=5 - [XDH_MOUSE]	2.299
D3Z2P8	Sulfotransferase 1A1 (Fragment) OS=Mus musculus GN=Sult1a1 PE=2 SV=1 - [D3Z2P8_MOUSE]	2.298
Q9WU79	Proline dehydrogenase 1, mitochondrial OS=Mus musculus GN=Prodh PE=2 SV=2 - [PROD_MOUSE]	2.288
Q5SVE1	Disintegrin and metalloproteinase domain-containing protein 23 OS=Mus musculus GN=Adam23 PE=2 SV=1 - [Q5SVE1_MOUSE]	2.264
B1AYL1	Protein Scn7a OS=Mus musculus GN=Scn7a PE=2 SV=1 - [B1AYL1_MOUSE]	2.260
Q8R0Y6	Cytosolic 10-formyltetrahydrofolate dehydrogenase OS=Mus musculus GN=Aldh1l1 PE=2 SV=1 - [AL1L1_MOUSE]	2.241
Q8K406	Leucine-rich repeat LGI family member 3 OS=Mus musculus GN=Lgi3 PE=1 SV=1 - [LGI3_MOUSE]	2.235
P14602	Heat shock protein beta-1 OS=Mus musculus GN=Hspb1 PE=1 SV=3 - [HSPB1_MOUSE]	2.204
P24288	Branched-chain-amino-acid aminotransferase, cytosolic OS=Mus musculus GN=Bcat1 PE=2 SV=2 - [BCAT1_MOUSE]	2.148
F6X0U1	Acyl-coenzyme A thioesterase THEM5 (Fragment) OS=Mus musculus GN=Them5 PE=2 SV=1 - [F6X0U1_MOUSE]	2.128
Q9R1Q8	Transgelin-3 OS=Mus musculus GN=Tagln3 PE=1 SV=1 - [TAGL3_MOUSE]	2.114
P06801	NADP-dependent malic enzyme OS=Mus musculus GN=Me1 PE=1 SV=2 - [MAOX_MOUSE]	2.091
Q9R0P9	Ubiquitin carboxyl-terminal hydrolase isozyme L1 OS=Mus musculus GN=Uchl1 PE=1 SV=1 - [UCHL1_MOUSE]	2.024
E0CXZ9	Voltage-gated potassium channel subunit beta-2 OS=Mus musculus GN=Kcnab2 PE=2 SV=1 - [E0CXZ9_MOUSE]	1.987
P15105	Glutamine synthetase OS=Mus musculus GN=Glul PE=1 SV=6 - [GLNA_MOUSE]	1.975
P17809	Solute carrier family 2, facilitated glucose transporter member 1 OS=Mus musculus GN=Slc2a1 PE=1 SV=4 - [GTR1_MOUSE]	1.965
Q8BQV2	Choline O-acetyltransferase OS=Mus musculus GN=Chat PE=2 SV=1 - [Q8BQV2_MOUSE]	1.964

P16388	Potassium voltage-gated channel subfamily A member 1 OS=Mus musculus GN=Kcna1 PE=2 SV=1 - [KCNA1_MOUSE]	1.955
Q64669	NAD(P)H dehydrogenase [quinone] 1 OS=Mus musculus GN=Nqo1 PE=1 SV=3 - [NQO1_MOUSE]	1.932
Q9JHW9	Aldehyde dehydrogenase family 1 member A3 OS=Mus musculus GN=Aldh1a3 PE=2 SV=1 - [AL1A3_MOUSE]	1.898
Q2VLH6	Scavenger receptor cysteine-rich type 1 protein M130 OS=Mus musculus GN=Cd163 PE=1 SV=2 - [C163A_MOUSE]	1.895
Q3UPR9	Somatomedin-B and thrombospondin type-1 domain-containing protein OS=Mus musculus GN=Sbspon PE=2 SV=1 - [SBSPO_MOUSE]	1.890
P47867	Secretogranin-3 OS=Mus musculus GN=Scg3 PE=1 SV=1 - [SCG3_MOUSE]	1.889
Q61644	Protein kinase C and casein kinase substrate in neurons protein 1 OS=Mus musculus GN=Pacsin1 PE=1 SV=1 - [PACN1_MOUSE]	1.887
P68368	Tubulin alpha-4A chain OS=Mus musculus GN=Tuba4a PE=1 SV=1 - [TBA4A_MOUSE]	1.879
F6TMY4	Protein Sptbn5 (Fragment) OS=Mus musculus GN=Sptbn5 PE=4 SV=1 - [F6TMY4_MOUSE]	1.866
Q8R1G2	Carboxymethylenebutenolidase homolog OS=Mus musculus GN=Cmbl PE=2 SV=1 - [CMBL_MOUSE]	1.857
P10649	Glutathione S-transferase Mu 1 OS=Mus musculus GN=Gstm1 PE=1 SV=2 - [GSTM1_MOUSE]	1.852
Q8CGA4	UPF0452 protein C7orf41 homolog OS=Mus musculus PE=2 SV=1 - [CG041_MOUSE]	1.836

Supplementary Table 1b: Top 50 proteins exhibiting decreased expression between P12-P24 in the sciatic nerve

Accession	Description	P24/P12 Ratio
P02772	Alpha-fetoprotein OS=Mus musculus GN=Afp PE=2 SV=1 - [FETA_MOUSE]	0.128
P70180	Atrial natriuretic peptide receptor 3 OS=Mus musculus GN=Npr3 PE=1 SV=3 - [ANPRC_MOUSE]	0.331
P09535	Insulin-like growth factor II OS=Mus musculus GN=Igf2 PE=1 SV=1 - [IGF2_MOUSE]	0.359
G5E832	Adenomatosis polyposis coli 2 OS=Mus musculus GN=Apc2 PE=4 SV=1 - [G5E832_MOUSE]	0.396
P49718	DNA replication licensing factor MCM5 OS=Mus musculus GN=Mcm5 PE=2 SV=1 - [MCM5_MOUSE]	0.397
Q61881	DNA replication licensing factor MCM7 OS=Mus musculus GN=Mcm7 PE=2 SV=1 - [MCM7_MOUSE]	0.398
P03987-2	Isoform 2 of Ig gamma-3 chain C region OS=Mus musculus - [IGHG3_MOUSE]	0.421
Q61576	Peptidyl-prolyl cis-trans isomerase FKBP10 OS=Mus musculus GN=Fkbp10 PE=1 SV=2 - [FKB10_MOUSE]	0.431
Q3V1T4	Prolyl 3-hydroxylase 1 OS=Mus musculus GN=Lepre1 PE=2 SV=2 - [P3H1_MOUSE]	0.443
P08121	Collagen alpha-1(III) chain OS=Mus musculus GN=Col3a1 PE=2 SV=4 - [CO3A1_MOUSE]	0.443
Q8BKG3	Inactive tyrosine-protein kinase 7 OS=Mus musculus GN=Ptk7 PE=1 SV=1 - [PTK7_MOUSE]	0.443
Q61500	Integral membrane protein 2A OS=Mus musculus GN=Itm2a PE=2 SV=2 - [ITM2A_MOUSE]	0.472
P11276	Fibronectin OS=Mus musculus GN=Fn1 PE=1 SV=4 - [FINC_MOUSE]	0.490
Q8CG70	Prolyl 3-hydroxylase 3 OS=Mus musculus GN=Leprel2 PE=2 SV=1 - [P3H3_MOUSE]	0.512
Q91VK1	Basic leucine zipper and W2 domain-containing protein 2 OS=Mus musculus GN=Bzw2 PE=1 SV=1 - [BZW2_MOUSE]	0.513
Q9CY57-5	Isoform 5 of Chromatin target of PRMT1 protein OS=Mus musculus GN=Chtop - [CHTOP_MOUSE]	0.514
Q922W5	Pyrroline-5-carboxylate reductase 1, mitochondrial OS=Mus musculus GN=Pycr1 PE=1 SV=1 - [P5CR1_MOUSE]	0.516
Q921X9	Protein disulfide-isomerase A5 OS=Mus musculus GN=Pdia5 PE=2 SV=1 - [PDIA5_MOUSE]	0.518
Q9DCC1	RNA guanylyltransferase and 5'-phosphatase, isoform CRA_a OS=Mus musculus GN=Rngtt PE=2 SV=1 - [Q9DCC1_MOUSE]	0.520
Q8BMK4	Cytoskeleton-associated protein 4 OS=Mus musculus GN=Ckap4 PE=2 SV=2 - [CKAP4_MOUSE]	0.525

Q8C4J7	Transducin beta-like protein 3 OS=Mus musculus GN=Tbl3 PE=2 SV=1 - [TBL3_MOUSE]	0.527
P30412	Peptidyl-prolyl cis-trans isomerase C OS=Mus musculus GN=Ppic PE=1 SV=1 - [PPIC_MOUSE]	0.532
Q61555	Fibrillin-2 OS=Mus musculus GN=Fbn2 PE=1 SV=2 - [FBN2_MOUSE]	0.535
Q99LJ6	Glutathione peroxidase 7 OS=Mus musculus GN=Gpx7 PE=2 SV=1 - [GPX7_MOUSE]	0.539
E9QMH7	Inhibitor of nuclear factor kappa-B kinase-interacting protein OS=Mus musculus GN=Ikbip PE=2 SV=1 - [E9QMH7_MOUSE]	0.545
Q07113	Cation-independent mannose-6-phosphate receptor OS=Mus musculus GN=Igf2r PE=1 SV=1 - [MPRI_MOUSE]	0.550
D3YVW2	Golgi integral membrane protein 4 OS=Mus musculus GN=Golim4 PE=2 SV=1 - [D3YVW2_MOUSE]	0.561
O89086	Putative RNA-binding protein 3 OS=Mus musculus GN=Rbm3 PE=1 SV=1 - [RBM3_MOUSE]	0.561
P28667	MARCKS-related protein OS=Mus musculus GN=Marcksl1 PE=1 SV=2 - [MRP_MOUSE]	0.562
Q922Q8	Leucine-rich repeat-containing protein 59 OS=Mus musculus GN=Lrrc59 PE=2 SV=1 - [LRC59_MOUSE]	0.565
Q62148	Retinal dehydrogenase 2 OS=Mus musculus GN=Aldh1a2 PE=1 SV=2 - [AL1A2_MOUSE]	0.569
Q62009	Periostin OS=Mus musculus GN=Postn PE=1 SV=2 - [POSTN_MOUSE]	0.570
E9PWF0	Thrombospondin-3 OS=Mus musculus GN=Thbs3 PE=2 SV=1 - [E9PWF0_MOUSE]	0.571
Q3V1M1	Immunoglobulin superfamily member 10 OS=Mus musculus GN=Igsf10 PE=2 SV=2 - [IGS10_MOUSE]	0.572
Q9CQS8	Protein transport protein Sec61 subunit beta OS=Mus musculus GN=Sec61b PE=1 SV=3 - [SC61B_MOUSE]	0.573
Q9CY50	Translocon-associated protein subunit alpha OS=Mus musculus GN=Ssr1 PE=1 SV=1 - [SSRA_MOUSE]	0.575
Q9D1M7	Peptidyl-prolyl cis-trans isomerase FKBP11 OS=Mus musculus GN=Fkbp11 PE=2 SV=1 - [FKB11_MOUSE]	0.577
O35405	Phospholipase D3 OS=Mus musculus GN=Pld3 PE=2 SV=1 - [PLD3_MOUSE]	0.580
Q8C850	Scavenger receptor class A member 3 OS=Mus musculus GN=Scara3 PE=2 SV=1 - [SCAR3_MOUSE]	0.580
A2AAY5	SH3 and PX domain-containing protein 2B OS=Mus musculus GN=Sh3pxd2b PE=1 SV=1 - [SPD2B_MOUSE]	0.585
P27659	60S ribosomal protein L3 OS=Mus musculus GN=Rpl3 PE=2 SV=3 - [RL3_MOUSE]	0.588
Q9Z247	Peptidyl-prolyl cis-trans isomerase FKBP9 OS=Mus musculus GN=Fkbp9 PE=1 SV=1 - [FKBP9_MOUSE]	0.589
P61514	60S ribosomal protein L37a OS=Mus musculus GN=Rpl37a PE=2 SV=2 - [RL37A_MOUSE]	0.590

E9QKE9	Homeobox protein cut-like 1 OS=Mus musculus GN=Cux1 PE=2 SV=1 - [E9QKE9_MOUSE]	0.590
E9Q0X4	Collagen alpha-1(XVI) chain OS=Mus musculus GN=Col16a1 PE=2 SV=1 - [E9Q0X4_MOUSE]	0.593
Q8VE73-3	Isoform 2 of Cullin-7 OS=Mus musculus GN=Cul7 - [CUL7_MOUSE]	0.594
Q60716-2	Isoform IIa of Prolyl 4-hydroxylase subunit alpha-2 OS=Mus musculus GN=P4ha2 - [P4HA2_MOUSE]	0.598
Q8CEC6	Peptidylprolyl isomerase domain and WD repeat-containing protein 1 OS=Mus musculus GN=Ppwd1 PE=2 SV=2 - [PPWD1_MOUSE]	0.604
P62855	40S ribosomal protein S26 OS=Mus musculus GN=Rps26 PE=2 SV=3 - [RS26_MOUSE]	0.611
Q9D0F3	Protein ERGIC-53 OS=Mus musculus GN=Lman1 PE=2 SV=1 - [LMAN1_MOUSE]	0.616

Appendix 2

Supplementary Table 2a: Top 50 proteins exhibiting increased expression between P12-P24 in the lumbrical muscles

Accession	Description	P24/P12 Ratio
P07759	Serine protease inhibitor A3K OS=Mus musculus GN=Serpina3k PE=1 SV=2 - [SPA3K_MOUSE]	7.162
Q5XKE0	Myosin-binding protein C, fast-type OS=Mus musculus GN=Mybpc2 PE=1 SV=1 - [MYPC2_MOUSE]	5.143
P04247	Myoglobin OS=Mus musculus GN=Mb PE=1 SV=3 - [MYG_MOUSE]	4.596
P00329	Alcohol dehydrogenase 1 OS=Mus musculus GN=Adh1 PE=2 SV=2 - [ADH1_MOUSE]	4.484
Q9DBG1	Sterol 26-hydroxylase, mitochondrial OS=Mus musculus GN=Cyp27a1 PE=1 SV=1 - [CP27A_MOUSE]	4.229
Q5SX39	Myosin-4 OS=Mus musculus GN=Myh4 PE=1 SV=1 - [MYH4_MOUSE]	4.087
Q9CQC9	GTP-binding protein SAR1b OS=Mus musculus GN=Sar1b PE=1 SV=1 - [SAR1B_MOUSE]	3.820
G5E8K5-5	Isoform 5 of Ankyrin-3 OS=Mus musculus GN=Ank3 - [ANK3_MOUSE]	3.814
A2AI91	Phosphorylase b kinase regulatory subunit alpha, skeletal muscle isoform OS=Mus musculus GN=Phka1 PE=2 SV=1 - [A2AI91_MOUSE]	3.755
B2RS77	Ankyrin repeat domain 2 (Stretch responsive muscle) OS=Mus musculus GN=Ankrd2 PE=2 SV=1 - [B2RS77_MOUSE]	3.607
Q7TSH2	Phosphorylase b kinase regulatory subunit beta OS=Mus musculus GN=Phkb PE=1 SV=1 - [KPBB_MOUSE]	3.602
Q62234	Myomesin-1 OS=Mus musculus GN=Myom1 PE=1 SV=2 - [MYOM1_MOUSE]	3.573
J3QNP9	Protein Gm590 OS=Mus musculus GN=Gm590 PE=4 SV=1 - [J3QNP9_MOUSE]	3.468
Q8BZ71	SH3 and cysteine-rich domain-containing protein 3 OS=Mus musculus GN=Stac3 PE=2 SV=1 - [STAC3_MOUSE]	3.436
Q8R429	Sarcoplasmic/endoplasmic reticulum calcium ATPase 1 OS=Mus musculus GN=Atp2a1 PE=2 SV=1 - [AT2A1_MOUSE]	3.412
P0C5K1	Serine/threonine-protein kinase SBK2 OS=Mus musculus GN=Sbk2 PE=2 SV=2 - [SBK2_MOUSE]	3.329
Q9R059	Four and a half LIM domains protein 3 OS=Mus musculus GN=Fhl3 PE=2 SV=2 - [FHL3_MOUSE]	3.272
P70402	Myosin-binding protein H OS=Mus musculus GN=Mybph PE=1 SV=2 - [MYBPH_MOUSE]	3.263
O08528	Hexokinase-2 OS=Mus musculus GN=Hk2 PE=1 SV=1 - [HXK2_MOUSE]	3.237
E9QJU4	Myozenin-3 OS=Mus musculus GN=Myoz3 PE=4 SV=1 - [E9QJU4_MOUSE]	3.230
F6QI82	Chloride channel protein 1 (Fragment) OS=Mus musculus GN=Clcn1 PE=4 SV=1 - [F6QI82_MOUSE]	3.182
O09165	Calsequestrin-1 OS=Mus musculus GN=Casq1 PE=2 SV=3 - [CASQ1_MOUSE]	3.170
Q9D1F9	Protein Slc37a4 OS=Mus musculus GN=Slc37a4 PE=2 SV=1 - [Q9D1F9_MOUSE]	3.146

Q8CC36	Cerebral dopamine neurotrophic factor OS=Mus musculus GN=Cdnf PE=1 SV=1 - [CDNF_MOUSE]	3.134
Q8BGT5	Alanine aminotransferase 2 OS=Mus musculus GN=Gpt2 PE=2 SV=1 - [ALAT2_MOUSE]	3.116
O88492	Perilipin-4 OS=Mus musculus GN=Plin4 PE=1 SV=2 - [PLIN4_MOUSE]	3.087
P57787	Monocarboxylate transporter 4 OS=Mus musculus GN=Slc16a3 PE=1 SV=1 - [MOT4_MOUSE]	3.056
O70548	Telethonin OS=Mus musculus GN=Tcap PE=2 SV=1 - [TELT_MOUSE]	3.035
Q9QYG0-2	Isoform 2 of Protein NDRG2 OS=Mus musculus GN=Ndrg2 - [NDRG2_MOUSE]	3.017
Q6P8J7	Creatine kinase S-type, mitochondrial OS=Mus musculus GN=Ckmt2 PE=1 SV=1 - [KCRS_MOUSE]	3.004
Q9JKS4-6	Isoform 6 of LIM domain-binding protein 3 OS=Mus musculus GN=Ldb3 - [LDB3_MOUSE]	2.964
Q91V77	Protein S100-A1 OS=Mus musculus GN=S100a1 PE=4 SV=1 - [Q91V77_MOUSE]	2.943
P07934	Phosphorylase b kinase gamma catalytic chain, skeletal muscle/heart isoform OS=Mus musculus GN=Phkg1 PE=2 SV=3 - [PHKG1_MOUSE]	2.930
Q9CRA2	PDZ and LIM domain protein 5 OS=Mus musculus GN=Pdlim5 PE=2 SV=1 - [Q9CRA2_MOUSE]	2.922
Q8VCR8	Myosin light chain kinase 2, skeletal/cardiac muscle OS=Mus musculus GN=Mylk2 PE=2 SV=2 - [MYLK2_MOUSE]	2.900
P14094	Sodium/potassium-transporting ATPase subunit beta-1 OS=Mus musculus GN=Atp1b1 PE=1 SV=1 - [AT1B1_MOUSE]	2.890
P13707	Glycerol-3-phosphate dehydrogenase [NAD(+)], cytoplasmic OS=Mus musculus GN=Gpd1 PE=1 SV=3 - [GPDA_MOUSE]	2.872
P14142	Solute carrier family 2, facilitated glucose transporter member 4 OS=Mus musculus GN=Slc2a4 PE=1 SV=3 - [GTR4_MOUSE]	2.736
Q7TNG8	Probable D-lactate dehydrogenase, mitochondrial OS=Mus musculus GN=Ldhd PE=1 SV=1 - [LDHD_MOUSE]	2.715
Q02566	Myosin-6 OS=Mus musculus GN=Myh6 PE=1 SV=2 - [MYH6_MOUSE]	2.712
Q6PIE5	Sodium/potassium-transporting ATPase subunit alpha-2 OS=Mus musculus GN=Atp1a2 PE=1 SV=1 - [AT1A2_MOUSE]	2.710
Q91WC3	Long-chain-fatty-acid--CoA ligase 6 OS=Mus musculus GN=Acsl6 PE=2 SV=1 - [ACSL6_MOUSE]	2.708
Q8BH86-2	Isoform 2 of UPF0317 protein C14orf159 homolog, mitochondrial OS=Mus musculus - [CN159_MOUSE]	2.702
A2A542	Voltage-dependent L-type calcium channel subunit beta-1 OS=Mus musculus GN=Cacnb1 PE=2 SV=1 - [A2A542_MOUSE]	2.678
Q9ET80	Junctophilin-1 OS=Mus musculus GN=Jph1 PE=1 SV=1 - [JPH1_MOUSE]	2.660
Q9DCM2	Glutathione S-transferase kappa 1 OS=Mus musculus GN=Gstk1 PE=1 SV=3 - [GSTK1_MOUSE]	2.640
P28650	Adenylosuccinate synthetase isozyme 1 OS=Mus musculus GN=Adssl1 PE=1 SV=2 - [PURA1_MOUSE]	2.638
Q5SX40	Myosin-1 OS=Mus musculus GN=Myh1 PE=1 SV=1 - [MYH1_MOUSE]	2.634
P05064	Fructose-bisphosphate aldolase A OS=Mus musculus GN=Aldoa PE=1 SV=2 - [ALDOA_MOUSE]	2.623
P35385	Heat shock protein beta-7 OS=Mus musculus GN=Hspb7 PE=1 SV=3 - [HSPB7_MOUSE]	2.621

Supplementary Table 2b: Top 50 proteins exhibiting decreased expression between P12-P24 in the lumbrical muscles

Accession	Description	P24/P12 Ratio
P28667	MARCKS-related protein OS=Mus musculus GN=Marcksl1 PE=1 SV=2 - [MRP_MOUSE]	0.206
Q9D1D6	Collagen triple helix repeat-containing protein 1 OS=Mus musculus GN=Cthrc1 PE=2 SV=2 - [CTHR1_MOUSE]	0.225
P06837	Neuromodulin OS=Mus musculus GN=Gap43 PE=1 SV=1 - [NEUM_MOUSE]	0.229
Q01320	DNA topoisomerase 2-alpha OS=Mus musculus GN=Top2a PE=1 SV=2 - [TOP2A_MOUSE]	0.245
P97311	DNA replication licensing factor MCM6 OS=Mus musculus GN=Mcm6 PE=1 SV=1 - [MCM6_MOUSE]	0.249
P13541	Myosin-3 OS=Mus musculus GN=Myh3 PE=2 SV=2 - [MYH3_MOUSE]	0.256
P26645	Myristoylated alanine-rich C-kinase substrate OS=Mus musculus GN=Marcks PE=1 SV=2 - [MARCS_MOUSE]	0.258
Q07646-2	Isoform 2 of Mesoderm-specific transcript protein OS=Mus musculus GN=Mest - [MEST_MOUSE]	0.272
P25206	DNA replication licensing factor MCM3 OS=Mus musculus GN=Mcm3 PE=1 SV=2 - [MCM3_MOUSE]	0.283
Q91XV3	Brain acid soluble protein 1 OS=Mus musculus GN=Basp1 PE=1 SV=3 - [BASP1_MOUSE]	0.299
D3Z1Z8	Stathmin (Fragment) OS=Mus musculus GN=Stmn1 PE=2 SV=1 - [D3Z1Z8_MOUSE]	0.300
E9PWG6	Protein Ncapg OS=Mus musculus GN=Ncapg PE=4 SV=1 - [E9PWG6_MOUSE]	0.306
P49718	DNA replication licensing factor MCM5 OS=Mus musculus GN=Mcm5 PE=2 SV=1 - [MCM5_MOUSE]	0.311
P01837	Ig kappa chain C region OS=Mus musculus PE=1 SV=1 - [IGKC_MOUSE]	0.312
P70677	Caspase-3 OS=Mus musculus GN=Casp3 PE=1 SV=1 - [CASP3_MOUSE]	0.319
Q9ET66	Peptidase inhibitor 16 OS=Mus musculus GN=Pi16 PE=2 SV=1 - [PI16_MOUSE]	0.322
P13542	Myosin-8 OS=Mus musculus GN=Myh8 PE=1 SV=2 - [MYH8_MOUSE]	0.322
P97321-3	Isoform 3 of Seprase OS=Mus musculus GN=Fap - [SEPR_MOUSE]	0.325
P62965	Cellular retinoic acid-binding protein 1 OS=Mus musculus GN=Crabp1 PE=1 SV=2 - [RABP1_MOUSE]	0.326
O35646	Calpain-6 OS=Mus musculus GN=Capn6 PE=1 SV=2 - [CAN6_MOUSE]	0.332
Q05186	Reticulocalbin-1 OS=Mus musculus GN=Rcn1 PE=1 SV=1 - [RCN1_MOUSE]	0.341
Q8BH97	Reticulocalbin-3 OS=Mus musculus GN=Rcn3 PE=2 SV=1 - [RCN3_MOUSE]	0.350
Q6WVG3	BTB/POZ domain-containing protein KCTD12 OS=Mus musculus GN=Kctd12 PE=1 SV=1 - [KCD12_MOUSE]	0.355
Q61881	DNA replication licensing factor MCM7 OS=Mus musculus GN=Mcm7 PE=2 SV=1 - [MCM7_MOUSE]	0.357

Q3V1T4	Prolyl 3-hydroxylase 1 OS=Mus musculus GN=Lepre1 PE=2 SV=2 - [P3H1_MOUSE]	0.358
P61750	ADP-ribosylation factor 4 OS=Mus musculus GN=Arf4 PE=2 SV=2 - [ARF4_MOUSE]	0.371
P26350	Prothymosin alpha OS=Mus musculus GN=Ptma PE=1 SV=2 - [PTMA_MOUSE]	0.376
Q8C167-2	Isoform 2 of Prolyl endopeptidase-like OS=Mus musculus GN=Prepl - [PPCEL_MOUSE]	0.379
Q8CG48	Structural maintenance of chromosomes protein 2 OS=Mus musculus GN=Smc2 PE=1 SV=2 - [SMC2_MOUSE]	0.380
Q9Z247	Peptidyl-prolyl cis-trans isomerase FKBP9 OS=Mus musculus GN=Fkbp9 PE=1 SV=1 - [FKBP9_MOUSE]	0.381
P01864	Ig gamma-2A chain C region secreted form OS=Mus musculus PE=1 SV=1 - [GCAB_MOUSE]	0.386
Q8K297	Procollagen galactosyltransferase 1 OS=Mus musculus GN=Colgalt1 PE=1 SV=2 - [GT251_MOUSE]	0.388
Q60715-2	Isoform 2 of Prolyl 4-hydroxylase subunit alpha-1 OS=Mus musculus GN=P4ha1 - [P4HA1_MOUSE]	0.392
Q5I012-4	Isoform 4 of Putative sodium-coupled neutral amino acid transporter 10 OS=Mus musculus GN=Slc38a10 - [S38AA_MOUSE]	0.397
Q922W5	Pyrroline-5-carboxylate reductase 1, mitochondrial OS=Mus musculus GN=Pycr1 PE=1 SV=1 - [P5CR1_MOUSE]	0.403
P09535	Insulin-like growth factor II OS=Mus musculus GN=Igf2 PE=1 SV=1 - [IGF2_MOUSE]	0.410
Q3UQ28	Peroxidasin homolog OS=Mus musculus GN=Pxdn PE=2 SV=2 - [PXDN_MOUSE]	0.415
P41731	CD63 antigen OS=Mus musculus GN=Cd63 PE=1 SV=2 - [CD63_MOUSE]	0.417
P19324	Serpin H1 OS=Mus musculus GN=Serpinh1 PE=1 SV=3 - [SERPH_MOUSE]	0.423
P50543	Protein S100-A11 OS=Mus musculus GN=S100a11 PE=2 SV=1 - [S10AB_MOUSE]	0.424
Q9QXS6-3	Isoform E2 of Drebrin OS=Mus musculus GN=Dbn1 - [DREB_MOUSE]	0.426
Q62356	Follistatin-related protein 1 OS=Mus musculus GN=Fstl1 PE=1 SV=2 - [FSTL1_MOUSE]	0.428
Q8BZQ7	Anaphase-promoting complex subunit 2 OS=Mus musculus GN=Anapc2 PE=1 SV=2 - [ANC2_MOUSE]	0.431
Q9D1M7	Peptidyl-prolyl cis-trans isomerase FKBP11 OS=Mus musculus GN=Fkbp11 PE=2 SV=1 - [FKB11_MOUSE]	0.431
P27046	Alpha-mannosidase 2 OS=Mus musculus GN=Man2a1 PE=1 SV=2 - [MA2A1_MOUSE]	0.433
Q9JIG8	PRA1 family protein 2 OS=Mus musculus GN=Praf2 PE=2 SV=1 - [PRAF2_MOUSE]	0.435
P29351-3	Isoform 3 of Tyrosine-protein phosphatase non-receptor type 6 OS=Mus musculus GN=Ptpn6 - [PTN6_MOUSE]	0.436
Q9JI44	DNA methyltransferase 1-associated protein 1 OS=Mus musculus GN=Dmap1 PE=1 SV=1 - [DMAP1_MOUSE]	0.436
Q8BV57	Soluble scavenger receptor cysteine-rich domain-containing protein SSC5D OS=Mus musculus GN=Ssc5d PE=1 SV=1 - [SRCRL_MOUSE]	0.436
Q9Z110-2	Isoform Short of Delta-1-pyrroline-5-carboxylate synthase OS=Mus musculus GN=Aldh18a1 - [P5CS_MOUSE]	0.437

Appendix 3

Supplementary Table 3: Statistically altered functional clusters of **unfiltered proteins** exhibiting consistent alterations in expression in sciatic nerve from P12 to P24.

Up from P12-P24 in Nerve		**Down from P12-P24 in Nerve**	
Cluster Name	Enrichment Score	Cluster Name	Enrichment Score
Oxidation reduction	4.82	Ribonucleoprotein complex/RNA processing	19.47
Membrane-bound vesicles	3.86	RNA processing/RNA binding	11.92
Actin binding	3.58	Intracellular organelle lumen	10.28
Aldehyde dehydrogenase (NAD-dependant)	3.14	Endoplasmic reticulum	8.98
Actin cytoskeleton	3.11	Ribosomal activity	8.12
Calcium binding	3.04	Endoplasmic reticulum membrane	5.59
Nucleotide binding	3.01	WD40-repeat motif	3.95
Vesicular endocytosis	2.73	Translation initiation factors	3.65
Calcium binding	2.61	Ribonucleoprotein complex biogenesis	3.38
Magnesium binding	2.43	Like-Sm (L-Sm) ribonucleoprotein core	3.36

Appendix 4

Supplementary Table 4: Statistically altered functional clusters of **unfiltered proteins** exhibiting consistent alterations in expression in lumbrical muscles from P12 to P24.

Up from P12-P24 in Muscle		**Down from P12-P24 in Muscle**	
Cluster Name	Enrichment Score	Cluster Name	Enrichment Score
Mitochondria	125.7	Endoplasmic reticulum	7.56
Electron transport chain/ oxidative phosphorylation	47.34	Protein transport	7.07
Myofibril contraction	19.74	Cytoskeletal protein binding	5.86
Mitochondrial matrix	18.83	Membrane-bound vesicle	5.66
Mitochondrial electron chain transport	14.32	Lysosomes	5.63
Redox cofactor	11.44	Vesicular transport	4.73
Glucose metabolism	11.41	Lipid binding	4.55
Cellular respiration	10.79	Golgi-associated vesicular transport	4.21
Nucleotide binding	8.23	Endoplasmic reticulum	3.5
ATP decomposition	6.88	Actomyosin cortex	3.22

Appendix 5

Poster presentations and published abstracts.

Alannah J Mole*, **Rachel A Kline*,** Natalie L Courtney* and Lyndsay M Murray (2016). The relationship and consequence of neuromuscular junction pathology and p53 pathway activation in mouse models of spinal muscular atrophy. *Equal contribution

Conference poster and abstract: 20th International SMA Researcher Meeting, Anaheim, CA, USA.

Natalie L Courtney, Penelope Boyd, Jollil Ross, Erkan Y Osman, Kevin Kaifer, **Rachel A Kline,** Ariana Tiberi, Thomas H Gillingwater, Chris Lorson and Lyndsay M Murray (2016). Modifiers of motor neuron vulnerability in mouse models of SMA.

Conference poster and abstract: 20th International SMA Researcher Meeting, Anaheim, CA, USA.

Rachel A Kline, Natalie L Courtney, Alannah J Mole and Lyndsay M Murray (2016)**.** When do motor neurons get sick in SMA?

Conference poster and abstract: 20th International SMA Researcher Meeting, Anaheim, CA, USA.

Rachel A Kline and Lyndsay M Murray (2016). Motor Neurons in Spinal Muscular Atrophy: “How much damage is too much damage?”

Poster presentation: The Anne Rowling Regenerative Neurology Clinic and Euan MacDonald Centre Open Night, Edinburgh, UK.